

DISSERTATION

ESTIMATION OF SNOW MICROPHYSICAL PROPERTIES WITH APPLICATION
TO MILLIMETER-WAVELENGTH RADAR RETRIEVALS FOR SNOWFALL RATE

Submitted By

Norman Bryce Wood

Department of Atmospheric Science

In partial fulfillment of the requirements

For the Degree of Doctor of Philosophy

Colorado State University

Fort Collins, Colorado

Summer 2011

Doctoral Committee:

Advisor: Graeme L. Stephens

William R. Cotton
Steven R. Fassnacht
Christian D. Kummerow
Sergey Y. Matrosov

Copyright by Norman Bryce Wood 2011

All Rights Reserved

ABSTRACT

ESTIMATION OF SNOW MICROPHYSICAL PROPERTIES WITH APPLICATION TO MILLIMETER-WAVELENGTH RADAR RETRIEVALS OF SNOWFALL RATE

The need for measuring snowfall is driven by the roles snow plays providing freshwater resources and affecting climate. Snow accumulations are an important resource for ecological and human needs and in many areas appear vulnerable to climate change. Snow cover modifies surface heat fluxes over areas extensive enough to influence climate at regional and perhaps global scales. Seasonal runoff from snowmelt, along with over-ocean snowfall, contributes to freshening in the Arctic and high-latitude North Atlantic oceans. Yet much of the Earth's area for which snowfall plays such significant roles is not well-monitored by observations.

Radar reflectivity at 94 GHz is sensitive to scattering by snow particles and CloudSat, in a near-polar orbit, provides vertically resolved measurements of 94 GHz reflectivity at latitudes from 82 N to 82 S. While not global in areal coverage, CloudSat does provide observations sampled from regions where snowfall is the dominant form of precipitation and an important component of hydrologic processes. The work presented in this study seeks to exploit these observations by developing and assessing a physically-base snowfall retrieval which uses an explicit representation of snow microphysical properties.

As the reflectivity-based snowfall retrieval problem is significantly underconstrained, a priori information about snow microphysical properties is required. The approaches typically used to develop relations between reflectivity and snowfall rate, so-called Ze-S relations, require assumptions about particle properties such as mass, area, fallspeed, and shape. Limited information about the distributions of these properties makes difficult the

characterization of how uncertainties in the properties influence uncertainties in the Ze-S relations.

To address this, the study proceeded in two parts. In the first, probability distributions for snow particle microphysical properties were assessed using optimal estimation applied to multi-sensor surface-based snow observations from a field campaign. Mass properties were moderately well determined by the observations, the area properties less so. The retrieval revealed nontrivial correlations between mass and area parameters not apparent in prior studies. Synthetic testing showed that the performance of the retrieval was hampered by uncertainties in the fallspeed forward model. The mass and area properties obtained from this retrieval were used to construct particle models including 94 GHz scattering properties for dry snow. These properties were insufficient to constrain scattering properties to match observed 94 GHz reflectivities. Vertical aspect ratio supplied a sufficient additional constraint.

In the second part, the CloudSat retrieval, designed to estimate vertical profiles of snow size distribution parameters from reflectivity profiles, was applied to measurements from the field campaign and from an orbit of CloudSat observations. Uncertainties in the mass and area microphysical properties, obtained from the first part of this study, were substantial contributors to the uncertainties in the retrieved snowfall rates. Snowfall rate fractional uncertainties were typically 140% to 200%. Accumulations of snowfall calculated from the retrieval results matched observed accumulations to within 13%, however, when allowances were made for snowfall with properties likely inconsistent with the snow particle model. Information content metrics showed that the size distribution slope parameters were moderately to strongly constrained by the reflectivity observations, while the intercept parameters were determined primarily by the a priori constraints. Results from the CloudSat orbit demonstrated the ability of the CloudSat retrieval to represent a range of scene-dependent Ze-S relations.

ACKNOWLEDGMENTS

One of the pleasant consequences of an extended research project is the opportunity to work with many talented and supportive people. I've benefited greatly from the support of my advisor, Dr. Graeme Stephens, and thank him for that and for his willingness to allow me to pursue this research on a rather independent path. Dr. Tristan L'Ecuyer has provided unflinching encouragement for this work and freely shared his advice and expertise when needed. My interactions with him have been a great source of inspiration and insight, and I owe him a particular and significant debt of gratitude. My discussions with Mick Christi and Drs. Richard Austin, John Haynes, Sue van den Heever, Derek Posselt, and Kentaroh Suzuki in particular have also helped shape the course of this research.

My appreciation goes to my committee members: Dr. Bill Cotton, Dr. Steven Fassnacht, Dr. Chris Kummerow, and Dr. Sergey Matrosov for their ongoing willingness to serve and support this project.

My thanks also go to Noel Bryant, whose support with administration and group resources has allowed me to focus on the needs of this research; to Jamie Schmidt, who has repeatedly helped me work through the hiccups of this doctoral program; and to Natalie Tourville, Ian Wittmeyer, and Dr. Matt Rogers, who have often helped keep much-needed computing resources functioning.

Much of this work relies on observations obtained during the C3VP field campaign, a project jointly sponsored by Environment Canada, NASA, and the Department of Defense Center for Geosciences/Atmospheric Research. Dr. David Hudak and Peter Rodriguez of Environment Canada were centrally involved in C3VP's execution and the subsequent management of its data. Dr. Larry Bliven of NASA provided the SVI observations used throughout, and Gwo-Jong Huang of Colorado State University shared his reanalysis of 2DVD observations from C3VP. Drs. Frederic Fabry of McGill University and Rob Cifelli of

the Cooperative Institute for Research in the Atmosphere also provided data and advice. Dr. Andy Heymsfield of NCAR has been a great resource for discussions of snow microphysics and measurements. I thank them for generously sharing their expertise and time.

Finally and most importantly, my wife Jill and children Avery and Connor have given me the incentive to pursue this work. They have patiently and lovingly accepted the demands placed on them as this project was completed, and for that I will be always grateful.

Financial support for this work was provided by the National Aeronautics and Space Administration through research grant #NAS5-99327 for CloudSat activities. CloudSat observations were provided by the CloudSat Data Processing Center at Colorado State University. Computing resources for discrete dipole modeling were provided by the Community Computing Facility of the National Center for Atmospheric Research through its allocations program for graduate students. Much of the computing and analysis for this work was performed using open source software, principally Python and its libraries SciPy and NumPy, with graphics created by XmGrace and Gnuplot.

TABLE OF CONTENTS

List of Symbols	ix
1 Introduction	1
1.1 Objectives and outline	6
2 C3VP Events	8
2.1 Observations	9
2.1.1 Particle size and fallspeed	9
2.1.2 Radar reflectivity	12
2.1.3 Snowfall rate	12
2.2 Snowfall events	14
3 The snow microphysics retrieval method	22
3.1 Optimal estimation method	22
3.2 Forward model governing equations	25
3.3 Forward model implementation	29
3.4 a priori estimates of the state	34
4 Measurement and forward model uncertainties	42
4.1 Measurement uncertainties \mathbf{S}_y	44
4.1.1 Radar reflectivity	44
4.1.2 Snowfall rate	50
4.1.3 Size resolved fallspeeds	51
4.2 Forward model uncertainties \mathbf{S}_F	54
4.2.1 Radar reflectivity forward model	54

4.2.1.1	Uncertainties due to backscattering properties	54
4.2.1.2	Uncertainties due to discretization and truncation	58
4.2.2	Snowfall rate	61
4.2.3	Fallspeeds	63
4.3	Uncertainties due to parameters \mathbf{S}_B	66
4.3.1	Size distribution uncertainties	67
4.3.2	Variances for other parameters	76
5	Snow microphysics retrieval: Performance and results	77
5.1	Synthetic test cases	77
5.1.1	Results of synthetic tests	80
5.2	Application to C3VP snowfall events	86
5.2.1	Retrieved properties	86
5.3	Uncertainties and observing system design	94
6	Particle models	97
6.1	The discrete dipole approximation (DDA) method	100
6.1.1	Particle shapes	102
6.2	Construction of dipole arrays	104
6.3	DDA calculations	106
6.3.1	Scattering properties	108
6.4	Assessments	113
6.4.1	SVI dataset	113
6.4.2	Shape and reflectivity	114
6.4.3	Random dipole effects	117
6.4.4	Truncation and discretization	117
7	The CloudSat snowfall retrieval	123
7.1	CloudSat and the Cloud Profiling Radar	124
7.2	Retrieval formulation	126
7.2.1	Theoretical basis	126

7.2.1.1	Size distribution	129
7.2.2	Retrieval implementation	130
7.3	Measurement and forward model uncertainties \mathbf{S}_ϵ	134
7.3.1	Measurement uncertainties \mathbf{S}_y	135
7.3.2	Forward model uncertainties \mathbf{S}_F	136
7.3.3	Uncertainties due to parameters, $\mathbf{S}_B^{ss,na}$	138
7.3.3.1	Estimating \mathbf{K}_b	140
7.3.4	Uncertainties due to other forward model assumptions, $\mathbf{S}_F^{ss,na}$	145
7.3.4.1	Uncertainties due to shape	145
7.3.4.2	Uncertainties due to assumed size distribution form	148
7.3.4.3	Estimate of $\mathbf{S}_F^{ss,na}$	148
7.4	Scene characterization	151
7.5	A priori estimate of the state	152
7.6	Snowfall estimation	157
8	Retrieval Results	163
8.1	Application to ACR observations	163
8.1.1	Information content	168
8.2	An application to CloudSat observations	175
8.2.1	Snowfall rate uncertainties	177
8.2.2	Reflectivity-snowfall rate relations	180
8.2.3	Results from CARE	184
9	Discussion and conclusions	193
9.1	Overview of the method	194
9.2	Principal results	196
9.2.1	The snow microphysics retrieval	196
9.2.2	The CloudSat snowfall retrieval	197
9.3	Prospects for future work	199
	Bibliography	202

Appendix A	Disdrometer dimensional errors	216
Appendix B	A priori data sets	220
B.1	Analysis of Kajikawa observations	220

List of Symbols

a_0	MH2005 Reynolds number correction coefficient
A	The averaging kernel matrix, or “A matrix”
A_p	Snow particle horizontally-projected area
α	Snow particle mass coefficient
$\tilde{\mathbf{b}}$	Forward model parameters
b_0	MH2005 Reynolds number correction exponent
β	Snow particle mass exponent
β_{ext}	Volume extinction coefficient
C_0	Limiting drag coefficient
C_d	Drag coefficient \mathbf{x} State vector
d	Dipole spacing for discrete dipole models
d_s	Degrees of freedom for signal
D_M	Snow particle maximum dimension
D_{obs}	Snow particle observed dimension (e.g., by disdrometer)
D_{ev}	Equivalent volume diameter
δ_0	Particle boundary layer thickness parameter
ΔD_i	Size distribution bin widths
f	In relation to the SVI, a factor that relates particle size to depth of field. In other contexts, a fractional uncertainty.
f_{Ze}	Fractional uncertainty in Ze
$\mathbf{F}(\mathbf{x}, \tilde{\mathbf{b}})$	Forward model

ϕ	Effective ratio of D_{obs} to D_M
γ	Snow particle A_p coefficient
H	Shannon information content
k	Radar specific attenuation
k_{abs}	Gas mass absorption coefficient
$\ K_i\ ^2$	Radar dielectric factor for ice
$\ K_w\ ^2$	Radar dielectric factor for water
\mathbf{K}	Jacobian of the forward model with respect to the state
$\tilde{\mathbf{K}}$	Jacobian of the forward model with respect to the retrieved state
\mathbf{K}_b	Jacobian of the forward model with respect to the forward model parameters, $\tilde{\mathbf{b}}$
$\hat{\mathbf{K}}_{P,x}$	Jacobian of the snowfall rate P with respect to the state vector
$\hat{\mathbf{K}}_{P,b}$	Jacobian of the snowfall rate P with respect to parameters used to calculate P
\mathbf{K}_v	Jacobian of the forward model with respect to fallspeeds
λ	Slope parameter of exponential size distribution
λ_{ap}	a priori estimate of λ
Λ	Radar wavelength
μ	In the context of fallspeeds, the dynamic viscosity of air
n_{ice}	Complex refractive index of ice
n_{liq}	Complex refractive index of liquid water
N_0	Intercept parameter of exponential size distribution
$N_{0,ap}$	a priori estimate of N_0

p	Atmospheric pressure
P	Precipitation (snowfall) rate
Q_{ext}	Particle extinction efficiency
Q_{bk}	Differential backscattering cross-section normalized by πr_{ev}^2
r_A	Snow particle area ratio
r_{ev}	Equivalent volume radius
Re	Reynolds number
ρ_a	Density of air
ρ_{ice}	Density of ice
ρ_{liq}	Density of liquid water
$\boldsymbol{\rho}_v$	Fallspeed error correlation matrix
$s^2(x)$	Variance of variable x
$s(x, y)$	Covariance of variables x and y
S	In the context of Ze-S relations, snowfall rate
\mathbf{S}_a	Covariance matrix representing uncertainties in the a priori estimate of the state
\mathbf{S}_b	Covariance matrix representing uncertainties in forward model parameters $\tilde{\mathbf{b}}$
\mathbf{S}_B	Covariance matrix representing forward model uncertainties due to uncertainties in forward model parameters, \mathbf{S}_b
$\mathbf{S}_B^{ss,na}$	\mathbf{S}_B specifically for the forward model for singly-scattered, nonattenuated equivalent reflectivity factor
\mathbf{S}_F	Covariance matrix representing forward model uncertainties
$\mathbf{S}_F^{ss,na}$	\mathbf{S}_F specifically for the forward model for singly-scattered, nonattenuated equivalent reflectivity factor

$\mathbf{S}_{F,v}$	Covariance matrix representing uncertainties in the forward model due to uncertainties in fallspeeds
$\hat{\mathbf{S}}_p$	Covariance matrix describing uncertainties in snowfall rate P at the retrieved state
$\hat{\mathbf{S}}_{P,b}$	Covariance matrix describing uncertainties in snowfall rate P at the retrieved state, specifically due to uncertainties in parameters used to calculate P
$\hat{\mathbf{S}}_{P,exp}$	Covariance matrix describing uncertainties in snowfall rate P at the retrieved state, specifically due to uncertainties caused by the assumption of an exponential distribution
$\hat{\mathbf{S}}_{P,v}$	Covariance matrix describing uncertainties in snowfall rate P at the retrieved state, specifically due to uncertainties in fallspeeds
$\hat{\mathbf{S}}_{P,x}$	Covariance matrix describing uncertainties in snowfall rate P at the retrieved state, specifically due to uncertainties in the retrieved state
\mathbf{S}_v	Covariance matrix representing uncertainties in fallspeeds
$\hat{\mathbf{S}}_x$	Covariance matrix representing uncertainties in the retrieved state
\mathbf{S}_y	Covariance matrix representing measurement uncertainties
\mathbf{S}_ϵ	Covariance matrix representing total uncertainties, due to both forward model and measurement uncertainties
σ	Snow particle A_p exponent
σ_{bk}	Particle backscattering cross-section
σ_{ext}	Particle extinction cross-section
T	Atmospheric temperature
\mathcal{T}	Radar one-way transmission
$\hat{\mathbf{x}}$	Retrieved state vector

\mathbf{x}_a	a priori estimate of the state vector
X	Davies, or Best, number
\mathbf{y}	Observation vector
Z_e	Equivalent radar reflectivity factor
$Z_e^{ss,a}$	Singly-scattered, attenuated equivalent reflectivity factor
$Z_e^{ms,a}$	Multiply-scattered, attenuated equivalent reflectivity factor
$Z_e^{ss,na}$	Singly-scattered, nonattenuated equivalent reflectivity factor
2DVD	2-D Video Disdrometer
ACR	Airborne Cloud Radar
B6r	6-armed bullet rosette snow particle
B6pf	Branched 6-arm thick planar particle with porosities
B8pr-30	Branched 8-arm spatial particle with porosities, 0.5 aspect ratio
B8pr-45	Branched 8-arm spatial particle with porosities, 0.71 aspect ratio
BP1	Branched plate (broad-branched) snow particle
BP2	Branched plate (stellar) snow particle
C3VP	Canadian CloudSat/CALIPSO Validation Project
CALIOP	Cloud-Aerosol Lidar with Orthogonal Polarization
CALIPSO	Cloud-Aerosol Lidar and Infrared Pathfinder Satellite Observation
CARE	Centre for Atmospheric Research Experiments
CLEX-10	The Tenth Cloud Layer Experiment
CPR	Cloud Profiling Radar

CVI	Counterflow Virtual Impactor
DDA	Discrete dipole approximation
DDSCAT	Discrete dipole approximation scattering software
DFIR	Double fence intercomparison reference
Ep	Scalene ellipsoid snow particle with porosities
FD12P	Vaisala FD12P weather sensor
HC	Hexagonal column snow particle
HP	Hexagonal plate snow particle
HPp	Hexagonal plate with porosities
HW2010	Heymsfield and Westbrook, 2010 fallspeed model
LWE	Liquid water equivalent
MH2005	Mitchell and Heymsfield, 2005 fallspeed model
MSC	Meteorological Service of Canada
MSL	Mean sea level
OE	Optimal estimation
PDF	Probability density function
POLPPI	Polarized plan-position indicator
POSS	Precipitation Occurrence Sensor System
RSD	Residual standard deviation
SPp	Branched plate-like shape with 6 branches and porosities
SVI	Snow Video Imager

VertiX	Vertically-pointing X-band radar
WKR	Meteorological Service of Canada's King City radar
WMO	World Meteorological Organization

Chapter 1

Introduction

Snow and snow cover are significant components of the Earth's hydrologic and climate systems. For large areas of the Earth, fresh water to meet the needs of riverine ecosystems, of agriculture, of human consumption, or of hydroelectric power generation derives principally from snowmelt. Barnett et al. (2005) described them as including much of the Earth's land surface poleward of $\pm 45^\circ$, and most mountainous terrain except that nearest the equator. In their study, Barnett et al. specifically looked at areas where limited storage capacity would put these freshwater resources at risk under climate change scenarios, a subset of the total area dependent on snow for water resources. They found that nearly one-sixth of the world's population live in these areas classified as snowpack-dependent and at-risk, and approximately one-fourth of the global gross domestic product originates from these areas.

Snow and snow cover can have potentially significant climatological impacts at regional and perhaps global scales. Snow cover dramatically increases shortwave surface albedo of most natural surfaces, leading to reduced shortwave radiative heat transfer into the surface. In early energy balance climate models (e.g., Sellers, 1969), a positive feedback mechanism was identified in which increases in snow and ice cover produced cooling which led to further increases in snow and ice cover. The actual role of snow is more complex, involving changes to sensible and latent heat fluxes and to longwave emission from the surface that vary over the life of the snow cover. These other effects may offset or overcome the albedo effect,

leading to increased net heat flux into the snow-covered surface until snowmelt occurs (Cohen and Rind, 1991).

Modeling studies have shown that perturbations to snow cover can have far-ranging consequences. In a study with a general circulation model, Barnett et al. (1989) found that increased snow depths led to cooler surface air and tropospheric temperatures in regions where snow cover was rapidly melting or had recently melted. In their study, increased snow depth over Eurasia was associated with a weaker Asian summer monsoon. Vavrus (2007) examined the effects of terrestrial snow cover on global climate, comparing general circulation model simulations with normal and suppressed snow cover. In addition to tropospheric warming and large increases in the surface areas occupied by permafrost, he found that the occurrence of extreme cold air outbreaks was significantly reduced by the lack of snow cover. Alexander et al. (2010) looked at the impacts of changes to snow cover expected to occur due to greenhouse gas forcing over the span of a century. Reductions in snow cover and snow depth warmed surface air temperatures in the Northern Hemisphere by 1°-3°C during spring and fall seasons. Tropospheric temperatures warmed by as much as 0.6°-0.7°C, and dynamical responses were identified in the troposphere and stratosphere.

Changes in snowfall at higher north latitudes may impact freshening of the North Atlantic Ocean and the strength of the Atlantic Meridional Overturning Circulation. In the central Arctic, surface precipitation is predominantly snow, while over the North Atlantic (and presumably over land surfaces at similar latitudes), surface precipitation varies between rain and snow depending on season (Clark et al., 1996) but is dependent on precipitating ice aloft. Peterson et al. (2006) attributed more than half of the cumulative freshwater input anomaly in the Arctic and high-latitude North Atlantic Oceans over the previous fifty years to increases in net precipitation (precipitation minus evaporation) over land and oceans. The increases from these sources, estimated at 20,000 km³, significantly exceeded the estimated contributions from glacial melt (2000 km³) and also exceeded the contribution from reductions in sea ice (15,000 km³).

An accurate understanding of snow microphysical properties and the processes that produce snow is essential for accurately modeling snow and assessing the susceptibility of snow to future climate perturbations. Representations of these processes in mesoscale models

and higher-resolution climate models use parameterizations that in turn depend on various assumptions about snow microphysical properties. As an example, single-moment bulk microphysical schemes may prognose snow mass mixing ratio, and rely on assumed values for the snow size distribution intercept parameter and snow particle density in order to diagnose other microphysical properties like slope parameter or total number concentration. In many cases, the assumed values are based on mid-latitude observations, and the broader applicability of the assumptions, especially to high-latitude regions where snowfall is the dominant form of precipitation, is not clear. Morrison and Pinto (2006) found that treatments of snow number concentration in microphysical schemes with assumptions based on mid-latitude observations were inadequate for simulating long-lived mixed-phase stratus common to the Arctic.

The microphysical processes that produce snow and control its properties (e.g., depositional growth, riming, aggregation, collisional breakup) are linked to vertical transport plus vertically-varying temperature and humidity. Changes in snow size distributions with height, observed using airborne in situ measurements, have been interpreted as signatures of these microphysical processes (e.g., Lo and Passarelli, 1982). Retrieved profiles of microphysical properties have potential use for evaluating the parameterizations of these processes. Useful evaluations require an understanding of the variability of these properties and the uncertainties inherent in the retrieved quantities.

The launch of CloudSat in April, 2006 made available vertical profiles of 94 GHz radar reflectivity observed at latitudes from 82°N to 82°S. While designed as a cloud radar, scattering by precipitation-sized ice particles is significant at 94 GHz. The CloudSat observations are made at near-nadir, with a footprint of approximately 1.7 km along-track by 1.4 km cross-track (Stephens et al., 2008; Tanelli et al., 2008). The spatial sampling is not suitable for global mapping of surface snowfall, but the vertically-resolved observations, the high spatial resolution and the range of latitudes observed make CloudSat a potentially important platform for the study of snow microphysical properties and processes. With appropriate consideration of sampling statistics, CloudSat observations may also have use in making longer-term (seasonal to annual) estimates of snowfall accumulations.

Retrievals may treat these microphysical properties implicitly or explicitly. This difference is encapsulated in the forward model - the component of the retrieval algorithm that relates the snowfall rate or microphysical state \mathbf{x} to the observations \mathbf{y} . Examples of retrievals for which the microphysical properties are implicit include those that use precalculated Ze-S relationships (Matrosov, 2007; Liu, 2008a; Kulie and Bennartz, 2009) or that use a database of atmospheric columns containing vertically-distributed hydrometeors for which \mathbf{x} and \mathbf{y} have been precalculated (Skofronick-Jackson et al., 2004; Noh et al., 2006). Examples for which the representation of microphysical properties are explicit include those that use a physically-based forward model to relate \mathbf{y} to \mathbf{x} , then apply techniques to invert this relation (e.g., Grecu and Olson, 2008).

The primary difficulty of using explicit microphysics is the complex relation between the microphysical state \mathbf{x} and the observed quantities \mathbf{y} . For radar reflectivity observations, the relevant physical quantities are the size-varying number concentration, backscatter and extinction cross-sections of the snow particles. The backscatter and extinction cross-sections can be related to particle mass and shape. In order to calculate snowfall rate, the horizontally-projected areas of the particles, which are also shape-dependent, are needed as well (Mitchell and Heymsfield, 2005). Particle shape varies widely over the range from small pristine particles to large aggregates. With the simplest of representations for these size-dependent quantities (exponential size distributions, power laws for mass and area as functions of particle size, and assumed shape), the number of unknown microphysical parameters in a single radar bin greatly exceeds the number of measurements, resulting in a significantly underconstrained retrieval problem.

Techniques exist for dealing with such underconstrained problems. Generally, these techniques involve the use of a priori information about the microphysical properties in a Bayesian probabilistic framework. For retrievals using explicit microphysics with physical forward models, the a priori information can also be treated explicitly using variational techniques such as optimal estimation (Rodgers, 2000). With this approach, the a priori information about the microphysical properties is represented using probability density functions (PDFs) which describe the expected values for these properties, their variances, and their covariances. These PDFs become part of a cost function which is then minimized

to obtain a posterior PDF describing the expected values and uncertainties for the retrieved state.

The a priori microphysical information needed for the CloudSat retrieval includes snow particle mass and horizontally-projected area, which together determine fallspeed and a particle's contribution to snowfall rate. These properties are often expressed using power laws on particle size (Mitchell, 1996), and the coefficients and exponents of the power laws function as microphysical parameters. Determining these parameters has typically involved analysis of single-particle observations (e.g., Mitchell et al., 1990; Heymsfield and Westbrook, 2010), or bulk approaches in which particle size distributions are observed and related to an integral property of the distribution like accumulated precipitation or radar reflectivity (e.g., Brandes et al., 2007). Few such studies evaluated mass and area parameters simultaneously, so physical consistency among area and mass parameters has not been assured, and information regarding covariances between the parameters, which can be important retrieval constraints, has been lacking. Especially for the single-particle studies, sample sizes have been small and the studies have been performed primarily in mountain locations, limiting the characterization of uncertainties in the estimated parameters.

Appropriate multi-sensor observations may help determine these parameters, and such suites of observations are becoming more common as elements of snow-focused ground validation campaigns associated with satellite observing missions. These campaigns can provide nearly colocated measurements of bulk properties such as precipitation rate and radar reflectivity at multiple wavelengths, along with size-resolved observations such as snow particle number concentration and fallspeed. Optimal estimation is also well-suited to problems in which multi-sensor observations are used to determine a state defined by multiple parameters. Optimal estimation produces estimates of the expected values for the state variables as well as their variances and the covariances between them. The simultaneous determination of multiple parameters related to mass and horizontally-projected area ensures their physical consistency, and the automated nature of most of the relevant measurements ensures substantial sampling during snowfall events. While the locations at which ground validation campaigns have been conducted are limited, the potential exists for such campaigns to observe varied locations and snow regimes.

1.1 Objectives and outline

The work presented in this study focused in two areas. In the first area, an effort was made to improve the characterization of snow microphysical properties and their uncertainties. A novel optimal estimation retrieval scheme was developed which estimates detailed snow microphysical properties using intensive ground-based observations of snowfall. In this retrieval, observations of snowfall rate, snow particle size distribution, size-resolved fallspeeds and 9.35 GHz radar reflectivity are used to estimate the parameters of power laws describing particle mass and horizontally-projected area as functions of particle size. The retrieval results are expressed in terms of a PDF which defines the expected values and uncertainties for these parameters. This snow microphysics retrieval was applied to four snowfall events, two involving stratiform snowfall and two involving lake effect snow, from a ground validation campaign (the Canadian CloudSat/CALIPSO Validation Project, or C3VP; Hudak et al., 2006a) held in southern Ontario in 2006-2007.

For this first part, the observations used for the snow microphysics retrieval are described in Chapter 2, followed by a description of the retrieval method and the necessary a priori estimates of the state to be retrieved in Chapter 3. Next, the uncertainties for the multi-sensor observations and their forward models are derived in Chapter 4. Finally, the retrieval is applied first to synthetic test cases which are used to evaluate the retrieval performance, then to actual observations from C3VP with the results presented in Chapter 5.

In the second area, the objective was to exploit the capabilities of CloudSat by developing and evaluating a physically-based retrieval with explicit microphysics for use with vertical profiles of 94 GHz radar reflectivity. This retrieval was formulated using optimal estimation with a priori constraints to address the underconstrained nature of the problem. A priori constraints on microphysical properties were constructed using results from the snow microphysics retrieval, along with other surface and aircraft-based in situ observations of snow from C3VP. The snow microphysics retrieval results were also used to construct radar scattering models that were physically consistent with the a priori microphysical properties. Evaluations of the retrieval were performed by applying it to an orbit of CloudSat observations coincident with a C3VP snowfall event, and by applying it to observations

from a surface-based 95 GHz radar for which coincident snowfall rate and microphysical observations were available.

For this second part, models for particle microphysics and scattering properties are constructed in Chapter 6 using the results from the snow microphysics retrieval, then the CloudSat retrieval is defined in Chapter 7. This definition includes the formulation of the retrieval, an evaluation of the measurement and forward model uncertainties, a description of the method by which snowy scenes are identified, an assessment of the necessary a priori estimates, and a description of the method by which snowfall rates are calculated from the retrieved state. In Chapter 8, the retrieval is applied, first to observations from a ground-based 95 GHz radar, then to CloudSat observations. The results from the application to the ground-based radar observations are evaluated using coincident snowfall rate observations and information content metrics are determined. Using the results from the application to CloudSat observations, the relation between snowfall rate and radar reflectivity is examined and compared to results from other studies. Additionally, for a portion of the CloudSat observations associated with a C3VP snowfall event, the retrieval results (size distribution parameters, snowfall rates and ice water contents derived from the retrieval results) are compared against surface and in situ aircraft observations. Finally, the principal results are summarized along with prospects for future work in Chapter 9.

Chapter 2

C3VP Events

During four intensive observing periods (IOPs) in Northern Hemisphere winter 2006/07, an extensive set of surface- and aircraft-based in situ and remote sensing observations of clouds and precipitation were collected in south-central Ontario as part of the Canadian CloudSat/CALIPSO Validation Project (C3VP). C3VP was a multi-agency field project, hosted by Environment Canada and held jointly with the Tenth Cloud Layer Experiment (CLEX-10). These observations were coordinated with passage of the National Aeronautics and Space Administration (NASA) Earth Observing System afternoon constellation (or "A-Train") of satellites over the operations area. The primary objectives of the experiment were to provide high-quality observations that would allow validation of CloudSat and CALIPSO data products and verification of the physical formulations used in the retrieval algorithms (Hudak et al., 2006a). An enhanced surface measurement site was established at the Meteorological Service of Canada's (MSC) Centre for Atmospheric Research Experiments (CARE) at Egbert, Ontario, approximately 80 km north of Toronto. Participants included MSC, NASA through the CloudSat and CALIPSO science organizations and the Global Precipitation Mission Ground Validation activity, and the United States Department of Defense Center for Geosciences/Atmospheric Research.

2.1 Observations

In addition to CARE’s normal instrumentation (a full complement of meteorological instruments, dual frequency depolarization lidar, and 915 MHz wind profiler), the facility was augmented with an extensive array of surface observing and remote sensing instruments, a partial list including disdrometers, snowfall precipitation gauges, a vertically pointed 95 GHz (W-band) polarization radar, a vertically-pointed 9.35 GHz (X-band) Doppler radar, a scanning multi-frequency Doppler polarization radar, profiling microwave radiometers, and 10 GHz Precipitation Occurrence Sensor System (POSS). The site and surrounding region were also observed by MSC’s C-band polarimetric scanning Doppler radar located at King City, Ontario, about 34 km from CARE.

2.1.1 Particle size and fallspeed

A number of instruments installed at CARE provided observations of particle size and fallspeed, including Colorado State University’s 2-D Video Disdrometer (2DVD) (Thurai and Bringi, 2005) and the NASA Snow Video Imager (SVI) (Newman et al., 2009). The 2DVD uses two horizontal light sheets, parallel but offset in the vertical, and each light sheet illuminates a horizontal array of photodetectors in a line scan camera. As a particle falls through a light sheet, it shadows some of the photodetectors, and the array is scanned rapidly to determine which photodetectors are shadowed. A stack of horizontal shadow images of the particle results from the scans and from this stack, information about the horizontal dimensions of the particle can be obtained. The lightsheets are orthogonal, so particles are observed from two different directions (Hanesch, 1999; Kruger and Krajewski, 2002; Schönhuber et al., 2007).

If a particle is observed by both cameras and the corresponding images can be matched, the time interval between the two images can be used to determine the particle’s fallspeed. The irregular shape of snow particles complicates image matching, since the orthogonal views will see two distinct sides of a particle and the particle’s orientation may change. Hanesch (1999) defined a matching algorithm which applies a number of criteria to match particle images. The criteria are based on the vertical extent of the particles, the ratio of

the widths observed by the two cameras, the ratio of maximum width to height, and an allowed range of fallspeeds. Huang et al. (2010) used similar criteria, but applied weights to each criterion and the best match was chosen based on the image whose weighted sum is a maximum. The fallspeeds used in this work are the results of Huang et al.’s analysis of the 2DVD observations.

Given particle sizes and fallspeeds, the particle size distribution can be determined as

$$N(D_i) = \frac{1}{\Delta t \Delta D_i} \sum_{j=1}^{j=Np_i} \frac{1}{A_j v_{i,j}}, \quad (2.1)$$

where i is the index of the size distribution bin, D_i is the characteristic particle size for the i -th bin, Δt is the sampling time interval, ΔD_i is the width of the i -th size bin, Np_i is the number of particles in the i -th size bin, A_j is the horizontal measurement area associated with the j -th particle, and $v_{i,j}$ is the fallspeed of the j -th particle in the i -th size bin. If matching does not succeed, however, the unmatched particle cannot be used in the size distribution calculation since fallspeed is not known and the particle’s contribution to the size distribution via (2.1) cannot be determined (Hanesch, 1999; Huang et al., 2010). The resulting data loss can lead to errors in the estimated size distribution.

To avoid these errors, the size distributions used for this work were obtained from a different instrument, the Snow Video Imager (SVI), located adjacent to the 2DVD. The SVI uses a video camera to capture 2D images of particles and so directly observes a 3D volume defined by the camera’s 2D field of view and the depth of field (Newman et al., 2009). For a single image frame, the size distribution is

$$N(D_i) = \frac{1}{\Delta D_i} \sum_{j=1}^{j=Np_i} \frac{1}{A_{i,j} L_{i,j}}, \quad (2.2)$$

where $A_{i,j}$ is the area of the camera field of view and $L_{i,j}$ is the depth of field associated with the j -th particle in the i -th size bin. Np_i is the total number of particles in the size bin and ΔD_i is the bin width. Both the field of view and depth of field vary with particle size. Typically, multiple image frames contribute to an observed sized distribution, and the total sample volume increases with each frame, giving

$$N(D_i) = \frac{1}{N_f \Delta D_i} \sum_{k=1}^{N_f} \sum_{j=1}^{(Np_i)_k} \frac{1}{A_{ijk} L_{ijk}}, \quad (2.3)$$

where N_f is the number of frames and $(Np_i)_k$ is the total number of particles in the k -th image frame and the i -th bin. The SVI, then, provides an estimate of size distribution which is independent of particle fallspeed observations.

Various definitions of D may be used with each of these instruments. For the SVI, since a two dimensional image is obtained for each particle, D may be determined in several different ways (Newman et al., 2009). Each image pixel represents dimensions of 0.05 mm by 0.1 mm, nominally, so the projected area of each particle can be calculated and D can be found, for example, as the diameter of an equal area circle. Alternately, the maximum horizontal width can be used or the feret diameter, the length between two points at maximum separation on the perimeter of the image. For this work, the SVI size distributions were based on the feret diameter. For the 2DVD, a common approach is to estimate the volume of the observed particle, then report the diameter of an equal-volume sphere, D_{app} (Kruger and Krajewski, 2002; Huang et al., 2010). As described above, each orthogonal camera produces a stacked series of line scan shadow images as a particle falls through its field of view. Provided images can be matched, fallspeed is known and the vertical dimension of each scan line can be determined. From this, the volume of the particle can be estimated by assuming each scan line represents an ellipsoidal disk whose axes are equal to the lengths of the scan lines observed by each camera (Kruger and Krajewski, 2002). For purposes of these retrievals, an estimate of the maximum dimension D_M of the particle is more useful. The rematched 2DVD data (Huang et al., 2010) provides the maximum width of each of the two scan line images for each particle. The particle size is then taken as the larger of these two maximum widths.

Each 2DVD line scan camera uses an array of photodetectors to map a horizontal distance of about 10 cm, giving a horizontal resolution of 0.172 mm (Camera A) and 0.1725 mm (Camera B) for this particular instrument. Vertical resolution depends on the fallspeed of the particle and the frequency at which the line scan cameras are sampled. For this instrument, a fallspeed of 10 m s⁻¹ gives a vertical resolution of 0.195 mm (Thurai and Bringi,

2005). Vertical resolution would be proportionately finer at slower fallspeeds. As noted above, the resolution of the SVI images is 0.05 mm x 0.1 mm. The SVI size distributions are reported in discrete size bins of width 0.25 mm for sizes from 0 to 26 mm at 1 min resolution, but observations of particles smaller than 0.3 mm are discarded during the SVI image processing (Newman et al., 2009).

2.1.2 Radar reflectivity

Radar reflectivities were measured by both the McGill University Vertically Pointing X-band (VertiX) Doppler radar (Fabry and Zawadzki, 1995) and the MSC King City radar (WKR) (Hudak et al., 2006b). The VertiX operates at 9.35 GHz with a 2° beamwidth and was configured with 37.5 m vertical resolution. Measurements were reported at 10 s intervals. It was located at CARE in proximity to other snowfall measuring instruments. During the first and second IOPs, the VertiX suffered degraded performance due to a hardware failure. The VertiX was taken out of service for repairs after the second IOP and returned to service near the end of the third IOP. Because of ground clutter, range bins below approximately 350 m above ground level (AGL) were typically not usable under snowfall conditions.

The King City radar is a C-band dual polarization scanning Doppler radar located just north of Toronto and used for both operational and research purposes (Hudak et al., 2006b). To provide near-surface observations in the vicinity of the CARE site during C3VP, the radar performed frequent plan position indicator (POLPPI) scans at a 0.2° elevation angle during snow events. This elevation angle placed the beam centerline approximately 320 m AGL at the CARE site. These scans used a range resolution of 125 m and azimuth resolution of 0.5°, but the data used in this study were averaged over a 2-km range interval and 2° azimuth interval (approximately 1.1 km) located over the CARE site.

2.1.3 Snowfall rate

For snowfall, the principal precipitation observations at the CARE site were made by a manual Tretyakov gauge installed within a vertical octagonal double fence and operated by the Canadian Climate Centre. This configuration, referred to as a double fence intercomparison reference (DFIR), is recognized as producing high-quality measurements of

snow accumulation and was selected by the World Meteorological Organization (WMO) as a practical secondary standard for use in the WMO intercomparison of solid precipitation measurements (Goodison et al., 1998). At CARE, observations were recorded at 1300 and 2100 UTC (0800 and 1600 local time); however, precipitation measurements with higher time resolution were required for the retrievals performed in this work.

Several other instruments operating at CARE during C3VP provided estimates of precipitation rates at higher time resolution, including a Vaisala FD12P and a Precipitation Occurrence Sensor System (POSS). Rates from both the FD12P and the POSS were recorded at 1-minute resolution. The FD12P uses an optical scattering sensor along with a heated capacitive sensor to estimate precipitation amounts (Vaisala, 2002). The POSS is a bistatic X-band Doppler radar which was originally developed by the Meteorological Service of Canada as an automated instrument for detecting and typing precipitation (Sheppard, 1990). Sheppard and Joe (2008) have recently developed an algorithm by which the POSS can be used to estimate precipitation rate. The algorithm relies on scattering properties modeled using spheres and oblate spheroids for snow particles and assumes size distributions follow Sekhon and Srivastava (1970). Rates from the FD12P were used for the retrievals. Lacking observations from replicate FD12P instruments, comparisons between the FD12P and POSS rates were used to estimate measurement uncertainties for the FD12P rates (see Section 4.1.2).

To correct for biases in the FD12P rates, the FD12P rates were adjusted so that the resulting accumulations matched those recorded by the DFIR. For each snowfall event used in this study, the DFIR accumulation was calculated from the 2100 UTC measurement the day before the event to the 1300 UTC measurement the day after the event, and the FD12P accumulations were calculated over the same time period. The ratio of these two accumulations was used to scale the FD12P rates for the event. The FD12P consistently underestimated accumulations relative to the DFIR. The accumulation ratios (DFIR/FD12P) ranged from 1.15 to 1.98.

2.2 Snowfall events

The analyses presented here focus on four snowfall events which occurred during the winter 2006/07 field operations. These events were selected mainly because of completeness of the required data, but also because they represent a modest range of snowfall conditions. Daily operations logs from CLEX-10 (CIRA, 2009) along with comments from observers on the ground at CARE provide details about the characteristics of three of the cases. Event A (6 December 2006) was associated with a weak low passing northeastward over Ontario that produced snowfall at CARE mainly between about 1200 and 1530 UTC. In the vicinity of CARE, aircraft observations showed liquid phase near cloud top with mixed phase and ice below. The snowfall at CARE was described as light and dry early in the day, transitioning to moderate wet snow later. VertiX echo top heights were about 4 km AGL during the precipitation and the SVI size distributions showed tails extending to 4 mm - 8 mm (Figure 2.1). Temperatures during the most significant snowfall period were near freezing. The 24-hour snowfall accumulation for the event was 3.2 mm liquid water equivalent (LWE).

Event B (7 December 2006) consisted of lake effect snow squalls that resulted from the cold air mass and northwesterly winds that followed the system of the previous day. CARE received snowfall over most of the day, with a 24-hour accumulation of 10.2 mm LWE. Temperatures were near freezing early in the day and decreased with time, reaching 255 K at the day's end (Figure 2.2). The VertiX echo top heights were shallower than the previous day, varying from 1 km to 3 km AGL. The SVI size distributions were similar to those of the previous day but more variable over time. A period after 2100 UTC showed high concentrations of particles smaller than 2 mm and was associated with the coldest temperatures of the day.

Event C (27-28 January 2007) was a second lake effect snow event, which resulted as a warm front near CARE shifted to the south during the evening of 27 January and cold northwesterly winds entered the area. Snowfall occurred mainly between 0100 and 0400 UTC, at temperatures between 267 and 270 K. Snowfall rates at CARE were initially light, but rapidly increased as a heavy snow band lingered over the site (Figure 2.3). Extremely large snowflakes, near 10 mm in diameter, fell during the periods of heavy snow and visibility

was near zero. The SVI size distributions showed particles with sizes up to 10 mm early in the event. Total accumulations for the day were 4.6 mm LWE.

The final event (14 February 2007, Event D) occurred between the third and fourth IOPs, and details of the conditions on the surface and aloft are lacking. The system producing this snowfall was significantly deeper than the other three events, with VertiX echo top heights extending to about 6 km AGL (Figure 2.4). Observations from precipitation gauges show that snowfall occurred largely throughout the day and produced accumulations of 8.3 mm LWE. This was also the coldest event, with temperatures ranging from 256 to 261 K during the snowfall. The SVI size distributions were extremely narrow compared to the earlier events, with the largest detected particles ranging in size from 2 mm to 3 mm for much of the event. The characteristics of the four events are summarized in Table 2.1.

The causes for the large DFIR/FD12P accumulation ratios for events C and D are not clear. The FD12P uses both an optical sensor and a heated capacitive sensor to estimate precipitation rate for snow. The signal from the capacitive sensor is sensitive to the water content of the snow and is used to compute a scale factor with which the optical estimate of precipitation rate is adjusted, but the capacitive sensor is subject to undercatch (Vaisala, 2002). For event C, however, winds were light (Figure 2.5), suggesting that undercatch should not have been significant. Winds were stronger for event D, generally below 5 m s⁻¹, but ranging as high as 6 m s⁻¹ for short periods. Additionally, the size distributions for event D suggest high concentrations of small particles were present (Figure 2.4). For this event, undercatch by the Vaisala capacitive sensor may have been significant and biased the FD12P precipitation rate estimates low.

Table 2.1: Properties of C3VP cases. For Event B, echo top heights in parentheses are for intermittent lake effect snow bands. The fraction of day snowing represents the fraction of time for which the surface observations of precipitation rate were nonzero, while the time ranges show the approximate time period over which retrievals were performed. The maximum snowfall rates are evaluated using the 1-minute FD12P rates, rescaled to match DFIR accumulations. Maximum values of Ze are taken from the 10-second VertiX data for range bin 13 (approximately 450 m AGL). ⁺The retrievals for 28 Jan 2007 also include several results from near 20:37 UTC.

Event	A	B	C	D
Date	6 Dec 2006	7 Dec 2006	28 Jan 2007	14 Feb 2007
Fraction of day snowing	0.25	0.80	0.27	0.81
Max. rate, mm LWE h ⁻¹	2.7	5.2	5.9	3.3
Time, UTC	1230-1530	0000-2359	0100-0500 ⁺	0130-1730
Max Ze, dB	21.3	25.5	28.8	19.7
Day accumulation, mm LWE	3.2	10.2	4.6	8.3
DFIR/FD12P accumulation ratio	1.15	1.29	1.68	1.98
VertiX echo top height, km	4.0	1.75 - 3.0 (1.0 - 1.5)	2.5	6.0 - 3.0

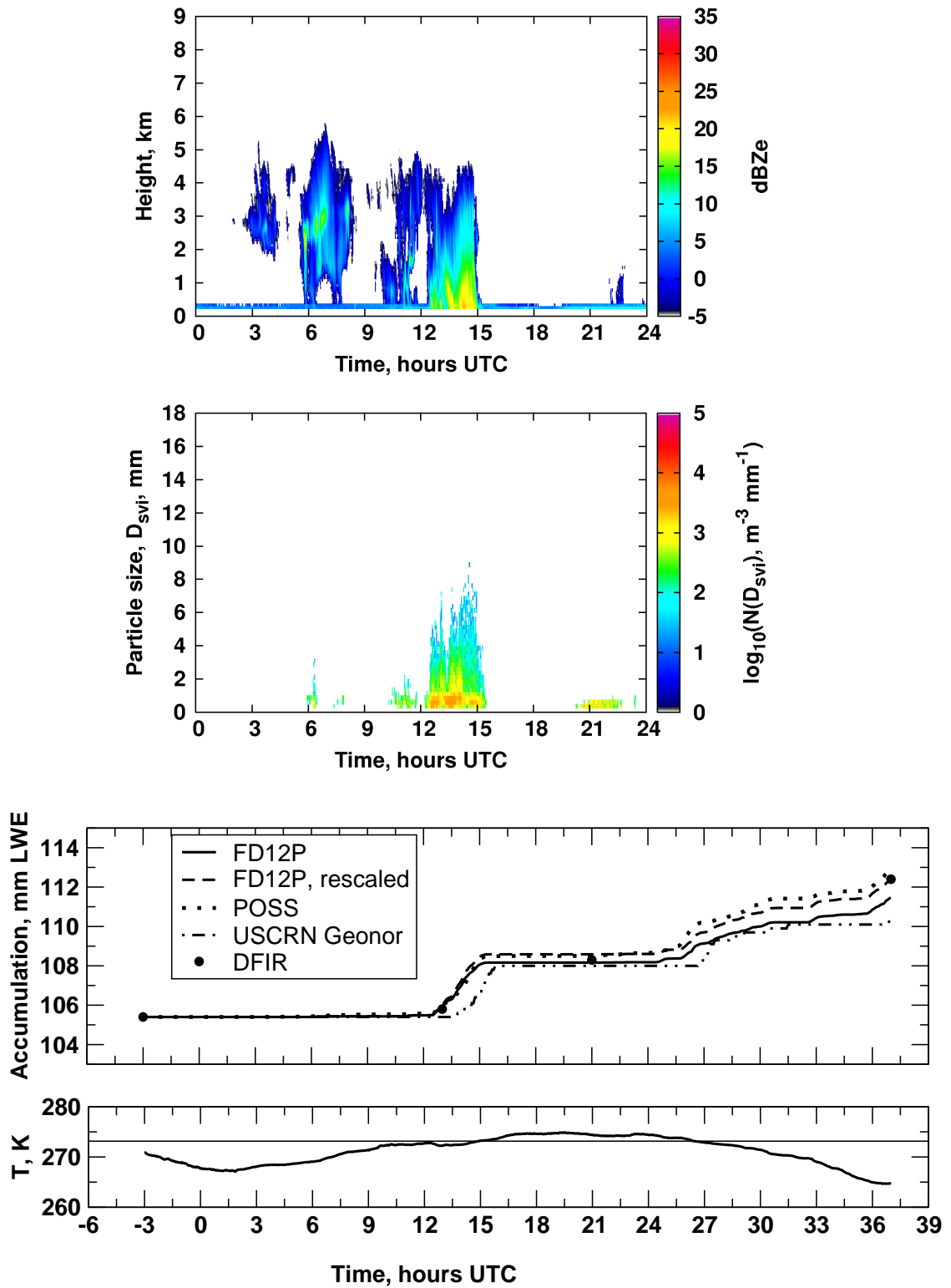


Figure 2.1: C3VP observations for event A. From top panel to bottom: Vertix reflectivity, SVI size distributions, snow accumulations from various instruments, and the 2-meter air temperature from the meteorological tower.

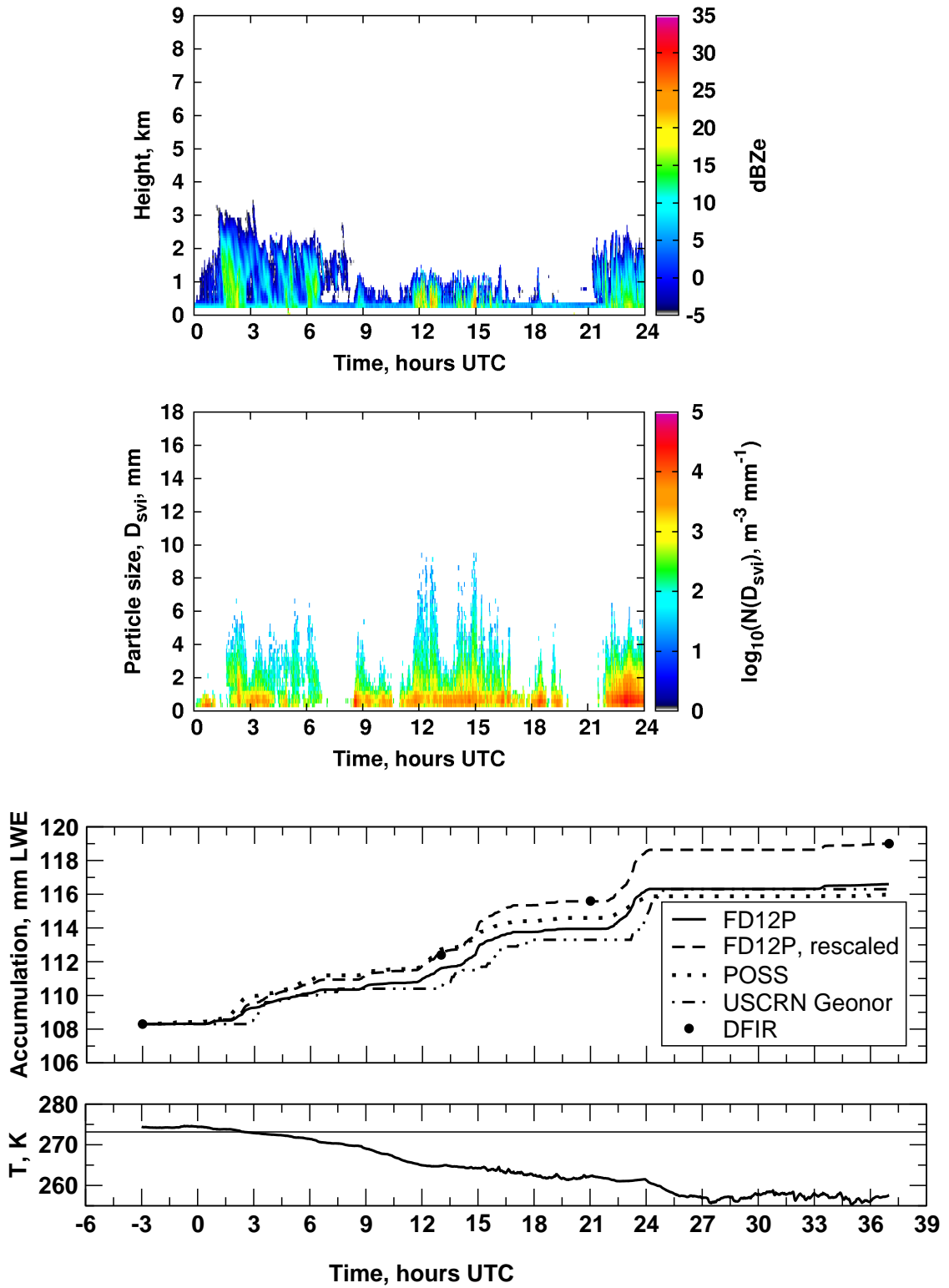


Figure 2.2: C3VP observations for event B. Panels are as described for Figure 2.1.

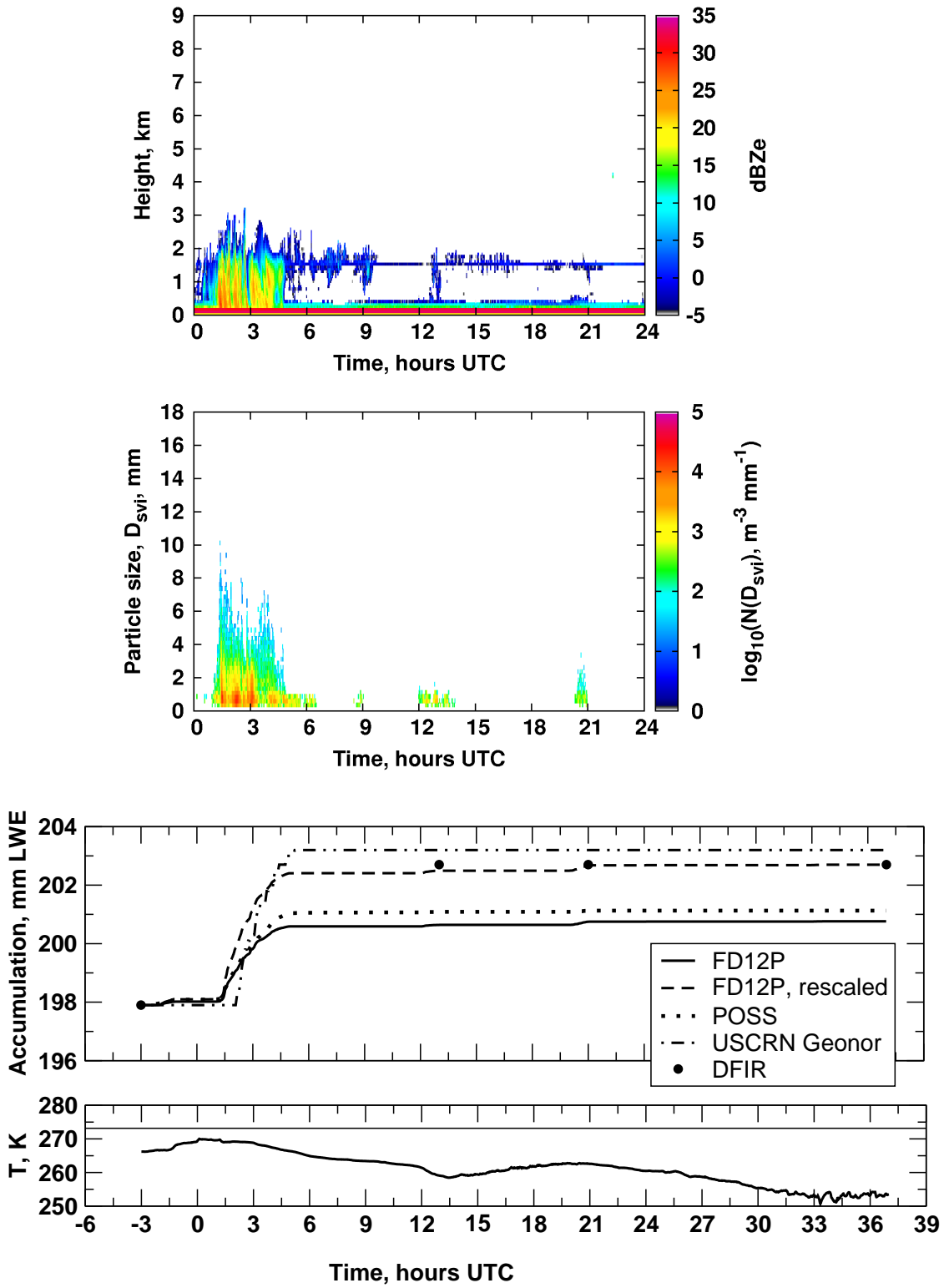


Figure 2.3: C3VP observations for event C. Panels are as described for Figure 2.1.

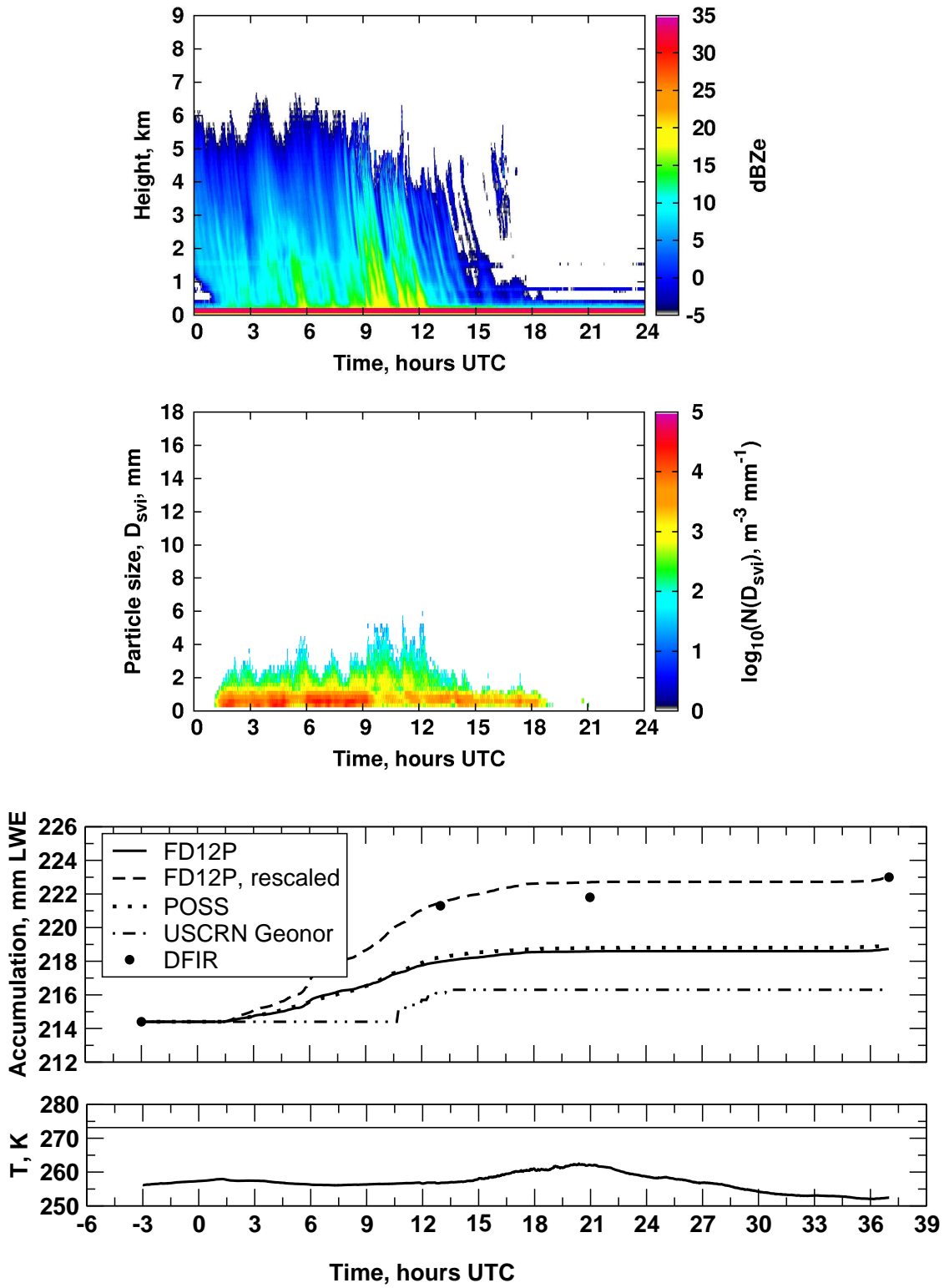


Figure 2.4: C3VP observations for event D. Panels are as described for Figure 2.1.

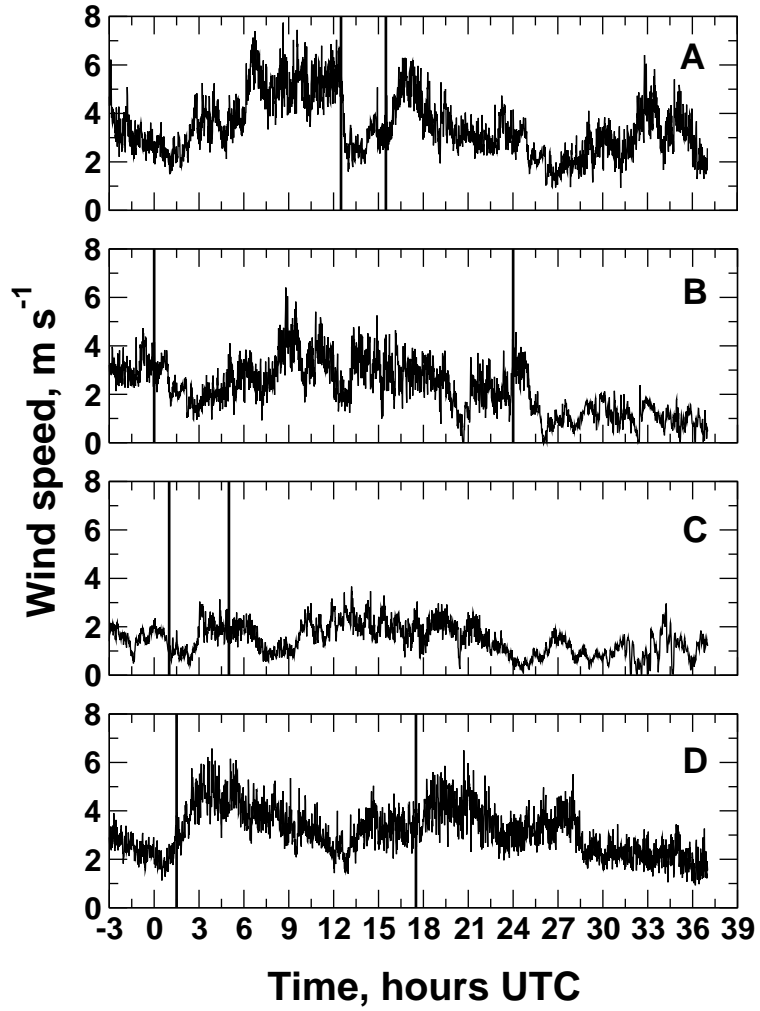


Figure 2.5: Wind speeds from the meteorology tower. Panels are labeled by event in the upper right corner. The heavy vertical lines indicate the approximate start and stop times for precipitation per Table 2.1.

Chapter 3

The snow microphysics retrieval method

Optimal estimation (OE) (Rodgers, 1976, 2000) is well suited to estimation problems with multi-sensor observations. OE requires an explicit forward model that defines a functional relationship between the observations and the quantities to be retrieved, or state variables. This forward model is recognized as an approximation to the true physical relationship, so forward model errors must also be quantified along with observational uncertainties. A tenet of optimal estimation is that measurements are used to improve an inherently uncertain, a priori knowledge of the state variables. Consequently, the a priori knowledge of the state must be quantified. The following sections describe the development of these three components (forward model, forward model and observation uncertainties, and a priori state), following a general description of the optimal estimation method.

3.1 Optimal estimation method

Given a vector of observations \mathbf{y} and a state vector \mathbf{x} of unknown quantities to be retrieved from the observations, a corresponding forward model $\mathbf{F}(\mathbf{x}, \tilde{\mathbf{b}})$ is constructed which relates \mathbf{x} and \mathbf{y} . The forward model may require other parameters, $\tilde{\mathbf{b}}$, not to be retrieved, where the tilde indicates that these parameters may be known imperfectly. The forward model is typically an approximation of the true physical relation between \mathbf{x} and \mathbf{y} , and there are

uncertainties associated with both the observations \mathbf{y} and the parameters $\tilde{\mathbf{b}}$. Allowing for these uncertainties gives the statement of the forward problem:

$$\mathbf{y} = \mathbf{F}(\mathbf{x}, \tilde{\mathbf{b}}) + \boldsymbol{\epsilon}, \quad (3.1)$$

where $\boldsymbol{\epsilon}$ represents the total uncertainty, due both to measurement uncertainty and to uncertainties in the forward model. These uncertainties may be due to both systematic and random errors.

Prior information about the state vector may be available, e.g. in the form of expected values \mathbf{x}_a and their covariances \mathbf{S}_a . It is desired to find the state $\hat{\mathbf{x}}$ which maximizes the posterior conditional probability density function $P(\mathbf{x} | \mathbf{y})$. This is done by constructing the cost function

$$\Phi(\mathbf{x}, \mathbf{y}, \mathbf{x}_a) = \left(\mathbf{y} - \mathbf{F}(\mathbf{x}, \tilde{\mathbf{b}})\right)^\top \mathbf{S}_\epsilon^{-1} \left(\mathbf{y} - \mathbf{F}(\mathbf{x}, \tilde{\mathbf{b}})\right) + (\mathbf{x} - \mathbf{x}_a)^\top \mathbf{S}_a^{-1} (\mathbf{x} - \mathbf{x}_a), \quad (3.2)$$

and minimizing with respect to \mathbf{x} , where \mathbf{S}_ϵ is the covariance matrix representing the uncertainties $\boldsymbol{\epsilon}$. If $\boldsymbol{\epsilon}$ contains systematic errors which can be identified, it is desirable to correct for them by adjusting the model or measurements and determining a corrected \mathbf{S}_ϵ (Marks and Rodger, 1993).

Provided the forward model is not excessively nonlinear, the vector $\hat{\mathbf{x}}$ which minimizes the cost function can be found by Newtonian iteration:

$$\hat{\mathbf{x}}_{i+1} = \hat{\mathbf{x}}_i + \left(\mathbf{S}_a^{-1} + \mathbf{K}_i^\top \mathbf{S}_\epsilon^{-1} \mathbf{K}_i\right)^{-1} \left[\mathbf{K}_i^\top \mathbf{S}_\epsilon^{-1} \left(\mathbf{y} - \mathbf{F}(\hat{\mathbf{x}}_i, \tilde{\mathbf{b}})\right) - \mathbf{S}_a^{-1} (\hat{\mathbf{x}}_i - \mathbf{x}_a)\right], \quad (3.3)$$

where \mathbf{K} is the Jacobian of the forward model with respect to the state vector, and $\mathbf{K}_i = \mathbf{K}(\hat{\mathbf{x}}_i)$. Iteration continues until the covariance-weighted difference in successive state vector estimates is much smaller than the number of state vector elements. At convergence, the covariance of the solution $\hat{\mathbf{x}}$ is obtained as

$$\hat{\mathbf{S}}_x = \left(\hat{\mathbf{K}}^\top \mathbf{S}_\epsilon^{-1} \hat{\mathbf{K}} + \mathbf{S}_a^{-1} \right)^{-1}, \quad (3.4)$$

where $\hat{\mathbf{K}} = \mathbf{K}(\hat{\mathbf{x}})$. As a diagnostic test of the results, a χ^2 statistic is calculated using the retrieved state vector in (3.2). A value near N_y , the number of observations, suggests correct convergence.

Along with the estimate of the state vector and its covariance, a number of other diagnostic quantities can be obtained from the optimal estimation results, chiefly the averaging kernel matrix, or \mathbf{A} matrix:

$$\mathbf{A} = \left(\hat{\mathbf{K}}^\top \mathbf{S}_\epsilon^{-1} \hat{\mathbf{K}} + \mathbf{S}_a^{-1} \right)^{-1} \hat{\mathbf{K}}^\top \mathbf{S}_\epsilon^{-1} \hat{\mathbf{K}}. \quad (3.5)$$

\mathbf{A} gives the sensitivity of the retrieval to the true state and has elements of the form

$$\mathbf{A} = \frac{\partial \hat{\mathbf{x}}}{\partial \mathbf{x}} = \begin{bmatrix} \frac{\partial \hat{x}_1}{\partial x_1} & \cdots & \frac{\partial \hat{x}_1}{\partial x_N} \\ \vdots & \ddots & \vdots \\ \frac{\partial \hat{x}_N}{\partial x_1} & \cdots & \frac{\partial \hat{x}_N}{\partial x_N} \end{bmatrix}, \quad (3.6)$$

where N is the number of state vector elements.

The role of \mathbf{A} can be interpreted using a linearized representation of the departure of the solution from the a priori,

$$\hat{\mathbf{x}} = (\mathbf{I} - \mathbf{A})\mathbf{x}_a + \mathbf{A}\mathbf{x} + \mathbf{G}_y\boldsymbol{\epsilon}, \quad (3.7)$$

where \mathbf{G}_y gives the sensitivity of the retrieval to the measurements. This representation illustrates that the nearer is \mathbf{A} to diagonal, the more directly a particular element of $\hat{\mathbf{x}}$ is determined by its particular true state and a priori value. As an example, ignoring for a moment the error terms $\boldsymbol{\epsilon}$, the first element of $\hat{\mathbf{x}}$ is given by

$$\hat{x}_1 = \left(1 - \frac{\partial \hat{x}_1}{\partial x_1} \right) x_{1,a} - \sum_{k=2,N} \frac{\partial \hat{x}_1}{\partial x_k} x_{k,a} + \frac{\partial \hat{x}_1}{\partial x_1} x_1 + \sum_{k=2,N} \frac{\partial \hat{x}_1}{\partial x_k} x_k. \quad (3.8)$$

Provided \mathbf{A} is diagonal, the summations vanish and

$$\hat{x}_1 = \left(1 - \frac{\partial \hat{x}_1}{\partial x_1}\right) x_{1,a} + \frac{\partial \hat{x}_1}{\partial x_1} x_1. \quad (3.9)$$

From this last expression it can be seen that as the partial derivative approaches unity, the retrieved value is determined more completely by the true state rather than the a priori. In the general case when \mathbf{A} is not diagonal, an element of the retrieved state vector is a blend of information from multiple elements of the true state vector and the a priori state vector. From (3.7) then, one may estimate the degree to which elements of the state vector are determined by the true state as opposed to the a priori.

The degrees of freedom for signal, d_s , describes the number of independent quantities provided by the measurements which are significant compared to the combined forward model and measurement uncertainties. The degrees of freedom for signal can be shown to be equal to the trace of the \mathbf{A} matrix (Rodgers, 2000).

The Shannon Information Content, H , measures how much the measurements reduce the uncertainty in the retrieved state in comparison to the a priori uncertainty in the state (Rodgers, 2000):

$$H = \frac{1}{2} \log_2 \left| \mathbf{S}_a \hat{\mathbf{S}}_x^{-1} \right|. \quad (3.10)$$

When expressed using base-2 logarithms, the information content describes binary bits of resolution provided by the measurements, suggesting that 2^H distinct states can be resolved (L'Ecuyer et al., 2006).

3.2 Forward model governing equations

For these retrievals, the observational constraints were provided by snowfall rate, radar reflectivity, and fallspeeds. Snowfall rate is determined by the size distribution $N(D)$, particle masses $m(D)$ and fallspeeds $V(D)$ as

$$P = \frac{1}{\rho_{liq}} \int_{D_{min}}^{D_{max}} N(D) m(D) V(D) dD \quad (3.11)$$

where P is in depth units (e.g., mm h⁻¹ LWE) and ρ_{liq} is liquid water density. D is a characteristic dimension of the particles and the integration limits assert that a finite range of particle sizes contribute to snowfall rate. D may be defined in various ways, as maximum horizontal dimension, equal-area diameter, or equal-volume diameter for example. For (3.11) the particular choice of D is not significant, provided a consistent choice is used for defining size distribution, mass and fallspeed.

For modeling the radar reflectivity factor, it can be assumed that scattering by snow particles follows the Rayleigh approximation for spheres and that attenuation by snow particles and by atmospheric gases can be ignored at 9.35 GHz. For particles in the Rayleigh regime, Atlas et al. (1953) showed that low density, irregularly shaped dry snow particles can be treated as equal volume spheres to calculate radar scattering properties with small error. This assumption is examined further in the discussion of forward model errors. Matrosov (1998) gave estimates of attenuation by particles and gases under winter conditions. Attenuation in dry snow was given as 0.001 dB km⁻¹ for a snowfall rate of 2 mm h⁻¹ LWE, and that for water vapor and oxygen was given as 0.01 dB km⁻¹. Both are insignificant contributions to forward model error for the small ranges used in this work. The effective radar reflectivity factor is then (Battán, 1973)

$$Ze = \frac{\Lambda^4}{\|K_w\|^2 \pi^5} \eta, \quad (3.12)$$

where Λ is the radar wavelength, $K_w = (n_{liq}^2 - 1)/(n_{liq}^2 + 2)$ and n_{liq} is the complex refractive index of liquid water. The radar reflectivity η is

$$\eta = \int_{D_{min}}^{D_{max}} N(D) \sigma_{bk}(D) dD, \quad (3.13)$$

where $\sigma_{bk}(D)$ is the backscatter cross section. Given a snow particle of size D with mass $m(D)$, the diameter of an equal-volume sphere with the density of ice ρ_{ice} is

$$D_{ev} = \left(\frac{6m(D)}{\pi\rho_{ice}} \right)^{1/3}. \quad (3.14)$$

D_{ev} is not a physical dimension of the particle, but is the diameter of a solid-ice sphere whose volume is equal to the actual volume of the nonspherical particle. The density ρ_{ice} is that of solid ice, 0.917 g cm^{-3} . For scattering in the Rayleigh regime by spherical particles, the backscatter cross section for a particle of size D_{ev} is (Battan, 1973)

$$\sigma_{bk} = \frac{\|K_i\|^2 \pi^5}{\Lambda^4} D_{ev}^6, \quad (3.15)$$

where $K_i = (n_{ice}^2 - 1)/(n_{ice}^2 + 2)$ and n_{ice} is the complex refractive index of ice. Combining the relations (3.12 - 3.15) gives the equivalent reflectivity factor (hereafter, radar reflectivity, or reflectivity) as

$$Ze = \frac{36}{\pi^2 \rho_{ice}^2} \frac{\|K_i\|^2}{\|K_w\|^2} \int_{D_{min}}^{D_{max}} N(D) [m(D)]^2 dD. \quad (3.16)$$

As in (3.11), the particular choice of D is not significant provided a consistent choice is used for both the size distribution and mass.

Fallspeeds are often represented as power functions of particle size, but such representations give limited information about the microphysical properties of the particles, and the parameters of such functions are specific to the particular observations from which they were derived (Heymsfield and Westbrook, 2010). Alternately, fallspeeds may be described using explicit, physically-based relations (e.g., Bohm, 1989; Mitchell, 1996), which is the approach taken here. As described by Mitchell (1996), the dimensionless Best, or Davies, number X relates the Reynolds number Re and drag coefficient C_d for a falling particle and is expressed in terms of the particle mass and the particle area projected normal to the direction of motion:

$$X(D) = C_d Re^2 = \frac{2D^2 \rho_a}{\mu^2} g \frac{m(D)}{A_p(D)}, \quad (3.17)$$

where $A_p(D)$ is the projected area of the particle, ρ_a is the air density, μ is the viscosity, and g is gravitational acceleration. Treating air as an ideal gas allows density and viscosity to be calculated from air temperature and pressure via Sutherland's formula (Sutherland, 1893).

Arguments based on boundary layer theory for a blunt body (Abraham, 1970) also provide a relation between Re and C_d :

$$C_d = C_0 \left(1 + \frac{\delta_0}{Re^{1/2}} \right)^2, \quad (3.18)$$

where δ_0 is a unitless constant related to boundary layer thickness and C_0 is the limiting drag coefficient under conditions dominated by pressure drag. This expression is obtained by considering the effective projected area to be the true projected area augmented by the attached boundary layer. Bohm (1989) estimated values of $C_0 = 0.6$ and $\delta_0 = 5.83$. Combining (3.17) and (3.18) gives an expression for Re in terms of the Best number which, as shown in (3.17), is dependent on particle mass and projected area:

$$Re(D) = \frac{\delta_0^2}{4} \left[\left(1 + \frac{4\sqrt{X(D)}}{\delta_0^2\sqrt{C_0}} \right)^{1/2} - 1 \right]^2. \quad (3.19)$$

Finally, the fallspeed can be found from

$$V(D) = \frac{Re(D)\mu}{\rho_a D}. \quad (3.20)$$

Note that D appears explicitly in the expressions for $V(D)$ and $X(D)$, making these expressions sensitive to the choice of D . For fallspeeds of nonspherical ice particles, D is taken typically to be the maximum dimension of the particle or the maximum dimension of the horizontal projection of the particle.

Mitchell and Heymsfield (2005) suggested a parameterized modification to the $Re - X$ relation to accommodate larger particles like aggregates, arguing that the porous nature of aggregates leads to enhancement of the boundary layer effect described by Abraham (1970):

$$Re(D) = \frac{\delta_0^2}{4} \left[\left(1 + \frac{4\sqrt{X(D)}}{\delta_0^2\sqrt{C_0}} \right)^{1/2} - 1 \right]^2 - a_0 [X(D)]^{b_0}, \quad (3.21)$$

with $a_0 = 0.0017$ and $b_0 = 0.8$. They found the parameterization effective for $X < 10^8$. This relation is used with (3.17) as the primary model for fallspeed (hereafter referred to as MH2005) in this work. The modification results in somewhat smaller Reynolds numbers for aggregates, which have large Best numbers. At smaller Best numbers, the relation is minimally changed from that of Mitchell (1996), and so should be adequate for pristine

particles as well. See Figure 1 of Mitchell (1996) and Figure 2 of Mitchell and Heymsfield (2005).

Recently, Heymsfield and Westbrook (2010) proposed a modified Best number which appeared to better reproduce fallspeeds for particles over a wide range of area ratios, defined as the ratio of A_p to the area of a circle of diameter D ,:

$$X(D) = \frac{2D^2\rho_a}{\mu^2}g\frac{m(D)}{A_p(D)}[r_A(D)]^{1/2}, \quad (3.22)$$

where $r_A(D)$ is the area ratio. Heymsfield and Westbrook also made estimates of C_0 and δ_0 , applying fits of the form of (3.18) to observations of a range of particles, and found $C_0 = 0.35$ and $\delta_0 = 8.0$. A fallspeed model using this modified Best number along with (3.19) (hereafter referred to as HW2010) is also tested in this work. For HW2010, fallspeed is then dependent on particle size D , the particle mass, the projected area, air density and air viscosity, as well as the parameters δ_0 and C_0 . MH2005 has additional dependencies on a_0 and b_0 .

3.3 Forward model implementation

To complete the forward model based on the relations described above, the variation of both mass and horizontally-projected area with D must be represented. Power laws were used to describe these mass-dimension and area-dimension relations (e.g. Locatelli and Hobbs, 1974; Mitchell, 1996):

$$m(D_M) = \alpha D_M^\beta, \quad (3.23)$$

$$A_p(D_M) = \gamma D_M^\sigma. \quad (3.24)$$

D_M denotes the maximum dimension of the particle, consistent with the requirements of the fallspeed relations described above. These values for α , β , γ , and σ apply to the full range of particle sizes, in contrast to the values used by Mitchell (1996) which are specific to particular size ranges and particle habits. The values in this work should then be seen as representative values for particles of all sizes. Particle masses are capped to be no more

than that of an ice sphere of the same diameter. Similarly, particle areas are capped to be no more than that of a circle of the same diameter. The coefficients and exponents α , β , γ , and σ are then elements of the state vector \mathbf{x} to be retrieved. Because the coefficients α and γ are expected to be significantly more variable than the remaining state vector elements (Mitchell, 1996), they are transformed to $\ln(\alpha)$ and $\ln(\gamma)$ in the retrieval. The values for α , β , γ , and σ in this work are in cgs units, with D_M in centimeters and α and γ taking appropriate units, depending on the power of D_M , to give mass in grams and area in square centimeters.

Care must be taken, however, in interpreting the D values associated with the disdrometer observations. The disdrometers whose observations were used for this study observe particles in elevation view rather than plan view, so dimensions are obtained from images projected into the vertical rather than horizontal plane. This viewing geometry makes the measurement of a particle’s maximum horizontal dimension dependent on the rotation of the particle about the vertical axis and the canting angles. Additionally, the D values reported by various disdrometers can differ considerably (e.g., equal area D , equal volume D , maximum scan line width, maximum horizontal extent) because of differences in measurement and data processing techniques.

Depending on the shape and orientation of a particle, these dimensions can be quite different from the true maximum dimension D_M . Figure 3.1 shows the ratio, denoted as ϕ , of the disdrometer-observed dimensions D_{obs} to the true D_M obtained from simulations for a range of particle shapes and orientations. Details of the simulations are described in Appendix A. In extreme cases, D_{obs} may be as small as 30% of D_M , but a more reasonable estimate, based on judicious choice of measurement technique and on expected particle shape, is about 80%.

Potter (1991) described the effects of misinterpreting D in the context of bulk microphysics parameterizations. For retrievals, misinterpreting these dimensions can cause significant forward model biases that may cause retrieval failure or erroneous convergence (again, see Appendix A). To correct for these biases, one might make an a priori estimate of ϕ and include it as an element of the forward model parameter vector $\tilde{\mathbf{b}}$ with correct accounting of its uncertainty in the model-measurement error covariance matrix \mathbf{S}_ϵ . Alternately, one

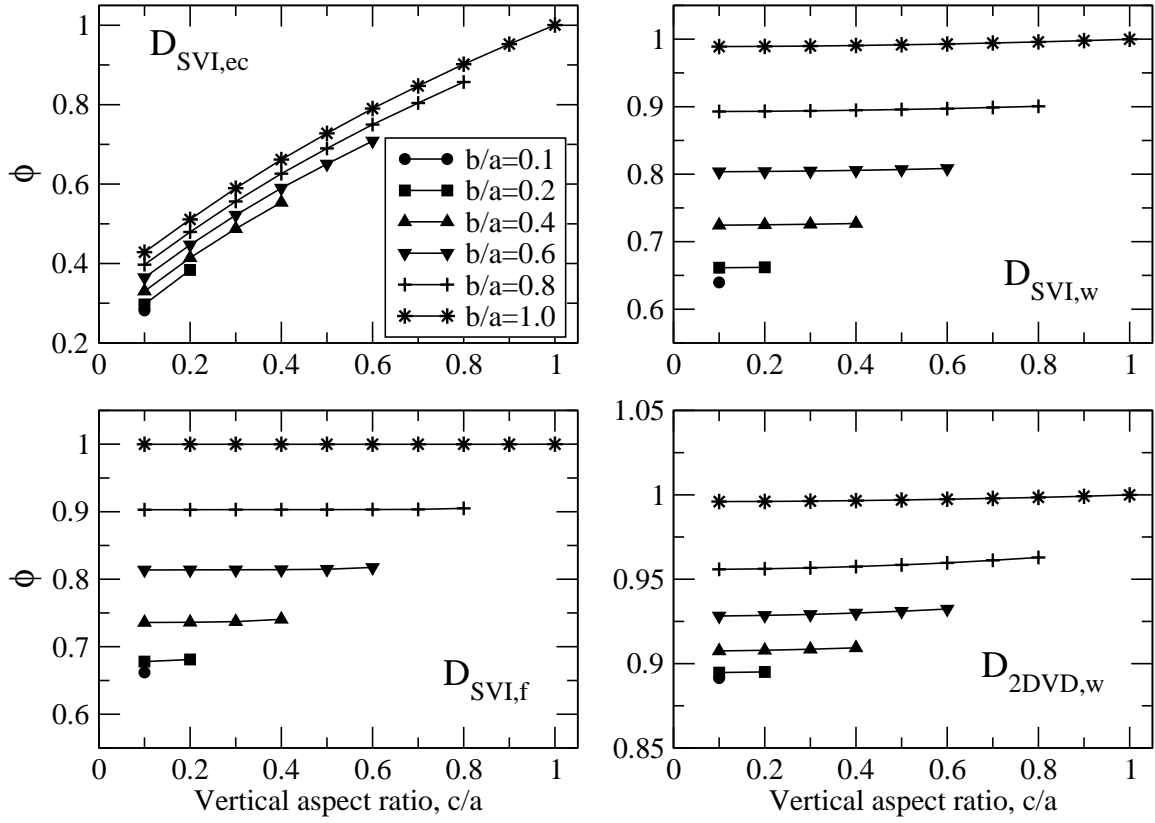


Figure 3.1: Values of ϕ , the ratio of D observed by SVI and 2DVD disdrometers to true maximum dimension D_M .

may include ϕ as a variable in the state vector and allow it to be retrieved (Rodgers, 2000). This latter approach was used for these retrievals. The variable ϕ , assumed to be constant over all sizes in the observed distribution, is introduced such that

$$\begin{aligned} D_M &\approx D_{obs}/\phi \\ N(D_M) &\approx \phi N(D_{obs}). \end{aligned} \quad (3.25)$$

A single value of ϕ is applied to all particle sizes in the observed distribution. In essence, then, ϕ is a representative mean value. The resulting state vector to be retrieved is then

$$\mathbf{x} = \begin{bmatrix} \ln(\alpha) \\ \beta \\ \ln(\gamma) \\ \sigma \\ \phi \end{bmatrix}. \quad (3.26)$$

Applying the mass-dimension power law to (3.16) gives the forward model for radar reflectivity

$$Ze = \frac{\alpha^2 36}{\pi^2 \rho_{ice}^2} \frac{\|K_i\|^2}{\|K_w\|^2} \int_{D_{min}}^{D_{max}} N(D_M) D_M^{2\beta} dD_M, \quad (3.27)$$

subject to the cap on particle mass described above. Similarly, applying the mass and area power laws to (3.11) gives the forward model for snowfall rate

$$P = \frac{\alpha}{\rho_{liq}} \int_{D_{min}}^{D_{max}} N(D_M) D_M^\beta V(D_M, \alpha, \beta, \gamma, \sigma) dD_M \quad (3.28)$$

The corresponding observation vector consists of the radar reflectivity, snowfall rate, and particle fallspeed observations. From (3.17) and (3.22) it is apparent that fallspeeds

are dependent on the ratio of mass to area:

$$\frac{m(D_M)}{A_p(D_M)} = \frac{\alpha}{\gamma} D_M^{\beta-\sigma}. \quad (3.29)$$

It would be possible to determine the two fallspeed parameters α/γ and $\beta - \sigma$ independently of the optimal estimation routine, using just the fallspeed observations. In this approach, which is not used here, an initial retrieval would be performed to fit α/γ and $\beta - \sigma$ to a set of fallspeed observations. Then these values would be used as observations in the optimal estimation retrieval, which would then determine the mass-dimension variables α and β . Alternately, the fallspeed parameters could be determined simultaneously with the mass-dimension parameters as part of the optimal estimation routine. This alternate approach is desirable, since it allows the the fallspeed observations and their uncertainties to be considered simultaneously with the observations of snowfall rate and radar reflectivity and their uncertainties in determining the optimum retrieved state.

Although it would be possible to include in the observation vector \mathbf{y} all the observed particle fallspeeds, this approach would most likely give excessive weight to fitting of the fallspeeds. Instead, mean fallspeeds and their associated standard deviations were computed for three predetermined size ranges: V_0 : 4.0 +/- 0.50 mm; V_1 : 2.0 +/- 0.25 mm; and V_2 : 1.0 +/- 0.25 mm. These ranges were chosen on an ad-hoc basis to describe the shape of a typical $V(D)$ curve with enough separation in size to minimize redundant information and to minimize the number of retrievals which could not be performed due to a lack of large particle fallspeed observations. The wider bin at the largest size was needed to ensure an adequate number of particle in most of the retrievals. A more detailed treatment that would examine the information content for various parts of the $V(D)$ curve could be beneficial but is beyond the scope of this work.

Given the three mean fallspeeds, three observations are constructed. V_0 is used as the first observation. The remaining two observations are constructed as fallspeed differences:

$\Delta V_1 = V_0 - V_1$ and $\Delta V_2 = V_0 - V_2$. The resulting vector of observations is then

$$\mathbf{y} = \begin{bmatrix} Ze \\ P \\ V_0 \\ \Delta V_1 \\ \Delta V_2 \end{bmatrix}. \quad (3.30)$$

Note that, although the size distribution is also observed by the SVI, it is considered part of the forward model parameters, $\tilde{\mathbf{b}}$, since it is independent of the state vector and information about the size distribution is not retrieved. These size distribution parameters include both the values of the size distribution $N(D_{obs})$ itself and the values of the independent variables D_{obs} on which the size distribution is defined.

3.4 a priori estimates of the state

A priori knowledge of the microphysical state is encoded in the retrieval via the a priori state vector, \mathbf{x}_a , and the a priori covariance matrix, \mathbf{S}_a . Together, these two variables describe the prior knowledge of the PDF of the state vector, which is in the form of a multivariate normal distribution. Given the state vector (3.26), the corresponding a priori state vector is

$$\mathbf{x}_a = \begin{bmatrix} \ln(\alpha_a) \\ \beta_a \\ \ln(\gamma_a) \\ \sigma_a \\ \phi_a \end{bmatrix} \quad (3.31)$$

and the a priori covariance matrix is

$$\mathbf{S}_a = \begin{bmatrix} s^2(\ln(\alpha_a)) & s(\ln(\alpha_a), \beta_a) & s(\ln(\alpha_a), \ln(\gamma_a)) & s(\ln(\alpha_a), \sigma_a) & s(\ln(\alpha_a), \phi_a) \\ & s^2(\beta_a) & s(\beta_a, \ln(\gamma_a)) & s(\beta_a, \sigma_a) & s(\beta_a, \phi_a) \\ & & s^2(\ln(\gamma_a)) & s(\ln(\gamma_a), \sigma_a) & s(\ln(\gamma_a), \phi_a) \\ & & & s^2(\sigma_a) & s(\sigma_a, \phi_a) \\ & & & & s^2(\phi_a) \end{bmatrix} \quad (3.32)$$

where only the upper triangular portion has been shown, $s^2(\cdot)$ are variances, and $s(\cdot, \cdot)$ are covariances.

For this work, the elements of \mathbf{x}_a and \mathbf{S}_a were estimated using the results from prior studies of snow microphysical properties and results from a new analysis of snow particle observations made previously by Kajikawa (Kajikawa, 1972, 1975, 1982, hereafter referred to as the Kajikawa observations). These prior studies, described in more detail below, made estimates of the parameters of mass- and area-dimension power laws for snow particles. The observations used in these studies represent a range of environmental states, and the estimated parameters from these studies were treated as samples drawn from the environmental distribution of the state vector, \mathbf{x} . Using these samples, expected values were calculated along with variances and covariances. These expected values, variances and covariances were then used as the elements of \mathbf{x}_a and \mathbf{S}_a . Although some information regarding habit might be obtained from the C3VP observations and used to construct habit-dependent a priori constraints, this habit information will likely be lacking in remote sensing observations such as CloudSat reflectivity profiles. Therefore, all prior observations are combined to construct a habit-independent a priori constraint.

This approach has a number of shortcomings. First, the breadth of sampling is limited. The number of existing studies is small and the results in multiple studies are in some cases derived from the same set of observations. Additionally, mountain locations were typically used for these studies that were based on observations at the surface. Such limited sampling

may not give an accurate accounting of the frequency of occurrence of different states. Second, these prior studies were not oriented toward providing the information needed by optimal estimation retrievals. Generally, estimates of uncertainties in the microphysical parameters or distribution widths were not provided. Finally, and most significantly, the fact that a set of parameters is an outlier when compared to other sets does not indicate a low probability of occurrence. Instead, the outlying set may simply represent a state whose properties lie far from the environmental mean properties. The outlying set may actually represent a state that occurs frequently. To compensate for these limitations, one must not make the a priori constraints too restrictive, especially in terms of penalizing outlying states by giving them a low probability of occurrence. It may be appropriate to artificially broaden the distribution derived from the prior observations while maintaining observed correlations between variables.

To construct the a priori constraint, estimates were made of the expected values of α , β , γ , σ , and ϕ , along with their variances and covariances. Lacking direct observations of ϕ , values for ϕ_a and $s^2(\phi_a)$ were estimated from the particle modeling described in Appendix A as 0.825 and 0.125^2 (Figure A.1, lower left panel) The value 0.825 is appropriate based on the use of SVI feret diameter and a typical particle aspect ratio of 0.60 to 0.70 (Korolev and Isaac, 2003). A priori covariances between ϕ and other state variables are unknown and were set to zero. Also, because studies from which simultaneously estimated mass- and area-dimension power law parameters can be determined are uncommon (the Kajikawa observations are a rare exception), covariances between α and γ , α and σ , β and γ , and β and σ were neglected and set to zero. The development of the remaining expected values, variances and covariances for the mass- and area-dimension power law parameters, including overviews of the prior studies, is now described.

Snow particle mass-dimension relations have typically been developed using one of two general approaches. The first approach uses dimensional relationships obtained from measurements of snow particles (Ono, 1969; Auer and Veal, 1970; Hobbs et al., 1974). The dimensional relationships, such as those giving thickness as a function of plate diameter, are used to express the particle volume which is then multiplied by an estimated density to give mass as a function of dimension (Davis, 1974; Kim, 2004). In the second, a snow

particle is collected and its dimension measured, then the particle is melted, typically on either a hydrophobic surface or a filter paper, and the diameter of the resulting water drop or water spot is measured. This allows the mass to be determined (e.g., Nakaya and Terada, 1935; Kajikawa, 1972). This second method avoids uncertainties inherent in the evaluation of the particle volume and in the density. With the first approach, the dimensional and density relations may come from distinct, potentially inconsistent sets of observations. Most of the data selected here to develop the a priori mass-dimension relation employed the second method.

Power laws were used to describe the variation of snow particle mass with size as early as 1935 (Nakaya and Terada, 1935). The reported power laws were simple, with exponents of 1 for needles; 2 for dendrites and rimed crystals; and 3 for graupel. More recent studies have employed power laws with variable exponents. Zikmunda and Vali (1972) developed mass-dimension power laws for snow particles collected at Elk Mountain Observatory, at an elevation of 3350 m above mean sea level (MSL) in the Medicine Bow range of Wyoming, focusing on several types of rimed particles. The observations of Locatelli and Hobbs (1974) were taken in the Cascade Mountains of Washington at elevations of 750 to 1500 m MSL and included a range of aggregates, rimed particles and graupel. For these two studies, particle counts were reported for each habit, along with correlation coefficients for the fitted power laws, but no estimates of uncertainties in the fitted parameters. Mitchell et al. (1990) developed mass-dimension power laws based on observations of orographic snowfall collected at a site at 2100 m MSL near Donner Pass in the central Sierra Nevada Mountains in California. Along with particle counts and correlation coefficients, Mitchell et al. reported on the within-habit variability of the coefficients and exponents of the fitted power laws by comparing results from two distinct winter seasons of observations. The observed particles included various pristine shapes, both rimed and unrimed, and aggregates. Over all the observed habits, the mean difference in α was 31%, while for β it was 10%. Maximum differences for α and β were 75% and 32%, respectively. Mitchell (1996) compiled mass-dimension power laws from these and other sources, and also used previously published dimensional and density information (e.g., Auer and Veal, 1970; Heymsfield and Knollenberg, 1972) from both aircraft and surface observations to synthesize additional mass power

laws. Values for α and β from these studies are tabulated by habit and particle size in Table B.1 of Appendix B.

Area-dimension power laws can be developed directly from dimensional relationships for simply-shaped habits (e.g., hexagonal plates and columns). For more complex shapes (e.g., dendrites), particle images must be analyzed. Enlarged photomicrographs may be evaluated using a planimeter (Heymsfield, 1972), or by overlaying a fine grid and counting grid squares. Areas for raster images, as might be obtained from digital cameras, scans of photomicrographs, or aircraft-borne particle probes, may be obtained by automated counting of pixels (Heymsfield and Miloshevich, 2003); edge detection techniques have been applied to define the edge contours of particles in such images (Heymsfield and Westbrook, 2010). Heymsfield (1972) evaluated photomicrographs collected by Nakaya (e.g., Nakaya and Tuno, 1934), measuring areas for a number of stellar and dendritic crystals using a planimeter as an intermediate step to estimating particle density. Mitchell (1996) summarized area-dimension power laws from a number of earlier studies (e.g., Auer and Veal, 1970; Davis, 1974; Mitchell et al., 1996). Heymsfield and Miloshevich (2003) provided power laws obtained from airborne cloud particle imager and balloon replicator data, wind tunnel crystal growth studies, and several sets of surface observations, including those of Kajikawa. Since the Kajikawa observations were reanalyzed in this work to obtain new area-dimension relations, the new results were used in lieu of the results given by Heymsfield and Miloshevich (2003), but other results from Heymsfield and Miloshevich (2003) were utilized. Values for γ and σ from these studies are tabulated by habit and particle size in Table B.3 of Appendix B.

Masahiro Kajikawa collected measurements of snow particles over several winter seasons in Japan, observing a wide range of planar and columnar habits, including both single crystals and some early aggregates, at Hokkaido University’s Mount Tiene observatory (1024 m MSL) (Kajikawa, 1972, 1982) and graupel at a location near sea level in Akita on Japan’s western coast (Kajikawa, 1975). Bullet rosettes and side planes were obtained by Kajikawa at Akita University’s Mount Hachimantai observatory (1200 m MSL) (Heymsfield et al., 2002). Heymsfield and Kajikawa (1987) utilized Kajikawa’s observations of the planar crystals and graupel to develop mass-dimension power laws for these habits. Recently,

Heymsfield and Westbrook (2010) reanalyzed Kajikawa’s particle images to obtain improved estimates of dimensions and areas. These reanalyzed data were used to develop new area-dimension and mass-dimension power laws based on maximum dimension, and a description of these revised power laws is provided in Appendix B.

The new power laws derived from the reanalysis of the Kajikawa observations along with the power laws from the earlier studies described above constitute the a priori information about the mass- and area-dimension power laws. Where duplicate results could be identified (e.g., some mass-dimension relations which appear both in Locatelli and Hobbs (1974) and Mitchell (1996)), the duplicate results were omitted except for those from the original source. Figures 3.2 and 3.3 show scatterplots of α vs β and γ vs σ , respectively. Points are labeled by habit, and in some cases suffixes “(s)” and “(l)” are used to indicate “smaller” or “larger” sizes of the same habit. Other suffixes are as described in Tables B.1 and B.3. Additionally, the habits are further grouped into broad classifications which are denoted by color. The most striking feature of both figures is the degree of correlation between the logarithms of the coefficients (α , γ) and the exponents (β , σ). These correlations will likely supply useful constraints for the microphysics retrieval. The color coding helps illustrate differences between the broad classifications. For mass, graupel-like particles tend to have larger exponents and coefficients than other particle types, and branched planar particles tend to have smaller coefficients than other particles with similar exponents. For area, columnar particles tend to have smaller coefficients and exponents than other particle types, and plates tend to have larger coefficients than other particles with similar exponents.

From these samples, bivariate normal distributions were determined for the mass- and area-dimension power law parameters (Table 3.1). As suggested by the plots (Figs. 3.2 and 3.3), the correlations between the exponents and logarithms of the coefficients are very high. The plots also show the 1 standard deviation uncertainty bars based on the calculated variances (shorter error bars). These distributions formed the a priori constraints for the C3VP microphysics retrieval.

Table 3.1: Estimates of the a priori state for use in the C3VP microphysics retrieval.

	Means	Correlation	Variances	Covariances
$\ln(\alpha)$	-6.181	0.753	2.474	0.585
β	2.067		0.244	
$\ln(\gamma)$	-1.556	0.836	0.392	0.118
σ	1.785		0.0507	

Chapter 4

Measurement and forward model uncertainties

The total error ϵ (3.1) can be expanded as (Rodgers, 2000)

$$\epsilon = \epsilon_Y + \Delta \mathbf{F}(\mathbf{x}, \mathbf{b}) + \frac{\partial \mathbf{F}}{\partial \mathbf{b}}(\mathbf{b} - \tilde{\mathbf{b}}) \quad (4.1)$$

where ϵ_Y is the contribution from measurement error, the second term on the right is the contribution due to the forward model's approximation of the actual physics, and the third term is the contribution from error in the forward model parameters. These errors may consist of both systematic biases and random components. Once recognized biases have been corrected, the residual uncertainties are characterized by the covariance matrix \mathbf{S}_ϵ

$$\begin{aligned} \mathbf{S}_\epsilon &= \mathbf{S}_y + \mathbf{S}_F + \mathbf{K}_b \mathbf{S}_b \mathbf{K}_b^T \\ &= \mathbf{S}_y + \mathbf{S}_F + \mathbf{S}_B \end{aligned} \quad (4.2)$$

where the definitions of the terms on the right parallel those for ϵ . In the third term, which is the contribution due to uncertainty in the forward model parameters, \mathbf{K}_b is the Jacobian of the forward model with respect to the parameters and \mathbf{S}_b is the covariance matrix for the

parameters. The product $\mathbf{K}_b \mathbf{S}_b \mathbf{K}_b^\top$ is denoted as \mathbf{S}_B . The matrix \mathbf{S}_y has the form

$$\mathbf{S}_y = \begin{bmatrix} s_y^2(Ze) & 0 & 0 & 0 & 0 \\ 0 & s_y^2(P) & 0 & 0 & 0 \\ 0 & 0 & s_y^2(V_0) & s_y(V_0, \Delta V_1) & s_y(V_0, \Delta V_2) \\ 0 & 0 & s_y(V_0, \Delta V_1) & s_y^2(\Delta V_1) & s_y(\Delta V_1, \Delta V_2) \\ 0 & 0 & s_y(V_0, \Delta V_2) & s_y(\Delta V_1, \Delta V_2) & s_y^2(\Delta V_2) \end{bmatrix}. \quad (4.3)$$

In this matrix and in \mathbf{S}_F and \mathbf{S}_B , the terms $s_y^2(\cdot)$ and $s_y(\cdot, \cdot)$ represent variances and covariances, respectively. The covariances of the fallspeed terms result from using differences to define the fallspeed observations ΔV_1 and ΔV_2 . The matrix \mathbf{S}_F has the form

$$\mathbf{S}_F = \begin{bmatrix} s_F^2(Ze) & s_F^2(Ze, P) & 0 & 0 & 0 \\ s_F^2(Ze, P) & s_F^2(P) & s_F(P, V_0) & s_F(P, \Delta V_1) & s_F(P, \Delta V_2) \\ 0 & s_F(P, V_0) & s_F^2(V_0) & s_F(V_0, \Delta V_1) & s_F(V_0, \Delta V_2) \\ 0 & s_F(P, \Delta V_1) & s_F(V_0, \Delta V_1) & s_F^2(\Delta V_1) & s_F(\Delta V_1, \Delta V_2) \\ 0 & s_F(P, \Delta V_2) & s_F(V_0, \Delta V_2) & s_F(\Delta V_1, \Delta V_2) & s_F^2(\Delta V_2) \end{bmatrix}. \quad (4.4)$$

For \mathbf{S}_F , covariances between the snowfall rate P and the fallspeed terms arise because of common dependence on the fallspeed forward model, and covariances between P and the radar reflectivity Ze arise because of the integrations over size distribution. Finally, the forward models for Ze and P share common parameters from $\tilde{\mathbf{b}}$, as do the forward models

for P and $(V_0, \Delta V_1, \Delta V_2)$. As a result, the form of \mathbf{S}_B is

$$\mathbf{S}_B = \begin{bmatrix} s_B^2(Ze) & s_B(Ze, P) & 0 & 0 & 0 \\ s_B(Ze, P) & s_B^2(P) & s_B(P, V_0) & s_B(P, \Delta V_1) & s_B(P, \Delta V_2) \\ 0 & s_B(P, V_0) & s_B^2(V_0) & s_B(V_0, \Delta V_1) & s_B(V_0, \Delta V_2) \\ 0 & s_B(P, \Delta V_1) & s_B(V_0, \Delta V_1) & s_B^2(\Delta V_1) & s_B(\Delta V_1, \Delta V_2) \\ 0 & s_B(P, \Delta V_2) & s_B(V_0, \Delta V_2) & s_B(\Delta V_1, \Delta V_2) & s_B^2(\Delta V_2) \end{bmatrix}. \quad (4.5)$$

The following sections describe the estimation of each of these matrices.

4.1 Measurement uncertainties \mathbf{S}_y

4.1.1 Radar reflectivity

VertiX radar reflectivity observations were used for the retrievals because of the radar's proximity to other instruments, its high temporal resolution, and the continuity of its observations during periods of snowfall. For use in the retrieval, reflectivities were averaged in linear units into 5-minute means, consistent with the averaging time for the SVI observations. Because of ground clutter, reflectivities near the surface were unusable, making it necessary to estimate reflectivities at the surface using the features of reflectivities aloft. Based on inspection of time-height plots of reflectivities during the four snow events, observations at the thirteenth radar range bin, with a center height of 469 m AGL, appeared largely uncontaminated by ground clutter even under conditions of very light snow. Reflectivities at lower altitudes appeared frequently to be affected by ground clutter.

The principal sources of error for the VertiX reflectivities are expected to be due to radar calibration and due to the estimation of reflectivities at the surface using reflectivities aloft. Other potential sources of error include beam filling and inhomogeneity of the 5-minute samples (mixing of precipitating and non-precipitating targets). The small pulse volume of the VertiX, along with the fact that bin 13 is well below observed echo top

heights (Table 2.1), make significant beam filling issues unlikely. To address homogeneity, two simple diagnostic quantities were calculated for each average: the fractional standard deviation of Z_e (in linear units), and the count of observations in the sample that have both small reflectivities and small Doppler velocities. Small values for both quantities suggest a sample contains observations mainly of precipitating targets with reasonably homogeneous reflectivities. These two diagnostics were used to identify suspect retrieval results.

The calibration biases for the VertiX reflectivities were evaluated using comparisons against observations over the CARE site by the King City C-band radar (WKR) during snow events. The calibration accuracy of the King City radar is typically taken to be better than ± 1 dBZ (Thurai et al., 2008). Differences between the King City and VertiX reflectivities may be partly due to the differences in radar wavelength. For X-band, departures from Rayleigh scattering are expected for snow particles larger than about $D_M = 5$ mm (Matrosov et al., 2009), while for C-band, the Rayleigh approximation should be valid to somewhat larger sizes. The resulting reflectivity differences will cause errors in the calibration of the VertiX, but these errors are expected to be minor compared to other error sources discussed below and are ignored. Comparisons were limited to dry snow cases, based on evaluations of near-surface temperature and soundings, so that attenuation of the King City radar beam would be negligible. The King City radar reflectivities had been provided as mean values over a region 2 km in range by 2° in azimuth above the CARE site from POLPPI scans taken during each of the four events. Specifically for these calibration comparisons, the VertiX observations were matched in time to the King City radar observations and averaged spatially and temporally. The centerline of the WKR beam was estimated to be at 320 m AGL for the POLPPI scans. By limiting calibration cases to those with reflectivities larger than 5 dBZe, the lowest range bin which could be used confidently was at a height of 350 m AGL. The VertiX reflectivity samples were then taken vertically up to a height of 750 m AGL in order to be approximately consistent with the King City radar's beamwidth of 0.62° , and over a two-minute time period. The VertiX reflectivity samples were weighted using a vertically varying weight defined by a Gaussian curve with a mean of 320 m to match the estimated WKR beam centerline height and a width parameter of 156 m to match the WKR beamwidth. The biases were determined separately for events A and B

combined (pre-repair) and for events C and D combined (post-repair). For events A and B the bias was -7.72 (0.39, 80) dBZe, while for events C and D it was -2.89 (0.14, 63) where the numbers in parentheses are the standard error and number of samples, respectively.

The vertical separation between VertiX bin 13 and the surface complicates estimating the reflectivity at the surface. The vertical distance between VertiX bin 13 and the surface induces a time delay between the appearance of precipitation features aloft and their appearance at the surface. Given a typical fallspeed for snow of 1 m s^{-1} , the delay would be about 8 minutes. To correct for the time delay, two time series were constructed for each event: one of VertiX reflectivities at bin 13, and one of reflectivities synthesized from 2DVD measurements at the surface using an assumed mass-dimension relation. By identifying the occurrence of similar features in both time series, a series of time calibration pairs was determined for each event. Each pair consisted of the time associated with the feature on the surface, and the time at which the feature appeared in the VertiX reflectivities. The set of calibration pairs was used to construct cubic spline interpolators that calculated the time offsets required for bin 13 reflectivities to match the times of the surface observations.

Horizontal advection makes it extremely unlikely that a particular precipitation parcel observed overhead by the VertiX would eventually arrive at the surface in the same location as the radar. In an idealized environment of constant vertical wind shear and no directional shear, precipitation parcels formed aloft and falling with constant speed follow parabolic trajectories to the surface (Marshall, 1953). Figure 4.1 is a cartoon illustration of a precipitation generating cell advecting across the radar field of view and shows trajectories of precipitation parcels formed by the cell at discrete times. The parcel formed by the cell and observed by the radar at t_0 will arrive at the surface some time later and some distance downwind of the radar. The parcel that actually does arrive at the surface in the vicinity of the radar was actually formed by the cell earlier and some distance upwind. At t_0 , the parcels have advected along the portions of the trajectories marked by solid lines and are arranged into the familiar “mare’s tail” pattern.

With increasing time, the parcels descend and advect leftward in the figure. In the radar observations, this process produces a time series in which a region of high reflectivity moves downward with time. Presented in time-height coordinates, the appearance is that

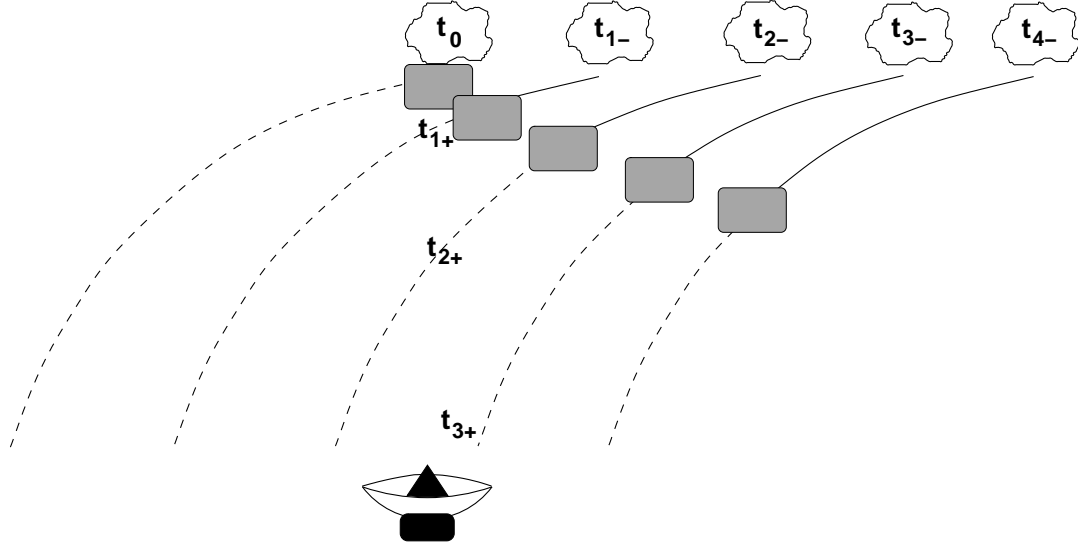


Figure 4.1: Cartoon example of trajectory of precipitation parcel in time-height coordinates.

of slantwise precipitation trails (e.g., Figure 4.2), suggesting naively that a single parcel produced over the radar at time t_0 has simply drifted downward, arriving at the surface some time in the future. In truth, however, the radar sees a series of parcels produced at varying times in the past by the generating cell.

The parcel originating at t_3 in Figure 4.1 arrives at the surface at some time t_{3+} in the future. During this transit time, processes such as aggregation, sublimation and particle size sorting can modify the parcel's microphysical properties and its radar reflectivity. The effects of these processes on the reflectivity could be evaluated by examining reflectivity gradients along the parcel's trajectory, if sufficient observations were available. Then, given an observation of reflectivity aloft at t_{3-} , the reflectivity at the surface could be estimated. As noted above, however, a vertically-pointing radar observes a series of parcels, descending in height, which were produced at varying times by the generating cell. Thus the changes in reflectivity from parcel to parcel in the radar's field of view represent not only the affects of microphysical processes along the trajectories, but also changes over time in the characteristics of the generating cell. Provided those changes in the generating cell are not significant, the reflectivity observed aloft at time t_0 will be reasonably similar to that at t_{3-} , and the required gradient can be evaluated from the series of descending parcels observed in the radar field of view, with adjustments for time offsets. Lacking more detailed observations,

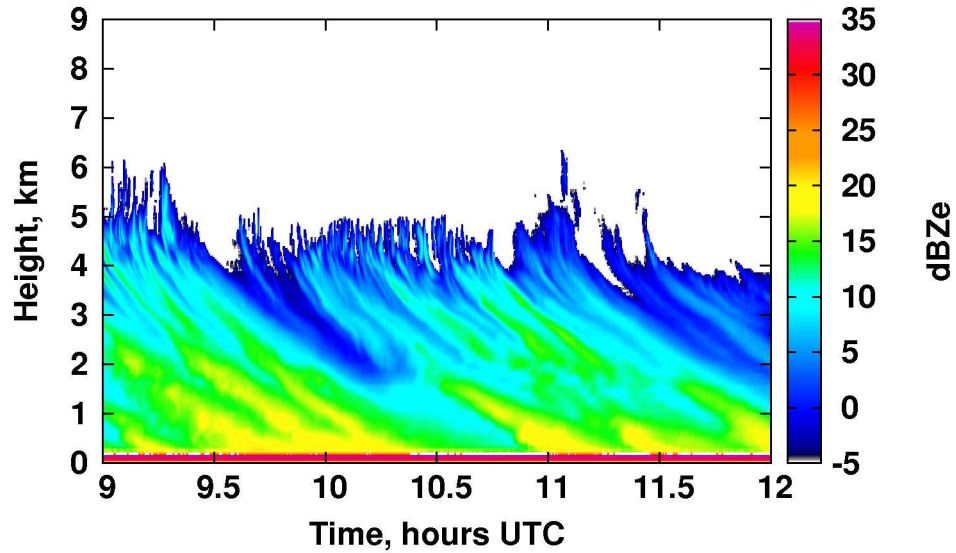


Figure 4.2: Slanted precipitation trails in time-height coordinates. The figure shows details of the VertiX reflectivity profiles from event D.

this assumption was used and the resulting uncertainties were estimated, as described in the following.

In order to calculate the desired gradient, the relative time offsets δt between adjacent vertical bins have to be determined. First, the total time offsets between the surface and bin 13 were determined as described above. Next, the time offsets calculated in the first step are assumed to vary linearly with height in the radar bins adjacent to bin 13. This assumption was applied to bins 10 through 16, and is equivalent to assuming the fallspeeds of precipitation particles are unchanging with height, which is reasonable for short vertical distances for dry snow. Five-minute moving averages of reflectivity were constructed for bins 10 through 16. Given a series of observation times at the surface, taken at five minute intervals, the appropriate time offsets were calculated for bins 10 through 16 and used to select reflectivities in each bin from the series of five-minute moving averages. Finally, a linear least squares fit was done to determine the reflectivity gradient. Because bins below bin 13 were used, these fits were only done provided the bin 13 reflectivity exceeded a 5 dBZe threshold to reduce the potential for errors due to ground clutter. Mean gradients ranged from -4 to -7 dBZe km^{-1} , but exhibited considerable variability (Table 4.1). These results are reasonably consistent with those of Matrosov et al. (2007), who found a mean vertical

Table 4.1: Reflectivity gradients at bin 13 and bin 24, and errors for simulating bin 13 reflectivity using bin 24 reflectivity with the local reflectivity gradient. For mean gradients, numbers in parentheses give the standard deviations and the numbers of samples. For errors, the values shown are the means and, in parentheses, the standard deviations.

	Mean Gradient, dB/km		Errors, dBZe		
Event	bin 13	bin 24	Actual gradient	Mean gradient	Zero gradient
A	-6.7 (4.4, 34)	-5.4 (3.5, 31)	0.011 (1.67)	-0.18 (1.96)	-2.65 (1.96)
B	-4.4 (8.2, 114)	-3.3 (6.0, 68)	1.40 (3.16)	0.40 (3.29)	-1.10 (3.29)
C	-4.7 (7.1, 52)	-3.6 (5.3, 50)	0.98 (3.62)	0.94 (3.59)	-0.70 (3.59)
D	-4.2 (3.2, 156)	-4.5 (4.4, 155)	0.37 (1.97)	0.72 (2.03)	-1.35 (2.03)

gradient of 5.1 dBZ km^{-1} from scanning X-band radar observations above the freezing level of precipitating winter clouds on the western slope of California’s Sierra Nevada mountains.

To test the uncertainties introduced by this approach, the same analysis was repeated, except that the local gradients were evaluated about bin 25 and used to predict reflectivities at bin 13. For most of the events, the mean bin 25 gradients were slightly smaller than those at bin 13, and somewhat less variable (Table 4.1). The estimated bin 13 reflectivities were calculated in three ways: by using the instantaneous gradient, by using the event-specific mean gradient, and by assuming zero gradient (bin 13 reflectivity equal to the time-adjusted bin 25 reflectivity). For all three methods, the errors were approximately normally distributed. The zero gradient method resulted in negatively-biased estimates for the bin 13 reflectivity while the other two methods produced mostly positive biases, somewhat smaller in magnitude than those for the zero gradient method. When the instantaneous gradients were used, biases and standard deviations were not substantially better than those when the mean gradients were used. Consequently, the event-specific mean gradients were used to estimate the near-surface reflectivities, and the uncertainties were modeled using the corresponding standard deviations given in Table 4.1.

4.1.2 Snowfall rate

The instruments used for precipitation rate measurements were introduced in Section 2.1.3. As noted by Sheppard and Joe (2008), the lack of reference standard instruments for field measurements of precipitation rate hinders assessment of uncertainties for observations like those of the POSS and FD12P. Uncertainty estimates were developed for this work by first making the FD12P and POSS rates consistent with the DFIR accumulations, then comparing the resulting rates. For each time interval for which the DFIR reported a snowfall accumulation over the course of the winter 2006/07 C3VP observations, the corresponding 1-minute FD12P and POSS rates were rescaled so their accumulations matched that of the DFIR. Any required time averaging was then performed and differences between the rates computed. Finally, the differences were binned according to precipitation rate, and mean absolute differences determined for each bin. These mean absolute differences were used to model the uncertainty as a function of precipitation rate (Figure 4.3). For rates less than $0.05 \text{ mm LWE h}^{-1}$, the uncertainty was fixed at $0.03 \text{ mm LWE h}^{-1}$. For larger rates up to $0.5 \text{ mm LWE h}^{-1}$, the uncertainty was estimated as 50% of the observed rate, while for rates larger than $0.5 \text{ mm LWE h}^{-1}$, uncertainty was estimated as 30% of the observed rate.

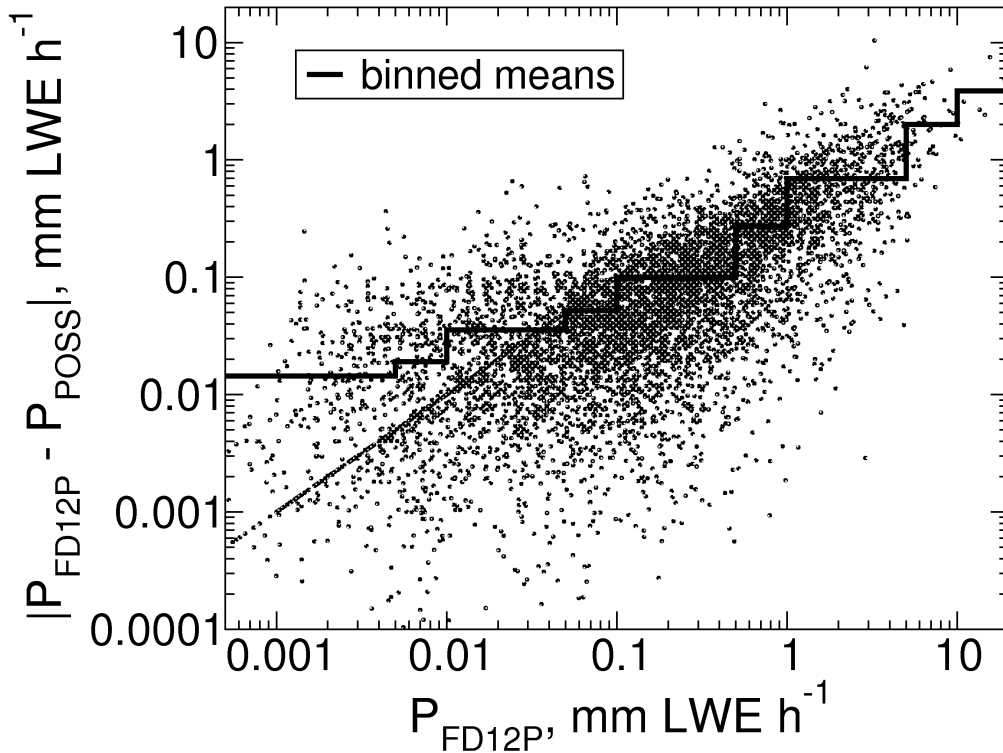


Figure 4.3: Absolute differences in precipitation rates between the FD12P and POSS instruments, and binned mean differences used to estimate uncertainties in precipitation rates. Precipitation rates are 5-min averages.

4.1.3 Size resolved fallspeeds

The retrieval requires three measures of size resolved fallspeeds: V_0 , ΔV_1 , and ΔV_2 . As described in Section 3.3, these measures are based on fallspeeds V_0 , V_1 , and V_2 evaluated at particle sizes D_M of 4.0 ± 0.50 mm, 2.0 ± 0.25 mm, and 1.0 ± 0.25 mm, respectively. These fallspeeds are mean values, obtained by subsetting the 2DVD observations of individual particles for a given 5-minute sample into these three particle size ranges. Uncertainties exist both in the fallspeeds of the individual particles and in their associated particle sizes. Kruger and Krajewski (2002) provided a detailed examination of the operation of the 2DVD and issues which affect the precision and accuracy of its observations.

Uncertainties in the measured individual particle sizes arise because of issues such as calibration errors, the discrete resolution of the photodetector arrays, blurring and horizontal motion of the particles (Kruger and Krajewski, 2002). Based on the results of calibration tests using spherical particles, Brandes et al. (2007) estimated that the particle dimensions measured by the 2DVD have standard errors ranging from 14% for particles with diameter 0.5 mm to less than 1.5% for those with diameter 10 mm. These errors are small compared to the bin widths over which the fallspeeds are averaged. Since the 2DVD particle sizes used in this work are the larger of the sizes obtained from either camera, particle mismatches will also contribute to size errors. These uncertainties have not been quantified, but are expected to be unbiased and, given adequate sample size, not significant. For the two smallest size ranges, samples are typically on the order of 100 particles. More importantly, as described in Appendix A, the observed particle size likely underestimates the true D_M . To correct for this bias, a small adjustment, based on the assumption of a horizontal aspect ratio of 0.6, is made to the particle size ranges. This aspect ratio may not be appropriate for all particle shapes, but the adjustment for the 2DVD is not strongly sensitive to the choice of aspect ratio (Figure 3.1, lower right panel).

For fallspeeds, uncertainties occur primarily due to particle matching errors, wind effects, and the discrete time intervals at which the line scan cameras are sampled (Kruger and Krajewski, 2002), but are difficult to quantify. Wind causes higher variability in the measured particle fallspeeds (Brandes et al., 2007). The CSU 2DVD is a low-profile model, designed to reduce problems related to wind, and was partially surrounded at CARE by a semi-circular double fence (Huang et al., 2010). To further reduce the impact of wind effects, retrievals are limited to cases with winds less than 5 m s^{-1} at 2 m AGL. The 2DVD scans the line scan cameras at a fixed frequency that, for the CSU instrument, is about 55.55 kHz. This causes the travel times between the planes of the two line scan cameras to be quantized (Kruger and Krajewski, 2002), but this is a more significant issue for fast-falling raindrops than for snow. Examining the dispersion of raindrop fallspeeds under calm wind conditions, Brandes et al. (2007) estimated standard errors of 0.4 m s^{-1} for raindrops with diameters of 0.5 mm or less, and less than 0.2 m s^{-1} for raindrops with diameters larger than 2 mm, but it is unclear how uncertainties for snow fallspeeds would compare. Because of

the difficulties of identifying matching particles, especially at small particle sizes, the 2DVD fallspeeds often exhibit large numbers of outliers at small particle sizes. The approach used for these retrievals is to use the observed variability of the snow fallspeeds as an estimate of the fallspeed uncertainty. Based on the results of tests described in section 4.2.2 regarding the effects of binning and averaging fallspeeds from the 2DVD, a filter was applied to the binned fallspeeds before means and variances were computed. Following a method described by Brandes et al. (2008), for each binned sample the mode fallspeed was found and fallspeeds deviating from the mode by more than 0.5 m s^{-1} were discarded, then means were computed along with the sampling variances of the mean for each filtered sample:

$$\begin{aligned}
 s_y^2(V_0) &= s^2(v_0)/N_{V_0} \\
 s_y^2(V_1) &= s^2(v_1)/N_{V_1} \\
 s_y^2(V_2) &= s^2(v_2)/N_{V_2},
 \end{aligned}
 \tag{4.6}$$

where v_0 , v_1 , and v_2 are the set of observed single particle fallspeeds after filtering and N_{V_0} , N_{V_1} and N_{V_2} are the corresponding sample sizes. Assuming the errors in the fallspeeds are uncorrelated, the required variances and covariances can be found as

$$\begin{aligned}
 s_y^2(\Delta V_1) &= s_y^2(V_0) + s_y^2(V_1) \\
 s_y^2(\Delta V_2) &= s_y^2(V_0) + s_y^2(V_2) \\
 s_y(V_0, \Delta V_1) &= s_y^2(V_0) \\
 s_y(V_0, \Delta V_2) &= s_y^2(V_0) \\
 s_y(\Delta V_1, \Delta V_2) &= s_y^2(V_0).
 \end{aligned}
 \tag{4.7}$$

4.2 Forward model uncertainties \mathbf{S}_F

4.2.1 Radar reflectivity forward model

The principal approximations made by the reflectivity forward model are 1) that snow particles scatter according to the Rayleigh model for spheres and 2) that the particle size distribution is discrete and complete (i.e., not truncated), such that the reflectivity can be accurately calculated numerically. The biases and covariances associated with these assumptions are evaluated using the method described by Marks and Rodger (1993). Briefly, given a state \mathbf{x} and the approximate parameters $\tilde{\mathbf{b}}$, the differences between the forward model and higher-quality models can be found. Assembling the differences for an ensemble of states, the bias and covariance \mathbf{S}_F can be determined.

4.2.1.1 Uncertainties due to backscattering properties

To evaluate the uncertainties due to snow particle scattering properties, reflectivities calculated using the Rayleigh approximation for ice spheres were compared against reflectivities calculated from scattering properties obtained using the discrete dipole approximation (DDA) model DDSCAT (version 6.1) of Draine and Flatau (1994) for a variety of particle shapes. DDA calculations were performed for several distinct pristine habits and also for aggregate-like particles. Pristine habits included hexagonal columns (HC), hexagonal plates (HP), two varieties of branched plates (BP1, a broad-branched crystal, P1c; and BP2, a stellar crystal, P1d), and 6-arm bullet rosettes (B6r). DDA models for the pristine habits were constructed using various mass, dimensional and density relations obtained from published observational studies (Table 4.2). The primary aggregate model consisted of an 8-arm rosette-like structure composed of intersecting thick hexagonal columns arranged into a spatial configuration (Figure 4.4, right). An alternate model, consisting of 6 arms whose centerlines are coplanar (Figure 4.4, left) was given limited testing for comparison to the 8-arm model.

For the primary aggregate model, several mass dimension relations were tested including 1) $\alpha = 0.003$, $\beta = 1.8$, 2) $\alpha = 0.00183$, $\beta = 1.4$, and 3) $\alpha = 0.008$, $\beta = 2.1$. The first relation is similar to that found by Locatelli and Hobbs (1974) for “Aggregates of densely rimed

Table 4.2: Sources of mass, area, and other dimensional constraints for pristine particle models. “Other dimensions” includes thickness vs. diameter for HP and BP, width vs. length for HC, and single-bullet width vs. length for B6r. B6r rosette masses from Mitchell (1996) were for 5-arm rosettes and were scaled upward by 6/5 to represent 6-arm rosettes. B6r were also constrained using bullet bulk density estimates from Heymsfield (1972). The size limit for B6r was estimated by using the maximum bullet length observed by H72 of 0.8 mm and assuming two diametrically-opposed bullets. Crystal habit descriptors follow Magono and Lee (1996). Key: AV70, Auer and Veal (1970); H72, Heymsfield (1972); M96, Mitchell (1996).

Habit	Mass	Area	Other dimensions	Size limit, D_M , mm
HC	M96		AV70: C1e, C1f	2.5 (AV70, C1f)
HP	M96		AV70: P1a, P1b, P2e, P2f	3.0 (M96)
BP	M96: P1c	M96: P1c	AV70: P1c, P1d, P2a, P2b	1.0 (M96 P1c), 3.5 (AV70, P1d)
B6r	M96		H72	1.6 (H72)

radiating assemblages of dendrites or dendrites” and the second matches that which they found for “Aggregates of unrimed radiating assemblages of dendrites or dendrites.” The third is an extreme case, similar to the that used by Locatelli and Hobbs for “Graupellike snow of lump type”, but extended to much larger sizes. Horizontally-projected areas were estimated using the “Aggregate hybrid approach” parameterization for area ratio of Heymsfield et al. (2002).

Particles were assumed to be oriented with their longest axes nominally horizontal, and to be oriented randomly about the vertical axis. The radar beam was taken to be vertically incident. Canting angles were also applied. Matrosov et al. (2005b) found that a Gaussian distribution with a mean of 0° and standard deviation of 9° was appropriate for canting angles for pristine dendritic crystals. The degree to which this finding applies to irregular and aggregate particles is not clear. As an approximation, and to accommodate DDSCAT’s standard treatment, canting angles ranged over $\pm 10^\circ$ and were distributed uniformly in the cosine of the angle.

Among the pristine particles, the B6r backscattering cross-sections most closely matched those for Rayleigh ice spheres, while the other three habits exceeded the Rayleigh values. The HP cross-sections were a factor of 2.5 larger than Rayleigh over most of the size range,



Figure 4.4: Aggregate particle shapes. On the left is a 6-arm particle with arms in a single plane, and on the right is an 8-arm particle with arms oriented spatially.

while the ratios for the BP and HC particles were approximately 1.5 times larger (Figure 4.5). These results are consistent with those of Atlas et al. (1953), who applied a Rayleigh model for spheroids, and showed that the backscattered intensities from oriented ice spheroids could be appreciably larger than those for spheres. For a vertically pointed radar and oblate spheroids with the figure axis vertical, the backscattering intensity was enhanced by a factor of more than 2 relative to spheres when the spheroids were extremely flattened, similar to the DDA results for hexagonal plates. For prolate spheroids with the figure axis horizontal, the enhancement was about a factor of 1.5 relative to spheres when the spheroids were extremely elongated, similar to the DDA results for columns.

At small sizes, the backscattering cross-sections for aggregates were somewhat larger than those of Rayleigh spheres. For these small sizes, the aggregate models approximate slightly flattened, dense ice particles and would be expected to have somewhat enhanced backscattering compared to Rayleigh ice spheres. The behavior at larger sizes is different for the 6-arm flattened and 8-arm spatial particles. The cross-section of the more compact 6-arm particle essentially matches Rayleigh, while the cross-sections of the 8-arm spatial particles fall to about 80% of Rayleigh. The ratios for the 8-arm spatial particles were only slightly sensitive to the mass-dimension relation at these large sizes.

To determine the impact on reflectivity of these departures from Rayleigh sphere scattering, an ensemble of test cases was constructed using SVI size distributions taken over a range of snow events during C3VP. The size distribution rescaling factor ϕ was set to expected values for the particular particle habit (0.65 for HC, 0.95 for HP and BP1, 0.80 for BP2 and B6r, 0.80 for aggregates). For each case, DDA reflectivities were calculated by applying the various pristine particle backscattering cross-sections at small sizes with either the B6pf or B8pr (0.003, 1.8) aggregate cross-sections at large sizes. At sizes beyond

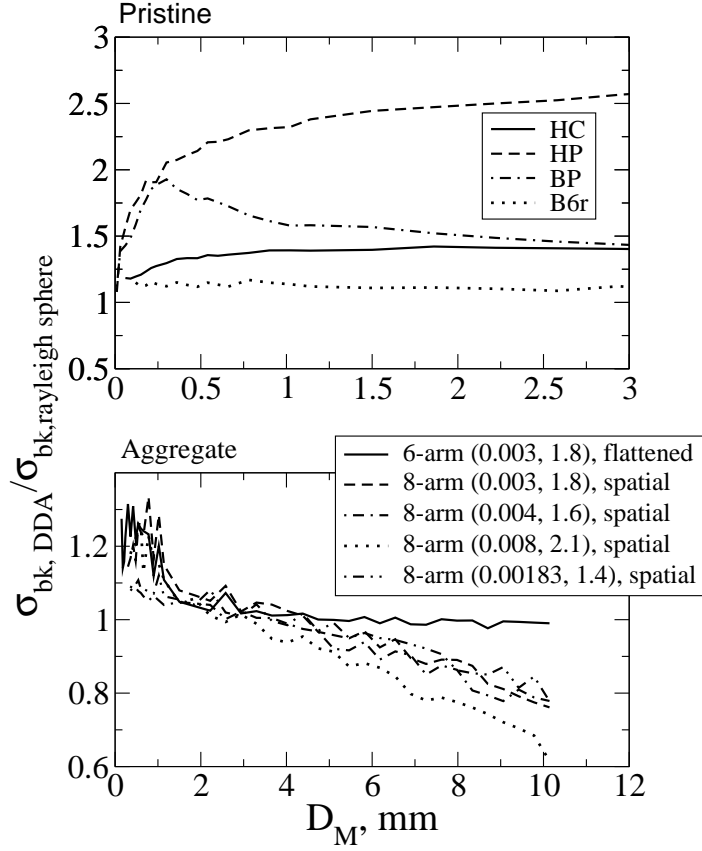


Figure 4.5: Ratios of DDA backscattering cross-sections to cross-sections for equal-mass spheres as a function of the maximum dimension D_M of the DDA particle. The upper panel shows ratios for pristine particles, including hexagonal columns (HC), hexagonal plates (HP), branched plates (BP), and 6-arm bullet rosettes (B6r). The lower panel shows ratios for various forms of aggregate models, where the numbers in parentheses give the values of the mass-dimension parameters α and β .

the largest ($D_M \approx 10$ mm) for which DDA calculations were completed, the backscattering efficiency was estimated by extrapolating from the two largest sizes. The transition from pristine to aggregate scattering properties was done over a size range starting at $D_M = 0.6$ mm and ending at the size limits shown in Table 4.2, and the fraction of pristine particles varied linearly with D_M over the size range. For each pristine-aggregate particle combination, the resulting DDA reflectivities were compared against the corresponding Rayleigh sphere reflectivities.

The DDA reflectivities were generally larger than the Rayleigh model when reflectivities were small, and slightly smaller than the Rayleigh model when reflectivities were large (Figure 4.6). Averaged over the ensemble of test cases, the bias of the Rayleigh sphere reflectivities relative to the DDA reflectivities ranged from -1.5 dBZe at -5 dBZe to +1.0 dBZe at 35 dBZe. The root mean square (RMS) values of the residual errors after bias correction varied between 0.2 and 0.6 dBZe over the same range. Consolidating all the ensemble states, a linear bias correction was determined to be

$$\overline{\delta_F(Ze)} = -0.049Z_{Rayl} - 1.17, \quad (4.8)$$

where Z_{Rayl} is the reflectivity in dB modeled using Rayleigh spheres and the corresponding variance was modeled as $s_F^2(Ze) = 0.42$.

4.2.1.2 Uncertainties due to discretization and truncation

For particles larger than 17 mm, the 2DVD can detect smaller number concentrations than can the SVI, and the maximum detectable size for the 2DVD is significantly larger than that for the SVI (Figure 4.7). The number concentration detection limits were calculated as one particle per unit sampling volume per unit size interval. This difference in detection limits suggests that the 2DVD individual particle observations can be used to estimate the effects of discretization and size distribution truncation on the reflectivities and snowfall rates calculated from the SVI observations. Simulated SVI size distributions can be calculated from the 2DVD individual particle observations, then reflectivities and snowfall rates can be calculated using both the original 2DVD observations and the simulated SVI distributions.

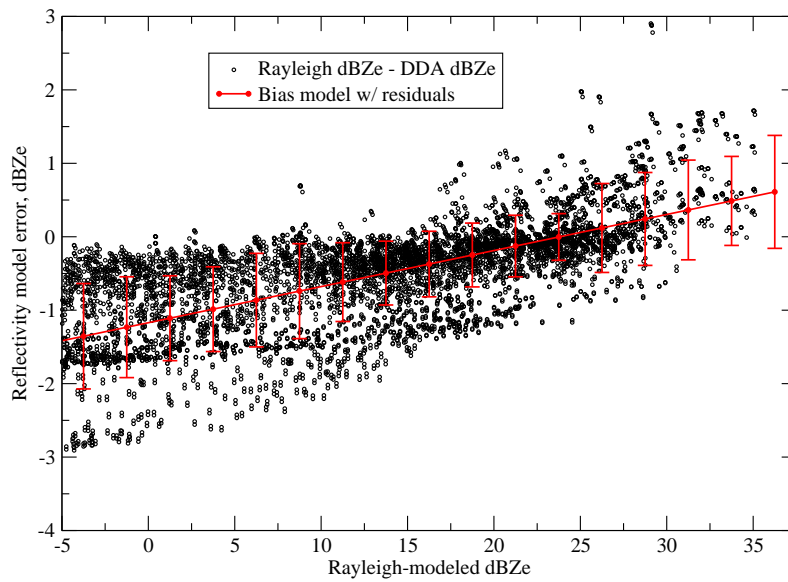


Figure 4.6: Rayleigh model errors relative to reflectivities calculated using DDA scattering properties for observed SVI size distributions. Points show the difference between Rayleigh modeled reflectivity and DDA-modeled reflectivity for each size distribution observation. The fitted line shows a linear estimate of the bias, while the error bars show the RMSE calculated from the residual differences after bias correction.

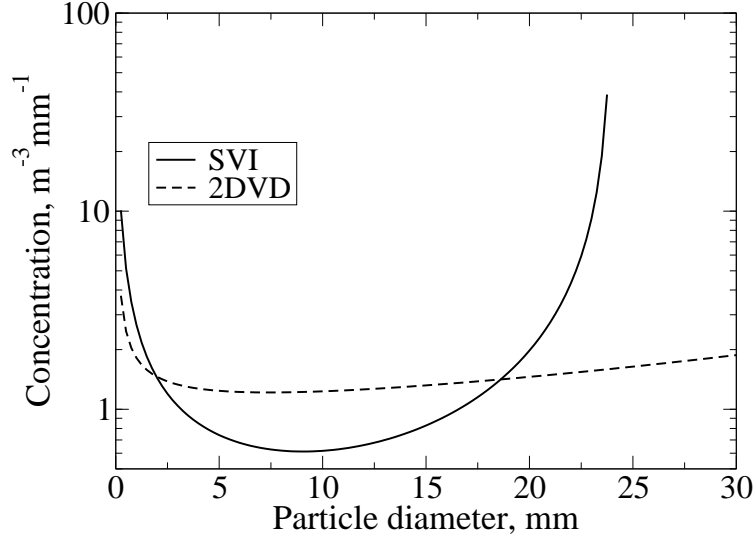


Figure 4.7: Comparison of minimum detectable concentrations for the SVI and the 2DVD, assuming 5 minute samples, 0.25 mm size bins and spherical particles which must be fully within the sensing area. The 2DVD values use fallspeeds from MH2005 with mass and area parameterizations for “Aggregates of side planes, columns and bullets” from Mitchell (1996).

Differences between the reflectivities and between the snowfall rates provide information about the likely errors due to truncation and discretization.

To accomplish this, distinct 5-minute samples of the 2DVD individual particle observations were first binned into the size intervals used by the SVI and discrete size distributions were calculated using (2.1). For size intervals at which the calculated size distribution fell below the SVI minimum detectable value, the calculated distribution was set to zero, forming the simulated discrete, truncated size distributions. A single case, then, consisted of the original 2DVD single particle data, a discrete size distribution, and a discrete-truncated size distribution.

Given a particular case of 2DVD individual particle observations and an assumed mass-dimension relation, the reference radar reflectivity was calculated directly per (2.1), (3.16) and (3.23) as the sum over all the particles of the backscatter cross sections per unit volume:

$$Z_e = \frac{\alpha^2 36}{\pi^2 \rho_{ice}^2} \frac{\|K_i\|^2}{\|K_w\|^2} \frac{1}{\Delta t} \sum_{j=0}^{j=N_p} \frac{D_j^{2\beta}}{A_j v_j}. \quad (4.9)$$

Reflectivities were then calculated using the simulated SVI discrete and discrete-truncated size distribution, using (3.27) evaluated via Simpson’s rule. The differences between these two reflectivities and the reference reflectivity represent the forward model errors due to discretization and due to combined discretization and truncation of the size distribution. Provided the mass-dimension relation (3.23) is applicable over the entire size distribution, differences in dBZe will depend on β and not on α , since dBZe differences represent ratios of Ze. The cap on particle mass (to be no more than that of an ice sphere) means that some dependence on α may occur but is likely to be weak because the cap affects only very small particles.

2DVD observations from snow events on seven different days during C3VP (the four events studied here and three additional events: 17, 20 and 22 January 2007) were used to evaluate these errors. Values for α ranged from 0.001 to 0.009 in 0.002 increments, while those for β ranged independently from 1.4 to 2.4 in 0.2 increments. Reflectivity differences in dBZe and fractional snowfall rate differences were calculated for 685 distinct 5-minute samples of the 2DVD observations, then biases and error covariances were calculated (Table 4.3). The statistical properties were largely independent of α , as was expected. The table shows errors for both discretization only and discretization plus truncation for comparison. Except as noted, this description focuses on the errors due to discretization plus truncation. The reflectivity bias became more negative as β increased, ranging from -0.75 to -1.21 dBZe, while the residual errors increased from 0.62 to 2.08 dBZe. Both biases and residual errors in dBZe were found to be approximately linearly dependent on β (Table 4.3), and were modeled as

$$\begin{aligned}\overline{\delta_F(Ze)} &= -0.26\beta - 0.38 \\ s_F^2(Ze) &= (0.99\beta - 0.78)^2\end{aligned}\tag{4.10}$$

4.2.2 Snowfall rate

The snowfall rate forward model is simply an integration of the product of particle mass, size distribution and fallspeed over all particle sizes, as shown in (3.28). The snowfall

Table 4.3: Biases, standard deviations of errors and error correlations due to size distribution truncation and discretization for radar reflectivity and snowfall rate. Numbers outside parentheses are due to both discretization and truncation, while those inside parentheses are for discretization only.

β	Reflectivity, dBZe		Snowfall rate, fractional		Correlation
	Bias	SD	Bias	SD	coefficient
1.4	-0.75 (-0.64)	0.62 (0.37)	0.051 (0.053)	0.14 (0.14)	0.43 (0.59)
1.6	-0.81 (-0.64)	0.81 (0.38)	0.047 (0.051)	0.14 (0.14)	0.37 (0.54)
1.8	-0.88 (-0.64)	1.07 (0.40)	0.040 (0.045)	0.14 (0.14)	0.34 (0.50)
2.0	-0.98 (-0.65)	1.36 (0.42)	0.031 (0.037)	0.14 (0.14)	0.34 (0.46)
2.2	-1.09 (-0.65)	1.70 (0.44)	0.0198 (0.028)	0.15 (0.15)	0.35 (0.42)
2.4	-1.21 (-0.66)	2.08 (0.45)	0.0078 (0.018)	0.15 (0.15)	0.36 (0.38)

rate and reflectivity forward models share the assumption regarding the adequacy of the discrete, truncated size distributions observed by the SVI. Snowfall rate uncertainties are also produced by uncertainties in the forward model for fallspeed. This section focuses on the uncertainties due to size distribution discretization and truncation, and the assessment of uncertainties caused by the fallspeed model are deferred to the next section.

The snowfall rate biases and covariances were evaluated following the same process as described above for radar reflectivity. The reference snowfall rates were calculated directly from the 2DVD individual particle observations as

$$P = \frac{\alpha}{\Delta t \rho_{liq}} \sum_{j=0}^{j=N_p} \frac{D_j^\beta}{A_j}. \quad (4.11)$$

Snowfall rates were then calculated with the discrete and discrete-truncated size distributions using (3.28), again evaluated via Simpson’s rule. As was true for the reflectivities, the differences between these two snowfall rates and the reference rates provide information about the forward model errors due to discretization and due to discretization plus truncation. Snowfall rate differences should scale linearly with α , again except for small departures due to the cap on particle mass. Snowfall rate biases and covariances were evaluated in terms of fractional snowfall rate to reduce dependence on α .

For snowfall rate, bias decreased from 5.1% to 0.78% with increasing β while the residual errors were nearly constant at 14-15% of the reference snowfall rate (Table 4.3). Correlations between the reflectivity and snowfall rate errors were generally about 0.35, except for the $\beta = 1.4$ case for which the correlation was 0.43. The snowfall rate errors proved to be exceptionally sensitive to how $V(D_i)$ was evaluated. Using a simple mean from a 2DVD sample centered on D_i and taken over a 0.25 mm size interval resulted in significant positive biases (not shown), likely due to the effects of extreme positive outliers which become increasingly common at smaller particle sizes. To ameliorate these effects, a filter was applied to the fallspeed observations following Brandes et al. (2008). For each sample the mode fallspeed was found and fallspeeds deviating from the mode by more than 0.5 m s⁻¹ were discarded before averaging.

As was true for reflectivity, the bias in fractional snowfall rate was also approximately linearly dependent on β . Residual errors were essentially independent of β . These were modeled as

$$\begin{aligned}\overline{\delta_F(P)} &= (-0.023\beta + 0.083)P \\ s_F^2(P) &= (0.14P)^2.\end{aligned}\tag{4.12}$$

Finally the error covariance between the reflectivity and snowfall rate was modeled as

$$s_F(Ze, P) = 0.35 (s_F(Ze)) (s_F(P)).\tag{4.13}$$

4.2.3 Fallspeeds

Uncertainties due to approximations in the forward model for fallspeeds are more difficult to assess. Unlike the previously discussed sources of uncertainty for the snowfall rate and reflectivity forward models, there are not higher-quality fallspeed models against which to compare. In their study of previously reported laboratory and in situ measurements of ice particle fallspeeds, Heymsfield and Westbrook (2010) estimated the uncertainty of fallspeeds calculated with their method to be less than 30%, developing their estimate by binning single particle fallspeed errors by area ratio and determining the median fallspeed error. Mitchell

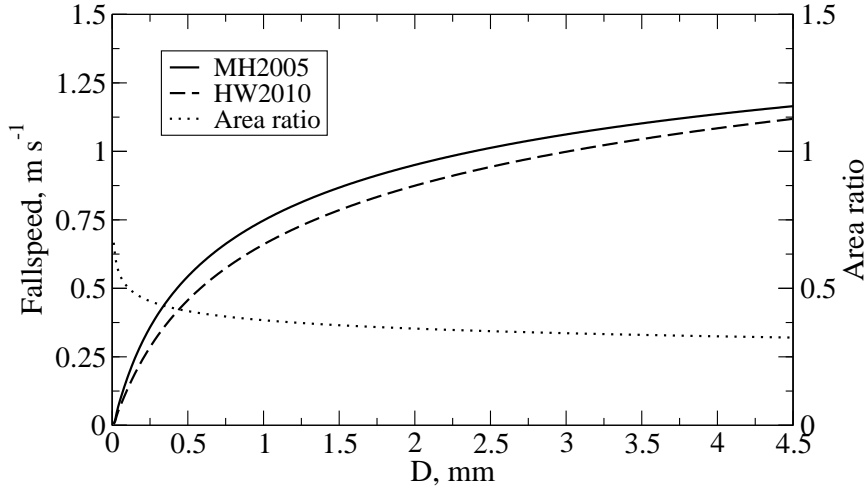


Figure 4.8: Comparison of fallspeeds from the MH2005 and HW2010 models, using the Mitchell (1996) mass and area power law parameters for “Aggregates of side planes, columns and bullets.”

and Heymsfield (2005) did not provide a similar estimate; however, examining the scatter in the Reynolds numbers of observed particles about their model (their Figure 2), suggests that 30% - 50% uncertainty is not unreasonable. Accordingly, an uncertainty of 30% was adopted for fallspeeds from both models. A comparison of the two models, MH2005 and HW2010, using the Mitchell (1996) mass and area power laws for aggregates of side planes, columns and bullets shows modest but nonnegligible differences between the two models (Figure 4.8), so retrievals were performed using both models.

The contribution to \mathbf{S}_F due to the fallspeed forward model uncertainties must be determined. Provided the covariance matrix for the fallspeed uncertainties, \mathbf{S}_v is known, the contribution to \mathbf{S}_F is given by

$$\mathbf{S}_{F,v} = \mathbf{K}_v \mathbf{S}_v \mathbf{K}_v^T \quad (4.14)$$

where \mathbf{K}_v is the Jacobian of the forward model with respect to the fallspeeds. The first row, $\frac{\partial Ze}{\partial \mathbf{v}}$, is uniformly zero since Ze has no dependence on the fallspeeds. The second row, $\frac{\partial P}{\partial \mathbf{v}}$,

follows the numerical treatment used to integrate (3.28), and with trapezoidal integration becomes

$$\frac{\partial P}{\partial \mathbf{v}} = \frac{1}{\rho_{liq}} \left[N(D_{M,0}) m(D_{M,0}) \frac{\Delta D_{M,0}}{2} \right. \quad (4.15)$$

$$N(D_{M,1}) m(D_{M,1}) \Delta D_{M,1} \cdots$$

$$\cdots$$

$$\left. N(D_{M,K}) m(D_{M,K}) \frac{\Delta D_{M,K}}{2} \right]$$

where K is the number of discrete bins in the size distribution and ΔD_M are the widths of the size bins. In the third row of K_v , $\frac{\partial V_0}{\partial \mathbf{v}}$ has a value of one at the size bin at which V_0 is defined (i.e., at $D_M = 4mm$) and is zero elsewhere. The fourth and fifth rows are obtained similarly as $\frac{\partial(V_0-V_1)}{\partial \mathbf{v}}$ and $\frac{\partial(V_0-V_2)}{\partial \mathbf{v}}$.

The estimate of forward model fallspeed uncertainties given above requires covariances of the fallspeed errors as a function of particle size, \mathbf{S}_v . Lacking a higher-quality forward model, estimates of \mathbf{S}_v were obtained by performing simple fits of the MH2005 and HW2010 fallspeed forward models to the observed 2DVD fallspeeds, then evaluating correlations between the fitting errors. The 2DVD fallspeed observations were taken from the same seven events used to evaluate the discretization and truncation errors. As in that evaluation, the fallspeeds from 5-minute samples were binned into the same size distribution bins used by the SVI, then filtered as described in Section 4.2.2 before means and standard errors were calculated. The fallspeed forward model was then fitted to the mean fallspeeds using a nonlinear least squares technique and fitting errors were found for each size bin. Paired errors (error for size bin i paired with error for size bin j) were collected for each sample over all samples, then correlations between errors were calculated, forming a fallspeed error correlation matrix $\boldsymbol{\rho}_v$. At the initial resolution of 1 size bin, the correlation matrix showed considerable bin-to-bin variability, and a 5 bin x 5 bin moving window average was applied to smooth the variations (Figure 4.9). From the error correlation matrix, the values of the elements of the error covariance matrix \mathbf{S}_v are

$$s_v^2(v_i, v_j) = \boldsymbol{\rho}_v[i, j] f^2 v_i v_j$$

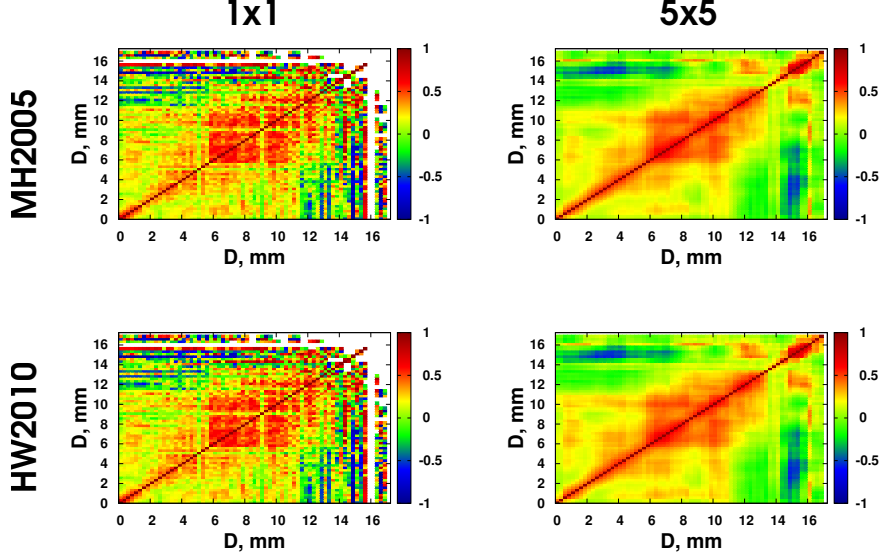


Figure 4.9: Fallspeed forward model error correlations. Correlations are shown for the initial resolution of 1 bin x 1 bin (left), and a smoothed resolution of 5 bins x 5 bins (right) for both the MH2005 (top) and HW2010 (bottom) fallspeed forward models.

where f is the fractional error for the fallspeeds, taken to be 30% as noted above, with v_i and v_j the fallspeeds for bin i and bin j .

4.3 Uncertainties due to parameters \mathbf{S}_B

Parameters used by the components of the forward model include not only the density of ice and the dielectric properties of ice and water, which are reasonably well-determined, but also the discrete values of the size distribution $N(D_i)$, the associated sizes D_i , and environmental properties like temperature and pressure. Estimating \mathbf{S}_B requires that the parameter dependencies of each forward model be identified, that variances for each of the parameters be estimated, that the parameter covariance matrix, \mathbf{S}_b , be constructed, and that the Jacobian of the forward model with respect to the parameters, \mathbf{K}_b , be calculated. Parameter dependencies shared by the forward model components will result in covariances between errors in the forward modeled state vector variables, as described above when \mathbf{S}_B was introduced. Table 4.4 summarizes the parameter dependencies of the forward model components. Dependencies on T and p , atmospheric temperature and pressure, arise through the dependence of fallspeeds on atmospheric density and viscosity. Although $\|K_i\|^2$

Table 4.4: Parameter dependencies of the forward model components.

Component	Parameters
Ze	$D_i, N(D_i), \ K_i\ ^2$
P	$D_i, N(D_i), T, p, \delta_0, C_0, a_0, b_0$
V_0	$T, p, \delta_0, C_0, a_0, b_0$
ΔV_1	$T, p, \delta_0, C_0, a_0, b_0$
ΔV_2	$T, p, \delta_0, C_0, a_0, b_0$

exhibits a dependence on temperature which would cause Ze to also be dependent on temperature, this dependence is weak over the expected atmospheric temperature range and is ignored. The matrix \mathbf{S}_b is shown in (4.16) and the corresponding Jacobian is shown in (4.17) where the dots indicate extension over all the discrete values of D_i and $N(D_i)$.

4.3.1 Size distribution uncertainties

The size distribution observations contribute to ϵ through several paths. The distributions constitute part of the vector $\tilde{\mathbf{b}}$ of forward model parameters for radar reflectivity and snowfall rate, so uncertainties contribute via the third term in (4.2). Additionally, the discrete form of the size distribution controls the resolution at which the numerical integrations in the forward model, used to calculate reflectivity and snowfall rate, are performed. Finally, the detection limits of the observing instrument, determined in part by the sample durations, produce a size distribution which may be truncated in comparison to the true distribution. The maximum size observable by the SVI is determined by the field of view and is nominally 24 mm, but minimum detectable concentrations are determined by sampling volumes which are in turn dependent on the duration of samples. Size distribution observations from the SVI were obtained at a nominal time resolution of 1 minute, but were averaged using distinct 5 minute samples to improve sampling volumes. These latter two error paths, discretization and truncation, can be considered errors caused by approximate physics in the forward model and were discussed as part of the reflectivity and snowfall rate forward model errors above.

Observational errors in the size distributions arise from a number of sources. As discussed in section 3.3, the particle dimension D_{obs} observed by the SVI will, for almost all typical particles, underestimate the true maximum dimension D_M of the particle. Adjustments to the size distribution to convert $N(D_{obs})$ to $N(D_M)$, and uncertainties in those adjustments, are handled via the state variable ϕ . The remaining principal measurement uncertainties are analytic uncertainties and sampling uncertainties. Analytic uncertainties include uncertainties in the particle counts caused by the measurement or analysis techniques, uncertainties in the measured particle size and uncertainties in the relationship used to estimate depth of field from particle size (Newman et al., 2009). Sampling uncertainties arise due to statistical fluctuations in the number of particles counted by the instrument. Because of the relatively small sample volumes of these types of instruments, both sources of uncertainty are likely significant.

To estimate the total uncertainty in a measured value of $N(D_{obs,i})$, analytic and sampling uncertainties were modeled separately and the resulting variances added. The SVI size distribution is determined as shown in (2.3). Both A_{ijk} and L_{ijk} depend on particle size:

$$A_{ijk} = (X_{fov} - D_{ijk})(Y_{fov} - D_{ijk}) \quad (4.18)$$

$$L_{ijk} = f D_{ijk} \quad (4.19)$$

where X_{fov} and Y_{fov} are the maximum width and height of the frame, f is an empirical factor relating particle size to depth of field, and D_{ijk} is the particle size (Newman et al., 2009). The relationship (4.19) was derived using the the feret diameter, the distance between the two furthest removed points on the SVI particle image, and this is consistent with the observed D used in these SVI data. Combining (2.3), (4.18) and (4.19) then simplifying the indexing, the size distribution can be written as

$$N(D_i) = \frac{1}{N_f \Delta D_i} \sum_{j=1}^{j=N_{p_i,tot}} \frac{1}{(X_{fov} - D_{ij})(Y_{fov} - D_{ij})f D_{ij}}. \quad (4.20)$$

$Np_{i,tot}$ is the total number of particles observed in the i -th bin accumulated over all image frames. The number of frames N_f , and the frame dimensions X_{fov} and Y_{fov} can be determined accurately, and ΔD_i is a specified constant, leaving $Np_{i,tot}$, f , and D_{ij} as sources of error.

The analytic uncertainty is caused by issues such as errors in the evaluation of D_{ij} , errors in the count of particles $Np_{i,tot}$, and the uncertainty in the value of f . Errors in the measured particle size D_{obs} are caused by blurring and lack of contrast in the image (Newman et al., 2009). These errors affect the estimates of the field of view A_{ijk} and depth of field L_{ijk} which then propagate as errors in the calculated size distribution via (4.20). Particle sizing errors also cause particles to be misclassified into size intervals. These classification errors can cause errors in the calculated size distribution, but, since undercounting in one interval will be accompanied by overcounting in nearby intervals, the effects on integrated quantities like reflectivity and snowfall rate calculations in the forward model are expected to be minor and are neglected. Errors in the count of particles $Np_{i,tot}$ can be caused by reappearance of particles and by obscuration. In environments with very low wind speeds a slowly falling particle may appear in multiple frames, causing it to be counted multiple times. Winds at 2 m AGL were generally in excess of 1.5 m s^{-1} during the four snow events, and such repeated counting is not expected to be a concern. Under conditions of high particle concentrations, a particle in the background of the sample volume may be obscured by a particle in the foreground. It is not known to what extent obscuration affects the SVI observations. Depth of field changes approximately linearly with particle size. For small particles, for which concentrations may be high, the depth of field is shallow, making obscuration unlikely. For large particles, depth of field is larger but concentrations are typically low, also making obscuration unlikely. Based on these arguments, errors in $Np_{i,tot}$ due to reappearance and obscuration were neglected.

Sampling errors affect the number of particles counted in the discrete size intervals and the distribution of particle sizes observed in a particular interval. The number of particles $Np_{i,tot}$ in a particular size bin observed arriving in the disdrometer sample volume at a particular instant is typically taken to be a random deviate distributed according to the Poisson distribution (Joss and Waldvogel, 1969) and contributes to sampling uncertainty

in the calculated size distribution values. The observed particles sizes D_{ij} also vary and are distributed according to a probability density function defined by the size distribution (Uijlenhoet et al., 2006). For the particles occupying a particular size bin i during an observation, both the sizes D_{ij} of the particles and the number of particles $Np_{i,tot}$ are realizations of random variables. For purposes of estimating sampling uncertainty, then, the form of $N(D_i)$ is that of a random sum of random variables (Feldman and Valdez-Flores, 2010), also known as a randomly stopped sum.

Analytic uncertainty

To estimate the analytic uncertainty, we assume that $Np_{i,tot}$ is measured with negligible uncertainty (e.g., overlapping or doubly-counted particles are uncommon). The measurements D_{ij} have uncertainties with variances $s^2(D_{ij})$ and are expected to be independent and identically distributed. The parameter f has uncertainty independent of the uncertainties in D_{ij} with variance $s^2(f)$. Representing $N(D_i)$ as N_i to simplify notation, (4.20) can be rewritten as

$$N_i = \frac{1}{N_f \Delta D_i} \sum_{j=1}^{j=Np_{i,tot}} x_j, \quad (4.21)$$

where

$$x_j = \frac{1}{(X_{fov} - D_j)(Y_{fov} - D_j)f \cdot D_j} \quad (4.22)$$

and where the i subscript for terms inside the sum has been omitted for clarity. The variances $s^2(x_j)$ can be estimated by error propagation as

$$s^2(x_j) = \left(\frac{\partial x_j}{\partial D_j} \right)^2 s^2(D_j) + \left(\frac{\partial x_j}{\partial f} \right)^2 s^2(f). \quad (4.23)$$

The variance $s^2(N_i)$ can be found as

$$s^2(N_i) = \left[\left(\frac{\partial N_i}{\partial x_1} \right)^2 s^2(x_1) + \left(\frac{\partial N_i}{\partial x_2} \right)^2 s^2(x_2) + \dots + \left(\frac{\partial N_i}{\partial x_{Np_{i,tot}}} \right)^2 s^2(x_{Np_{i,tot}}) \right]. \quad (4.24)$$

Since $\frac{\partial N_i}{\partial x_j} = \frac{1}{N_f \Delta D_i}$,

$$s^2(N_i) = \left[\frac{1}{N_f \Delta D_i} \right]^2 [s^2(x_1) + s^2(x_2) + \dots + s^2(x_{Np_{i,tot}})] \quad (4.25)$$

Provided the partial derivatives $\frac{\partial x_j}{\partial D_j}$ do not vary significantly over the size range for the bin, the values of $s^2(x_j)$ will also not vary significantly and can be approximated with a single value $s^2(x)$, giving

$$s^2(N_i) \approx \left[\frac{1}{N_f \Delta D_i} \right]^2 Np_i s^2(x). \quad (4.26)$$

Since single-particle measurements were not part of the processed SVI data, the derivatives $\frac{\partial x_j}{\partial D_j}$ and the variances $s^2(D_j)$ were estimated at the expected values of D on the size bin interval between D_i and D_{i+1} . For spherical particles, the uncertainty in particle size has been estimated at 18% (Newman et al., 2009), and that estimate was used for this work even though nonspherical snow particles are observed. Note that D_{ij} in this context is the dimension observed by the disdrometer, not an estimate of the particle maximum dimension. Newman et al. estimated the uncertainty in depth of field at 15% when particle size is known accurately, suggesting that f has an uncertainty of 15%, which was the value used for this work.

Sampling uncertainty

To evaluate the sampling uncertainty, $Np_{i,tot}$ is considered a random variable in addition to D_j . For rainfall, the number of particles observed in a given size interval by a volume sampling device like the SVI is often taken to be a Poisson-distributed random variable (Joss and Waldvogel, 1969; Gertzman and Atlas, 1977; Uijlenhoet et al., 2006). The same approach is taken here for snowfall, considering it to behave as a homogeneous marked Poisson process during the sampling time interval. The number of particles $Np_{i,tot}$ appearing in the SVI sampling volume then follows a Poisson distribution. The observed D_j form a sequence of random variables taken to be independent and identically distributed. As a result, the x_j are also independent and identically distributed. As noted above, the size

distribution value N_i is then the result of a random sum of random variables. Letting

$$y_i = \sum_{j=1}^{j=Np_{i,tot}} x_j \quad (4.27)$$

the variance of y_i can be shown to be

$$V[y_i] = V[x_j] E[Np_i] + [E[x_j]]^2 V[Np_i] \quad (4.28)$$

(Feldman and Valdez-Flores, 2010) by applying the law of total variance, where $V[\]$ indicates variance and $E[\]$ indicates expectation. Since $Np_{i,tot}$ is Poisson-distributed, the best estimate of the expectation and variance is the observed count, so that

$$V[y_i] = Np_{i,tot} V[x_j] + Np_{i,tot} [E[x_j]]^2. \quad (4.29)$$

Thus it is necessary to estimate the expectation and variance for x_j . These can be estimated via Taylor series expansion of $x(D)$. Since uncertainty in f does not contribute to sampling uncertainty, the expectation can be estimated as

$$E[x(D)] \approx x(\mu_D) + \frac{x''(\mu_D)}{2} s_D^2 \quad (4.30)$$

where μ_D and s_D^2 are the expectation and variance of D , respectively, and the primes indicate derivatives with respect to D . The variance can be estimated as

$$Var[x(D)] \approx (x'(\mu_D))^2 s_D^2 \quad (4.31)$$

As noted by Uijlenhoet et al. (2006), the particle size distribution can be written as the product of the total number concentration, N_{tot} , and the probability density function of particle sizes, $p(D)$. Taking the particle sizes to be distributed exponentially gives

$$N(D) = N_{tot} \lambda \exp(-\lambda D). \quad (4.32)$$

from which it can be seen that

$$p(D) = \lambda \exp(-\lambda D). \quad (4.33)$$

What are needed are estimates of the expectation and variance of D on subintervals of $p(D)$.

For a subinterval bounded by D_i and D_{i+1} , expectation and variance are defined by

$$\mu_D = \frac{\int_{D_i}^{D_{i+1}} p(D) D dD}{\int_{D_i}^{D_{i+1}} p(D) dD} \quad (4.34)$$

and

$$s_D^2 = \frac{\int_{D_i}^{D_{i+1}} p(D) (D - \mu_D)^2 dD}{\int_{D_i}^{D_{i+1}} p(D) dD}. \quad (4.35)$$

Evaluating these integrals for the exponential probability distribution gives

$$\mu_D = D_i + \frac{1}{\lambda} - \frac{(D_{i+1} - D_i) \exp(-\lambda (D_{i+1} - D_i))}{1 - \exp(-\lambda (D_{i+1} - D_i))} \quad (4.36)$$

and

$$s_D^2 = \frac{1}{\lambda^2} - \frac{\exp(-\lambda (D_{i+1} - D_i)) (D_{i+1} - D_i)^2}{(1 - \exp(-\lambda (D_{i+1} - D_i)))^2} \quad (4.37)$$

The value of λ is estimated by linear least squares fitting of $\ln(N_i)$ to D_i . Given these last two relations and λ , the expectation and variance of D can be determined for each size bin. From these, the expectation and variance of $x(D)$ can be found using (4.30) and (4.31). Next, the variance of y_i can be found via (4.29). Finally, since

$$N_i = \frac{1}{N_f \Delta D_i} y_i, \quad (4.38)$$

the variance of N_i is

$$V[N_i] = \left[\frac{1}{N_f \Delta D_i} \right]^2 V[y_i] \quad (4.39)$$

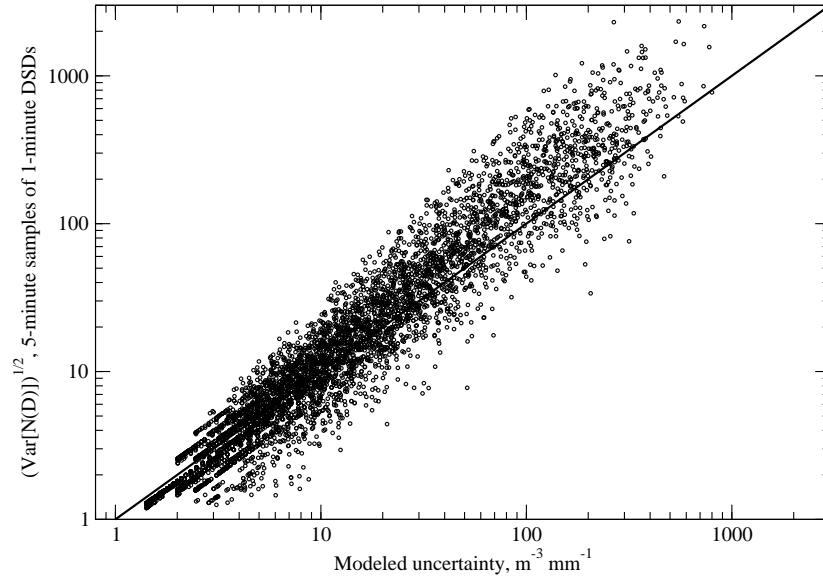


Figure 4.10: Comparison of uncertainties estimated from observations (square root of variance computed from samples of 5 1-minute particle size distributions) and those calculated from the statistical model for event B (7 Dec 2006).

Size distribution uncertainty model evaluation

As a simple check on the validity of the size distribution uncertainty model, distinct samples of the SVI observations were formed by repeatedly collecting five consecutive 1-minute SVI size distributions from the observations for event B. Variances were computed bin by bin for each sample. The statistical uncertainty model described above was then applied to the 5-minute average size distribution obtained from each sample, then the modeled analytic and sampling variances for each bin were summed. Both the empirical and modeled uncertainties spanned approximately three orders of magnitude (Figure 4.10). At small uncertainties, the modeled and empirical uncertainties were in good agreement. At large uncertainties, the modeled uncertainties for the 5-minute size distributions were somewhat smaller than the empirical uncertainties for the 1-minute size distributions. Given that the empirical uncertainties apply to 1-minute SVI observations, while the modeled uncertainties apply to 5-minute averages of the SVI observations, the differences appear reasonable.

4.3.2 Variances for other parameters

The remaining parameters in (4.16) for which variances are required are $\|K_i\|^2$, T , p , δ_0 , C_0 , a_0 , and b_0 . The value of $\|K_i\|^2$ used in this work was taken to be 0.177, a value appropriate for 9.35 GHz at 250 K from the compilation of Warren (1984). A newer compilation (Warren and Brandt, 2008) gives updated refractive indices for ice at 266 K. Comparing values from the two compilations shows essentially no change in the real part of the refractive index at 266 K (1.7860 versus 1.7861). The imaginary part decreases by a factor of about 4 in the new compilation (1.0306×10^{-3} versus 2.2089×10^{-4}), but this causes no significant change in $\|K_i\|^2$ (0.17803 versus 0.17807). The temperature sensitivity is somewhat more significant. Warren (1984) reports microwave optical properties at temperatures of -1° , -5° , -20° , and -60°C , and suggests interpolating the real part of the refractive index linearly with temperature, and the logarithm of the imaginary part linearly with temperature. Following this approach gives $\|K_i\|^2$ of 0.1782 at 272 K and 0.1760 at 230 K. Taking the difference in values as the uncertainty in $\|K_i\|^2$, it can be seen that this is a negligible source of uncertainty in the forward model compared to the observational and other forward model uncertainties in radar reflectivity.

The remaining parameters affect the calculation of fallspeeds. Temperature and pressure are used to calculate air viscosity, δ_0 and C_0 describe hydrodynamic properties of particles, and a_0 and b_0 are empirical constants used to improve the agreement between the MH2005 model and observed fallspeeds for aggregate particles (Mitchell and Heymsfield, 2005). The uncertainties in fallspeeds due to uncertainties in a_0 and b_0 were assumed to be subsumed in the uncertainty estimates for the fallspeed forward models, so uncertainties in a_0 and b_0 were ignored. Uncertainties in δ_0 and C_0 were obtained by comparing the values found by Heymsfield and Westbrook (2010) against the values used by Mitchell and Heymsfield (2005). The respective values of δ_0 were 8.0 and 5.83, and those for C_0 were 0.35 and 0.6. The differences (2.17 and 0.25) were used as the estimated uncertainties and were assumed to be uncorrelated. Reasonable uncertainties for temperature and pressure are likely to have minimal effects on air viscosity, and nominal uncertainties were taken to be 0.5°C and 1 kPa.

Chapter 5

Snow microphysics retrieval: Performance and results

Prior to considering the retrieval results, it is prudent to assess the performance of the retrieval. In assessing the performance, one seeks to quantify answers to questions such as:

- How well does the retrieved state agree with the true state?
- How independent and significant are the measurements?
- By how much do the measurements improve the knowledge of the state?

Questions such as these are best answered using synthetic test cases which represent realistic snowfall regimes. Given a selection of representative synthetic regimes, several metrics may be applied which provide quantitative information about the performance of the retrieval under various snowfall conditions. The results of these tests with synthetic cases are presented, followed by the results of the application of the retrieval to the snowfall events described in Chapter 2.

5.1 Synthetic test cases

The synthetic test cases used in this work were constructed using five snowfall regimes selected to encompass the extent of conditions observed during C3VP. The regimes were

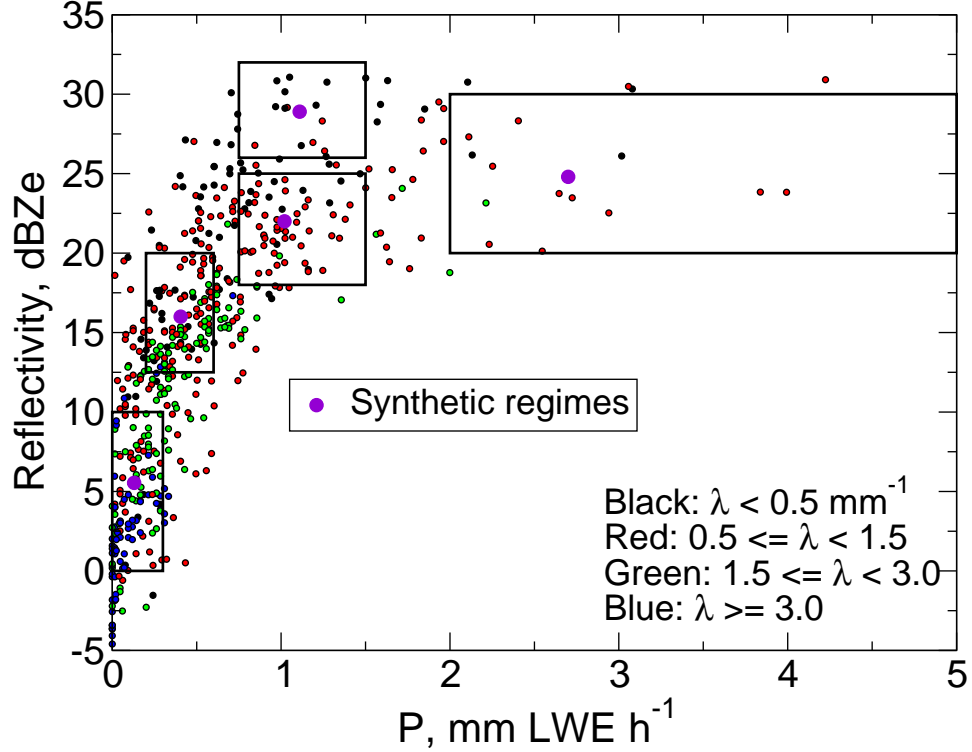


Figure 5.1: VertiX reflectivities versus FD12P snowfall rates from the 5-minute averages C3VP observations. VertiX reflectivities have been corrected to ground level, and snowfall rates have been scaled to match DFIR accumulations. Dot colors indicate the slope of an exponential distribution fitted to the observed size distribution. Boxes indicate boundaries used to define snowfall regimes, and large dots show averaged reflectivities and snowfall rates for each regime.

defined using subsets of the 5-minute average C3VP observations, selected as shown in Figure 5.1 using ranges of radar reflectivity and snowfall rate. The regimes represent conditions ranging from light snow with low reflectivity to heavy snow with corresponding high reflectivity, as well as several intermediate conditions.

The regimes were characterized by values for radar reflectivity, snowfall rate, size distribution parameters, and temperature (Table 5.1). Size distributions were modeled as exponential. For a particular regime, the characteristic values for radar reflectivity, snowfall rate, and temperature were determined as simple means of the observations within the associated subset. For the size distribution parameters, an exponential size distribution was fit to each SVI size distribution in the subset, giving a range of values for the intercept $N_0(D_{obs})$ and slope $\lambda(D_{obs})$. The characteristic values for the size distribution parameters were then determined as the simple means of these fitted values. Higher reflectivities and

Table 5.1: Characteristics of synthetic regimes.

Regime	Description	Ze	P	$\log(N_0(D_{obs}))$	$\lambda(D_{obs})$	T
		dBZe	mm LWE h ⁻¹	m ⁻³ mm ⁻¹	mm ⁻¹	K
A	Very light snow	5.54	0.13	4.17	2.81	263.
B	Light snow	16.0	0.405	3.66	1.31	261.
C	Moderate snow, low dBZe	22.0	1.02	3.42	0.835	263.
D	Moderate snow, high dBZe	28.9	1.11	2.81	0.517	271.
E	Heavy snow	24.8	2.70	4.43	1.017	265.

higher snowfall rates were associated with broader distributions (smaller values of λ) (Table 5.1).

For each regime, synthetic cases were constructed by applying a predefined set of assumed values for the exponents of the mass- and area-dimension relationships, β and σ , and for ϕ (Table 5.2). These values were selected to span the expected ranges for these variables, using the a priori values plus or minus approximately one standard deviation. Given the values for the exponential size distribution parameters $N_0(D_{obs})$ and $\lambda(D_{obs})$ associated with a particular regime, an assumed value for ϕ was used to construct an equivalent exponential distribution based on the maximum dimension, D_M . Using this $N(D_M)$ and the regime’s radar reflectivity along with the assumed value for β , the corresponding value for α was found via (3.27). Because particle masses are capped to be no larger than the masses of equal-diameter ice spheres, a non-linear least squares fitting routine was used to determine α . Finally, taking the assumed value for σ , the corresponding value for γ was found via (3.28), again using a nonlinear least squares technique due to the dependence of snowfall rate on fallspeed and due to the cap on particle area. Particle fallspeeds were modeled using MH2005. Each synthetic case was named by the regime, followed by a sequence of labels indicating the values of β , σ , and ϕ , in that order (e.g., following Table 5.2, “BP0m” indicates regime B, using the values $\beta = 2.6$, $\sigma = 1.785$, and $\phi = 0.725$). Combination of the five regimes with the assumed values of β , σ , and ϕ provided a total of 225 possible synthetic cases; however, 31 combinations did not result in usable cases. For these failed

Table 5.2: Values of state variables used to generate synthetic states and the textual labels used to identify them. Labels of “0” indicate values which are equal to the a priori values used in the snow microphysics retrieval. Labels of “M” and “m” indicate negative deviations from the a priori values, while labels of “p” and “P” indicate positive deviations.

Variable	Values and labels
β	“M”:1.6, “m”:1.9, “0”:2.067, “p”:2.3, “P”:2.6
σ	“m”:1.6, “0”:1.785, “p”:2.0
ϕ	“m”:0.725, “0”:0.825, “p”:0.925

cases, the causes of failure were either that α could not be made large enough to match the desired radar reflectivity due to the cap on particle mass (6 cases), that γ could not be made large enough to match the desired snowfall rate due to the cap on particle area (21 cases), or that γ could not be made small enough to match the desired snowfall rate (4 cases).

5.1.1 Results of synthetic tests

The information content metrics for the synthetic cases show that only about 2 independent and significant quantities are measured by the observations, and, with $H \approx 3$ for most of the synthetic cases, about 8 distinct states might be discernible within the a priori state space (Figure 5.2 and Table 5.3). H varies principally with the regime, with regimes consisting of lighter snow and lower reflectivity having somewhat smaller values of H than do those consisting of heavier snow and higher reflectivity. This behavior may be because the heavier snow regimes have broader distributions which might help constrain the exponents of the mass- and area-dimension relations. The averaged values of H for each regime show a marked dependence on the size distribution slope (Figure 5.3). In contrast, d_s varies only weakly over the set of synthetic cases.

The errors between the a priori state and the true states for these synthetic cases form the baseline against which the retrieval performance can be evaluated. These errors are the equivalent of assuming that the observations provide no information about the state, so that the retrieval simply returns the a priori state. The fractional error of an estimated

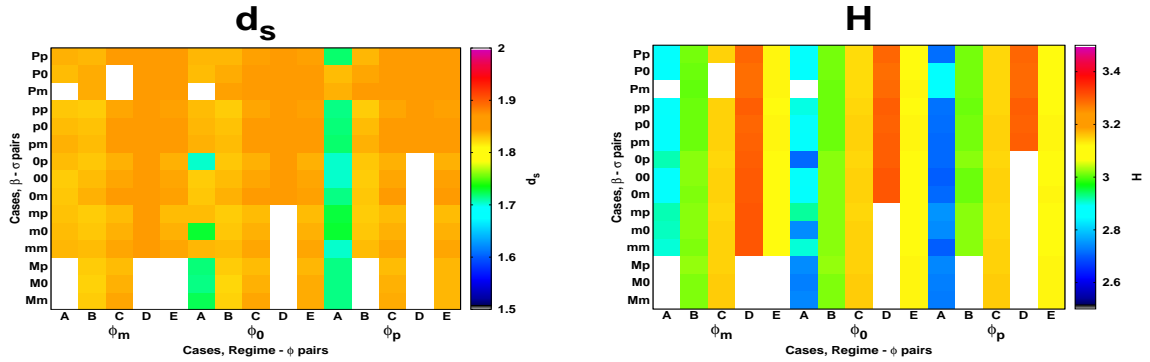


Figure 5.2: Information content metrics for the synthetic cases. For each panel, the abscissa gives the regime and ϕ value for the synthetic case, while the ordinate gives the values of β and σ , using the labels provided in Table 5.2. White regions of these panels show synthetic case configurations which did not result in usable cases.

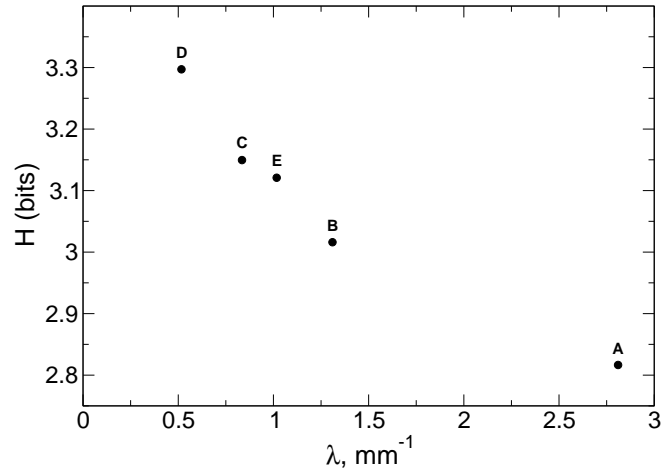


Figure 5.3: Regime-averaged Shannon information content H versus slope λ of the regime size distribution for the synthetic cases. Each point is labeled with the name of the synthetic regime per Table 5.1.

state variable \hat{x} is given by

$$\Delta(\hat{x}) = (\hat{x} - x) \frac{100\%}{|x|}, \quad (5.1)$$

where x is the true value. To compute these errors for the a priori state, the values of \hat{x} in (5.1) are taken to be the a priori values shown in Table 3.1. These errors are shown in Figure 5.4.

The regular patterns exhibited by the fractional errors for β , σ , and ϕ are an artifact of the method used to construct the synthetic cases: the true values for these variables were fixed as shown in Table 5.2. For $\ln(\alpha)$ and $\ln(\gamma)$, the true values vary depending on the properties of the regime and the values of the other state variables, causing the errors versus the a priori values to vary as well. For $\ln(\alpha)$, shown in the top left panel of Figure 5.4, errors vary primarily with β . Errors are predominantly negative when β is larger than its a priori value, and positive when β is smaller than its a priori value. This pattern results from the correlation between $\ln(\alpha)$ and β induced by the radar reflectivity forward model, (3.27).

The largest a priori fractional errors are associated with $\ln(\gamma)$. These large errors occur with synthetic cases for which the true value of γ is moderately large (0.5 - 0.7) compared to the a priori value of 0.211, leading to fractional errors of -250% to -500% in $\ln(\gamma)$. Many of these cases are for regime D, which combines high reflectivity with moderate snowfall rate. Presumably, γ has been made large for these cases in order to increase the particle area, reducing fallspeeds to match the moderate snowfall rate. These cases may not be represented well by the assumptions used in the forward models. In particular, an examination of the subset of observations used to define regime D shows that temperatures for 10 of the 14 members of the subset were in the range of 272 K to 273 K, while the other 4 were in the range 264 K to 269 K. Those 10 members were observed between 1230 and 1500 UTC on 6 December, 2006. Observers on the ground reported wet, sticky snowflakes during this period (Austin et al., 2007), while the forward model for radar backscattering is appropriate only for dry snow.

Generally, the retrieval improves upon the a priori errors. As an example, this improvement is made especially clear by comparing the panels for β errors in Figures 5.4 and 5.5.

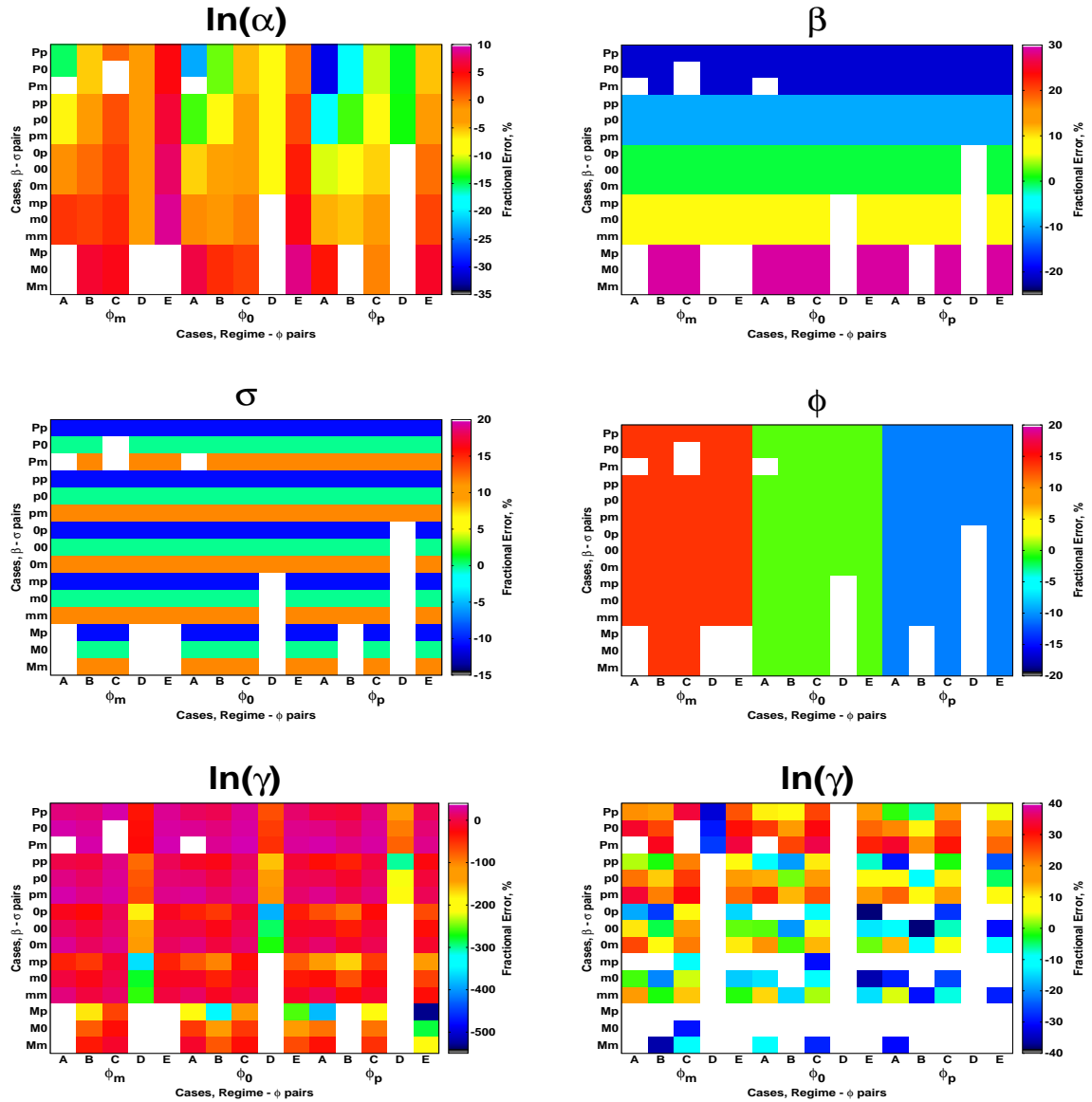


Figure 5.4: A priori errors for synthetic cases. Fractional errors between the a priori state and the true state for each state variable. Two panels are provided for $\ln(\gamma)$, one with full scale (bottom left) and one with reduced scale (bottom right). The axes of each panel are as described for Figure 5.2. In all but the bottom right panel, white regions show synthetic case configurations which did not results in usable cases.

Table 5.3: Statistics of fractional errors in per cent and information content metrics from the synthetic cases. The mean is given, followed by the standard deviation in parentheses.

Variable or metric	a priori	Retrieval, 1-sd a priori	Retrieval, 2-sd a priori
$\ln(\alpha)$	-3.19 (7.69)	-0.74 (4.28)	-0.77 (3.93)
β	-0.85 (15.68)	0.85 (10.79)	1.01 (8.55)
$\ln(\gamma)$	-44.35 (92.41)	-32.66 (68.92)	-20.29 (45.22)
σ	0.10 (9.09)	0.57 (8.88)	1.25 (9.46)
ϕ	0.97 (9.94)	-0.23 (9.59)	-1.17 (9.73)
H	-	3.07 (0.16)	5.26 (0.184)
d_s	-	1.83 (0.04)	2.53 (0.03)

The lower regions of the β panel in Figure 5.4 show strong positive errors (maroon and gold colors). These same regions in Figure 5.5 show smaller positive errors (red, orange and yellow colors). Similar comparisons can be made for the upper regions of the β panel, where the a priori errors are strongly negative. For $\ln(\alpha)$, it can also be seen by comparing the panels that the retrieval reduces the range of errors in comparison to the a priori. For the a priori, errors for $\ln(\alpha)$ range from -30.5% to 9.0%, while after the retrieval, the errors range from -16.0% to 8.0%. For the remaining state variables, the performance of the retrieval is less clear. For $\ln(\gamma)$, a minor narrowing of the distribution of the errors occurs (not shown).

Retrieval performance is summarized in Table 5.3, which shows the mean and standard deviation of the fractional errors (i.e., bias and scatter) for both the a priori and the retrieval. Bias and scatter for both $\ln(\alpha)$ and $\ln(\gamma)$ are reduced by the retrieval, although the improvements in $\ln(\gamma)$ are less substantial than those for $\ln(\alpha)$. The magnitude of the bias in β , which is smaller than 1%, is essentially unchanged by the retrieval but the scatter is reduced to less than 70% of its original value. For σ and ϕ , the retrieval has little impact, essentially leaving the already small biases and the scatter unchanged.

These results suggest that $\ln(\alpha)$, β , and $\ln(\gamma)$ are modestly constrained by the retrieval, while the measurements provide little information regarding σ and ϕ . To evaluate this, the diagonal elements of \mathbf{A} as described in (3.5) may be examined. Values for $\ln(\alpha)$ are near 1.0

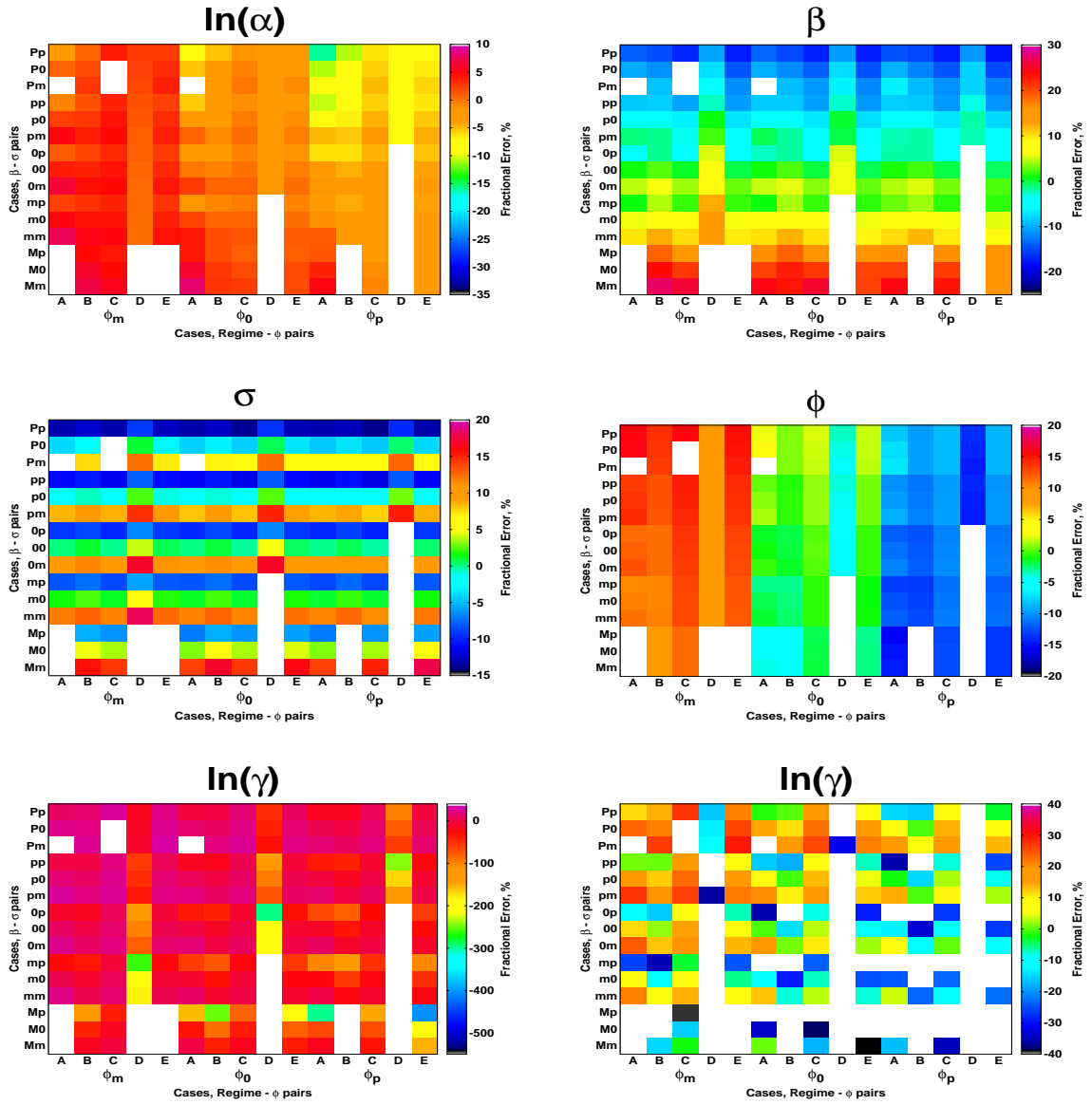


Figure 5.5: Retrieval errors for synthetic cases. Fractional errors between the retrieved state and the true state for each state variable. The panels use the same data ranges and are constructed as in Figure 5.4.

(Figure 5.6) indicating that its retrieved state is determined largely by the observations. In contrast, values for σ are less than 0.1, indicating its retrieved state is determined largely by the a priori. The values of the \mathbf{A} diagonal elements for the remaining state variables fall between 0.1 and 0.5, indicating the retrieved state for these variables is determined jointly by the observations and the a priori estimate of the state.

5.2 Application to C3VP snowfall events

The C3VP microphysics retrieval was applied to the four snowfall events described in Chapter 2. These events consist of a mix of lake-effect and synoptically-driven frontal precipitation. The primary purpose of the results from these retrievals is to form reasonable estimates of microphysical properties and their uncertainties for the CloudSat retrieval. Consequently, the analysis presented here focuses largely on that aspect of the results, but also examines information content properties that provide some insight into the design of the C3VP experiment. Retrievals were performed in two different configurations, representing two different fallspeed models (MH2005 and HW2010), as introduced in Section 3.2. The results presented here are for the MH2005 configuration, with comments regarding differences for the other configurations as necessary.

5.2.1 Retrieved properties

Retrieval results were obtained for 375 distinct samples from the four events, broken down as 33 from event A, 173 from B, 43 from C and 126 from D. Figure 5.7 shows scatterplots of the retrieved parameters for mass (upper panel) and area (lower panel). The a priori state, from Table 3.1, is represented by the orange crossbars, while the blue crossbars show the expected values and standard deviations for the posterior, retrieved state. The method for determining this representation of the retrieved state will be discussed below. Points are colorcoded to show the differences between events. The strongest contrasts are between events B and D. Event B was a light snow case with intermittent lake-effect snow squalls and fairly broad size distributions (Figure 2.2), while event D was associated with a deeper system with much narrower distributions (Figure 2.4). The results suggest the retrieval

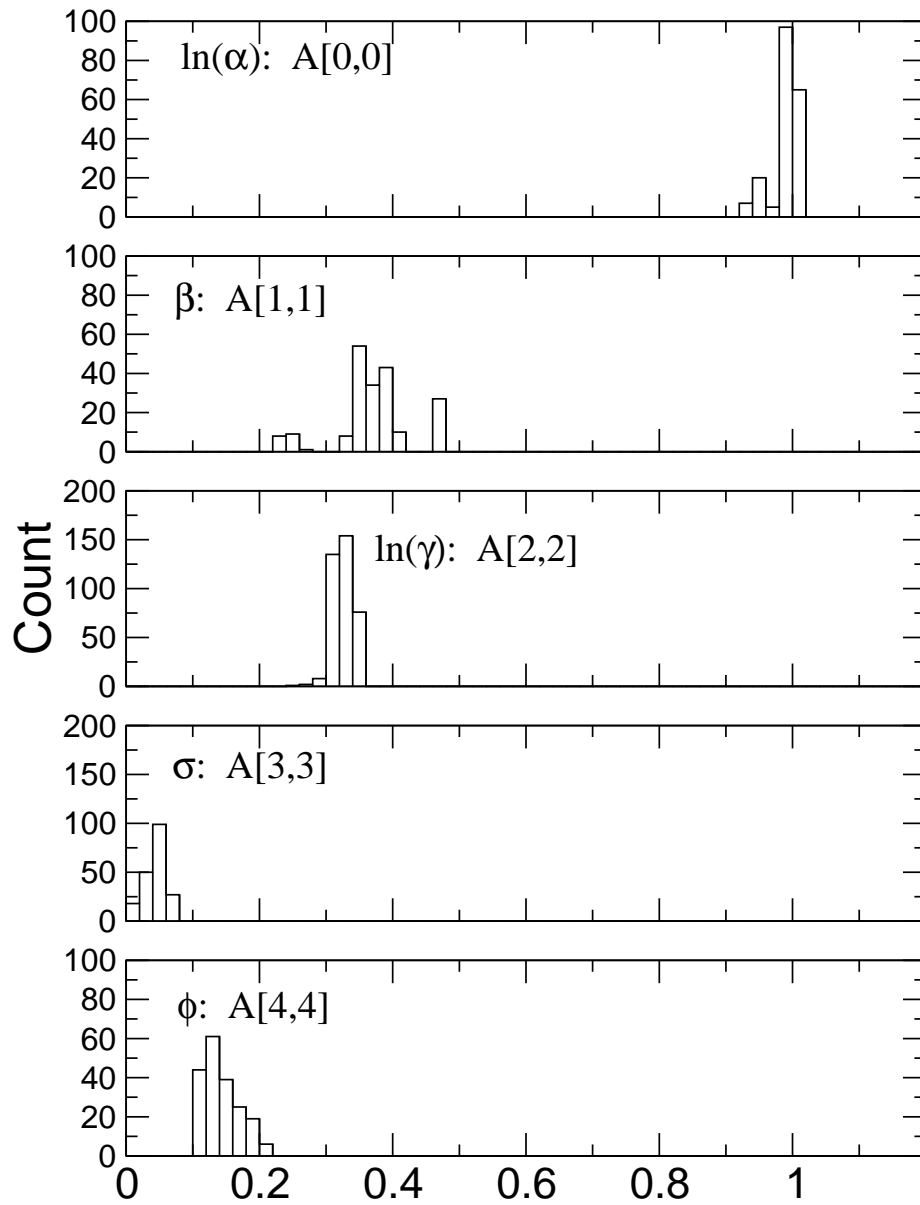


Figure 5.6: Diagonals of \mathbf{A} for synthetic cases.

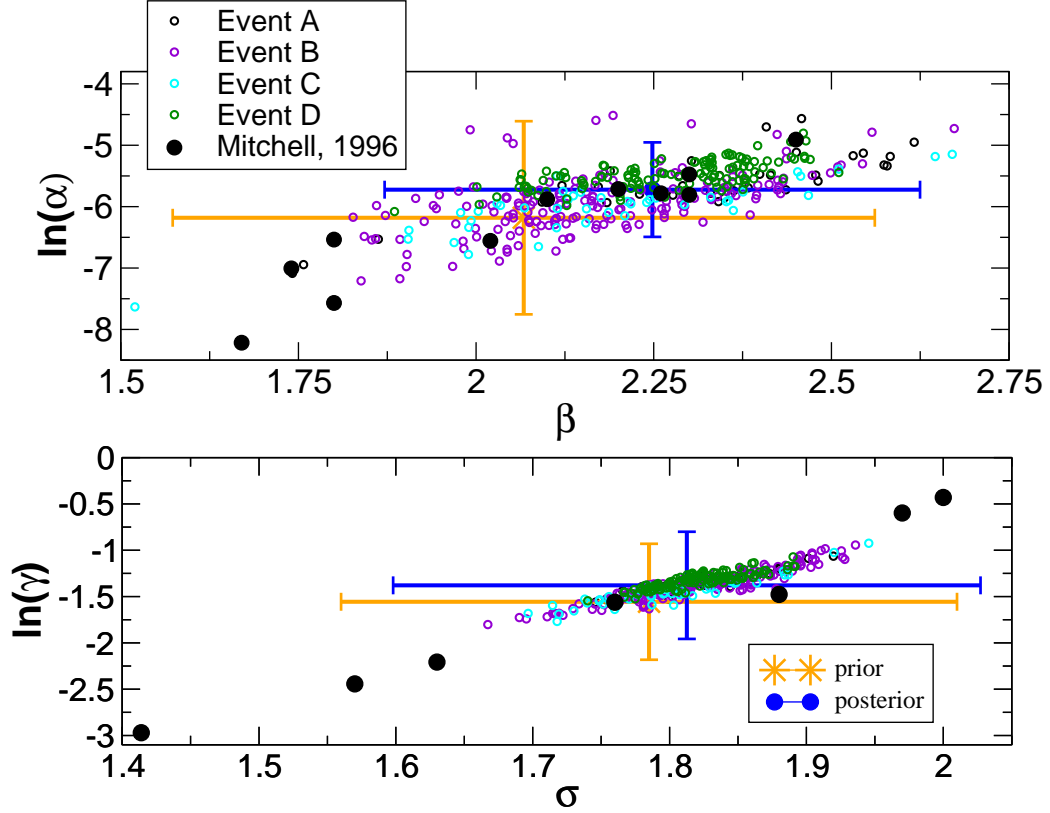


Figure 5.7: Microphysical mass and area parameters retrieved from C3VP. Points are color-coded by event. The orange points and error bars show the a priori expected values and standard deviations, while the blue points and error bars show them for the retrieved state. The heavy black points show results for larger and irregularly-shaped particles from Mitchell (1996).

method has some ability to distinguish the characteristics of particles produced by different microphysical processes, but that ability was not examined further in this work.

For the mass parameters, the standard deviations are reduced considerably compared to the a priori state, especially for the coefficient α , suggesting they are well-constrained by the observations. Retrieved values of β range mainly from 1.75 to 2.75, and α from about 0.001 to 0.01, with the expected values of the retrieved points at $\beta=2.248$, $\alpha=0.00311$. The heavy black points show values from Mitchell (1996) for a range of larger particles from that study (Table 5.4). The expected values of α and β from this study are similar to estimates from Mitchell for densely rimed dendrites (R2b), aggregates (S3 and S1(a)), rosettes (C2a), and side planes (S1). These expected values are considerably different than the often-used values described by Brown and Francis (1995) ($\beta= 1.9$, $\alpha=0.00294$ in cgs units), which were

Table 5.4: Mass and area parameters from Mitchell (1996) used in Figure 5.7.

Habit	Dmin	Dmax	β	$\ln(\alpha)$	σ	$\ln(\gamma)$
	μm	μm	(cgs)			
P1d	90	1500	1.67	-8.22	1.63	-2.21
N1e	300	–	1.74	-7.01	1.414	-2.97
P1c	100	1000	1.8	-7.57	1.76	-1.56
R1b	200	2400	1.8	-6.54	1.414	-2.97
P1b	40	2000	2.02	-6.56	1.97	-0.60
S3	800	4500	2.1	-5.88	1.88	-1.48
S1(a)	600	4100	2.2	-5.71	1.88	-1.48
C2a	200	1000	2.26	-5.78	1.57	-2.44
R2b	1800	4000	2.3	-5.81	1.76	-1.56
S1	300	2500	2.3	-5.48	1.88	-1.48
P1a	100	3000	2.45	-4.91	2.00	-0.43

taken from the results of Locatelli and Hobbs (1974). Locatelli and Hobbs reported these values for unrimed aggregates of bullets, columns and side planes, and also for aggregates of densely-rimmed dendrites or radiating assemblages of dendrites. Recent work by Heymsfield et al. (2010) using aircraft observations from six field campaigns has suggested that values of β near 2.1 are more appropriate for cloud and precipitating ice. They found corresponding values of α (cgs units) of 0.00359 for warm-topped non-convective clouds, 0.00574 for cold-topped non-convective clouds, and 0.00630 for convectively-generated clouds. The warm-topped cloud cases included observations from C3VP. The mass-dimension relations from Mitchell (1996) and Heymsfield et al. (2010) are all based on measurements of maximum particle dimension, while Locatelli and Hobbs (1974) used the diameter of an equal-area circle.

A number of studies have suggested values of α that are substantially larger than the value of 0.00311 from this study. Brandes et al. (2007) found $\alpha = 0.00890$ and $\beta = 2.1$ for snow along Colorado’s Front Range; however, their particle size was an equivalent volume diameter obtained from 2DVD observations and likely substantially smaller than the maxi-

mum dimension D_M used in this work. Further, their mass-dimension relation was given as a function of the size distribution median volume diameter, more a measure of distribution width, rather than actual particle size. Muramoto et al. (1995) presented a density relation which, based on their definition of particle volume, can be converted to a mass-dimension relation with $\alpha = 0.00987$ and $\beta = 2.594$. For particle size, they used the width of the particle as observed by a side-viewing camera with no correction for viewing geometry (i.e., ϕ used in this work). As was shown in Section 3.3, this approach underestimates D_M . Similar to Brandes et al. (2007), they presented their density relation as a function of the mean particle size of the observations, rather than as a function of actual particle size. Magono and Nakamura (1965) gave a density relation for observations of wet and dry snow. Using only their dry snow observations and converting their densities to masses using their definition of particle volume, a best-fit mass-dimension relation gives $\alpha = 0.00907$ and $\beta = 1.82$. Constraining β to 2.25 gives $\alpha = 0.00722$. They collected the snow particles on a flat surface, measured the longest horizontal dimension and the dimension normal to that, then used the geometric mean of those dimensions as the particle size. Again, this underestimates D_M .

Differences in how particle size is measured can have a substantial impact on estimates of α . Using ϕ as was defined in (3.25) and letting α_M be the value of α determined when particle size is given by D_M , the value α' associated with some other measure of particle size D_{obs} can be evaluated using

$$\begin{aligned}
 \alpha' D_{obs}^\beta &= \alpha_M D_M^\beta & (5.2) \\
 &= \alpha_M \left(\frac{D_{obs}}{\phi} \right)^\beta \\
 &= \left(\frac{\alpha_M}{\phi^\beta} \right) D_{obs}^\beta
 \end{aligned}$$

Estimating ϕ as 0.8 and using the expected value of β of 2.248, α' will be a factor of 1.7 larger than α_M . A significant part of the differences in mass-dimension coefficients may be explained by these differences in the treatment of particle size. Differences may also be due to differences in independent variables (median volume diameter or mean particle

size instead of actual particle size). The results of Heymsfield et al. (2010) indicate that differences in microphysical processes lead to differences in mass-dimension parameters, and the representativeness of these C3VP results should be explored further; however, when making comparisons against other studies it is also essential to ensure that the parameters are determined using similar definitions of particle size.

For the area-dimension parameters, the differences between the retrieved and a priori state are less substantial (Figure 5.7, lower panel). The standard deviations and the expected values for $\ln(\gamma)$ and σ are similar to those for the a priori state. As was done for the mass plot, several points from Mitchell (1996) which are representative of larger, irregular particles are shown for comparison. The two points nearest the expected values for the retrieved state correspond to densely rimed dendrites (R2b), aggregates (S3 and S1(a)), rosettes (C2a), and side planes (S1) (Table 5.4), the same habits that best matched the results for the mass parameters. Unlike the situation with the mass-dimension parameters, previous estimates of area-dimension parameters were based solely on particle maximum dimension, D_M . All known evaluations of area-dimension parameters were incorporated as the a priori state for the retrieval, and the retrieved values are consistent with those evaluations.

For ϕ , the parameter which relates the disdrometer-observed particle dimension to the true maximum dimension, the standard deviation is not substantially reduced but the expected value is reduced. Smaller values of ϕ are associated with narrower distributions (Figure 5.8), and there is some contrast between events B and D, but the significance of these differences has not been evaluated. The CloudSat snowfall retrieval will be cast in terms of particle maximum dimension D_M , so ϕ will not be necessary in its formulation; however, ϕ does provide some insight into the biases that are inherent in disdrometer and imager observations of snow particles. An understanding of these biases, and how they impact estimates of snow microphysical properties, is essential for the application of these sorts of ground validation observations.

Histograms of the A-matrix values (not shown) associated with each of the retrieved parameters confirm the impressions given by Figures 5.7 and 5.8. The values associated with $\ln(\alpha)$ range between 0.9 and 1.1, indicating it is strongly constrained by the measurements.

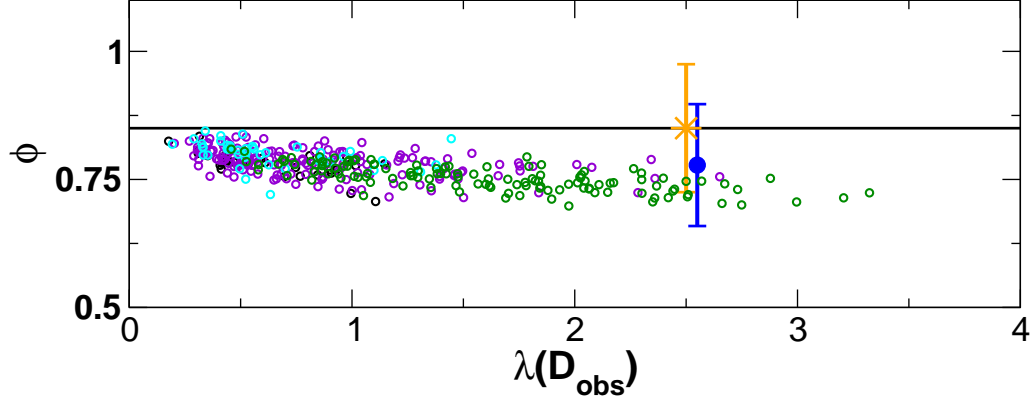


Figure 5.8: Microphysical shape parameter ϕ retrieved from C3VP. Colors for points and error bars are as in Figure 5.7. The black horizontal line shows the a priori expected value. The location of the prior and posterior error bars along the horizontal axis is not significant.

Values larger than 1 are unexpected, but have been reported previously (Connor et al., 2008) and may be related to nonzero a priori covariances. Values associated with β and $\ln(\gamma)$ are about 0.3, indicating a mix of information from the observations and the a priori constraints. Values associated with σ and ϕ average near 0.1, and suggest these parameters are influenced primarily by the a priori.

For each of the 375 samples, the microphysical retrieval produced an estimate of the expected values of $\ln(\alpha)$, β , $\ln(\gamma)$, σ and ϕ and their covariance matrix, describing a five-dimensional normal PDF that represents the retrieved state. For use in the CloudSat snowfall retrieval, these PDFs must be combined into a single representative PDF from which expected values and a covariance matrix can be obtained. This single PDF can be constructed by Monte Carlo sampling all of the 375 individual PDFs to produce a synthetic pooled sample that is representative of all the retrieval results. Samples containing 20,000 points, each point consisting of a vector $[\ln(\alpha), \beta, \ln(\gamma), \sigma, \phi]$, were drawn for each of the 375 retrieved PDFs, and these samples were accumulated into the pooled sample. Because the number of retrievals per event varied considerably, weighting was applied to the points in the pooled sample to equalize the importance of the events. Expected values and the covariance matrix were then calculated for the pooled sample. Ten realizations were performed and the final set of 10 expected value vectors and 10 covariance matrices were averaged. As noted above, ϕ is not required for the CloudSat snowfall retrieval, so it was omitted from

this analysis. From this pooled sample, expected values and the covariance matrix were evaluated. For the MH2005 version of the retrieval, the resulting expected values were

$$\begin{bmatrix} \ln(\alpha) \\ \beta \\ \ln(\gamma) \\ \sigma \end{bmatrix} = \begin{bmatrix} -5.723 \\ 2.248 \\ -1.379 \\ 1.813 \end{bmatrix} \quad (5.3)$$

and the covariance matrix was

$$\mathbf{S} = \begin{bmatrix} s^2(\ln(\alpha)) & s(\ln(\alpha), \beta) & s(\ln(\alpha), \ln(\gamma)) & s(\ln(\alpha), \sigma) \\ s(\beta, \ln(\alpha)) & s^2(\beta) & s(\beta, \ln(\gamma)) & s(\beta, \sigma) \\ s(\ln(\gamma), \ln(\alpha)) & s(\ln(\gamma), \beta) & s^2(\ln(\gamma)) & s(\ln(\gamma), \sigma) \\ s(\sigma, \ln(\alpha)) & s(\sigma, \beta) & s(\sigma, \ln(\gamma)) & s^2(\sigma) \end{bmatrix} \quad (5.4)$$

$$= \begin{bmatrix} 0.592 & 0.212 & 0.090 & 0.023 \\ 0.212 & 0.142 & 0.011 & 0.007 \\ 0.090 & 0.011 & 0.335 & 0.103 \\ 0.023 & 0.007 & 0.103 & 0.046 \end{bmatrix}.$$

Table 5.5 compares the prior expected values, variances and covariances against their posterior values. As was anticipated from Figure 5.7, the variances and covariances associated with the mass parameters have decreased, while those associated with the area parameters have changed little. For the mass parameters, this raises the question as to whether the posterior distribution obtained from the C3VP is an improved representation of the true distribution, or whether it represents a subset of the true distribution. Eventually, this ques-

tion can be answered in part by applying similar analyses to observations from additional experiments. For the present work, this posterior distribution is taken to be representative of the true distribution of these microphysical parameters.

One of the key questions to be answered by this analysis is whether covariances exist which were not present in the a priori. From (5.4), it can be seen that covariances that mix mass and area parameters (e.g., $s(\ln(\alpha), \ln(\gamma))$) are nonzero, while they were zero in the a priori. The corresponding correlation matrix is

$$\boldsymbol{\rho}_{corr} = \begin{bmatrix} 1.000 & 0.731 & 0.202 & 0.139 \\ 0.731 & 1.000 & 0.049 & 0.090 \\ 0.202 & 0.049 & 1.000 & 0.831 \\ 0.139 & 0.090 & 0.831 & 1.000 \end{bmatrix} \quad (5.5)$$

showing nontrivial correlations between $\ln(\alpha)$ and $\ln(\gamma)$ (0.202), between β and σ (0.090), and between $\ln(\alpha)$ and σ (0.139). The first two, in particular, likely arise because of the dependence of fallspeed on $\frac{\alpha}{\gamma}$ and on $\beta - \sigma$. These off-diagonal elements will help constrain the CloudSat retrieval forward model uncertainties caused by uncertainties in the microphysical parameters.

Table 5.5 also shows the results from the retrieval when configured with the HW2010 model for fallspeeds. The posterior state for the HW2010 configuration is essentially unchanged from that for the MH2005 configuration. For the CloudSat snowfall retrieval, the results from the MH2005 configuration were used.

5.3 Uncertainties and observing system design

The information content metrics provided by the microphysics retrieval provide a concise way to quantify the influence of changes in the observing system on the retrieval performance. For the observations themselves, significant uncertainties arose because of ground clutter in the VertiX radar profiles, the lack of replicate observations of snowfall rate, and

Table 5.5: Comparison of prior and posterior PDFs for the microphysics retrieval. “Exp” is expected value, “Var” is variance, and “Cov” is covariance.

	Prior			Posterior, MH2005			Posterior, HW2010		
	Exp	Var	Cov	Exp	Var	Cov	Exp	Var	Cov
$\ln(\alpha)$	-6.181	2.474	0.585	-5.723	0.592	0.212	-5.676	0.591	0.204
β	2.067	0.244		2.248	0.142		2.212	0.137	
$\ln(\gamma)$	-1.556	0.392	0.118	-1.379	0.335	0.103	-1.498	0.377	0.114
σ	1.785	0.0507		1.813	0.046		1.794	0.049	

the relatively small sample volume of the SVI. Additionally, uncertainties in the fallspeed forward model were substantial, estimated at 30% of the observed fallspeeds. Using the synthetic test cases, an experiment was performed in which a series of improvements was applied to these uncertainties and the information content metrics reevaluated.

First, it was assumed that reflectivity observations could be made with reduced ground clutter contamination, allowing the observed reflectivity to be nearer the surface observations of snowfall rate, size distribution and fallspeeds. This allowed the uncertainties defined in Table 4.1 to be omitted. Next, the uncertainties for the observed FD12P snowfall rates were reduced to half their values, simulating the improvements that would result from having four replicate snowfall rate observations. Third, more accurate size distributions were assumed, equivalent to increasing the SVI sample volume by a factor of six. This could be achieved by deploying additional instruments, by enlarging the field of view or depth of field of the SVI camera, by increasing the sample times, or by a combination of these changes. Finally, a more accurate fallspeed model was assumed, with uncertainties reduced from 30% to 10% of observed fallspeeds.

Results of these tests are shown in Table 5.6. Initial values of H and d_s are shown, along with the new values resulting from incrementally applying the improvements. The improvements to the observations themselves led to negligible improvements in d_s and modest improvements in H . This result is consistent with the interpretation of degrees of freedom for signal and information content. Reducing uncertainties in existing measurements does not introduce new independent information, but does allow the retrieval to better resolve the

Table 5.6: Changes in information content metrics due to improvements in observational and forward model uncertainties.

	Initial	Ze	P	N(D)	Fallspeed
H	3.07	3.86	3.87	3.90	4.80
d_s	1.83	1.89	1.90	1.90	2.32

retrieved state. Improvements to the fallspeed forward model, however, produced substantial improvements in H and more significant improvements in d_s . Not only is the retrieved state better resolved, but the retrieval is utilizing more of the information available in the observations. This simple experiment illustrates that proposed improvements to observing systems need to be considered in concert with the capabilities of the retrieval system.

Chapter 6

Particle models

In order to calculate radar reflectivities and snowfall rates for the snowfall retrieval scheme, size-resolved microphysical and radar scattering properties must be modeled for snow particles. As described in Section 3.2, particle mass and horizontally-projected area largely control a particle's fallspeed for given environmental conditions. Together, particle mass and fallspeed determine a particle's contribution to snowfall rate. Horizontally-projected area is determined by particle shape and orientation. Scattering by ice particles at 94 GHz depends on particle mass and, for larger precipitation-sized particles, also on particle shape and orientation. Even for small particles, nonsphericity may cause scattering properties to depart from the traditional Rayleigh model for spheres, as was shown in the evaluation of X-band forward model uncertainties for the snow microphysics retrieval (Section 4.2).

The required particle models must describe these properties in a physically consistent way, and the results from the snow microphysics retrieval provide a physically consistent description of some of these properties. The expected values for the microphysical parameters $\ln(\alpha)$, β , $\ln(\gamma)$ and σ given by (5.3) determine expected values for particle mass and horizontally-projected area as a function of snow particle size, from which size-resolved fallspeeds can be determined (Figure 6.1). The expected values for mass and horizontally-projected area also provide some constraints on particle scattering properties. The uncertainties for these microphysical parameters, described by the covariance matrix given in (5.4), contribute to uncertainties in the particle properties and in the quantities such as snowfall rate and radar reflectivity calculated from them. The methods for propagating

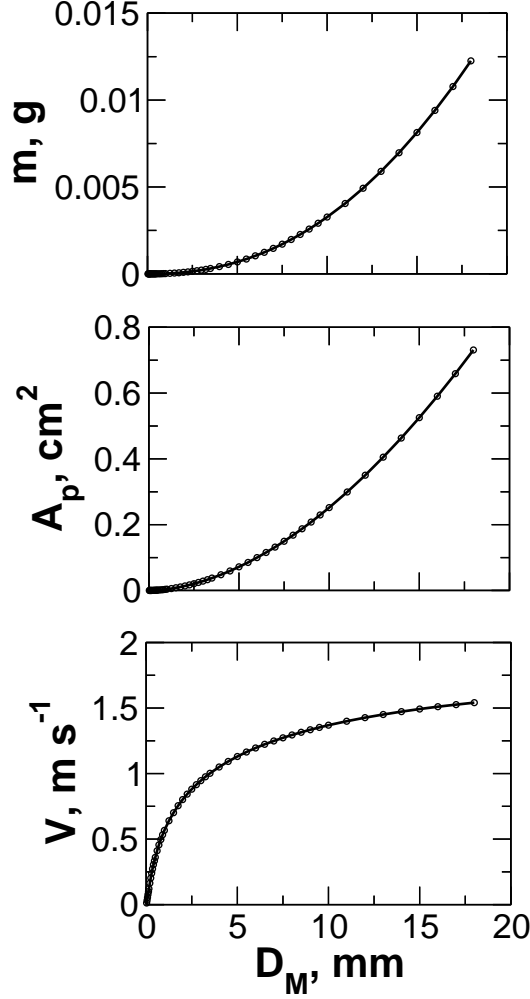


Figure 6.1: Masses, horizontally-projected areas, and fallspeeds versus snow particle size D_M based on the expected values for $\ln(\alpha)$, β , $\ln(\gamma)$ and σ from the microphysics retrieval. Fallspeeds are per MH2005.

the uncertainties of the microphysical parameters into the calculations for snowfall rate and radar reflectivity will be presented in Chapter 7. In this chapter, the expected values for these parameters are used to construct the required particle models and to assess other sources of uncertainty related to the particle models.

While the properties required to calculate snowfall rate (Figure 6.1) are easily determined from the microphysical parameters, the application of these properties to determine radar scattering properties is less straightforward. Over the range of particles sizes needed for the CloudSat retrieval, the scattering behavior of particles varies widely and the use of mass as the only constraint is not sufficient. Studies of radar backscatter at 94 GHz for a variety

of particle shapes suggest that the Rayleigh approximation begins to fail at r_{ev} values of 100 to 300 μm (Schneider and Stephens, 1995; Liu and Illingworth, 1997) where r_{ev} is the equivalent volume radius (i.e., the radius of a solid-ice sphere with volume equal to the actual ice volume of the non-spherical particle):

$$r_{ev} = \left[\frac{m(D_M)}{\rho_{ice}} \frac{3}{4\pi} \right]^{1/3}, \quad (6.1)$$

with ρ_{ice} the solid ice density of 0.917 g cm^{-3} . Deviations of particle shape from spherical also preclude the use of Mie theory (van de Hulst, 1981). Based on comparisons of 94 GHz backscatter properties of spheres with the properties of randomly oriented cubes and hexagonal columns, Mie theory is adequate in an approximate sense only for $r_{ev} < 500 \mu\text{m}$ (Liu and Illingworth, 1997).

Small particles may have near-pristine shapes, but larger particles are typically produced by aggregation and are irregular in shape. Aggregates are the dominant form of particle in vigorous mid-latitude storms (Jiusto and Weickmann, 1973), and Hobbs et al. (1974) identified aggregates as producing more than half the total mass of solid precipitation near the crest of the Cascade Mountains. The particle models must be representative of aggregates in the larger particle sizes. Attempts have been made to simulate millimeter-wavelength scattering properties of irregular, aggregate-like particles with Mie theory using spheres composed of a mixture of air and ice (the soft sphere approximation); however, comparisons against less approximate methods have shown the inability of soft sphere models to reproduce scattering properties across multiple frequencies (Petty and Huang, 2010). While the CloudSat retrieval uses only 94 GHz reflectivity observations, the potential future application of multiple frequency active and passive observations to the snowfall retrieval problem makes desirable the accurate modeling of multi-frequency scattering properties. Therefore, some information about particle shape must be provided for these models, and the method employed to calculate scattering properties should consider this shape information.

6.1 The discrete dipole approximation (DDA) method

While a number of techniques may be applied to calculate scattering properties for non-spherical ice particles (see e.g. Bohren and Singham (1991) for an overview), two methods, the discrete dipole approximation (DDA: Draine, 1988; Draine and Flatau, 1994) and the finite difference time domain method (Tang and Aydin, 1995), allow arbitrary geometries. The DDA, the method used for this work, replaces a continuous target with an array of discrete dipoles with specified polarizability. Subject to the incident electric field, which includes both the applied field and the fields generated by other dipoles, an oscillating dipole moment is induced at each point and the oscillating dipole, in turn, generates an electric field. The relation between the incident fields and the dipole polarizations is expressed as a set of coupled linear equations which are solved to find the polarizations. The various single scattering properties are then determined using the polarizations. The DDA implementation used for this work is DDSCAT (Drain and Flatau, 2010).

Given a desired particle shape, an appropriate dipole array must be constructed within that shape. DDSCAT requires that dipoles be placed on a simple cubic lattice. As each dipole represents a small element of mass, the number of dipoles must be such that the particle has the required mass. Additionally, the dipole array must be constructed so that an accurate DDA calculation is obtained. The primary criteria for accuracy are 1) that the spacing d between dipole locations be small compared to the wavelength of the applied field and 2) that the number of dipoles be sufficient to adequately describe the particle shape (Drain and Flatau, 2010). Based on comparisons versus Mie results for spheres, Draine and Flatau (1994) found that when accurate calculations of backscattering cross sections are needed, the criteria are satisfied by requiring

$$|n| \frac{2\pi}{\Lambda} d < 0.5 \quad (6.2)$$

where n is the complex refractive index of the dipole material and Λ is the wavelength of the incident radiation, and by requiring $N_{dipoles} > 10^4$, where $N_{dipoles}$ is the total number

of dipoles. The requirement given by (6.2) defines an upper limit on dipole spacing:

$$d < \frac{\Lambda}{4\pi |n|} \quad (6.3)$$

For more complex shapes the second criterion, that the number of dipoles be sufficient to adequately describe the particle shape, is more difficult to assess because of the lack of exact scattering properties. Okamoto et al. (1995) and Okamoto (2002) attempted to address this lack by comparing the results of DDA simulations performed with increasing values of $N_{dipoles}$. For randomly oriented particles, accuracies of 10% for Z_e were obtained when the criterion (6.2) was satisfied. However, the smallest aspect ratio (thickness divided by maximum dimension across the face of a planar particle) examined was 1/3, while for pristine planar crystals, aspect ratios may be in the range of 0.01 to 0.1 (Auer and Veal, 1970).

Following Okamoto's approach, a set of DDA calculations was made for a large planar particle for which the number of dipoles used through the thickness of the plate, N_s , was increased from 2 to 6. At $N_s = 2$, both the requirement on dipole spacing (6.2) and the requirement on $N_{dipoles}$ were met. Increases beyond $N_s = 6$ were not computationally feasible at this particle size. Because of the requirement that the dipoles be located on a cubic lattice, small increases in the number of dipoles along the small dimension of a particle can dramatically increase the total number of dipoles. Doubling the number of dipoles along a single dimension reduces the lattice spacing by a factor of 2 and results in an 8-fold increase in the total number of dipoles. The calculations showed differences in σ_{bk} of less than 3% and in σ_{ext} of less than 5% (Table 6.1), with the cross sections systematically decreasing as the number of dipoles was increased. Given that DDA particle shapes are highly idealized representations of natural, irregular snow particles, this level of uncertainty is not objectionable. For the scattering calculations used to produce the particle models in this work, the lattices for planar particles are constructed to allow no fewer than two dipoles through the thickness of the plate.

Table 6.1: Variation in scattering properties for a sector plate particle ($r_{ev} = 789.7\mu\text{m}$) with changes in N_s , the number of dipoles across the small dimension of the plate. σ_{bk} and σ_{ext} are the backscatter and extinction cross-sections, respectively.

N_s	$N_{dipoles}$	σ_{bk}, mm^2	$\sigma_{ext}, \text{mm}^2$
2	13,608	1.145	0.919
4	112,528	1.122	0.899
6	383,442	1.116	0.880

6.1.1 Particle shapes

It is necessary then to define desired particle shapes for use in the DDA calculations. The information on mass and horizontally-projected area obtained from the snow microphysics retrieval is not sufficient to uniquely define the particle shape, so assumptions must be made. It is visually apparent that for a typical snow particle, the distribution of mass within the volume envelope occupied by the particle is not isotropic. Rather, the mass is usually somewhat spatially clustered, or clumpy. This feature is particularly true for aggregates. For millimeter wavelengths, it is likely that the scattering properties of snow particles are not strongly sensitive to the fine structure of the spatial distribution of mass, but will be sensitive to the larger-scale structure (Matrosov, 2007). The objective of an assumed particle shape is then to reasonably capture the gross features of the spatial distribution of mass, but not to attempt to replicate particular fine features.

A broad distinction may be made between planar and spatial particles. As noted previously, pristine planar crystals may have aspect ratios of 0.01 to 0.1 (Auer and Veal, 1970). In contrast, aspect ratios for snow particles with $D_M < 1.0$ mm have been measured to be around 0.6 - 0.8 using a Cloud Particle Imager (Korolev and Isaac, 2003), although it should be noted that the observations were made at an inclination angle of 45° to horizontal. This observing angle would tend to overestimate aspect ratios for oblate particles oriented with their minor axis vertical. Additionally, planar particles would tend to present the planar face to a vertically-pointing radar, while spatial particles would present a more irregular face.

To address these factors, scattering calculations were made for a variety of shapes. For planar particles, a branched plate-like shape with six branches, designated as shape SPp, was used (Figure 6.2, upper left). While hexagonal plates and needles may have suitably small aspect ratios, here defined as the maximum vertical dimension divided by the maximum horizontal dimension D_M , their shapes are not sufficiently adjustable to meet the constraints on horizontally-projected area obtained from the microphysics retrieval. With the branched planar shape, the horizontally-projected area may be altered by changing the width of the branches. For narrow widths, the shape is much like a stellar crystal (P1d) (Magono and Lee, 1996) and has a small horizontally-projected area. As the branch width increases, the shape approaches that of a crystal with broad branches (P1c) and at the limit of maximum branch width, is a hexagonal plate (P1a). For purposes of comparison, calculations were also done for hexagonal plates (shape HPP) which met the mass constraints from the snow microphysics retrieval but not the constraints on horizontally-projected area.

Spatial particles were represented with clusters of thick hexagonal branches and with a scalene ellipsoid (Figure 6.2). These spatial shapes are considered to be simplistic, somewhat abstract representations of aggregate particles. For the clusters, the orientation of the branches controls the aspect ratio of the particle and for a given aspect ratio, the horizontally-projected area may be altered by changing the branch thickness. Three different configurations were examined: B6pf, with six branches all lying in the horizontal plane (Figure 6.2, upper middle); B8pr-30, with eight branches six of which intersected the horizontal plane at angles of 30° (Figure 6.2, lower left); and B8pf-45 with eight branches six of which intersected the horizontal plane at angles of 45° (Figure 6.2, lower right). For shape B6pf, both aspect ratio and horizontally-projected area get smaller as the branch thickness is reduced. Shape B8pr-30 has an aspect ratio of about 0.5, and B8pr-45 has an aspect ratio near 0.70.

The scalene ellipsoid is a simple shape which also has the ability to meet the constraints on horizontally projected area and aspect ratio, but whose shape is fundamentally differently than the branched particles (Figure 6.2, upper right). Given a desired size D_M , the length of the major horizontal axis is set to this size and the length of the vertical axis is set to $0.5D_M$. This choice provides the same aspect ratio as the B8pr-30 shape. The length of the

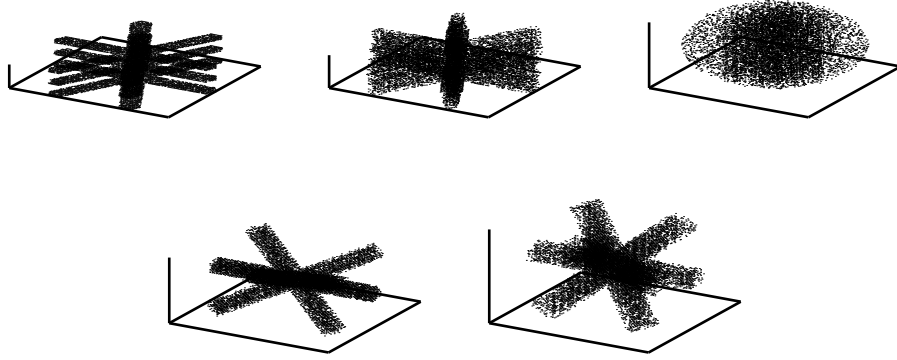


Figure 6.2: Examples of shapes for dipole arrays: SPp, upper left; B6pf, upper middle; Ep, upper right; B8pr-30, lower left; and B8pr-45, lower right.

minor horizontal axis is adjusted to match the required horizontally projected area. In the event the required length is less than $0.5D_M$, the minor horizontal axis is set to $0.5D_M$ and the required area is achieved by placing continuous porosities at random locations extending vertically through the particle. This approach ensures that the shape of the particle is such that it would fall with the proper orientation.

6.2 Construction of dipole arrays

Given a desired shape (SPp, B6pf, B8pr-30, B8pr-45, or Ep), dipole arrays must be constructed for a range of particle sizes. To construct an array for a particle with maximum dimension D_M , first particle mass m and horizontally-projected area A_p are determined using the power laws and values of α , β , γ , and σ from the snow microphysics retrieval. From the horizontally-projected area, the non-dimensional area ratio r_A can be calculated as

$$r_A = \frac{4A_p}{\pi D_M^2}. \quad (6.4)$$

and instances of the desired shape can be selected which match the area ratio to within a small error, taken to be 1%. For the Ep shape, in the event $r_A < 0.5$, a shape with $r_A = 0.5$ is used and the correct r_A is achieved when the dipole array is constructed.

Given an instance of the shape which matches the required area ratio, a three-dimensional cubic lattice with lattice spacing d is defined inside the shape (Figure 6.3, upper panel). Possible values for d are obtained by dividing the maximum dimension D_M by integer num-

bers of dipoles. The resulting lattice spacing must comply with the requirement of (6.3), and any which do not are discarded. Dipoles are considered to consist of solid ice. At 94.0 GHz, the complex refractive index for ice is $1.782 - i2.708e-03$, taken from Warren (1984) for a temperature of 250K, and this refractive index gives a maximum allowable value for d of $142 \mu\text{m}$ per (6.3). To permit the resulting dipole arrays to be used for calculations up to 183.0 GHz (a high frequency passive microwave observation channel) in future work, the maximum allowable value of d was further reduced to $73 \mu\text{m}$, based on a refractive index of $1.782 - i4.324e-03$, also from Warren.

Given a value for d , the mass of a single dipole is $d^3 \rho_{ice}$ and, knowing the required particle mass m , the required number of dipoles is

$$N_{dipoles} = \frac{m}{d^3 \rho_{ice}}. \quad (6.5)$$

If $N_{dipoles}$ exceeds the minimum allowed value of 10^4 , and if the lattice has enough nodes on which to place the dipoles, the lattice spacing is acceptable. In practice, a range of values of d will produce acceptable lattices. To reduce required computing resources, a lattice is chosen which makes the number of dipoles as small as possible without falling below the minimum value of 10^4 .

In essentially all cases, the number of available lattice nodes exceeds $N_{dipoles}$. In those cases, the dipoles are placed randomly on the lattice nodes in such a way that the particle dimension D_M and horizontally-projected area A_p are maintained at the required values (Figure 6.3, middle and lower panels). The resulting particle, rather than being solid ice, contains porosities. For the spatial particles, the combination of the gross structure imposed by the particle shape (B6pf, B8pr-30, B8pr-45, Ep) along with the porosities is intended to resemble aggregates of smaller, more structured particles. The porosities are normally not permitted to extend uninterrupted vertically through the particle in order to preserve A_p . The exception is the Ep shape when $r_A < 0.5$, in which case such porosities are allowed in order to produce the required r_A . This approach gives a particle model that matches the desired shape and that also matches the required D_M , A_p , and m . The matched values of D_M , A_p , and m ensure that the particle will have the desired fallspeed properties. The

random placement of dipoles does mean that the modeled scattering properties will have some amount of random variation. As noted earlier, however, scattering properties at millimeter wavelengths should not be strongly sensitive to the fine details of the particle structure. Additionally, since radar reflectivity is obtained by integrating over the particle size spectrum, the effects of random variations in scattering properties on radar reflectivity should be further reduced. The results from the DDA modeling were used to verify this expectation, as will be discussed in Section 6.4.

6.3 DDA calculations

DDA calculations were performed for discrete sizes ranging from $D_M = 0.025$ mm to $D_M = 18$ mm using DDSCAT version 7.1 (Drain and Flatau, 2010). The upper size limit was determined partly by computer hardware limitations. At the largest sizes, computer random access memory requirements were near 8 gigabytes for the aggregate particle models. For initial testing and evaluation, size increments varied from 0.025 mm for small particles to 1 mm for large particles. The suitability of this arrangement is examined as part of the evaluation of the DDA results (Section 6.4.4). Shapes such as SPp and HPp cannot be considered realistic at the larger particle sizes, but modeling such shapes may provide useful information about the sensitivity of scattering properties to particle shape. Particles were assumed to be oriented randomly with their longest dimension lying nominally in the horizontal plane (i.e., rotations in the horizontal plane were uniformly sampled), and were illuminated with a vertically incident, linearly polarized plane wave. Additionally, canting angles were applied, having values ranging over $\pm 10^\circ$ but sampled uniformly in the cosine of the angle following DDSCAT's standard method. This approach is an approximation, based roughly on the canting angle distributions found by Matrosov et al. (2005b) for pristine dendritic particles. Dipoles were modeled as solid ice, with a density of 0.917 g cm^{-3} and a refractive index of $1.782 - i2.708e-03$, consistent with Warren (1984) for a temperature of 250K and frequency of 94 GHz. Although the dielectric properties of ice at 94 GHz vary with temperature, the dependence is weak and using a constant value is not a significant source of error over the range of expected atmospheric temperatures.

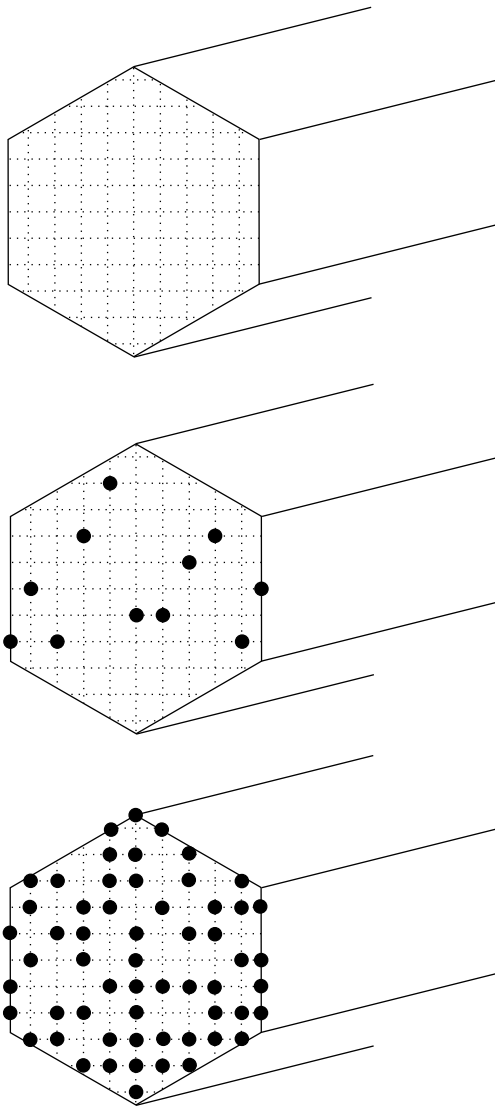


Figure 6.3: Cartoon illustrating the construction of a dipole array for DDA calculations. Given a desired shape which meets the specified maximum dimension and horizontally-projected area, first a cubic lattice is constructed within the shape (upper panel). Next, dipoles are placed so that the horizontally-projected area is completely occupied by dipoles (middle panel). Finally, the remaining dipoles, sufficient in number to meet the specified mass, are placed randomly on the lattice (lower panel).

6.3.1 Scattering properties

The DDA method models a number of particle scattering properties. Of primary relevance to this work are the backscattering and extinction cross-sections. DDSCAT provides the extinction efficiency relative to the cross-sectional area of an equivalent volume sphere

$$Q_{ext} = \frac{\sigma_{ext}}{\pi r_{ev}^2} = \frac{\sigma_{abs} + \sigma_{sca}}{\pi r_{ev}^2} \quad (6.6)$$

where σ_{ext} , σ_{abs} , and σ_{sca} are the extinction, absorption and scattering cross-sections, respectively, and r_{ev} is as given by 6.1. For backscattering, DDSCAT provides the differential backscatter cross-section normalized by πr_{ev}^2

$$Q_{bk} = \frac{1}{\pi r_{ev}^2} \left. \frac{\partial \sigma_{sca}}{\partial \Omega} \right|_{\Theta=\pi} \quad (6.7)$$

where Ω is solid angle and $\Theta = \pi$ indicates the derivative is evaluated in the backscattering direction. For simulating radar reflectivities, the backscatter cross-section is calculated from Q_{bk} as

$$\sigma_{bk} = 4\pi Q_{bk} \pi r_{ev}^2. \quad (6.8)$$

Figure 6.4 shows the resulting backscatter cross-sections for the planar SPp shape. For comparison, cross-sections for Rayleigh spheres, Mie spheres and the HPp shape are shown also. Cross-sections are plotted versus r_{ev} , and the relation between D_M and r_{ev} is shown in Figure 6.5. Since the DDA dipoles are taken to be solid ice, as are the Rayleigh and Mie spheres, particles with the same r_{ev} contain the same mass. For r_{ev} below about 0.7 mm, the SPp and HPp shapes have similar cross-sections. At these small sizes, the constraint on horizontally-projected area gives large area ratios, causing the SPp particles to be similar in shape to the HPp particles.

As was true in the analysis of X-band scattering properties, the backscatter cross-sections for these plate-like particles exceed the cross-sections for spheres in the Rayleigh regime, consistent with predictions by models for Rayleigh backscatter by oblate spheroids (Atlas et al., 1953). At the point where the HPp cross-sections fall below those for Rayleigh spheres,

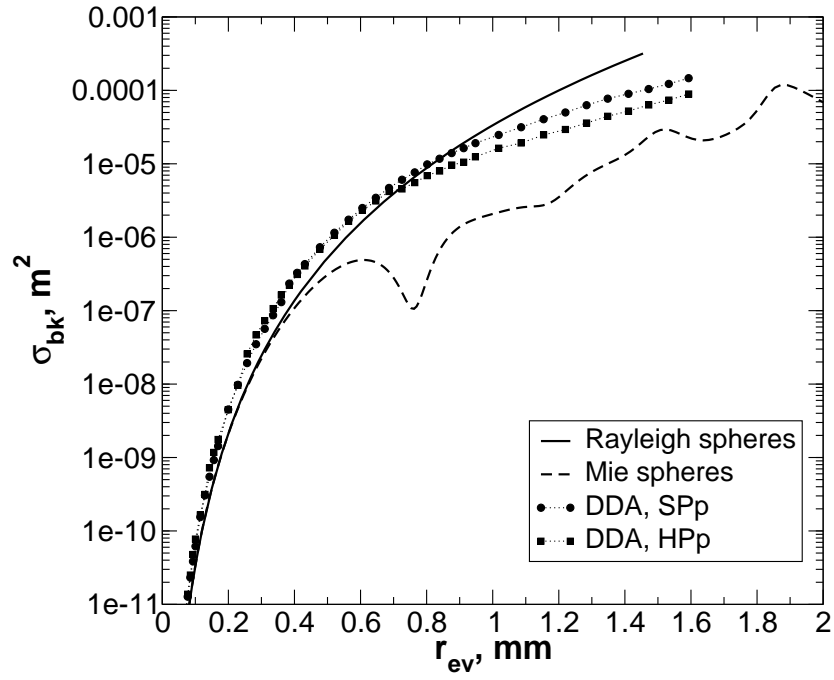


Figure 6.4: Backscatter cross-sections for planar particle models compared to Rayleigh and Mie solid ice spheres. For the nonspherical particles, the cross-sections are for a vertically-incident radar beam, and the equivalent volume radius r_{ev} is as given by (6.1).

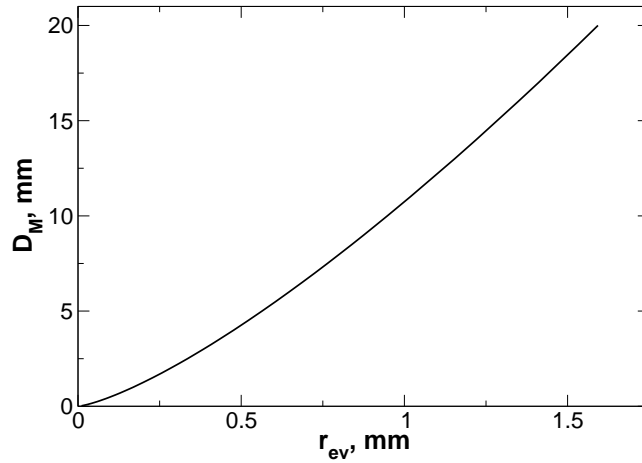


Figure 6.5: Particle maximum dimension D_M as a function of equivalent volume radius r_{ev} for the mass-dimension relation used for the particle models.

the size parameter based on r_{ev}

$$x_{ev} = \frac{2\pi r_{ev}}{\Lambda} \quad (6.9)$$

has a value of about 1.4. At r_{ev} larger than about 0.7 mm, the cross-sections for the HPp shape fall below those for the SPp shape. For a given size, the HPp particle has the same mass as the SPp particle, but has a larger horizontally projected area. Consequently, the HPp particle is thinner than the SPp, while the SPp is thicker and much of the mass is concentrated near the center of the particle. Additionally, for r_{ev} larger than about 0.73 mm, the HPp particles have an insufficient number of dipoles to ensure that the entire plate area is occupied by dipoles. As a result, there are porosities extending through the plate. These through-porosities occupy 20-30% of the plate area. These factors appear to be sufficient to cause the HPp cross-sections to fall below those of the SPp particles. Neither shape shows evidence of the resonance at $r_{ev}= 0.8$ mm that is apparent in the results for the Mie spheres.

Figure 6.6 shows the backscatter cross-sections for the spatial particles. As before, cross-sections for Rayleigh and Mie spheres are shown for comparison. The cross-sections for the more compact shape, B6pf, are similar to those for spheres for sizes up to $r_{ev}= 0.35$ mm. For the more spatially extended particles B8pr-30, B8pr-45 and Ep, the cross-sections fall below those for Rayleigh spheres at $r_{ev}= 0.15 - 0.2$ mm, corresponding to size parameters of 0.3 - 0.4. For the branched particles, as the aspect ratio of the particle increases, the backscatter cross-section decreases, although for some sizes the cross-sections for B8pr-30 and B8pr-45 are almost equal. The B8pr-30 and B8pr-45 shapes show Mie-like resonances, albeit with much smaller amplitude than the Mie sphere resonance at $r_{ev}= 0.8$ mm, while the B6pf shape shows none. The Ep shape shows markedly smaller cross-sections than the branched particles over most of the size range, and exhibits strong resonance features.

Over most of the shown size range, the cross-sections for the two extremes of the branched particles (B6pf versus B8pr-45) differ by at least an order of magnitude, indicating that additional information is needed to adequately constrain the scattering properties for these spatial particles. The observations previously described by Korolev and Isaac (2003) suggest that, for particles smaller than $D_M= 1.0$ mm, aspect ratios should be no larger

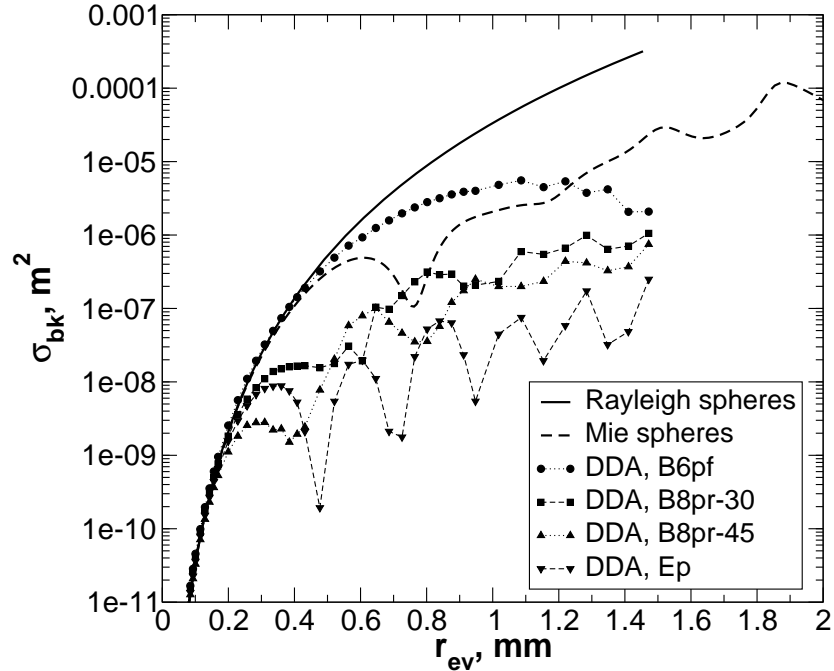


Figure 6.6: Backscatter cross-sections for spatial particle models compared to Rayleigh and Mie solid ice spheres. For the nonspherical particles, the cross-sections are for a vertically-incident radar beam, and the equivalent volume radius r_{ev} is as given by (6.1).

than 0.6 - 0.8. Magono and Nakamura (1965) used photographs of snow particles taken in elevation view to determine the horizontal and vertical dimensions of snow particles. They found that for particles with $D_{obs} < 10$. mm, aspect ratios were near 1.0, and that for larger particles, the horizontal dimension was substantially larger than the vertical dimension. Matrosov et al (2005a) found that scattering models based on particles with aspect ratios of 0.6 gave better agreement to aircraft-observed dual-frequency radar ratios than did models based on particles with aspect ratios of 1.0. These results suggest that the B8pr-30 or B8pr-45 shapes are more representative of the backscattering properties of true snow particles, especially in larger sizes, than is the B6pf shape.

Extinction cross-sections for planar and spatial particles are shown in Figures 6.7 and 6.8. The most striking difference in comparison to the backscatter cross-sections is the reduced sensitivity to shape. At the largest sizes, the differences in extinction cross-sections among the spatial particles are no more than $\pm 30\%$ relative to the B8pr-30 cross-sections. The less compact B8pr-45 shape has larger cross-sections than the more compact B8pr-30 and B6pf shapes, opposite the behavior shown for the backscatter cross-sections. One might

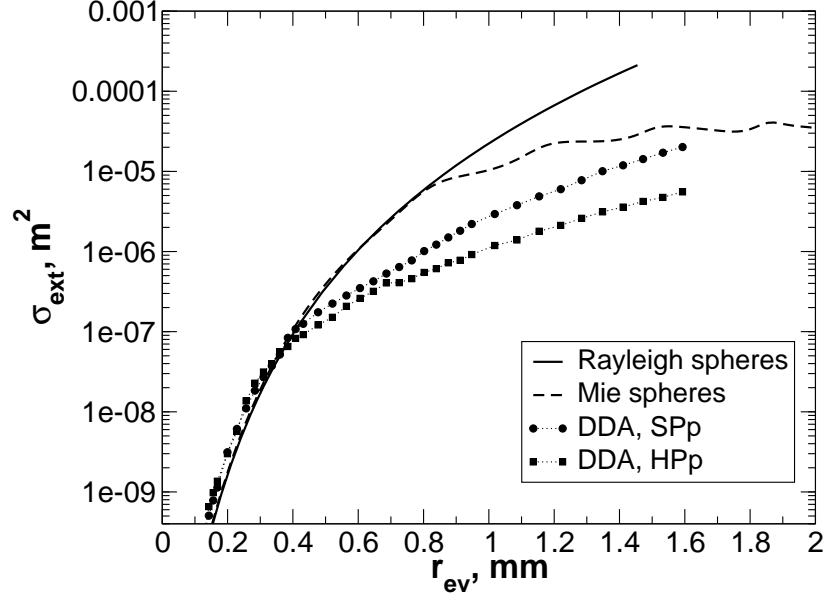


Figure 6.7: Extinction cross-sections for planar particle models compared to Rayleigh and Mie solid ice spheres. For the nonspherical particles, the cross-sections are for a vertically-incident radar beam, and the equivalent volume radius r_{ev} is as given by (6.1).

expect, then, that the very thin SPp shape would have the smallest extinction cross-sections, but instead the SPp has the highest. One significant difference between the SPp and B6pf shape is that the SPp shape presents a planar surface to the incident beam, while the B6pf and other spatial shapes present a more oblique surface. This difference may contribute to the enhanced extinction from the SPp shape compared to the spatial shapes.

The planar shapes SPp and HPp have similar extinction cross-sections for r_{ev} less than 0.7 mm. For r_{ev} above 0.7 mm, the differences increase, with the SPp cross-sections exceeding those of the HPp shape by a factor of about 3. As described in relation to the backscatter cross-sections, these differences seem linked to the thinness of the HPp shape and the presence of porosities extending through the plate. At smaller sizes, extinction cross-sections are similar to those for solid ice spheres up to $r_{ev}=0.25$ mm (spatial shapes) and up to $r_{ev}=0.4$ mm (planar shapes). As was true for the backscatter cross-sections, the extinction cross-sections for planar shapes at these small sizes somewhat exceed the Rayleigh sphere values.

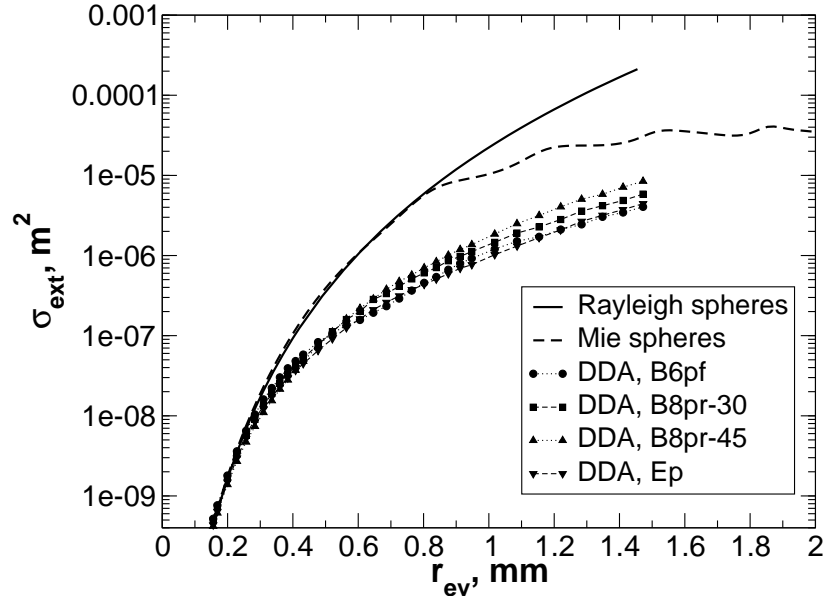


Figure 6.8: Extinction cross-sections for spatial particle models compared to Rayleigh and Mie solid ice spheres. For the nonspherical particles, the cross-sections are for a vertically-incident radar beam, and the equivalent volume radius r_{ev} is as given by (6.1).

6.4 Assessments

Uncertainties in these particle models will impact the performance of the CloudSat retrieval. To gain further insight into the suitability of the models, several assessments were performed to evaluate how the differences and uncertainties in the models affect reflectivity and attenuation.

6.4.1 SVI dataset

The size distributions for these assessments were obtained from the SVI observations for C3VP. The SVI operated nearly continuously at CARE during the 2006/07 C3VP observing season, capturing size distribution observations for snowfall events both during and outside the IOPs. The observations at 1-minute resolution were averaged using distinct 5-minute samples as was done for the snow microphysics retrievals. These distributions, based on the feret diameter, were converted to distributions on maximum dimension D_M using $\phi=0.778$, the value obtained from the snow microphysics retrieval. To increase the likelihood that the distributions were representative of dry snow, the dataset was screened using the air temperature observed at the 10-m meteorology tower at CARE. Distributions for which the

temperature was greater than 273 K were discarded. In all, about 9400 of the 5-minute averaged size distributions contained non-zero particle counts and of these about 7300 were frozen, giving over 600 hours of snow observations.

6.4.2 Shape and reflectivity

To evaluate the suitability of the particle models, reflectivities were simulated using the particle models in conjunction with the SVI size distribution dataset, and the simulated reflectivities were compared against simultaneously observed W-band radar reflectivities. The observed radar reflectivities were provided by the Airborne Cloud Radar (ACR) (Sadowy, 1999), a 95 GHz profiling radar deployed on the ground at the CARE site during C3VP. Although a formal calibration of the ACR was not performed immediately prior to C3VP, a previous intercomparison between the ACR and the University of Massachusetts Cloud Profiling Radar System showed average differences of 0.3 dBZe (Sekelsky et al., 1999). For the reflectivity comparisons presented here, the calibration error for the ACR reflectivity was assumed negligible, and it is noted that a nonnegligible bias in the ACR calibration could affect the results presented below.

The ACR pointed vertically, and was operated with a vertical range resolution of 120 m and a time resolution of about 2.8 s. The range bin nearest the surface was centered at 197 m AGL. Comparisons of the reflectivities in this bin versus reflectivities in the adjacent bin above suggest this lowest bin was not substantially affected by ground clutter for reflectivities above about -15 dBZe, so observations from this lowest bin were used. Comparisons were limited to cases for which the observed reflectivity was greater than -15 dBZe and the near-surface air temperature was less than 273 K. Valid cases were obtained for twelve distinct snow events occurring over 13 days from 2 December 2006 to 26 February 2007. Reflectivities in linear units were averaged in time using 5-minute samples, consistent with the treatment of the SVI observations. Given the proximity of the radar observation to the ground, unattenuated reflectivity was used for these comparisons. From (3.12) and (3.13), the unattenuated equivalent reflectivity factor for non-Rayleigh scatterers is given

by

$$Ze = \frac{\Lambda^4}{\|K_w\|^2 \pi^5} \int_{D_{M,min}}^{D_{M,max}} N(D_M) \sigma_{bk}(D_M) dD_M. \quad (6.10)$$

Since the DDA particle properties are defined on sizes different than the SVI D_M , the DDA properties were interpolated to the SVI sizes. Interpolations were done using the backscatter efficiencies (6.8), giving backscatter efficiencies at the SVI sizes which were then converted to backscatter cross-sections.

Of the five shapes considered, the B8pr-30 shape provided the best agreement to the full range of observed reflectivities, with a bias over all observations of -0.03 dBZe (Figure 6.9). The more compact shapes B6pf and SPp substantially overestimated reflectivities for most of the observed reflectivity range, while the less compact B8pr-45 and Ep underestimated reflectivities. Obviously, the use of the SPp shape over the full size range observed by the SVI represents an unrealistic and severe extrapolation. The largest observed dimensions D_M for this type of pristine shape (e.g., P1b, P1c, P1d, P1e) are typically 1 to 2 mm (see Tables B.1, B.3, B.4, B.5, B.6, and B.7 and associated references) while the particle models extend to $D_M = 18$ mm. Nevertheless, the result serves to illustrate the magnitude of errors that may be caused by the ill-considered use of such models.

The difference in bias between the B8pr-30 and the B8pr-45 shapes is due to differences in the vertical aspect ratios: the branches of the B8pr-30 particle make an angle of 30° with the horizontal plane, while those of the B8pr-45 particle make an angle of 45° . The vertical aspect ratio for the B8pr-30 particle is about 0.5 while that for the B8pr-45 is near 0.7, resulting in a particle that is more extended along the direction of propagation of the radar beam. Additionally, for a given particle size, the branches of the B8pr-45 particle are likely somewhat wider than those of the B8pr-30 particle. This increase in width is necessary for the particles to have equal A_p . The wider branches would cause the B8pr-45 particle to have somewhat larger volume than the B8pr-30 particle. Since for a given size, the particles have the same mass (i.e., the same number of dipoles), the dipoles in the B8pr-45 shape will not be as closely packed as in the B8pr-30 shape. In contrast, the Ep particle has the same vertical aspect ratio as the B8pr-30, but for most D_M the volume of the Ep particle substantially exceeds that of the B8pr-30, leading to a much less dense arrangement of

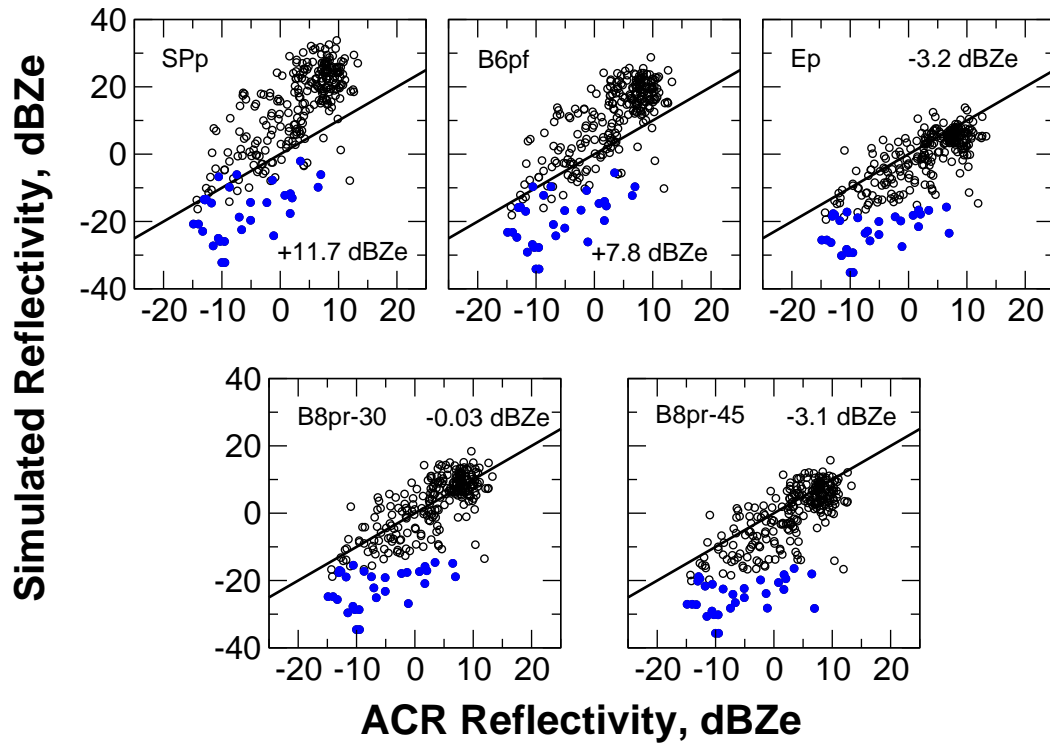


Figure 6.9: Comparisons of observed W-band reflectivities from the ACR versus those simulated using DDA models for various particle shapes. Comparisons are for cases with observed reflectivities larger than -15 dBZe and near-surface air temperatures less than 273 K. Cases include 12 snow events occurring on 13 days between 2 December 2006 and 26 February 2007. Observed reflectivities are at 197 m AGL, in the ACR range bin nearest the surface. The blue points indicate SVI size distributions with less than 100 particles in the sample and with those particles distributed across five or fewer size bins. The reflectivity biases, computed over all the well-sampled (black) points, are shown on each panel.

dipoles for the Ep particle. The resulting reflectivity bias for the Ep particle is similar to that of the B8pr-45, but the backscatter cross-sections are quite different for the two shapes (Figure 6.6).

The comparisons shown in Figure 6.9 also highlight the possible effects of the limited sample volume of the SVI compared to the radar. The blue points are cases for which the SVI detected fewer than 100 particles over the 5-minute sample with those particles distributed in five or fewer size bins, suggesting the size distributions may have been insufficiently sampled. An examination of the ACR operator’s log (Austin et al., 2007) showed that many of these cases were associated with the initiation or termination of snowfall at the surface, or with low level stratocumulus absent precipitation.

6.4.3 Random dipole effects

The random placement of dipoles on the lattice causes small variations in the scattering properties. To evaluate these variations and their influence on simulated reflectivities, four distinct realizations of the dipole arrays for the B8pr-30 shape were constructed and used to calculate backscatter and extinction cross-sections. These realizations were then used along with the SVI dataset to calculate radar reflectivity per (6.10) and specific attenuation

$$k = \frac{10}{\ln(10)} \int N(D_M) \sigma_{ext}(D_M) dD_M. \quad (6.11)$$

Evaluations were limited to cases for which the SVI size distribution was well-sampled (more than 100 particles observed or particles distributed over more than five size bins). At small particle sizes, the backscatter cross-sections were largely insensitive to the dipole locations as shown by the small fractional uncertainties (Figure 6.10). This result is consistent with the expectation that scattering properties are primarily sensitive to the equivalent volume diameter in the Rayleigh regime, as shown in (3.15). At larger sizes, fractional uncertainties were about 0.05, with values for particular sizes as large as 0.15 and as small as 0.015. As expected, since these random variations are uncorrelated over the range of particle sizes, the resulting uncertainties in the modeled radar reflectivity are negligible (Figure 6.11).

Extinction is less affected by the randomness of the dipole locations than is backscattering. Fractional uncertainties in the extinction cross-sections are typically about 0.01 (Figure 6.12, lower panel). When integrated over the size distribution, the resulting values of the one-way specific attenuation have uncertainties that are typically less than 0.002 dB km⁻¹ (Figure 6.13). The resulting uncertainties in the attenuation of the radar beam will be insignificant, and were ignored.

6.4.4 Truncation and discretization

By necessity, the DDA calculations can be applied to only a limited number of discrete sizes and over a limited size range. The choice of sizes and size range will introduce uncertainties into modeled radar reflectivities. The SVI dataset was again used to evaluate these uncertainties. For truncation, it was necessary to have size distributions and scattering properties

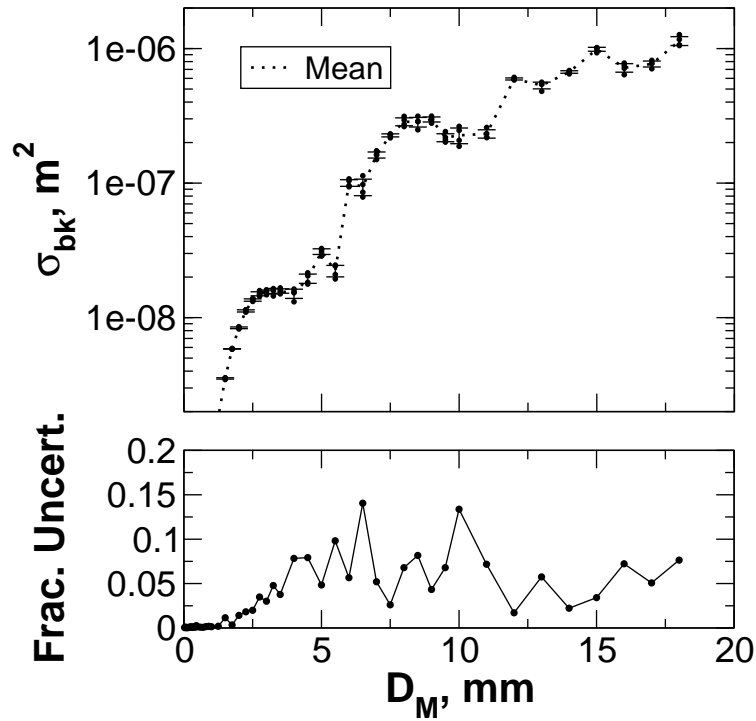


Figure 6.10: The variations in σ_{bk} for shape B8pr-30 due to the random placement of dipoles. The upper panel shows the mean and standard deviation (dotted line and error bars) along with data points from the distinct realizations. The bottom panel shows the fractional uncertainty for an individual realization, given by the standard deviation divided by the mean value.

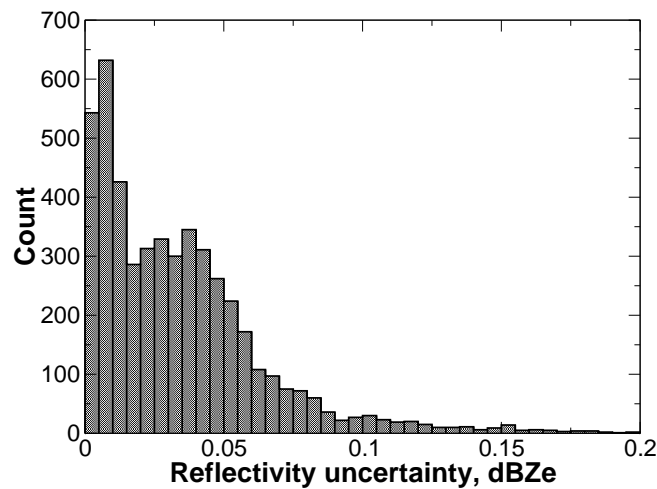


Figure 6.11: Histogram of radar reflectivity uncertainties for shape B8pr-30 due to the random placement of dipoles.

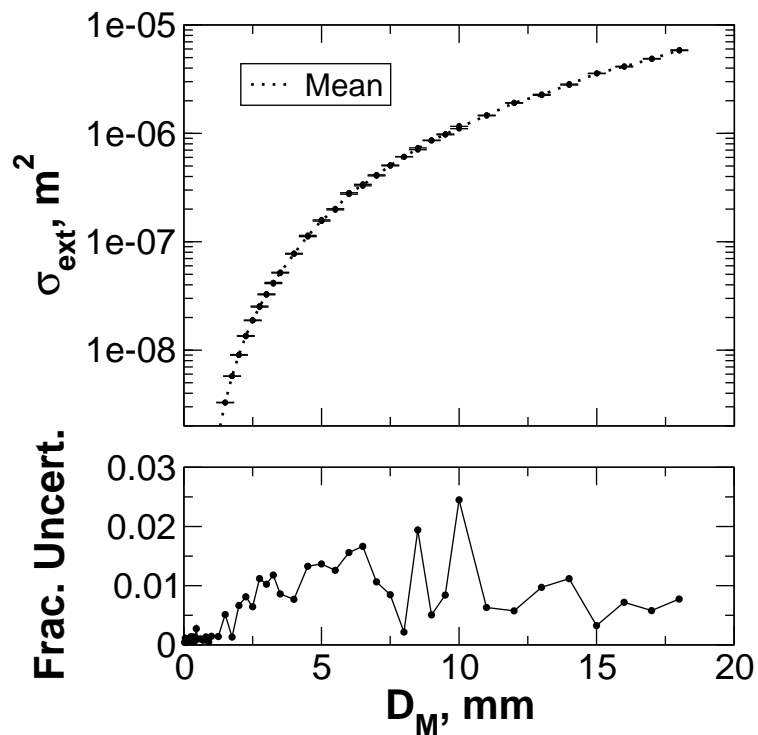


Figure 6.12: The variations in σ_{ext} for shape B8pr-30 due to the random placement of dipoles. Panels are as described for Figure 6.10.

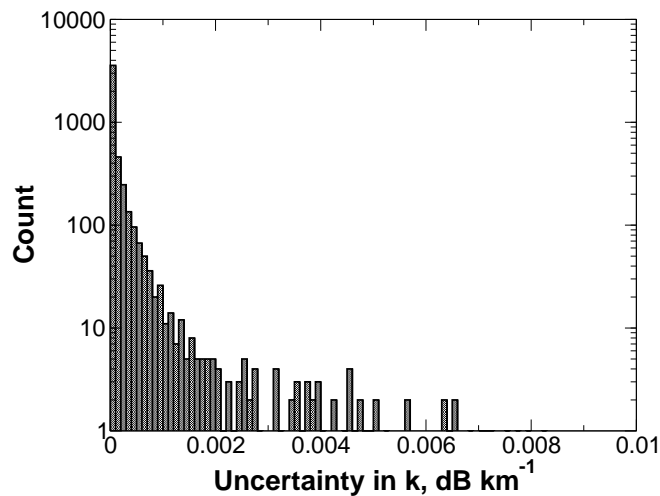


Figure 6.13: Histogram of uncertainties for specific attenuation, k , for shape B8pr-30 due to the random placement of dipoles.

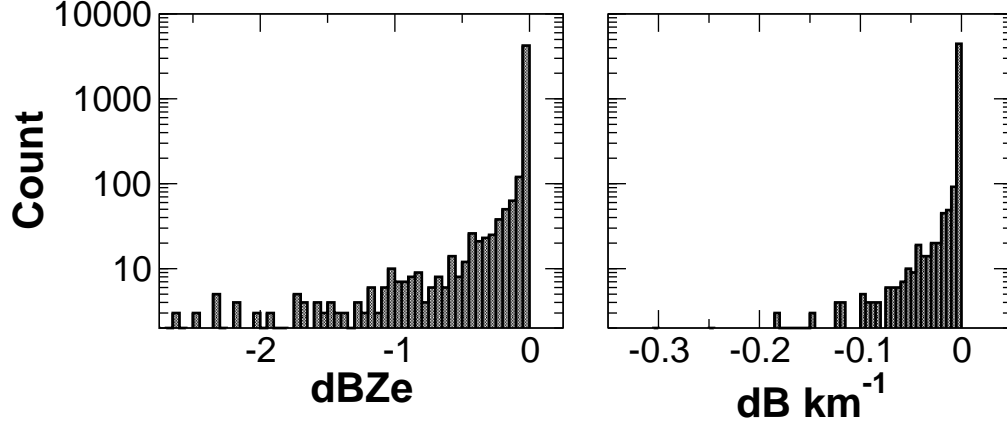


Figure 6.14: Histograms of truncation errors for reflectivity (left panel) and specific attenuation.

which extend beyond the upper size limit of $D_M = 18$ mm that was used for the particle property models. To produce the required size distributions, exponential distributions on D_M

$$N(D_M) = N_0 \exp(-\lambda D_M) \quad (6.12)$$

were fit to each size distribution in the SVI dataset (again limited to well-sampled distributions) to find the slope and intercept parameters N_0 and λ for that distribution. The parameters were then used to calculate size distribution values for sizes up to 40 mm. Using the scattering properties for the B8pr-30 particle model, backscatter and extinction cross-sections for these large sizes were found by linearly extrapolating Q_{bk} and Q_{ext} using the two largest particle sizes from the DDA results. Reflectivities and specific attenuation were then calculated with both the standard and augmented range of sizes. Errors in both reflectivity and specific attenuation were near zero for well over half the samples (Figure 6.14). The bias and scatter (mean and standard deviation of the truncation errors) were -0.11 (0.57) dBZe and -0.04 (1.97) dB km $^{-1}$. The comparatively large scatter in the errors for specific attenuation was due to fourteen outliers out of over 4800 datapoints for which the fitted values of λ were exceptionally small, less than 0.15 mm $^{-1}$. Removing these points reduced the bias and scatter for the specific attenuation to -0.005 (0.07) dB km $^{-1}$ for the specific attenuation, and that of the reflectivity to -0.09 (0.42) dBZe.

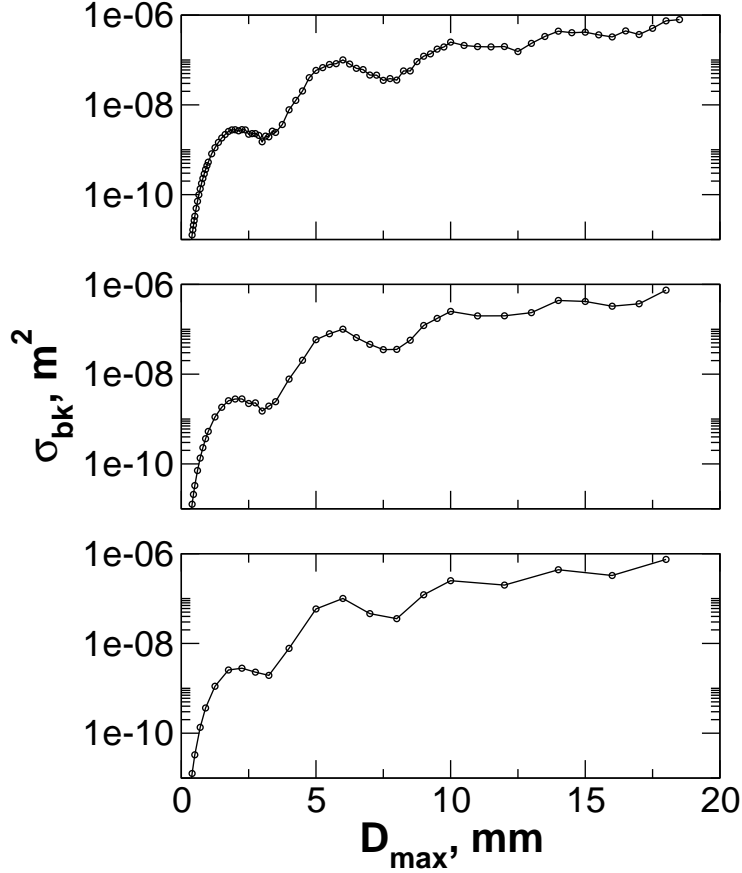


Figure 6.15: Backscatter cross-sections for the B8pr-45 shape at high (upper panel), standard (middle panel) and low particle size resolutions.

Discretization errors were evaluated using three versions of the B8pr-45 scattering properties that use different particle size resolutions: the standard resolution, one with high resolution, and one with low resolution. In the high resolution version, the spacing between particles sizes is halved and in the low resolution version, the spacing is doubled (Figure 6.15). Since σ_{ext} tends to be a smoothly varying function of particle size, specific attenuation is not strongly sensitive to discretization errors (Figure 6.16, right panels). In contrast, reflectivity shows strong sensitivity, with discretization errors about a factor of ten larger in magnitude for low resolution compared to standard resolution (Figure 6.16, left panels). The bias and scatter for the reflectivity discretization errors were -0.001 (0.021) dBZe for standard resolution and 0.15 (0.13) dBZe for low resolution. For specific attenuation, the values were -0.001 (0.020) dB km⁻¹ for standard resolution and 0.001 (0.016) dB km⁻¹ for low resolution.

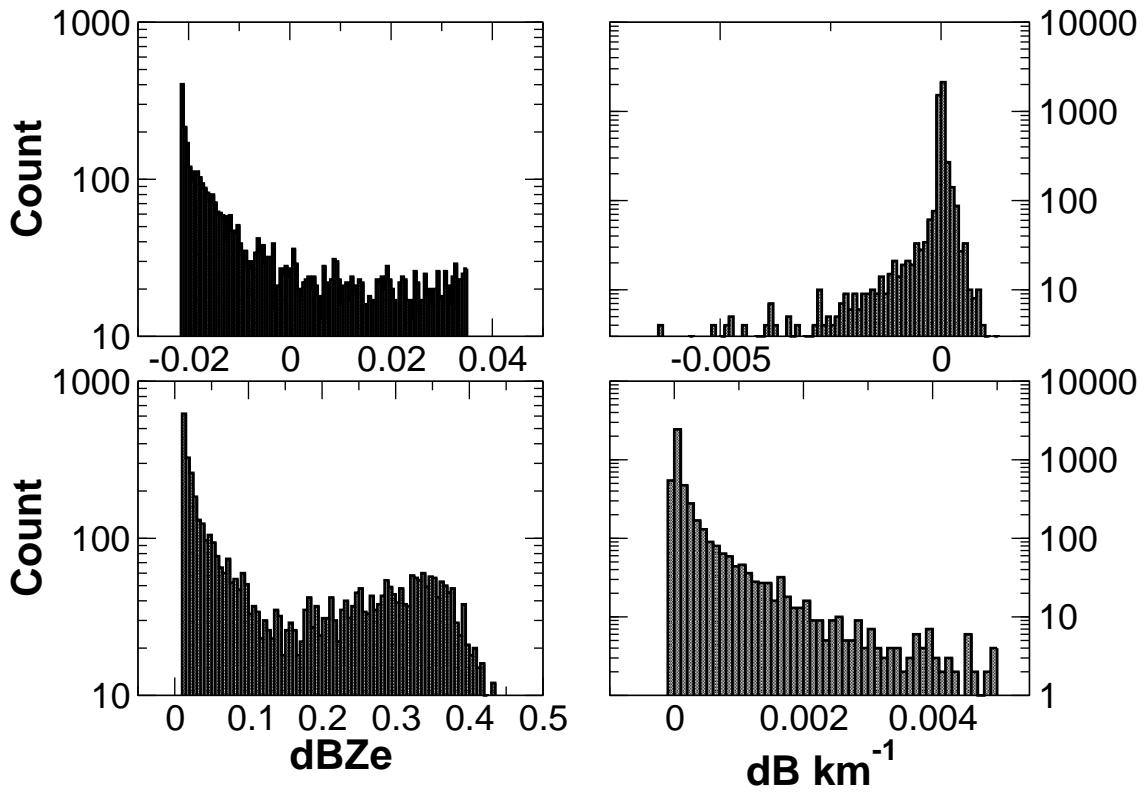


Figure 6.16: Histograms of discretization errors for reflectivity (left panels) and specific attenuation. The upper panels shows errors for standard resolution relative to high resolution, while the lower panels show errors for low resolution relative to high resolution. Note that the vertical axes are logarithmic.

Chapter 7

The CloudSat snowfall retrieval

As was described in section 3.2, snowfall rate depends on the abundance of particles of different sizes (the size distribution), the masses of those particles, and their fallspeeds. Fallspeed in turn depends on particle masses, horizontally-projected areas, and environmental conditions. In particular, snowfall rate depends on the microphysical properties of mass and horizontally-projected area. As was true for the snow microphysics retrieval, radar backscattering at 94 GHz is sensitive to size distribution and particle mass; however, at this higher frequency, backscattering is also sensitive to particle shape. With even simple models of the size distribution and of particle mass and area, observations of 94 GHz radar reflectivity alone are insufficient to constrain the models adequately to determine snowfall rate. To address this insufficiency, optimal estimation (Section 3.1) was used for the CloudSat snowfall retrieval. This approach enables the use of a priori information which helps constrain the retrievals.

By necessity, a number of the a priori assumptions used by the retrieval are particular to cloud ice and snow. Therefore, before applying the retrieval to a particular radar observation, it must be determined whether snow is present. This scene characterization is a critical element of the retrieval algorithm, and serves three important roles. First, it must evaluate whether snow is present in the scene observed by the radar. If so, a retrieval is performed. This evaluation helps ensure that the retrieval is applied appropriately. Second, if snow is present, the scene characterization must determine whether the snow observed by the radar is reaching the surface in the form of snow. Generally, CloudSat's observations

near the surface are obscured by ground clutter, and retrievals are made only for range bins somewhat above the surface. Temperature differences might cause snow aloft to arrive at the surface as rainfall. Finally, the scene characterizations directly determine the frequency of occurrence with which snow occurs in the resulting data product.

Because of ground clutter, the estimate of snowfall rate nearest the surface from the retrieval may be from several hundred meters to over a kilometer above the surface. If the retrieval is successful and the scene characterization shows that surface precipitation will be in the form of snow, an estimate must be made of the surface snowfall rate. This is done using the retrieval results from the lowest uncluttered radar bins.

The sections that follow start by describing the CloudSat data products used for the retrieval and the formulation of the retrieval. Next, measurement and forward model uncertainties are estimated. The results from the C3VP snow microphysics retrieval and the particle model development, including the covariance matrix for the microphysical parameters, are used to estimate uncertainties for radar reflectivity forward model. Following this, the scene characterization is described and the a priori estimates for the state variables are developed. Finally, the method for calculating profiles of snowfall rate and surface snowfall rates, including uncertainties, from the retrieval results is presented. This method also makes use of the C3VP snow microphysics retrieval results and the particle models, and the covariance matrix for the microphysical parameters is used to estimate snowfall rate uncertainties.

7.1 CloudSat and the Cloud Profiling Radar

CloudSat became operational in June, 2006, flying in formation as part of the A-train constellation of satellites (Stephens et al., 2008). The constellation follows a sun-synchronous orbit with an altitude of 705 - 730 km and an inclination of 98.2 degrees. The constellation makes its equator crossing around 1:30 pm local solar time and has an orbital period of about 99 minutes, resulting in a ground track that repeats every 16 days. The sole instrument on CloudSat is the Cloud Profiling Radar (CPR), operating at 94 GHz. The CPR points near-nadir and has a range resolution of 485 m, but oversampling is used to provide

data at a vertical resolution of 240 m. The along-track and cross-track resolutions are 1.7 and 1.4 km, respectively, and the minimum detectable signal is nominally about -30 dBZ (Tanelli et al., 2008).

The fundamental user dataset for CloudSat is the “Geometric Profile”, or 2B-GEOPROF, product (Mace, 2007). The 2B-GEOPROF algorithm examines the profile of backscattered power received by the radar, determines the significance of the signal, then reports the profile of equivalent reflectivity factors (Z_e) along with a mask indicating the significance of the reflectivity in each radar range bin. For valid radar data not contaminated by surface clutter, the mask values range from 6, indicating an echo of low significance, to 40, indicating a strong echo. The mask can be loosely taken as an indicator of the likelihood that a particular echo is due to the presence of hydrometeors. When a range bin is likely contaminated with surface clutter, the mask value is set to 5. The mask and reflectivity profiles provided by 2B-GEOPROF are the primary inputs to the snowfall retrieval algorithm. Distinguishing snowfall from rain in the CloudSat observations requires temperature information. This information is taken from the ECMWF-AUX product, an ancillary product derived from the European Centre for Medium-Range Weather Forecasts reanalysis data (Stephens et al., 2008). ECMWF-AUX provides profiles of temperature, humidity, and pressure subsetted to the CloudSat ground track and interpolated vertically to CloudSat’s range resolution. These temperature profiles are used to determine the phase of precipitation aloft and at the surface, and, along with pressure profiles, to calculate fallspeeds. Over ocean, the 2C-PRECIP-COLUMN product (Haynes et al., 2009) makes estimates of the melted mass fraction for precipitation reaching the surface. When available, these estimates are used to distinguish rain and snow at the surface; otherwise, the CloudSat snowfall retrieval makes an independent estimate of the melted mass fraction using ECMWF-AUX temperatures. The remainder of this chapter describes the structure of the CloudSat snowfall retrieval and the application of these datasets.

7.2 Retrieval formulation

7.2.1 Theoretical basis

At the higher frequencies used by cloud radars, scattering by precipitation-sized particles generally does not follow the Rayleigh approximation, and attenuation of the radar beam by hydrometeors and gases may be significant. Under these conditions and assuming single scattering, the effective radar reflectivity factor as a function of range from the radar is given by

$$Ze(R) = \frac{\Lambda^4}{\|K_w\|^2 \pi^5} \exp \left[-2 \int_{s=0}^{s=R} \beta_{ext}(s) ds \right] \int_{D_{min}}^{D_{max}} N(D, R) \sigma_{bk}(D, R) dD \quad (7.1)$$

where R is the range, s is the position along the path of the beam, $\sigma_{bk}(D, R)$ is the backscatter cross-section for particle size D at range R , $N(D, R)$ is the size distribution at range R , Λ is the radar wavelength, $\|K_w\|^2$ is the dielectric factor for water, and $\beta_{ext}(s)$ is the volume extinction coefficient along the path of the radar beam. The exponential term is the two-way transmission between the radar and the observed radar volume at range R and represents losses in the transmitted and reflected power due to scattering and absorption along the path to the target.

The volume extinction coefficient includes contributions due to scattering and absorption by hydrometeors and due to absorption by gases, and is given by

$$\beta_{ext}(s) = \int_{D_{min}}^{D_{max}} N(D, s) \sigma_{ext}(D, s) dD + \sum_i k_{abs,i}(s) \rho_i(s) \quad (7.2)$$

where $N(D, s)$ is the hydrometeor size distribution at position s , $\sigma_{ext}(D, s)$ is the hydrometeor extinction cross-section, $k_{abs,i}(s)$ is the mass absorption coefficient for gas species i , and $\rho_i(s)$ is the corresponding gas density. At 94 GHz, gaseous attenuation is predominantly due to water vapor; the two-way attenuation by water vapor in tropical atmospheres can approach 5 dB (Stephens et al., 2002). The 2B-GEOPROF product provides estimates of the two-way gaseous attenuation, and the snowfall retrieval algorithm uses these estimates to correct the 2B-GEOPROF reflectivities before a retrieval is performed.

Attenuation by frozen hydrometeors may also be substantial. In a study that used simulated vertical profiles containing dry snow and thick ice clouds to model CloudSat observations, Matrosov and Battaglia (2009) found the two-way attenuation could reach from 2 to 5 dB for snowfall rates ranging from 5 to 16 mm LWE h^{-1} . Under these heavier snow conditions, however, they showed multiple scattering will also be non-negligible for CloudSat's viewing geometry. In the simulated profiles they examined, multiple scattering was found to enhance reflectivities by 3-6 dBZ, partially offsetting the effects of attenuation by hydrometeors. The enhancement by multiple scattering in these simulated profiles was found to be similar to enhancements estimated experimentally for thick ice anvils by Bouniol et al. (2008). This compensating behavior in heavy snow caused the multiply-scattered attenuated reflectivity to lie between the singly-scattered nonattenuated and singly-scattered attenuated reflectivities (Figure 7.1). For light snow, with reflectivities less than about 10 dBZe, Matrosov and Battaglia (2009) found attenuation and multiple scattering to be insignificant.

The results of Matrosov and Battaglia show that both the singly-scattered attenuated and nonattenuated reflectivities are biased estimates of the multiply-scattered attenuated reflectivity. Absent an explicit multiple scattering model for heavy snow, the multiply-scattered attenuated reflectivity may be approximated using the singly-scattered attenuated and nonattenuated reflectivities as bounding values. Additionally, the uncertainties for this approximation can be estimated from the difference in the singly-scattered attenuated and nonattenuated reflectivities.

Liquid hydrometeors also produce attenuation. While the CloudSat snowfall retrieval will not be applied to profiles thought to contain liquid cloud and rain, supercooled liquid water may also attenuate the radar beam. A single-wavelength, nadir-pointing radar such as the CPR lacks means for identifying the presence of supercooled water. While a number of techniques have been proposed for detecting supercooled water (using differential radar reflectivity (Hogan et al., 2002), Doppler spectra (Zawadzki et al., 2001), and dual frequency radar observations (Gosset and Sauvageot, 1992)), none of these can be utilized with CPR observations. Some potential exists for the application of combined radar-lidar techniques (Hogan et al., 2003) given the availability of colocated observations from the CPR and from

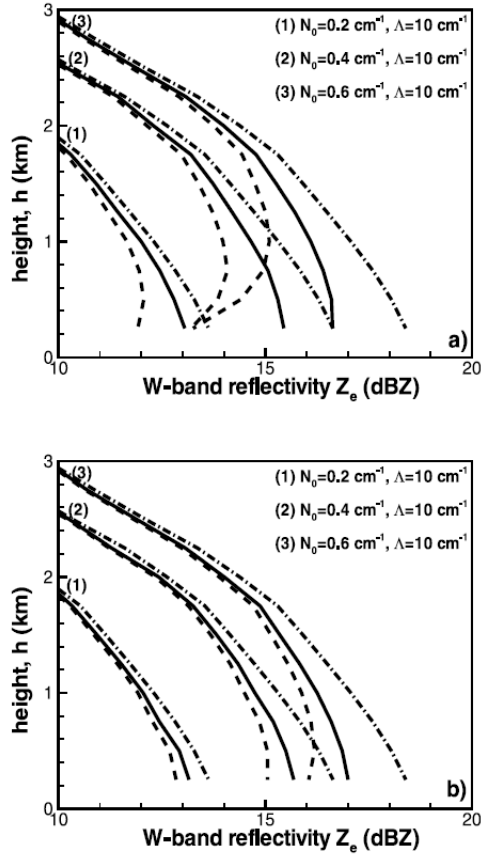


Figure 7.1: Evaluation of 94 GHz attenuation and multiple scattering effects for various snowfall profiles as modeled by Matrosov and Battaglia (2009) using soft ice sphere phase functions (upper panel) and solid ice sphere phase functions (lower panel). Lines represent single scattering with no attenuation (dot-dash), single scattering with attenuation (dash), and multiple scattering with attenuation (solid). Curve sets (1), (2), and (3) represent different snowfall characteristics as indicated by values for N_0 and λ . Figure copyright American Geophysical Union, 2009, used in accordance with AGU Terms of Use, <http://www.agu.org/pubs/authors/tou.shtml>.

the Cloud-Aerosol Lidar with Orthogonal Polarization (CALIOP) instrument on board the Cloud-Aerosol Lidar and Infrared Pathfinder Satellite Observation (CALIPSO) satellite (Winker et al., 2007). Future developments may allow for treatment of attenuation by supercooled liquid water in the retrieval; for this work, this attenuation is omitted.

7.2.1.1 Size distribution

The particle size distribution enters the forward model through the calculation of reflectivity and, when attenuation by hydrometeors is considered, through the calculation of β_{ext} . Distributions of snow particle sizes are frequently characterized as exponential

$$N(D) = N_0 \exp(-\lambda D) \tag{7.3}$$

where λ is the slope of the distribution and N_0 its intercept. D may be either the melted drop diameter or an actual dimension of the particle. The inverse of λ is a measure of the characteristic particle size of the distribution. Small values of λ indicate that the characteristic particle size of the distribution is large. When particles are spherical and D extends from zero to infinity, $\frac{1}{\lambda}$ is proportional to the median volume diameter of the distribution (Sekhon and Srivastava, 1970). Aircraft observations, typically made with optical array probes, provide size distributions based on actual particle dimensions rather than melted diameter. Exponential behavior, especially at larger particle sizes, has been confirmed in aircraft-based in situ observations under a wide range of atmospheric conditions (Braham, 1990; Passarelli, 1978; Lo and Passarelli, 1982; Gordon and Marwitz, 1984; Houze et al., 1979; Woods et al., 2008). For observations at the surface, estimates of size distributions based on actual particle dimensional have been far less common. Rogers (1973) used photographs of snowflakes to develop estimates of snow size distributions based on actual dimensions. Rogers also found snow size distributions to be exponential. For the Cloud-Sat snowfall retrieval, an exponential form is used in which D is the maximum particle dimension, D_M .

A number of studies based on aircraft observations have noted departures from exponential behavior. These departures often take forms in which concentrations of small particles

are enhanced or suppressed compared to an exponential fitted to the large-particle portion of the spectrum. Herzegh and Hobbs (1985) labeled these forms “super-exponential” and “sub-exponential”, respectively. Processes such as aggregation, fragmentation, riming-splintering and size-sorting, among others, all act to shape the size distribution and likely account for these departures to varying degrees. Other factors related to instrument performance, such as reduced sensitivity to small particles (Gordon and Marwitz, 1984) or particle shattering at instrument inlets (Field et al., 2006) may also affect the observed concentrations of small particles.

Brandes et al. (2007) evaluated both exponential and gamma forms for snow size distributions observed by a 2D video disdrometer over the course of several winter seasons. Gamma distributions have the capability to represent sub- or super-exponential behavior. Although about 22% of the observed snow distributions exhibited super-exponential features, more commonly the fitted gamma distributions were nearly equivalent to exponential distributions, with the mode of the distribution of fitted shape parameters being near a value of one. Heymsfield et al. (2008) examined the adequacy of exponential distributions for snow, looking at the ability of a fitted exponential distribution to reproduce ice water contents and Rayleigh reflectivities calculated directly from the binned particle size distributions. They found that parameters derived from higher moments of the particle size distribution, which are more directly related to ice water content and radar reflectivity, produced exponential distributions which generally provided good agreement with IWC and Ze values calculated from the observed, binned size distributions. Given these results, the exponential form appears a reasonable choice. Uncertainties associated with the use of the exponential distribution will be considered in the assessment of forward model uncertainties (Section 7.3.4).

7.2.2 Retrieval implementation

The CloudSat retrieval uses the optimal estimation technique previously described in Section 3.1. Observational constraints for this retrieval are provided by the vertical profile of

reflectivities observed by CloudSat and corrected for gaseous attenuation,

$$\mathbf{y} = \begin{bmatrix} Ze_1 \\ \vdots \\ Ze_N \end{bmatrix} \quad (7.4)$$

where N is the number of radar range bins containing snow. Because of the large range of Ze , the values used for the retrieval are in decibels.

The state at each radar bin is described by the exponential size distribution parameters N_0 and λ . Values for N_0 may range over several orders of magnitude, so $\log(N_0)$ was retrieved instead. The variability of λ is significantly smaller than that of N_0 ; however, examination of the fitted exponential distributions from C3VP snow events, used earlier for evaluating discretization and truncation errors, showed that the distribution of values for λ was strongly non-Gaussian (Figure 7.2). The log-transformed values are much less skewed, and accordingly, $\log(\lambda)$ was retrieved instead. The corresponding state vector to be retrieved is then

$$\mathbf{x} = \begin{bmatrix} \log(N_0)_1 \\ \vdots \\ \log(N_0)_N \\ \log(\lambda)_1 \\ \vdots \\ \log(\lambda)_N \end{bmatrix}. \quad (7.5)$$

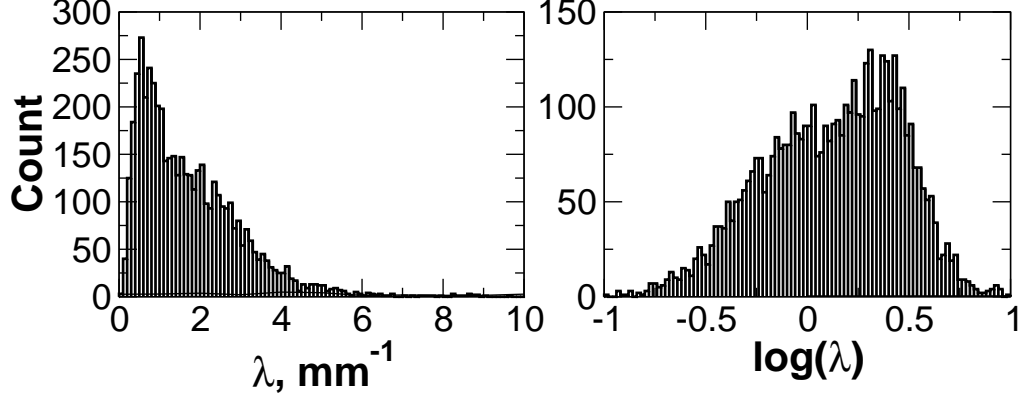


Figure 7.2: Distributions of λ and $\log(\lambda)$ obtained from fits to the SVI-observed size distributions on D_M for snow events from C3VP.

and the associated covariance matrix is

$$\mathbf{S}_x = \begin{bmatrix}
 s^2(\log(N_0)_1) & \dots & \dots & s(\log(N_0)_1, \log(\lambda)_N) \\
 \vdots & \ddots & \vdots & \vdots \\
 \vdots & s^2(\log(N_0)_N) & \vdots & \vdots \\
 \vdots & \vdots & s^2(\log(\lambda)_1) & \vdots \\
 \vdots & \vdots & \vdots & \ddots \\
 s(\log(N_0)_1, \log(\lambda)_N) & \dots & \dots & s^2(\log(\lambda)_N)
 \end{bmatrix}. \quad (7.6)$$

Following the reasoning described in the discussion of multiple scattering and attenuation, both the singly-scattered attenuated and nonattenuated reflectivities are modeled. Applying the exponential distribution with (6.10), the singly-scattered nonattenuated reflectivity $Z e^{ss,na}$ at range bin i is

$$Z e^{ss,na} \left(N_{0,i}; \lambda_i; \tilde{\mathbf{b}}_i \right) = \frac{\Lambda^4}{\|K_w\|^2 \pi^5} \int_{D_{M,min}}^{D_{M,max}} N_{0,i} \exp(-\lambda_i D_M) \sigma_{bk}(D_M, \tilde{\mathbf{b}}_i) dD_M. \quad (7.7)$$

The backscatter cross-section σ_{bk} has been written to show its dependence on a vector of parameters $\tilde{\mathbf{b}}_i$ as well as on D_M . The vector $\tilde{\mathbf{b}}_i$ includes the parameters for the mass- and area-dimension relations α , β , γ , and σ which were used to construct the particle models from which the scattering properties were calculated. The tilde indicates that these parameters are approximations of the true values. Following (7.1) and (7.2), the singly-scattered attenuated reflectivity $Ze^{ss,a}$ is

$$Ze^{ss,a} \left(N_{0,i}; \lambda_i; \tilde{\mathbf{b}}_i; R_i \right) = Ze^{ss,na} \left(N_{0,i}; \lambda_i; \tilde{\mathbf{b}}_i \right) (\mathcal{T}(R_{0,i}))^2 \quad (7.8)$$

where $R_{0,i}$ is the range to bin i and \mathcal{T} is the one-way transmission to the radar bin:

$$\mathcal{T}(R_{0,i}) = \mathcal{T}_{0,i} = \exp \left[- \int_{s=0}^{s=R_{0,i}} \beta_{ext}(s) ds \right]. \quad (7.9)$$

Since reflectivities have been corrected for gaseous attenuation, the volume extinction coefficient β_{ext} is

$$\beta_{ext}(s) = \int_{D_{M,min}}^{D_{M,max}} N_0(s) \exp(-\lambda(s)D_M) \sigma_{ext}(D_M, \tilde{\mathbf{b}}(s)) dD_M. \quad (7.10)$$

The dependence of \mathcal{T} on the vertical profile of N_0 and λ has been omitted from the notation for clarity.

The results of Matrosov and Battaglia (2009) shown in Figure 7.1 suggest that the multiply-scattered attenuated reflectivity $Ze^{ma,a}$ falls approximately midway between $Ze^{ss,a}$ and $Ze^{ss,na}$ in decibel units. Accordingly $Ze^{ms,a}$ at radar bin i is approximated as the geometric mean of the two singly-scattered reflectivities in linear units,

$$\begin{aligned} Ze_i^{ms,a} &\approx [Ze_i^{ss,na} Ze_i^{ss,a}]^{1/2} \\ &\approx Ze_i^{ss,na} \mathcal{T}_{0,i}. \end{aligned} \quad (7.11)$$

The vector \mathbf{F} of forward modeled reflectivities is then

$$\mathbf{F} = \begin{bmatrix} dBZe_1^{ms,a} \\ \vdots \\ dBZe_N^{ms,a} \end{bmatrix} = \begin{bmatrix} Ze_1^{ss,na}\mathcal{T}_{0,1} \\ \vdots \\ Ze_N^{ss,na}\mathcal{T}_{0,N} \end{bmatrix} \quad (7.12)$$

or, in decibel units,

$$\mathbf{F} = \begin{bmatrix} dBZe_1^{ss,na} + dB\mathcal{T}_{0,1} \\ \vdots \\ dBZe_N^{ss,na} + dB\mathcal{T}_{0,N} \end{bmatrix} \quad (7.13)$$

where $dB\mathcal{T}_{0,i} = 10 \log(\mathcal{T}_{0,i})$. This approach amounts to an estimated bias correction applied to the singly-scattered nonattenuated reflectivities $dBZe_i^{ss,na}$.

Uncertainties in the forward modeled reflectivities \mathbf{F} arise due to the approximate nature of (7.11) and due to uncertainties in the terms from which is calculated. These uncertainties, along with the uncertainties in the observed reflectivities, are evaluated in the following section.

7.3 Measurement and forward model uncertainties \mathbf{S}_ϵ

The error covariance matrix \mathbf{S}_ϵ describes the uncertainties associated with model-measurement differences for the CloudSat retrieval and is composed of two terms:

$$\mathbf{S}_\epsilon = \mathbf{S}_y + \mathbf{S}_F \quad (7.14)$$

where \mathbf{S}_y is the covariance matrix describing the measurement uncertainties and \mathbf{S}_F is the forward model error covariance matrix. Following the definition of the observation vector

(7.4), the form of \mathbf{S}_ϵ is

$$\mathbf{S}_\epsilon = \begin{bmatrix} s^2(Ze_1) & \cdots & s(Ze_1, Ze_N) \\ \vdots & \ddots & \vdots \\ s(Ze_N, Ze_1) & \cdots & s^2(Ze_N) \end{bmatrix} \quad (7.15)$$

where $s^2()$ are the reflectivity variances at each range bin and $s()$ are covariances between reflectivities at different bins.

7.3.1 Measurement uncertainties \mathbf{S}_y

Uncertainties in the CloudSat observed reflectivities arise from causes related to the CPR and to the assumptions about the observations. A primary assumption is that each radar range bin is filled with the scatterers of interest. In regards to estimates of snowfall, this assumption may fail at the edges of precipitation columns, for example. An evaluation of errors due to partial beam filling and the development of techniques to identify affected observations is beyond the scope of this work and such errors are omitted. Remaining sources of uncertainty include uncertainty in the absolute radiometric calibration and measurement noise. Calibration errors, which would result in a bias in the measured reflectivities, are expected to be less than 2 dB based on a prelaunch calibration error budget (Tanelli et al., 2008), but the value of this bias is unknown. The noise characteristics of the CPR vary with signal strength. For reflectivities above -10 dBZ, one standard deviation of noise as a fraction of the mean signal is about -16 dB, while for reflectivities below -10 dBZ, noise is an increasing fraction of the signal, reaching 0 dB at the minimum detectable signal of -30 dBZ (R. Austin, personal communication, 4 November, 2008). The resulting uncertainties range from 3 dBZ for a reflectivity of -30 dBZ to about 0.1 dBZ for reflectivities above -10 dBZe. (Figure 7.3). To construct \mathbf{S}_y , variances for each range bin are computed as the squares of these uncertainties and uncertainties in distinct range bins are considered to be uncorrelated, resulting in a diagonal form for \mathbf{S}_y .

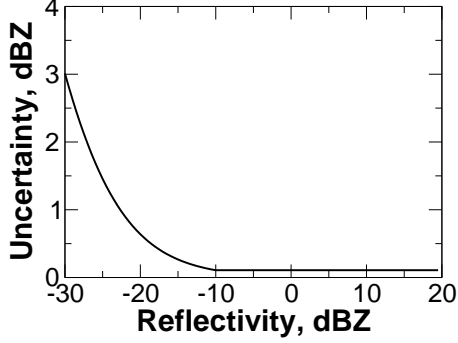


Figure 7.3: Upward uncertainties ($Ze + \delta Ze$) based on one standard deviation of noise for the CloudSat CPR.

7.3.2 Forward model uncertainties \mathbf{S}_F

The forward modeled reflectivities \mathbf{F} given by (7.12) have uncertainties due to two sources: first, the approximate nature of the transmission-based bias correction for multiple scattering and attenuation given in (7.11); and second, the uncertainties in the singly-scattered nonattenuated reflectivities $Ze_i^{ss,na}$. Assuming the errors from each of these two sources are uncorrelated, \mathbf{S}_F can be written as the sum of two covariance matrices:

$$\mathbf{S}_F = \mathbf{S}_{F1} + \mathbf{S}_{F2}, \quad (7.16)$$

where \mathbf{S}_{F1} is the covariance due to the approximate bias correction and \mathbf{S}_{F2} is the covariance due to uncertainties in $Ze_i^{ss,na}$. An explicit evaluation of \mathbf{S}_{F1} would require explicit modeling of radiative transfer with multiple scattering for a range of snowfall scenes (e.g., Matrosov and Battaglia, 2009). Lacking this, the values of $Ze^{ss,na}$ and $Ze^{ss,a}$ place upper and lower bounds on the expected value of $Ze^{ms,a}$ and can be used to make a rudimentary estimate of this uncertainty. In the results from Matrosov and Battaglia (2009) shown in Figure 7.1, $Ze^{ms,a}$ for soft ice sphere phase functions falls slightly above the midpoint of the interval, while $Ze^{ms,a}$ for solid ice sphere phase functions falls slightly below the midpoint. The estimate used here is that the uncertainty in $Ze^{ms,a}$ is one-half the difference between

$Ze^{ms,a}$ and $Ze^{ss,na}$ in decibel units. The resulting estimate of the variance is then

$$\begin{aligned} s^2(dBZe_i^{ms,a}) &= \left[\frac{1}{2} (dBZe_i^{ss,na} - dBZe_i^{ms,a}) \right]^2 \\ &= \left[\frac{1}{2} dB\mathcal{T}_{0,i} \right]^2 \end{aligned} \quad (7.17)$$

where the expressions from (7.13) have been used. This simple approach is not sufficient to diagnose vertical correlations in these uncertainties, so covariances between radar bins are set to zero, and $\mathbf{S}_{F,1}$ is

$$\mathbf{S}_{F1} = \begin{bmatrix} \left[\frac{1}{2} dB\mathcal{T}_{0,1} \right]^2 & & & 0 \\ & \ddots & & \\ & & & \\ 0 & & & \left[\frac{1}{2} dB\mathcal{T}_{0,N} \right]^2 \end{bmatrix}. \quad (7.18)$$

The covariance matrix \mathbf{S}_{F2} contains contributions from uncertainties in $dBZe_i^{ss,na}$. Two distinct sources contribute to these uncertainties,

$$\mathbf{S}_{F2} = \mathbf{S}_B^{ss,na} + \mathbf{S}_F^{ss,na} \quad (7.19)$$

where $\mathbf{S}_B^{ss,na}$ is the covariance matrix describing uncertainties due to the forward model parameters $\tilde{\mathbf{b}}$ and $\mathbf{S}_F^{ss,na}$ is the covariance matrix describing uncertainties due to other assumptions in the calculation of $Ze^{ss,na}$. These two matrices are evaluated in the following sections. Note that per (7.7) the vector $\tilde{\mathbf{b}}$ includes the microphysical parameters α , β , γ , and σ used to construct the particle models and calculate scattering properties. Uncertainties in these properties contribute to uncertainties in σ_{bk} , which in turn produce uncertainties in $Ze^{ss,na}$. These uncertainties are quantified in $\mathbf{S}_B^{ss,na}$. For the CloudSat retrieval, only the uncertainties in the singly-scattered nonattenuated reflectivities $Ze^{ss,na}$ are required. As part of this development, however, contributions to uncertainties in attenuation are also discussed.

7.3.3 Uncertainties due to parameters, $\mathbf{S}_B^{ss,na}$

The full forward model equation (7.7) for the singly-scattered nonattenuated reflectivity shows explicitly that the modeled reflectivity is dependent on the microphysical parameters α , β , γ , and σ used to construct the particle models. The covariance matrix $\mathbf{S}_B^{ss,na}$ quantifies the uncertainties in radar reflectivity due to the uncertainties in those parameters and is calculated as

$$\mathbf{S}_B^{ss,na} = \mathbf{K}_b \mathbf{S}_b \mathbf{K}_b^T \quad (7.20)$$

where \mathbf{K}_b is the Jacobian of the forward model reflectivities with respect to the parameters $\tilde{\mathbf{b}}$ and \mathbf{S}_b is the covariance matrix for the parameters. The general form of \mathbf{S}_b is

$$\mathbf{S}_b = \begin{bmatrix} \mathbf{S}_{b,1,1} & \cdots & \mathbf{S}_{b,1,N} \\ \vdots & \ddots & \vdots \\ \mathbf{S}_{b,i,1} & \mathbf{S}_{b,i,i} & \mathbf{S}_{b,i,N} \\ \vdots & & \vdots \\ \mathbf{S}_{b,N,1} & \cdots & \mathbf{S}_{b,N,N} \end{bmatrix}. \quad (7.21)$$

where the submatrices $\mathbf{S}_{b,i,j}$ are covariance matrices given by

$$\mathbf{S}_{b,i,j} = \begin{bmatrix} s(\ln(\alpha_i), \ln(\alpha_j)) & s(\ln(\alpha_i), \beta_j) & s(\ln(\alpha_i), \ln(\gamma_j)) & s(\ln(\alpha_i), \sigma_j) \\ s(\ln(\alpha_i), \beta_j) & s(\beta_i, \beta_j) & s(\beta_i, \ln(\gamma_j)) & s(\beta_i, \sigma_j) \\ s(\ln(\alpha_i), \ln(\gamma_j)) & s(\beta_i, \ln(\gamma_j)) & s(\ln(\gamma_i), \ln(\gamma_j)) & s(\ln(\gamma_i), \sigma_j) \\ s(\ln(\alpha_i), \sigma_j) & s(\beta_i, \sigma_j) & s(\ln(\gamma_i), \sigma_j) & s(\sigma_i, \sigma_j) \end{bmatrix} \quad (7.22)$$

and it is recognized that for $i = j$, the diagonal elements reduce to the variances $s^2(\ln(\alpha_i))$, $s^2(\beta_i)$, etc. Values for $\mathbf{S}_{b,i,i}$ are set to values provided by the results of the snow microphysics

retrieval and do not vary vertically:

$$\mathbf{S}_{b,i,i} = \begin{bmatrix} 0.592 & 0.212 & 0.090 & 0.023 \\ 0.212 & 0.142 & 0.011 & 0.007 \\ 0.090 & 0.011 & 0.335 & 0.103 \\ 0.028 & 0.007 & 0.103 & 0.046 \end{bmatrix}. \quad (7.23)$$

For $i \neq j$, $\mathbf{S}_{b,i,j}$ is the matrix describing the covariances between parameters at distinct range bins i and j . To determine values for $\mathbf{S}_{b,i,j}$, it is reasonable to assume some degree of vertical correlation for the errors in these parameters, and that these correlations decay over some vertical scale height, h . Modeling the decay in correlations as an exponential, the covariance between two parameters at different range bins, $s(\beta_i, \sigma_j)$ for example, can be estimated as

$$\begin{aligned} s(\beta_i, \sigma_j) &= \rho_{corr}(\beta_i, \sigma_j) (s^2(\beta_i) s^2(\sigma_j))^{1/2} \\ &= \rho_{corr}(\beta_i, \sigma_i) \exp(-\delta h_{i,j}/h) (s^2(\beta_i) s^2(\sigma_j))^{1/2} \end{aligned} \quad (7.24)$$

where $\delta h_{i,j}$ is the vertical distance between range bins i and j and ρ_{corr} is the correlation. At present, an analysis to determine h has not been performed and h is set to the dimension of a single range bin.

The required form for \mathbf{K}_b is then

$$\mathbf{K}_b = \begin{bmatrix} \mathbf{K}_{b,1,1} & \cdots & \mathbf{K}_{b,1,N} \\ \vdots & \ddots & \vdots \\ \mathbf{K}_{b,N,1} & \cdots & \mathbf{K}_{b,N,N} \end{bmatrix} \quad (7.25)$$

where the submatrices $\mathbf{K}_{b,i,j}$ are the Jacobians of the forward modeled reflectivity for range bin i with respect to the parameters at range bin j :

$$\mathbf{K}_{b,i,j} = \begin{bmatrix} \frac{\partial Z e_i}{\partial(\ln(\alpha_j))} & \frac{\partial Z e_i}{\partial(\beta_j)} & \frac{\partial Z e_i}{\partial(\ln(\gamma_j))} & \frac{\partial Z e_i}{\partial(\sigma_j)} \end{bmatrix}. \quad (7.26)$$

When $i = j$, $\mathbf{K}_{b,i,i}$ is the Jacobian of the forward modeled reflectivity at range bin i with respect to the local parameters:

$$\mathbf{K}_{b,i,i} = \begin{bmatrix} \frac{\partial Z e_i}{\partial(\ln(\alpha_i))} & \frac{\partial Z e_i}{\partial(\beta_i)} & \frac{\partial Z e_i}{\partial(\ln(\gamma_i))} & \frac{\partial Z e_i}{\partial(\sigma_i)} \end{bmatrix}. \quad (7.27)$$

In the case of a single scattering forward model with no attenuation, the forward modeled reflectivities are sensitive only to the local scattering properties as determined by the local parameters. In that case, the submatrices $\mathbf{K}_{b,i,j}$ are zero for $i \neq j$, and \mathbf{K}_b is block diagonal. In the general case of a forward model with attenuation and/or multiple scattering, the reflectivity for a particular range bin will also be sensitive to the scattering properties along the path between the bin and the radar. In that case, the submatrices $\mathbf{K}_{b,i,j}$ for which $i \geq j$ will be nonzero. Regardless of the type of forward model, reflectivities will not be sensitive to the scattering properties in bins further from the radar, thus $\mathbf{K}_{b,i,j} = 0$ for $i < j$. As a result, for models with multiple scattering or attenuation, \mathbf{K}_b will have lower triangular block form.

7.3.3.1 Estimating \mathbf{K}_b

Because analytic expressions are not available that relate the scattering properties to the microphysical parameters, the derivatives that appear in $\mathbf{K}_{b,i,j}$ must be evaluated numerically, for example,

$$\frac{\partial Z e_i}{\partial(b_j)} \approx \frac{Z e_i(b_j + \delta b_j) - Z e_i(b_j)}{\delta b_j}, \quad (7.28)$$

where b_j is the unperturbed value of an element of the microphysical parameter vector $\tilde{\mathbf{b}}$ and δb_j is the perturbation. These evaluations must be performed repeatedly as the retrieval iterates, as they are dependent on the current estimate of the state. Single sided differences

are considered sufficiently accurate to estimate these contributions to the forward model uncertainty, and reduce execution time compared to double sided differences.

Calculating the perturbed radar reflectivity, $Ze_i(b_j + \delta b_j)$ in the example above, requires the perturbed scattering properties, i.e., scattering properties for particle models constructed using the perturbed microphysical parameters. The perturbations to a parameter should be small, but large enough that the resulting difference in Ze is distinguishable from the uncertainty in Ze . If f_{Ze} is the fractional uncertainty in Ze , a reasonable approach (Dennis and Schnabel, 1983) is to take

$$\delta b_j = \sqrt{f_{Ze} b_j}. \quad (7.29)$$

Normally f_{Ze} would be determined by the precision of the calculation of Ze ; however, the use of random dipole locations for the DDA calculations of the scattering properties introduces additional uncertainties. From the tests on these uncertainties (Section 6.4.3), the fractional uncertainty for Ze in linear units is typically less than 0.02, suggesting that $\delta b_j \approx 0.15b_j$.

Perturbations of 15% were applied to each of the microphysical parameters, then DDA particle models were constructed and scattering properties calculated. The perturbed scattering properties were then compared to the uncertainties in those properties due to the random dipole locations. In the upper panels of Figures 7.4 and 7.5, ratios larger than 1 indicate the perturbations to the scattering property exceed the uncertainties for that property. Ratios exceed 1 for most of the particle sizes. At small sizes, the ratios are greatly in excess of 1, in response to the small uncertainties. For these small sizes, the scattering properties are in the Rayleigh regime and are largely insensitive to the random dipole locations. At larger sizes, the ratios are mostly on the order of 1 to 10, with ratios for a few sizes falling slightly below 1. The results suggest that the perturbed scattering properties are adequate for calculating the numerical derivatives needed for \mathbf{K}_b .

The derivatives for reflectivity and specific attenuation were evaluated using the size distributions from the SVI dataset. Reflectivity increases with increasing α but decreases with increasing β (Figure 7.6, upper panels). Increasing α causes mass to increase over the

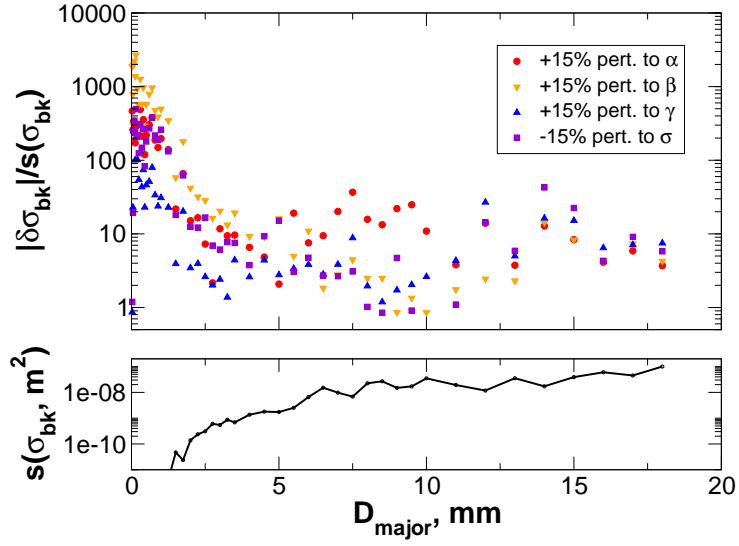


Figure 7.4: Magnitude of perturbations in σ_{bk} compared to uncertainties in σ_{bk} due to random dipole locations for the B8pr-30 shape. The lower panel shows the standard deviation of the unperturbed σ_{bk} versus particle size. In the upper panel, $|\delta\sigma_{bk}| = |\sigma'_{bk} - \sigma_{bk}|$ where σ'_{bk} is calculated using the perturbed values of α, β, γ , or σ .

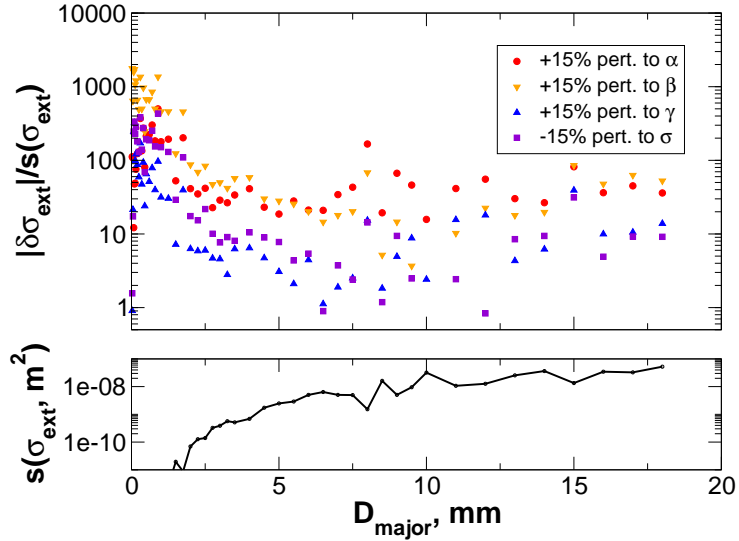


Figure 7.5: Magnitude of perturbations in σ_{ext} compared to uncertainties in σ_{ext} due to random dipole locations for the B8pr-30 shape. Lower and upper panels are otherwise as described for Figure 7.4.

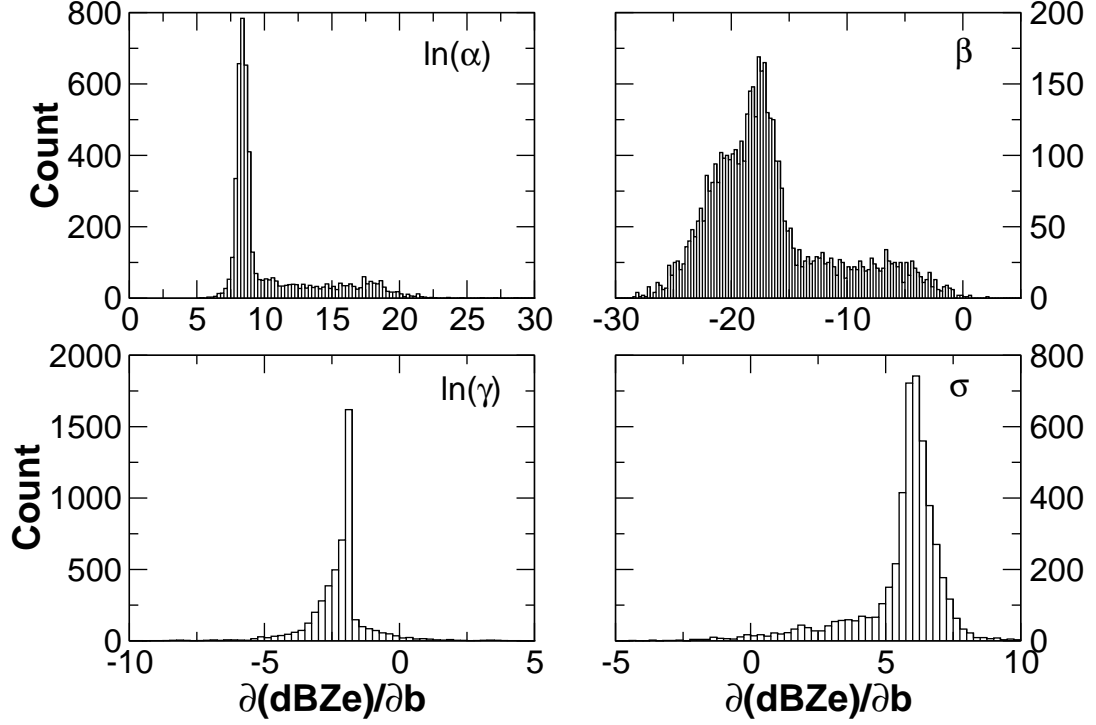


Figure 7.6: Derivatives of reflectivity with respect to the microphysical parameters α , β , γ , and σ used to construct the particle models. Derivatives for α and γ are taken with respect to the natural logarithms of these parameters.

entire size distribution, while increasing β causes masses to decrease for $D_M < 1$ cm and increase for $D_M > 1$ cm,

$$\frac{\partial m}{\partial \beta} = \frac{\partial}{\partial \beta} \alpha D_M^\beta = \alpha D_M^\beta \ln(D_M). \quad (7.30)$$

Negative values for $\frac{\partial dBZe}{\partial \beta}$ indicate that the reflectivities are dominated by contributions from particles smaller than 1 cm. Conversely, reflectivity decreases with increasing γ but increases with increasing σ (Figure 7.6, lower panels). Increasing γ causes horizontally projected areas A_p to increase over the entire size distribution, while increasing σ causes A_p to decrease for $D_M < 1$ cm and increase for $D_M > 1$ cm, parallel to the behavior for β . For a given mass and shape, increasing A_p produces a less compact particle, which tends to decrease reflectivity.

Specific attenuation behaves similarly to reflectivity. Specific attenuation increases with increasing α but decreases with increasing β (Figure 7.7, upper panels), responding to changes in mass in the same manner as reflectivity. Specific attenuation decreases with

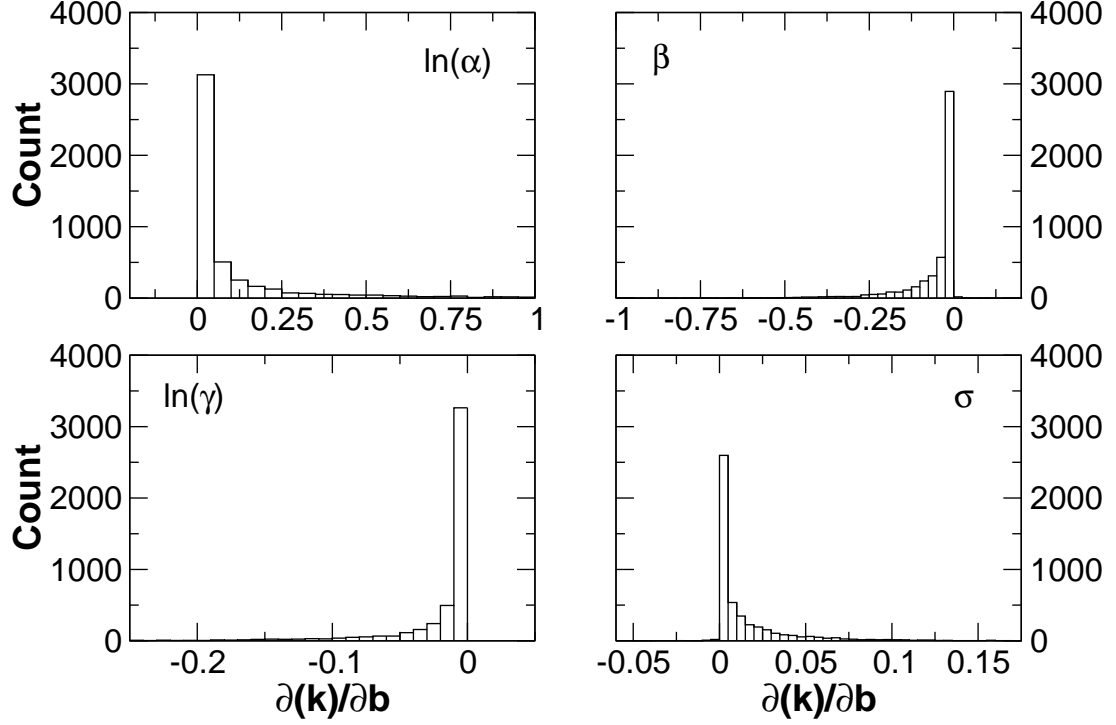


Figure 7.7: Derivatives of specific attenuation with respect to the microphysical parameters α , β , γ , and σ used to construct the particle models. Derivatives for α and γ are taken with respect to the natural logarithms of these parameters. Specific attenuation, k , is in dB km^{-1} .

increasing γ but increases with increasing σ (Figure 7.6, lower panels), responding to changes in A_p again in a manner consistent with the response of reflectivity to changes in A_p .

It would be useful to know how significantly the uncertainties in individual parameters α , β , γ , and σ contribute to uncertainties in the reflectivity and specific attenuation. In the formal evaluation of $S_B^{ss,na}$ via (7.20), however, the contribution due to uncertainty in a single parameter can not be isolated because of the presence of covariances between the parameters. In an approximate sense, estimates of these contributions can be obtained from the products of the derivatives and the parameter uncertainties (Table 7.1). Uncertainties for the parameters were estimated as the square roots of the variances shown in (7.23) and derivatives were estimated as the simple means of the values shown in Figures 7.6 and 7.7. The results suggest that uncertainties in reflectivity are dominated by contributions from α and β , while uncertainties in specific attenuation are due mainly to uncertainties in α .

Table 7.1: Estimates of the contributions of uncertainties in α , β , γ , and σ to uncertainties in reflectivity and specific attenuation.

Parameter	Reflectivity			Specific Attenuation	
	s(b)	$\frac{\partial dBZe}{\partial b}$	s(dBZe)	$\frac{\partial k}{\partial b}$	s(k)
$\ln(\alpha)$	0.769	10.4	8.00	0.163	0.125
β	0.377	-16.7	6.30	-0.061	0.023
$\ln(\gamma)$	0.579	-2.22	1.29	-0.027	0.016
σ	0.214	5.62	1.20	0.017	0.004

7.3.4 Uncertainties due to other forward model assumptions, $\mathbf{S}_F^{ss,na}$

In addition to the explicit dependence on the microphysical parameters α , β , γ , and σ used to construct the particle models, the forward modeled reflectivity depends on other assumptions described earlier: the choice of particle shape, the random placement of the dipoles in the DDA models, discretization and truncation of the integrations over the size distribution, and the use of the exponential distribution. These dependencies are responsible for additional uncertainties in the forward modeled reflectivities. Uncertainties due to random dipole placement, discretization and truncation were discussed earlier as part of the evaluation of the particle models. The remaining sources, shape and the use of the exponential distribution, are evaluated here.

7.3.4.1 Uncertainties due to shape

Determining the uncertainties due to shape is difficult because, as demonstrated in the assessments of the particle models (Section 6.4), the choice of an unrealistic particle shape can produce similarly unrealistic simulated reflectivities even when the particle model meets other microphysical constraints. The comparisons between observed and simulated reflectivities with various shapes showed that the B8pr-30 particle shape provided reasonable agreement with the observed reflectivities. The differences between the observed and simulated reflectivities for this shape include all error sources in the observations and forward model, including shape, microphysical parameters, and sampling differences between the

ACR and SVI observations used to construct the comparisons. To isolate uncertainties due to shape, it is necessary to compare particles which meet similar microphysical constraints (mass, horizontally projected area, and aspect ratio), but which do so with different, reasonable shapes. The shapes used for these comparisons are the B8pr-45, which has a larger aspect ratio compared to the B8pr-30, and the Ep, which has the same aspect ratio as the B8pr-30 but has a more isotropic distribution of mass. Both of these particles are less compact than the B8pr-30 and produce reflectivities that are biased low compared to the observations (Figure 6.9). Presumably, more compact but reasonable shapes could be constructed (smaller aspect ratio, less isotropic distribution of mass) which would be unbiased or positively biased. For each of these shapes, simulated reflectivities and specific attenuations were calculated using the SVI dataset and differenced from the B8pr-30 simulated reflectivities and specific attenuations. These differences were decomposed into biases and variances. The variances can be considered to represent the differences for particle models similar to the B8pr-45 or Ep shapes but which have been modified to give unbiased reflectivities and specific attenuations compared to the B8pr-30 shape, while the total differences (biases plus variances) represent the differences for the actual B8pr-45 and Ep particle models.

The resulting error estimates are shown in Figures 7.8 and 7.9. Reflectivity errors for the B8pr-45 shape range from near zero to 3 dB. The total reflectivity errors for the Ep shape ranges from 1 dB at low reflectivities to almost 6 dB at large reflectivities, while the error contributions from the variance are generally between 1 and 2 dB. The Ep shape is likely not representative of the larger aggregates typically present in high-reflectivity snowfall events, so the large total errors at reflectivities above 10 dBZe are considered unlikely. Accordingly, the uncertainty in reflectivity due to shape is taken to be a constant value of 2 dBZe. For values of β_{ext} below about 0.00025 m¹, all uncertainties increase approximately linearly with the value of β_{ext} . Above this value, the error contributions due to variance decrease while the total errors continue to increase, indicating the errors are dominated by the bias term. As an intermediate approximation to these results, the fractional uncertainty in β_{ext} is taken to be 0.1.

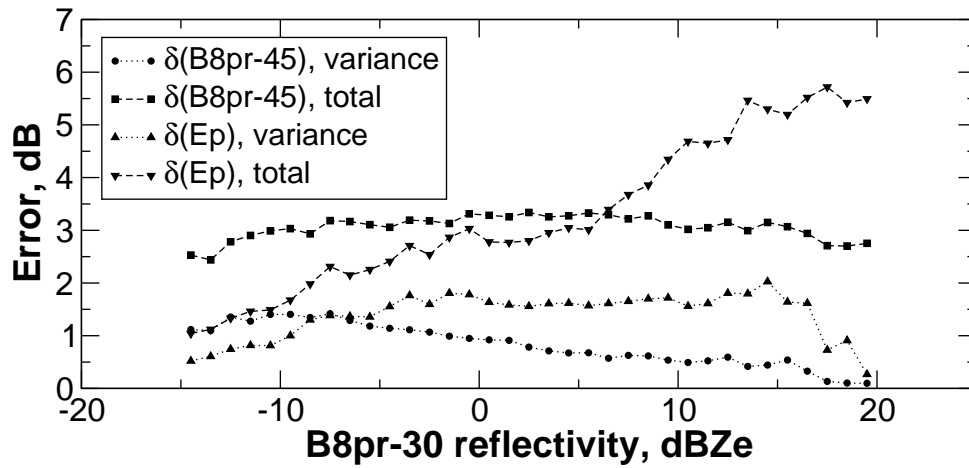


Figure 7.8: Errors in reflectivity for the Ep and B8pr-45 shapes compared to the B8pr-30 shape. Errors are decomposed into variance only and total (bias plus variance).

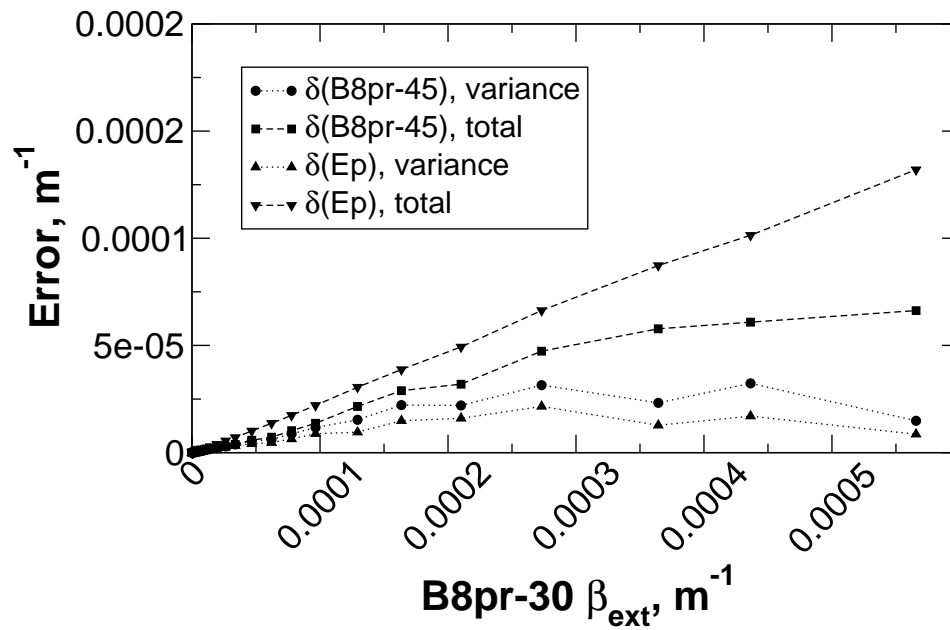


Figure 7.9: Errors in extinction coefficient for the Ep and B8pr-45 shapes compared to the B8pr-30 shape. Errors are decomposed into variance only and total (bias plus variance).

7.3.4.2 Uncertainties due to assumed size distribution form

Departures of the true particle size distribution from the assumed exponential form may also contribute to uncertainties between the forward model and the measurements. To evaluate these uncertainties, reflectivities and specific attenuation were evaluated using the B8pr-30 particle model with two different forms for the size distribution: 1) the observed discrete size distributions in the SVI dataset, and 2) exponential distributions fitted to the discrete SVI distributions. For each discrete SVI distribution, snowfall rate was calculated using the MH2005 model, and the corresponding fitted distribution was adjusted by scaling the intercept parameter N_0 to reproduce the same snowfall rate. Errors due to the assumed exponential distribution are negligible at high reflectivities but increase as reflectivity diminishes (Figure 7.10). A small positive bias is present below 0 dBZe, amounting to about +0.35 dB at -15 dBZe. The bias is negligible, and the total uncertainty is modeled using a fit to a simple decaying exponential for reflectivities larger than -15 dBZe (Figure 7.11):

$$s_F^2(\text{dBZe}) = [\exp(-(\text{dBZe} + 14) / 16)]^2. \quad (7.31)$$

Uncertainties in specific attenuation tend to increase with increasing reflectivity but are largely unbiased and negligible (Figure 7.12).

7.3.4.3 Estimate of $\mathbf{S}_F^{ss,na}$

The remaining contributions to the forward model uncertainties, due to discretization, truncation, and the random locations of the dipoles, were assessed in Section 6.4. The results from those assessments are summarized in Table 7.2, along with the results from the uncertainty assessments in this section. For the CloudSat retrieval, only the uncertainties in the singly-scattered nonattenuated reflectivity $Z e^{ss,na}$ are required. The contributions shown in Table 7.2 are expected to be uncorrelated. As a result, $\mathbf{S}_F^{ss,na}$ is diagonal and contains elements given by

$$S_F^{ss,na}[i, i] = (0.42)^2 + (2.)^2 + [\exp(-(\text{dBZe}_i^{ss,na} + 14) / 16)]^2. \quad (7.32)$$

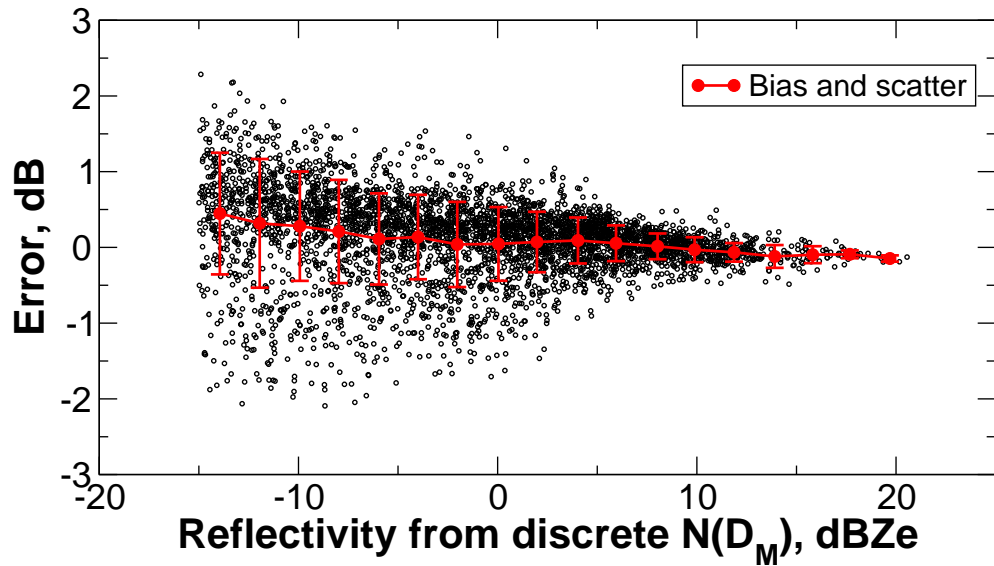


Figure 7.10: Differences between reflectivities calculated using the B8pr-30 with observed SVI size distributions and those calculated from fitted exponential distributions.

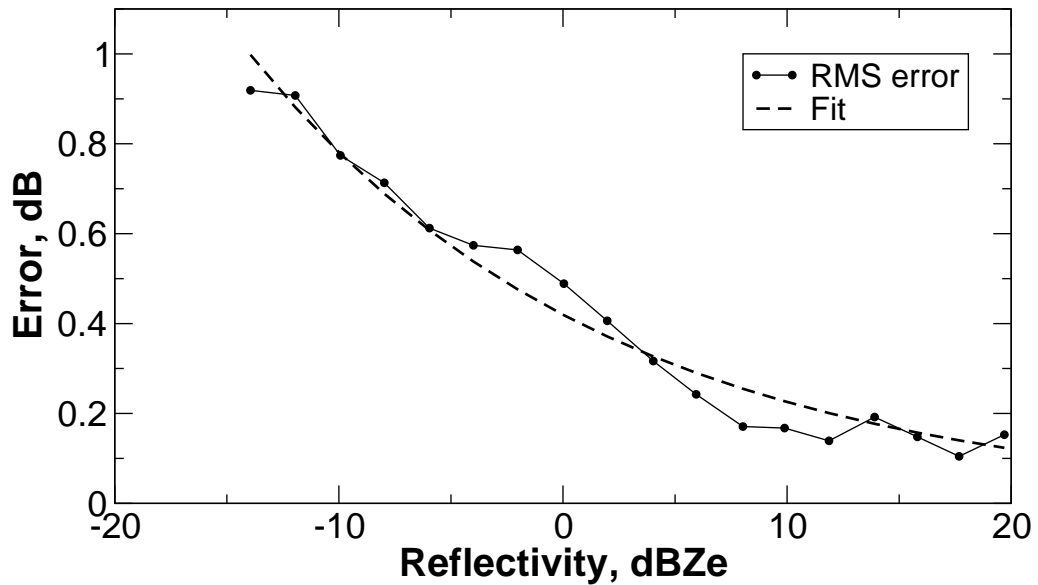


Figure 7.11: Actual RMS errors and the fitted model for the uncertainty due to the assumed exponential size distribution.

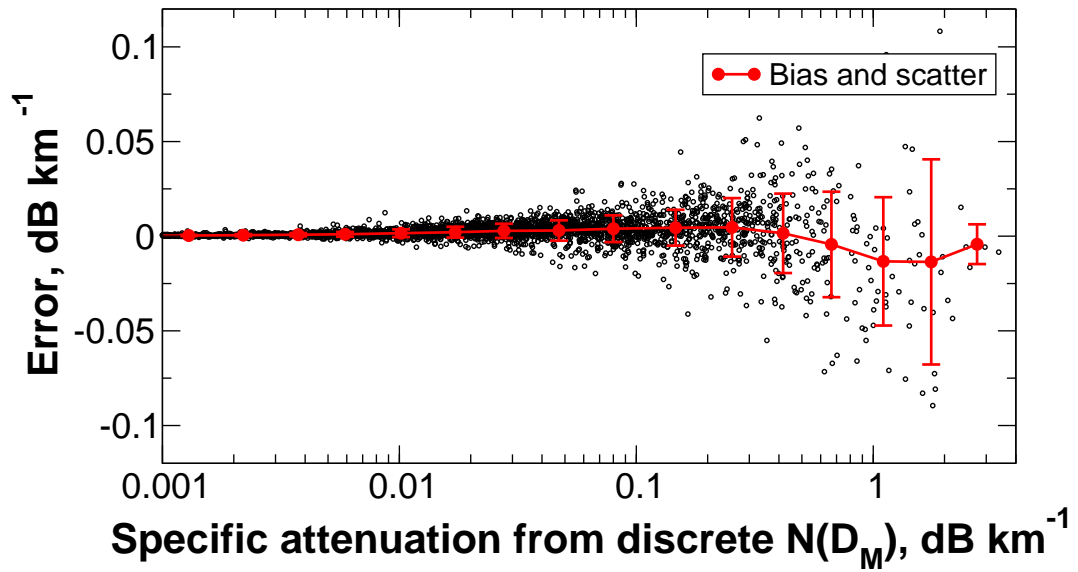


Figure 7.12: As in Figure 7.10 except for specific attenuation.

Table 7.2: Estimates for contributions to uncertainties in reflectivity and attenuation.

Source	Reflectivity, dBZe		β_{ext} , m^{-1}	
	$\overline{\delta_F}$	$s^2()$	$\overline{\delta_F}$	$s^2()$
Discretization	0.	0.	0.	0.
Truncation	0.	$(0.42)^2$	0.	0.
Random dipoles	0.	0.	0.	0.
Shape	0.	$(2.)^2$	0.	$(0.1\beta_{ext})^2$
Exp. dist.	0.	per (7.31)	0.	0.

7.4 Scene characterization

Scene characterization determines whether a retrieval should be performed and, if so, whether the retrieved snowfall reaches the surface without significant melting. Because ground clutter obscures the echos in the radar bins nearest the surface, these two evaluations are done independently.

To determine if a retrieval should be performed, clutter-contaminated range bins are removed from the profile using the 2B-GEOPROF cloud mask. Starting from the base of the profile, if the cloud mask value is less than or equal to the ground-clutter-indicating value of 5, the bin is removed. The lowest remaining bins are examined for significant radar returns, again using the cloud mask. If significant returns are present at the base of the profile, the lowest contiguous layer of significant returns is identified as a hydrometeor layer.

The characteristics of this hydrometeor layer are then evaluated. First the reflectivity profile in the layer is examined to determine if precipitation is present. At this point, the reflectivity profile has been corrected for gaseous attenuation. If the reflectivity at the base of the layer exceeds the precipitation threshold, a search is made for the precipitation echo top. The threshold for identifying precipitation and the precipitation echo top is taken to be -15 dBZe. This threshold is based on the identification of very light liquid precipitation at -10 dBZe in Ka-band radar observations by Stephens and Wood (2007) and the “Rain possible” and “Snow possible” thresholds of Haynes et al. (2009). The contiguous layer between the base and the precipitation echo top is identified as a precipitation layer.

Next, temperatures in the precipitation layer are examined to determine whether the precipitation is frozen, with three possible outcomes:

1. If all temperatures are below 0° C, the precipitation is considered to be snow.
2. If temperatures at the base of the layer are above freezing, but all other temperatures are below freezing, the position of the melting level within the layer is determined. If the melting is shallow, such that the melted mass fraction is expected to be less than 0.1, and occurs only at the base of the precipitation, the precipitation is considered to be snow. Using the results of the melting layer model of Haynes et al. (2009),

the maximum allowed thickness of the melting layer is 240. m. With an assumed environmental lapse rate of $6^\circ \text{ C km}^{-1}$, this approach is equivalent to assuming snow exists at temperatures up to 1.5° C . A similar threshold (2° C) was found by Liu (2008a) based on an analysis of present weather reports from shipboard and land station observations.

3. In all other cases, the precipitation is characterized as not snow.

Retrievals are performed only for the first two outcomes.

Next the surface conditions are characterized. If the 2C-PRECIP-COLUMN product has produced an estimate of the melted mass fraction at the surface, this estimate is used to distinguish rain from snow using a threshold of 0.1. If not, the temperature at the surface, here taken to be the ECMWF-AUX temperature in the radar bin identified as the surface bin in the 2B-GEOPROF product, is examined. If it is below freezing, precipitation at the surface is taken to be snow. If the temperature at the surface is above freezing, the height above the surface of the melting level is determined. As was done for the profile evaluation, if the depth of melting is less than 240. m, the precipitation is considered to be snow. In all other cases, the precipitation is taken to be not snow.

7.5 A priori estimate of the state

The a priori estimate of the state describes the prior knowledge of the joint PDF of the state variables, the vertical profiles of exponential size distribution parameters. In form it consists of a vector of expected values and the corresponding covariance matrix, having the same structure as the state vector \mathbf{x} (7.5) and its covariance matrix \mathbf{S}_x (7.6). The a priori estimate was developed from the SVI dataset and also from size distributions measured by Particle Measuring Systems 2D-C and 2D-P probes flown on the National Research Council Canada's Convair-580 during three C3VP research flights. Figure 7.13 shows the N_0 and λ values obtained from fits of the exponential size distribution function to the observed size spectra. Results of the same analysis performed on 2D-P observations of cloud and precipitating ice for the Wakasa Bay research flight on 27 Jan 2003 (Lobl et al., 2007) are

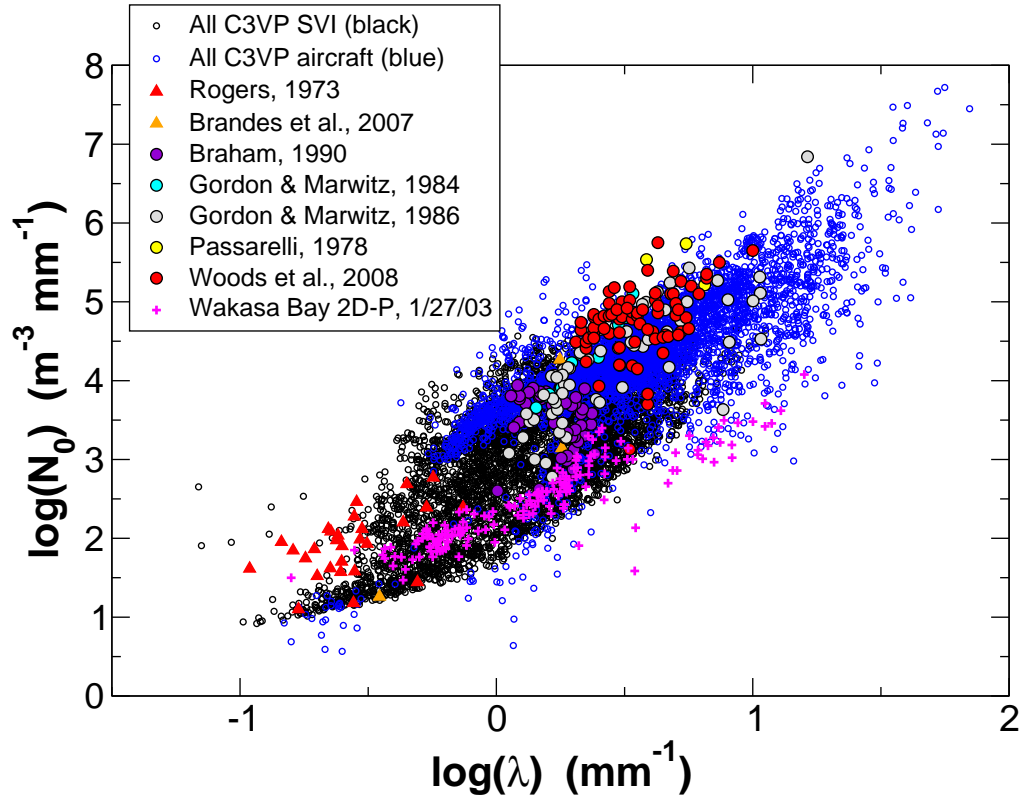


Figure 7.13: A priori estimates of λ and N_0 obtained from fits to size distributions from the SVI dataset (black circles) and from C3VP aircraft observations (blue circles). Larger, colored symbols represent values obtained from literature as noted in the legend, while the magenta “+” symbols shows fits to size distributions from a single research flight from the Wakasa Bay field experiment.

also shown, as are results from seven additional studies. Two of these earlier studies utilized surface observations (Rogers, 1973; Brandes et al., 2007) taken in and near the Front Range of the Rocky Mountains while the remaining five employed aircraft observations: Gordon and Marwitz (1984) and Gordon and Marwitz (1986) reported on observations over the central Sierra Nevada, Braham (1990) on lake effect snow over Lake Michigan, Passarelli (1978) on synoptic snowfall over central Illinois, and Woods et al. (2008) on both orographic and frontal wintertime precipitation in the Pacific Northwest. The results shown in the figure suggest that the C3VP observations adequately represent snowfall from a number of different regimes, although the number concentrations from several studies are at the margins of the C3VP observations.

The size distribution slope parameter λ varies with temperature in the C3VP observation. This variation is apparent in both the SVI and aircraft data (Figure 7.14). Similar log-linear variation with temperature has been described previously for exponential size distribution parameters (e.g., Houze et al., 1979; Woods et al., 2008; and works reviewed in Ryan, 1996). Since vertical profiles of temperature are available with the CloudSat ECMWF-AUX product, such relationships can be used to help construct the a priori constraints for the retrieval. A linear fit was constructed between $\log(\lambda)$ and T using the combined aircraft and SVI data, then residual standard deviations (RSDs) between the fit and the observations were calculated by binning the fitted and observed values in intervals of 2 K. The results of the fit and the bounds determined by ± 1 RSD are shown by the colored lines in Figure 7.14 (both panels). Points on the blue lines indicate the locations at which the RSDs were calculated. The figure also shows values from the additional studies mentioned above for comparison (lower panel). The narrow temperature ranges for the Wakasa Bay and Brandes et al. observations make comparisons against the C3VP temperature dependence uninformative. The Rogers (1973) observations are largely outside the bounds of the RSDs, but are generally consistent with the C3VP histogram at warmer temperatures. The aircraft observations other than Wakasa Bay follow a temperature trend similar to the C3VP observations.

Log-linear relations between the size distribution intercept parameter N_0 and temperature also have been described previously (again see Woods et al., 2008 and works reviewed in Ryan, 1996). Intercept parameters from the C3VP surface and aircraft observations exhibit a log-linear variation with temperature as well (Figure 7.15). In contrast to the results for $\log(\lambda)$, values of $\log(N_0)$ from the comparison studies lie mostly above the $+1$ RSD bound, but would lie largely within a $+2$ RSD bound.

Based on the similarity between the results from C3VP and results from other experiments, a priori states derived from the C3VP observations can be expected to represent a broader range of snowfall regimes and were used to develop a priori constraints for the CloudSat retrieval. Expected values for $\log(\lambda)$ and $\log(N_0)$ were estimated from the linear fits as

$$\log(\lambda_{ap}) = -0.03053(T - 273.) - 0.08258, \quad (7.33)$$

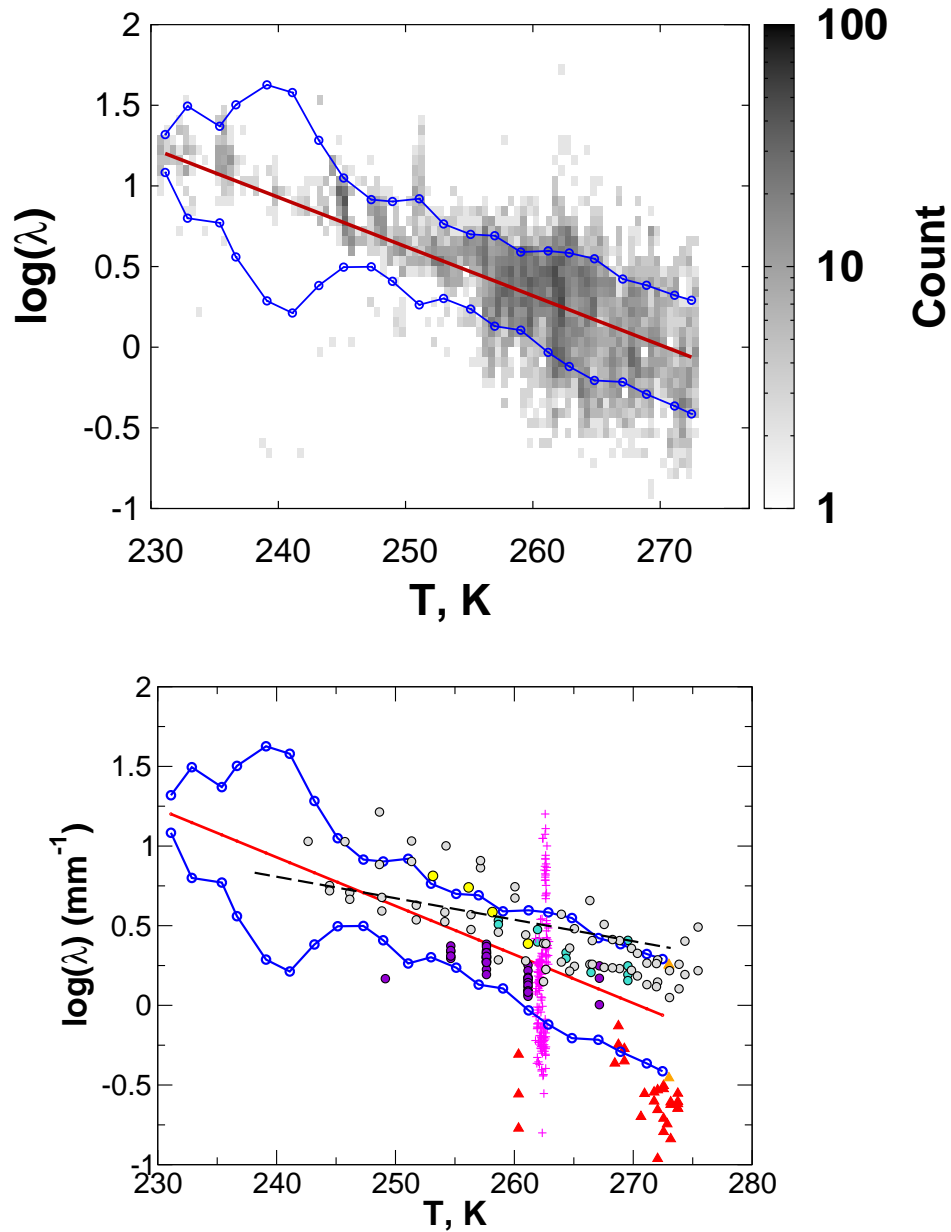


Figure 7.14: Dependence of $\log(\lambda)$ on temperature. Upper panel: The shaded gray shows the 2D histogram of $\log(\lambda)$ versus T for the C3VP surface and aircraft observations. The central line (red) shows the best-fit linear relationship, while the upper and lower blue lines show the bounds given by ± 1 residual standard deviation (RSD). Points on the blue lines show the locations at which RSDs were calculated. Lower panel: Fit results compared with results from other studies. Symbols match those from Figure 7.13, except that, in lieu of symbols for Woods et al. (2008), the dashed black line shows a linear best fit reported by the authors.

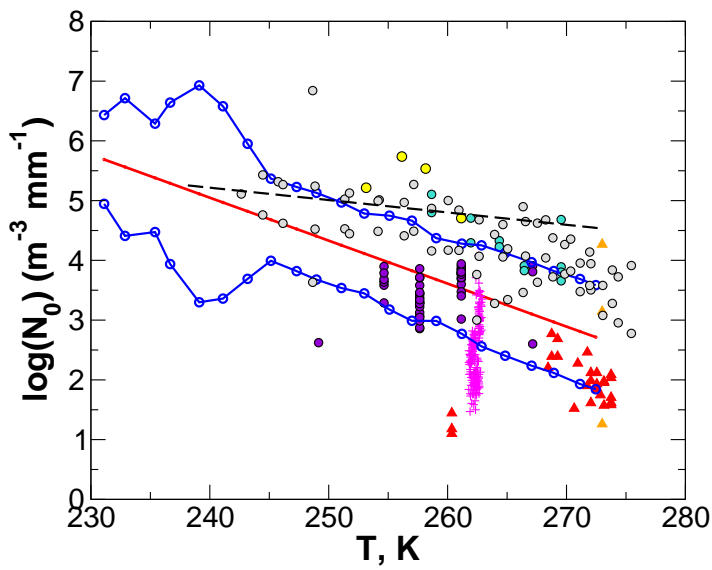
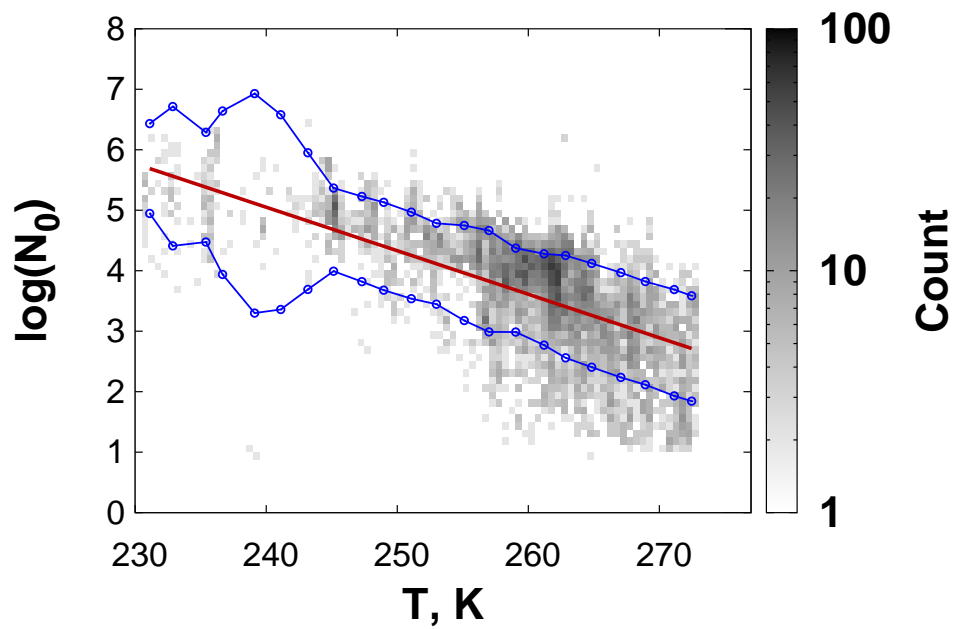


Figure 7.15: Dependence of $\log(N_0)$ on temperature. Upper panel: The shaded gray shows the 2D histogram of $\log(N_0)$ versus T for C3VP surface and aircraft observations. Lower panel: Fit results compared with results from other studies. Lines and points are as defined for Figure 7.14.

and

$$\log(N_{0,ap}) = -0.07193(T - 273.) + 2.665. \quad (7.34)$$

with λ in mm^{-1} and N_0 in $\text{m}^{-3} \text{mm}^{-1}$. The RSDs for $\log(N_0)$ and $\log(\lambda)$ show little variation with temperature (Figures 7.15 and 7.14), except in the vicinity of 240 K, where they increase substantially. The number of samples is small near this temperature, and the large RSDs are in response to a few outlying points with small λ and N_0 values. Accordingly, variances were treated as constant and were estimated as the squared RSDs averaged over all temperatures,

$$s^2(\log(\lambda_{ap})) = 0.133, \quad (7.35)$$

$$s^2(\log(N_{0,ap})) = 0.95. \quad (7.36)$$

To determine covariances between $\log(N_{0,ap})$ and $\log(\lambda_{ap})$, the observed values from the C3VP observations were again subsetted in temperature intervals of 2 K and correlation coefficients were calculated for each interval. The correlation coefficients ranged from 0.39 to 0.91 with a mean and standard deviation of 0.72 and 0.12. The a priori covariance was then modeled as $0.72(s(\log(\lambda_{ap}))s(\log(N_{0,ap})))$. These covariances, which apply to $\log(\lambda_{ap})$ and $\log(N_{0,ap})$ values for an individual radar bin, appear as off-diagonal elements in \mathbf{S}_a . While correlations likely exist between vertically separated radar bins, knowledge of these correlations is lacking and a topic for further research. The dependence of $\log(\lambda_{ap})$ and $\log(N_{0,ap})$ on temperature does impose some degree of structure on the vertical profiles of these values. Accordingly, other off-diagonal elements in \mathbf{S}_a are set to zero.

7.6 Snowfall estimation

Provided a retrieval is successful, the snowfall rate profile is calculated. Snowfall rates are calculated for each radar bin in the precipitation layer. For the assumed exponential

distribution, the snowfall rate in depth units at radar bin i is

$$P(N_{0,i}; \lambda_i; \tilde{\mathbf{b}}_i; T_i; p_i; \delta_0; C_0) = \frac{\alpha}{\rho_{liq}} N_{0,i} \bullet \int_{D_{M,min}}^{D_{M,max}} \exp(-\lambda_i D_M) D_M^\beta V(D_M, \tilde{\mathbf{b}}_i; T_i; p_i; \delta_0; C_0) dD_M \quad (7.37)$$

where $\tilde{\mathbf{b}}_i = (\alpha, \beta, \gamma, \sigma)$, T_i is the bin temperature, and p_i is the bin pressure. Fallspeeds are modeled per MH2005, and δ_0 and C_0 are parameters of that model as introduced in Section 3.2.

If the scene characterization indicated snow would be present at the surface, the surface snowfall rate is estimated as that at the bottom of the snowfall rate profile. Although a simple microphysical model (e.g. Matrosov and Battaglia, 2009) might be used for this estimate, the development and uncertainty characterization of such a model is left for future work.

Uncertainties for P are determined in a manner similar to that used for the forward model uncertainties. The total uncertainty in P , represented by the covariance matrix $\hat{\mathbf{S}}_p$, can be decomposed into $\hat{\mathbf{S}}_{P,x}$, the uncertainties attributable to the uncertainties in the retrieved state $\hat{\mathbf{x}}$; $\hat{\mathbf{S}}_{P,b}$, the uncertainties in the microphysical parameters $\tilde{\mathbf{b}}$; $\hat{\mathbf{S}}_{P,v}$, the uncertainties in the fallspeed model; and $\hat{\mathbf{S}}_{P,exp}$, the assumed exponential form for the size distribution:

$$\hat{\mathbf{S}}_P = \hat{\mathbf{S}}_{P,x} + \hat{\mathbf{S}}_{P,b} + \hat{\mathbf{S}}_{P,v} + \hat{\mathbf{S}}_{P,exp} \quad (7.38)$$

where the carets indicate the uncertainties are evaluated at the retrieved state. Note that $\hat{\mathbf{S}}_{P,b}$ includes uncertainties due to both the explicit dependence of P on α and β as shown in (7.37) and the implicit dependence on $\tilde{\mathbf{b}}$ through the fallspeed model. The remaining fallspeed uncertainties are included in $\hat{\mathbf{S}}_{P,v}$. These remaining uncertainties are related to the representativeness of the fallspeed model; to uncertainties in the fallspeed model parameters δ_0 , C_0 ; and to uncertainties in the environmental variables T and p .

The uncertainties attributable to the uncertainties in the retrieved state are evaluated as

$$\hat{\mathbf{S}}_{P,x} = \hat{\mathbf{K}}_{P,x} \hat{\mathbf{S}}_x \hat{\mathbf{K}}_{P,x}^T \quad (7.39)$$

The uncertainties in snowfall rate attributable to fallspeed uncertainties are evaluated in two parts. First, the contributions due to the representativeness of the fallspeed model are evaluated. These representativeness errors, described in Section 4.2.3, are given by the covariance matrix \mathbf{S}_v and are considered to be uncorrelated between radar bins. Since snowfall rate P in a given radar bin is independent of the state and parameters in other bins, the variance $s_a^2(P)_i$ for radar bin i can be found as

$$s_a^2(P)_i = \left(\hat{\mathbf{K}}_{P,v} \right)_i \mathbf{S}_v \left(\hat{\mathbf{K}}_{P,v} \right)_i^\top \quad (7.44)$$

where $\left(\hat{\mathbf{K}}_{P,v} \right)_i$ is the Jacobian of (7.37) with respect to the fallspeeds at the distinct particle sizes used for the particle models

$$\left(\hat{\mathbf{K}}_{P,v} \right)_i = \left[\begin{array}{ccc} \frac{\partial P_i}{\partial v_{i,0}} & \dots & \frac{\partial P_i}{\partial v_{i,K}} \end{array} \right] \quad (7.45)$$

and K is the number of distinct particle sizes. The uncertainties in δ_0 , C_0 , T_i and p_i are also expected to be independent and uncorrelated between radar bins. The variance $s_b^2(P)_i$ due to uncertainties in these parameters is found as

$$s_b^2(P)_i = \left(\frac{\partial P_i}{\partial \delta_0} \right)^2 s^2(\delta_0) + \left(\frac{\partial P_i}{\partial C_0} \right)^2 s^2(C_0) + \left(\frac{\partial P_i}{\partial T_i} \right)^2 s^2(T_i) + \left(\frac{\partial P_i}{\partial p_i} \right)^2 s^2(p_i). \quad (7.46)$$

The variances for δ_0 , C_0 , p_i are as described in 4.3.2. Uncertainties for T_i are taken to be 0.85, consistent with values from Eyre et al. (1993) for the lower troposphere. The covariance matrix $\hat{\mathbf{S}}_{P,v}$ is then a diagonal matrix whose nonzero elements are given by the sum of (7.44) and (7.46)

$$\hat{\mathbf{S}}_{P,v} = \left[\begin{array}{ccc} s_a^2(P)_0 + s_b^2(P)_0 & & 0 \\ & \ddots & \\ 0 & & s_a^2(P)_N + s_b^2(P)_N \end{array} \right]. \quad (7.47)$$

Uncertainties due to the assumed exponential form for the size distribution are evaluated in a manner similar to that used for the reflectivity and specific attenuation. Snowfall rate was evaluated using the B8pr-30 particle model with two different forms for the size distribution: 1) the observed discrete size distributions in the SVI dataset, and 2) exponential distributions fitted to the discrete SVI distributions. For each discrete SVI distribution, radar reflectivity Ze was calculated, and the corresponding fitted distribution was adjusted by scaling the intercept parameter N_0 to reproduce the same reflectivity. Snowfall rates were then calculated using the observed discrete distribution and the fitted distribution with scaled N_0 . Uncertainty was estimated as the difference between the pair of snowfall rates. Figure 7.16 shows fractional differences as a function the snowfall rate. Although the errors are largely unbiased, for snowfall rates below $0.1 \text{ mm LWE h}^{-1}$ the distribution of errors is skewed; nevertheless, as a first approximation the bias and skewness is ignored. A log-linear fit between the scatter in the fractional error and the snowfall rate

$$f = -0.06 \log(P) + 0.05 \quad (7.48)$$

is used to estimate the fractional uncertainty due to the use of the exponential distribution. The corresponding variance in the snowfall rate at radar bin i is then

$$s_{exp}^2(P)_i = f^2 P_i^2. \quad (7.49)$$

Information about vertical correlations for this type of uncertainty is lacking. For this work, these uncertainties are assumed to be uncorrelated in the vertical, and $\hat{\mathbf{S}}_{P,exp}$ is then

$$\hat{\mathbf{S}}_{P,exp} = \begin{bmatrix} s_{exp}^2(P)_0 & & 0 \\ & \ddots & \\ 0 & & s_{exp}^2(P)_N \end{bmatrix}. \quad (7.50)$$

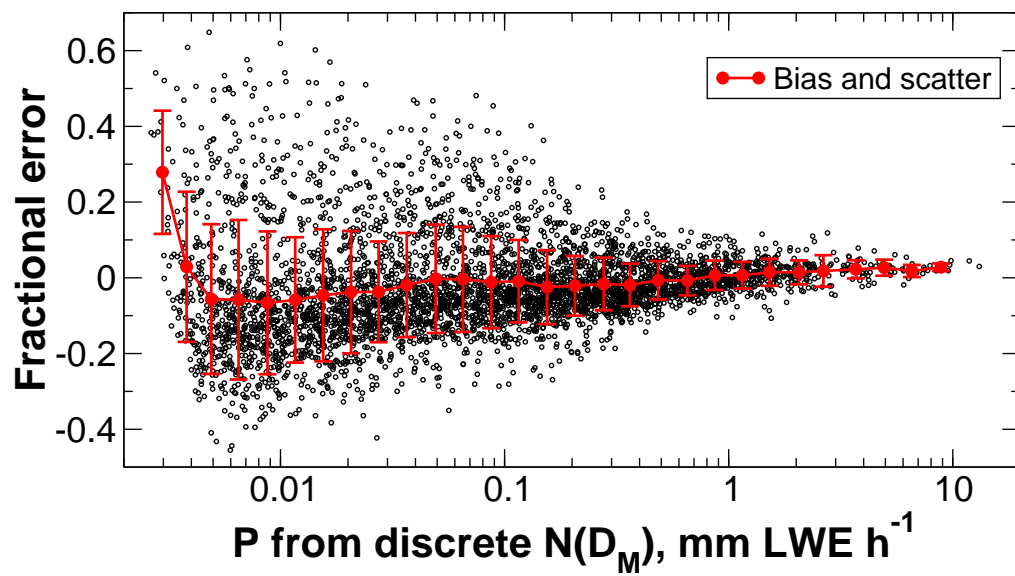


Figure 7.16: Fractional differences between snowfall rate calculated using the B8pr-30 particle model with observed SVI size distributions and those calculated from fitted exponential distributions.

Chapter 8

Retrieval Results

8.1 Application to ACR observations

The observations by the Airborne Cloud Radar (ACR) during C3VP provide the opportunity to compare retrieved snowfall against coincident measurements of snowfall rates and accumulations. Snowfall rate observations were obtained from the Vaisala FD12P and were scaled to provide unbiased accumulations relative to the DFIR. These observations were described previously in Section 2.1.3, and the ACR observations were introduced in Section 6.4.2. As was noted in that section, the calibration error in the ACR was taken to be negligible. The ACR was operated only during snow events of interest during IOPs. Generally these coincided with satellite overpasses and aircraft operations. In all, about 28 hours of ACR radar profiles were recorded at approximately 2.8 s intervals. These observations represent 17 distinct snow events that occurred over 18 days between 3 November 2006 and 2 March 2007; however, most of the accumulations were concentrated during nine of the events (see Table 8.1 later in this section). The data include three of the cases (A, B, and C) used in the snow microphysics retrieval. Of the nearly 36,000 ACR profiles, approximately 7300 are from these three cases.

The retrieval was applied to the ACR reflectivities observed in the range bin nearest the surface, at 197 m AGL. Temperatures and pressures needed by the retrieval to perform the scene characterization, calculate fallspeeds and establish the a priori states were obtained from nearby surface meteorology observations. The scene characterization was modified to

evaluate only this ACR reflectivity and this near-surface air temperature. Because the viewing geometry for the ACR is significantly different than that for CloudSat, it is unlikely that the multiple scattering correction (7.11) is appropriate; however, because the attenuation between the radar and the first range bin is negligible, this correction and the associated uncertainty (7.17) will also be negligible. Consequently, no changes were required to the radar reflectivity forward model and its uncertainties. The retrieved ACR snowfall rates, P_{ACR} , were matched to the nearest-in-time observed snowfall rate, P_{FD12P} . Because of the difference in temporal resolution (1 minute versus 2.8 seconds), a particular value of P_{FD12P} was typically matched to multiple values of P_{ACR} .

Time series of P_{ACR} and P_{FD12P} show a high degree of agreement over most of the observing period (Figure 8.1, upper panel). Two notable exceptions occur near time indices 25000 and 32500, when the FD12P recorded snowfall rates above 1 mm LWE h^{-1} while the retrieved values are substantially smaller. Examining the time series of ACR reflectivities shows that the ACR did not observe high reflectivities during these periods (Figure 8.1, lower panel). The first of these anomalies occurred 22 February 2007 from 11:20 to 12:05 UTC while the second occurred 1 March 2007 between 22:15 and 22:50 UTC. For both, the ACR operator made note of the heavy snowfall, suggesting that both the FD12P and the ACR observed similar snowfall rates (Austin et al., 2007).

For the 14 February anomaly, the ACR operator noted that precipitation in the form of ice pellets began at 10:40 UTC (Austin et al., 2007). By 11:15 UTC the precipitation consisted of snow mixed with ice pellets. This transition is apparent in the SVI observations. Between 11:00 and 12:00 UTC, the SVI showed a transition between two size distributions (Figure 8.2). Initially the distributions were narrow and had relatively high concentrations of small particles. Within a 10-minute span the distributions broadened considerably. They were approximately exponential for sizes above $D_{SVI} = 1.5$ mm, but had a pronounced superexponential shape at sizes below 1.5 mm. By 12:25 UTC, the precipitation had transitioned to light snow. Temperatures recorded at the meteorology tower remained between 0°C and -0.5°C during the period from 10:40 to 12:25 UTC. A radiosonde launched at 11:30 UTC, however, showed a shallow freezing layer above the surface with temperatures warming to near 0°C at 890 - 900 hPa. VertiX observations at 10:50 UTC confirmed an apparent

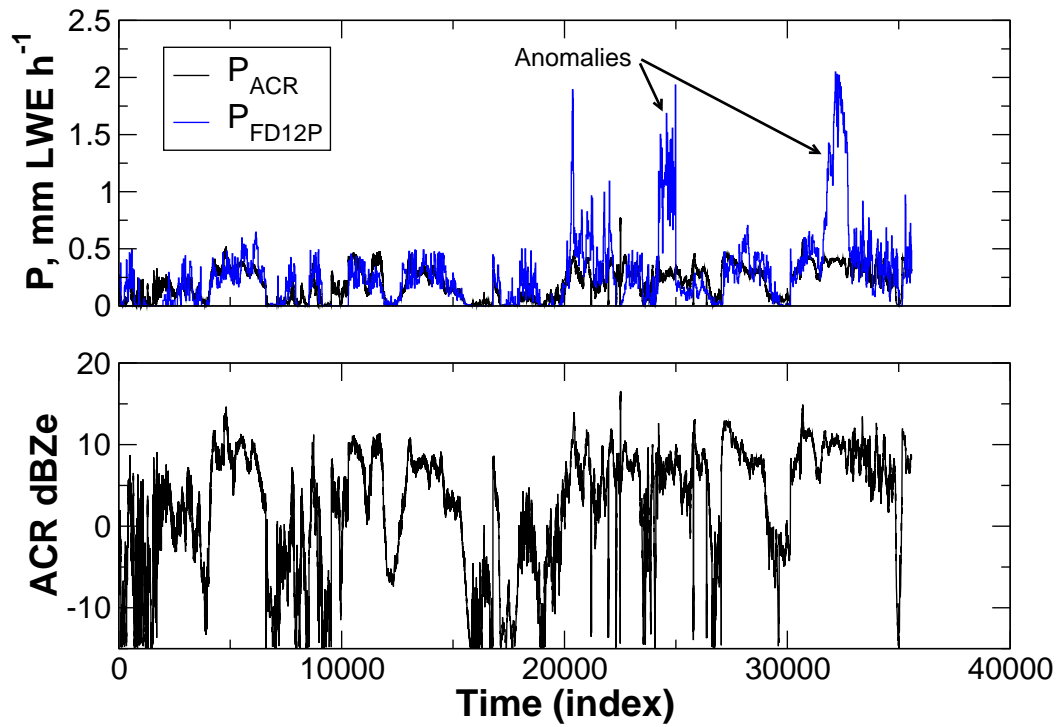


Figure 8.1: Upper panel: Time series of snowfall rates retrieved from ACR reflectivities and observed. Lower panel: Corresponding time series of ACR reflectivities. Each time index indicates a 2.8 s observation by the ACR. Snowfall rates retrieved for the ACR used the reflectivity in the range bin nearest the surface, at 197 m AGL.

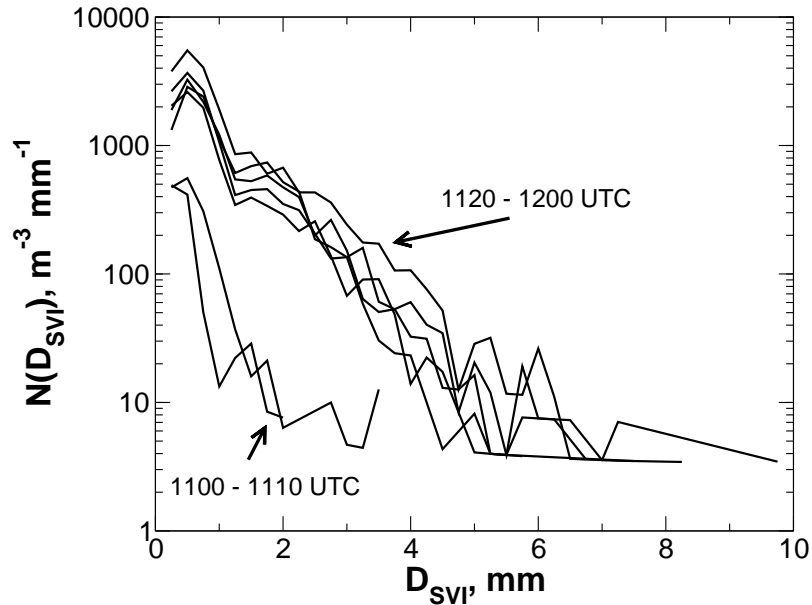


Figure 8.2: SVI size distributions during the 14 February anomaly.

melting level near 1 km AGL, with mean Doppler velocities of around 3 m s^{-1} below that level. At 11:15 UTC, the ACR operator reported there was “still a hint of a melting level at $\sim 0.7 \text{ km}$.” Because of the melting within the precipitating column, this particular scene would have been rejected by the normal CloudSat scene characterization.

For the 1 March anomaly, surface temperatures were considerably colder at -5°C . A sonde was launched at 20:00 UTC. Temperature decreased with height to -9°C at 900 hPa, then increased to a maximum of -2° at 835 hPa. At the time of a sonde launch at 02:30 UTC on 2 March, temperatures at 750 hPa were near 0°C . The -15 dBZe echo tops for the ACR were at 5 to 7 km AGL during this anomaly, well above the melting level height observed in the sonde. The ACR operator reported snow, at times heavy, between 20:43 UTC and 02:09 UTC on 2 March, but gave no details of the characteristics. The VertiX and SVI had been taken out of service at this time, so additional information about the scene is limited, but the Environment Canada forecast for the day called for heavy snow mixed with ice pellets, transitioning to freezing rain. If the melting level had been present during the anomaly, the standard CloudSat scene characterization would have rejected this scene. Lacking additional microphysical or visual observations of the snowfall, further characterization of the cause of the discrepancy between the retrieved versus observed precipitation rates is not possible.

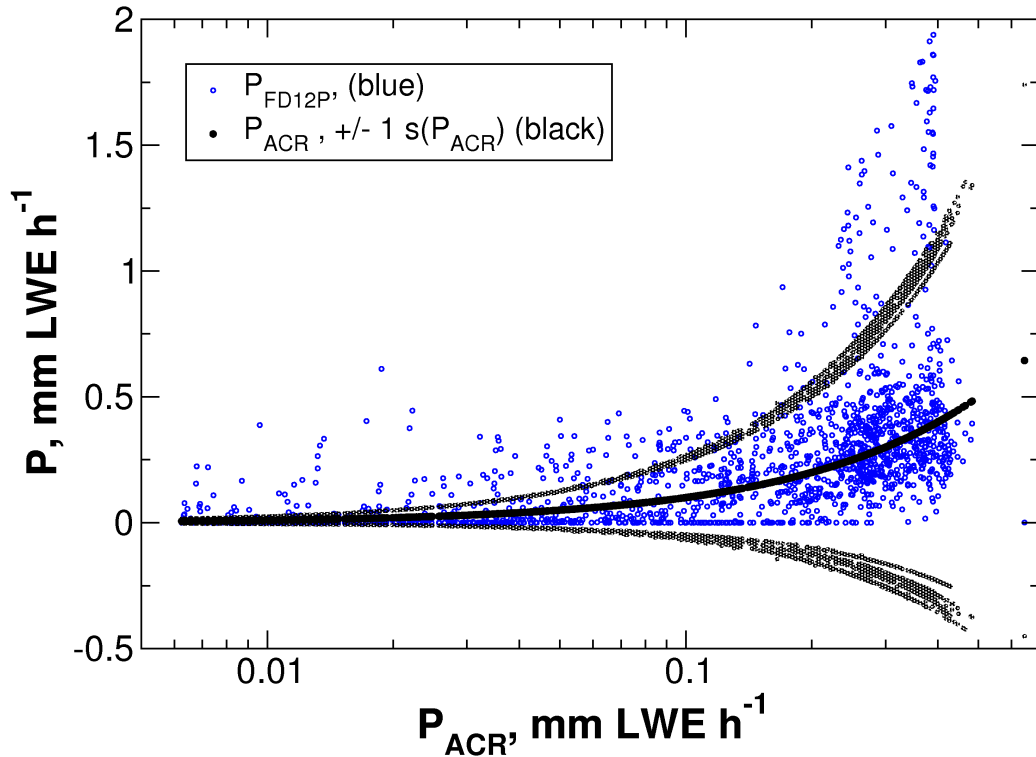


Figure 8.3: Comparison of snowfall rates retrieved from ACR reflectivities with observed FD12P rates. The central line of points in black is the 1:1 line, and the gray stippling shows the upper and lower uncertainty bounds on the retrieved rates based on ± 1 standard deviation. The spread in the upper and lower uncertainty bounds is due to the dependence of the uncertainty in P_{ACR} on the uncertainties in the retrieved state. Snowfall rates retrieved for the ACR used the reflectivity in the range bin nearest the surface, at 197 m AGL.

Figure 8.3 compares P_{ACR} and P_{FD12P} against the expected uncertainties in P_{ACR} . The time series of retrieved and observed precipitation rates were subsampled into distinct 1-minute samples, then the rates and P_{ACR} uncertainties were averaged. The uncertainties for P_{ACR} are about 140% to 200% of the retrieved rate. Sources of uncertainty will be examined in more detail in the discussion of the application of the retrieval to CloudSat observations in Section 8.2. P_{FD12P} generally lies within the uncertainty bounds on P_{ACR} . Of the approximately 1600 subsamples, the differences between P_{FD12P} and P_{ACR} exceed $1s(P_{ACR})$ in only 228 cases, and exceed $2s(P_{ACR})$ in only 116 cases. These comparisons ignore the 30% to 50% uncertainties in P_{FD12P} . Evaluated over all the subsamples, the bias of P_{ACR} relative to P_{FD12P} is $-0.066 \text{ mm LWE h}^{-1}$. The high P_{FD12P} values at the right of the plot are attributable to the anomalies discussed above.

Accumulations may also be calculated from P_{ACR} and P_{FD12P} (Figure 8.4). The accumulations were calculated both with (upper panel) and without (lower panel) the two anomalies described above. Uncertainties in P_{FD12P} were modeled as described in Section 4.1.2. Uncertainties in accumulations were calculated by assuming errors in precipitation rate were correlated within snow events, but uncorrelated between events. Accumulations are substantially in agreement during the first 16 hours but diverge somewhat beyond that. In the upper panel, the final difference between the accumulations is 2 mm. With the anomalies removed, that difference is reduced to 0.8 mm. The FD12P accumulations fall well within the uncertainties of the ACR accumulations. In the case the anomalies are removed, the mean accumulation from the ACR falls largely within the uncertainties of the FD12P accumulation.

The uncertainties in the microphysical properties introduce uncertainties in the forward modeled reflectivities as was described in Section 7.3.3. These uncertainties were extracted from the ACR retrieval results and are shown in Figure 8.5 (upper panel) as a function of observed reflectivity. The contributions from these microphysical property uncertainties dominate the total uncertainty in the forward modeled reflectivity. For large reflectivities, the large uncertainties allow the retrieval to depart substantially from the observed reflectivity (Figure 8.5, lower panel). As a result, the retrieved snowfall rates for these high-reflectivity cases will likely be smaller than would be expected based on the observed reflectivity.

8.1.1 Information content

A number of metrics related to information content were introduced in the description of the optimal estimation method (Section 3.1): the Shannon Information Content, H ; the averaging kernel matrix, \mathbf{A} ; and d_s , the number of degrees of freedom for signal. Figure 8.6 shows these metrics for the ACR retrievals. Values for H vary between 0.4 and 1.2, indicating that the measurements resolve between 1.3 and 2.3 distinct states. The degrees of freedom for signal, d_s , shows that the retrieval produces somewhat less than one independent piece of information that is significant compared to the measurement and forward model uncertainties. The lower two panels of Figure 8.6 show the diagonal elements of \mathbf{A} , whose

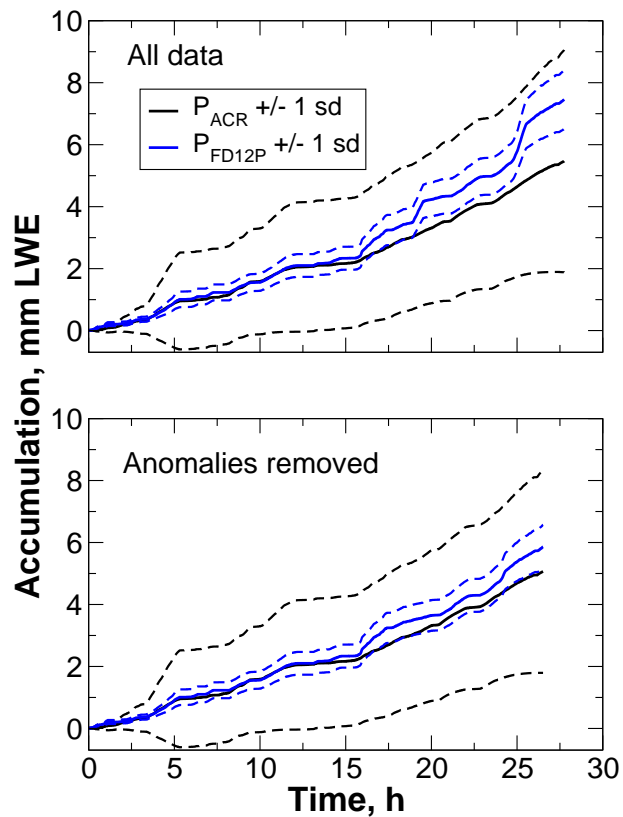


Figure 8.4: Snow accumulations computed from P_{ACR} and P_{FD12P} . The accumulations are for 17 snow events observed by the ACR on 18 days between 3 November 2006 and 2 March 2007, but accumulations are principally from nine events (Table 8.1). The events were concatenated sequentially in time and the time axis indicates the cumulative time over all events. The upper plot shows accumulations from all ACR observations, while in the lower plot the two anomalous events have been removed. The dashed lines bounding the accumulation show the accumulation uncertainties.

Table 8.1: Accumulations by event for the ACR retrievals. Two distinct events, indicated as (a) and (b), occurred on 20 Jan 2007. Duration shows the elapsed time of ACR observations for which retrievals were performed.

		Accumulations	
Date	Duration	ACR	FD12P
	h	mm LW	
3 Nov 2006	0.98	0.065	0.11
2 Dec 2006	0.16	0.007	0.00
6 Dec 2006	4.00	0.86	0.80
7 Dec 2006	1.08	0.038	0.093
8 Dec 2006	0.34	0.018	0.00
17 Jan 2007	0.09	9.3e-04	0.00
19 Jan 2007	0.46	0.061	0.13
20 Jan 2007 (a)	0.32	0.004	2.8e-04
20 Jan 2007 (b)	0.59	0.079	0.0
22 Jan 2007	4.29	0.92	0.90
23 Jan 2007	0.76	0.017	0.00
26 Jan 2007	0.93	0.045	0.085
27 Jan 2007	3.36	0.57	1.06
19 Feb 2007	0.97	0.26	0.18
22 Feb 2007	2.72	0.59	0.91
26 Feb 2007	2.41	0.58	0.64
1 Mar 2007	4.23	1.35	2.48

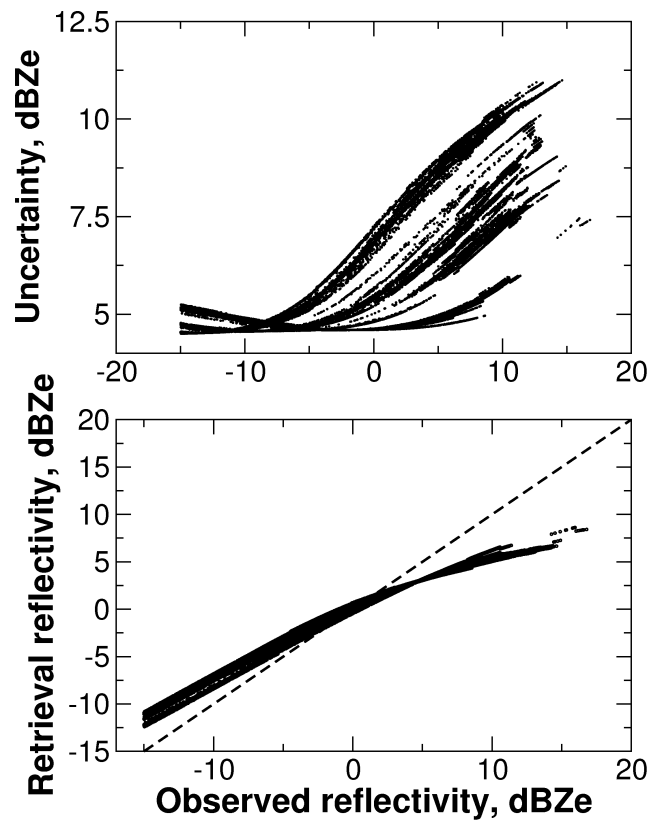


Figure 8.5: Upper panel: Uncertainties in forward-modeled reflectivity due to uncertainties in the microphysical properties of the particle models. Lower panel: Reflectivity produced by the retrieval compared to the observed reflectivity.

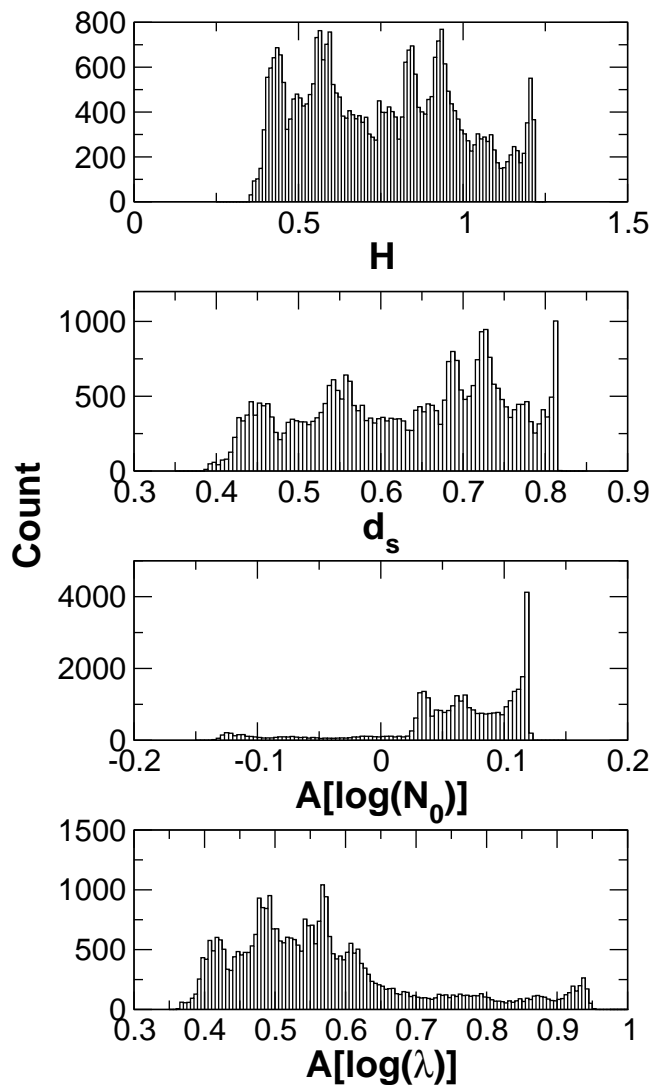


Figure 8.6: Distributions of information content metrics for the ACR retrieval.

sum gives d_s . While the element relevant to λ , $\mathbf{A}[\log(\lambda)]$, is consistently positive, the element for N_o , $\mathbf{A}[\log(N_0)]$ is near zero and is at times negative. These results show that $\log(\lambda)$ is moderately to strongly constrained by the reflectivity observation, while $\log(N_0)$ is largely dependent on the a priori constraint.

The shape of the size distribution plays a significant role in determining the values of these metrics. Information content H increases as the distribution narrows (Figure 8.7, panel a). The increase in H accompanies a substantial increase in the magnitude of the sensitivity of the forward model to $\log(\lambda)$ (panel b). This increased sensitivity allows the observed reflectivity to better constrain the retrieved state, particularly the value of $\log(\lambda)$.

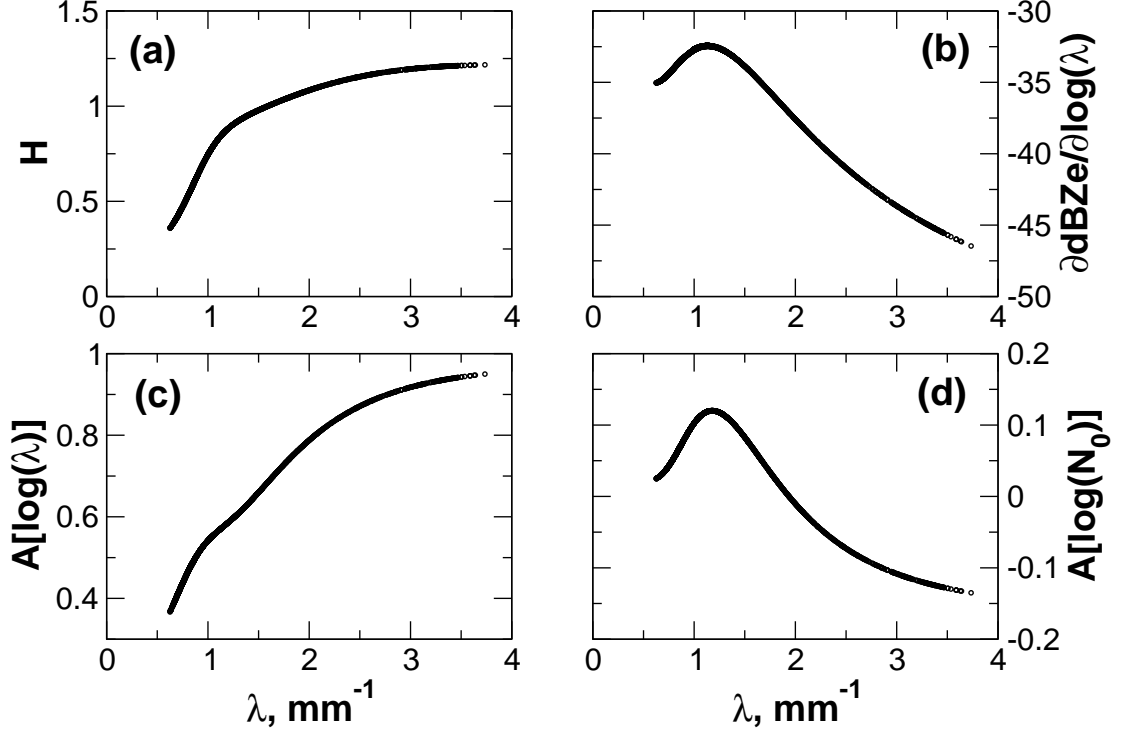


Figure 8.7: Information content metrics and the forward model Jacobian as functions of λ .

As a result, $\mathbf{A}[\log(\lambda)]$ increases from 0.4 to 0.95 as λ increases (panel c). The behavior of $\mathbf{A}[\log(N_0)]$ (panel d) is quite different. The values are small and are positive for small values of λ , but become negative as λ increases.

While the forward model is strongly sensitive to $\log(\lambda)$, its sensitivity to $\log(N_0)$ is 3-4 times smaller in magnitude. This sensitivity has a constant value of 10 owing to the reflectivity in dBZe being a linear function of $\log(N_0)$. Consequently, the retrieved value of $\log(\lambda)$ is influenced more strongly by the observations, while the the retrieved value of $\log(N_0)$ is influenced more by the a priori estimate of the state. This difference is reflected in panels (c) and (d) of Figure 8.7.

The negative values of $\mathbf{A}[\log(N_0)]$ do not seem to fit the normal paradigm which describes the \mathbf{A} matrix (Section 3.1). Their explanation reveals details of a significant behavior of this retrieval. In the application of the retrieval to a single radar bin, the value of

$\mathbf{A}[\log(N_0)]$ is given by

$$\mathbf{A}[\log(N_0)] = \left[s^2 \left(\log(\hat{N}_0) \right) \left(\frac{\partial dBZe}{\partial \log(N_0)} \right)^2 + s \left(\log(\hat{N}_0), \log(\hat{\lambda}) \right) \left(\frac{\partial dBZe}{\partial \log(N_0)} \right) \left(\frac{\partial dBZe}{\partial \log(\lambda)} \right) \right] [s_y^2 (dBZe)]^{-1}, \quad (8.1)$$

where the carets indicate retrieved values. In the first set of brackets on the right side, the sign of the first term is clearly positive, while that of the second term depends on the signs of the covariance and the two partial derivatives, which are the elements of the Jacobian of the forward model. As was shown above, $\frac{\partial dBZe}{\partial \log(N_0)}$ is positive while $\frac{\partial dBZe}{\partial \log(\lambda)}$ is negative. The covariance for the retrieved state changes very little from the a priori covariance, which is positive and represents a substantial positive correlation between $\log(\lambda)$ and $\log(N_0)$. This second term, then, is negative and as the magnitude of $\frac{\partial dBZe}{\partial \log(\lambda)}$ increases, the sign of $\mathbf{A}[\log(N_0)]$ changes from positive to negative.

These terms represent competing influences on the retrieved value of $\log(N_0)$. These competing influences arise from the a priori covariance and from the Jacobian of the forward model. The positive covariance requires that a positive adjustment in $\log(\lambda)$ be accompanied by a positive adjustment in $\log(N_0)$. In contrast, the Jacobian terms have differing signs. If the difference between the observed and forward model reflectivity calls for a positive adjustment to $\log(\lambda)$, the corresponding adjustment to $\log(N_0)$ would be negative.

Figure 8.8 shows this process schematically. The size distribution that represents the initial state is shown by the solid line. Assuming that the forward modeled reflectivity for this state overestimates the observed reflectivity (a positive error), two responses are possible: $\log(\lambda)$ could be increased, narrowing the distribution; and $\log(N_0)$ could be decreased, reducing the amplitude of the distribution. Absent the covariance between $\log(\lambda)$ and $\log(N_0)$, the retrieval would apply both adjustments, likely giving more weight to the adjustment of $\log(\lambda)$ because of the stronger sensitivity of the forward model to that variable. These adjustments are represented by the heavy arrows labeled $\delta \log(N_0)$ and $\delta \log(\lambda)$. Because of the positive covariance between $\log(N_0)$ and $\log(\lambda)$, however, an

increase in $\log(\lambda)$ produces an opposing response that increases $\log(N_0)$, shown by the upward-pointing heavy arrow. The resulting size distribution is shown by the dashed line.

For small λ (broad distributions), the magnitude of $\frac{\partial dBZe}{\partial \log(\lambda)}$ is relatively small, so the covariance-driven adjustment is small and does not overcome the initial reduction in $\log(N_0)$. In these cases, $\log(N_0)$ decreases in response to a positive error in the modeled reflectivity. This net response is consistent with the sensitivity of the forward model to $\log(N_0)$ and $\mathbf{A}[\log(N_0)]$ is positive. For large λ (narrower distributions), the magnitude of $\frac{\partial dBZe}{\partial \log(\lambda)}$ is larger. The covariance-driven adjustment is larger also and does overcome the initial reduction in $\log(N_0)$. As a result, $\log(N_0)$ increases in response to the positive error in the modeled reflectivity. Since this net response opposes the sensitivity of the forward model, $\mathbf{A}[\log(N_0)]$ is negative.

The combination of the strong positive covariance between $\log(N_0)$ and $\log(\lambda)$ and the comparatively weak sensitivity of the reflectivity to $\log(N_0)$ limits the behavior of the retrieval. For narrower distributions, the retrieval is prevented from simultaneously increasing $\log(\lambda)$ and decreasing $\log(N_0)$ in response to a positive error in reflectivity. The opposing behavior, decreasing $\log(\lambda)$ and increasing $\log(N_0)$ in response to a negative error in reflectivity, is also restricted. While correct in a climatological sense since $\log(\lambda)$ and $\log(N_0)$ are positively correlated, in nature there are likely scenes for which such responses would give a more accurate retrieval. This reasoning demonstrates how other measurements, specifically those with better sensitivity to $\log(N_0)$, would benefit the retrieval.

8.2 An application to CloudSat observations

CloudSat observations of snowfall events near CARE are useful for examining the performance of the snowfall retrieval. CARE is situated near the intersection of ascending and descending segments of the CloudSat ground track. As a result, within the span of the 16-day repeat cycle of the CloudSat orbit, CloudSat passes over the vicinity of CARE on two of those days. On the ascending segment, the CloudSat groundtrack lies 46 km east of CARE at its nearest point, while for the descending segment, the nearest point lies 24 km east of CARE. The ascending and descending segments pass near CARE at about 18:30 UTC

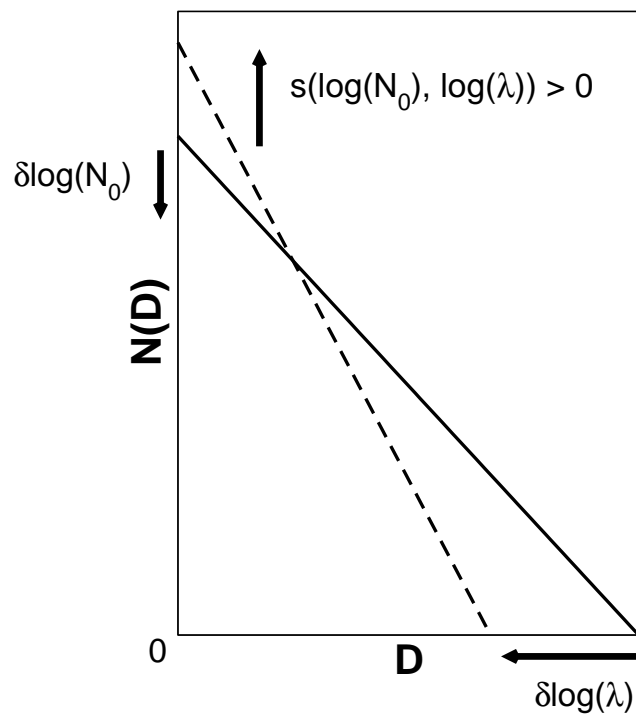


Figure 8.8: Schematic illustration of the retrieval process. The solid line represents the initial state of the retrieval while the dashed line shows the adjusted state assuming the initial state overestimates the observed reflectivity. The arrows labeled $\delta \log(\lambda)$ and $\delta \log(N_0)$ show the expected responses of the retrieval based on the sensitivities of the forward model. The arrow labeled $s(\log(N_0), \log(\lambda))$ shows the response due to positive covariance between λ and N_0 .

and 07:30 UTC, respectively. For several snow events during the C3VP IOPs, snow was observed both on the ground at CARE and by aircraft at the time of a CloudSat overpass.

One such event occurred on 22 January 2007. The snowfall retrieval was applied to the entire orbit of CloudSat observations associated with this event (CloudSat granule 3916). The granule consists of 37,081 CloudSat profiles at latitudes between 82°N and 82°S. First, the retrieval results from the full orbit are characterized in terms of the uncertainties in the retrieved snowfall rates and the relationship between reflectivity and snowfall rate, then results from the retrieval in the vicinity of CARE are examined and compared against ground and aircraft observations. For this particular orbit, the retrieval produced snowfall rates for about 52,000 radar reflectivity observations.

8.2.1 Snowfall rate uncertainties

As was described in section 7.6, the covariances for the retrieved state $\log(\lambda)$ and $\log(N_0)$ along with other variance sources can be propagated into the snowfall rate calculation to give an explicit estimate of the posterior variance of the snowfall rate. Per (7.38), these other sources are the variances in the microphysical parameters for the forward model (α , β , γ , and σ), variances in the fallspeed parameterization, and variances due to the assumed exponential distribution. From the retrieval results for this orbit, variances from each of these sources were tabulated separately, then binned by snowfall rate and averaged. Figure 8.9 shows the resulting fractions of the total snowfall rate variance due to each of these sources. Almost 90% of the snowfall rate variance is due to the variances in the retrieved state and in the microphysical parameters. The contribution due to the assumption of an exponential distribution is negligible, and that due to the variances in the fallspeed parameterization is about 10% - 15%. As snowfall rates increase, the contribution from the retrieved state variances increases, while that from the microphysical parameters decreases.

The uncertainties in snowfall rate, taken to be the square root of the variances, were evaluated similarly by binning the uncertainties by snowfall rate then averaging and taking standard deviations. Mean fractional uncertainties range from 145% to 175%, and the range for +/- 1 standard deviation extends from about 140% to 200% (Figure 8.10). The uncertainties have a pronounced minimum at a snowfall rate of about 0.08 mm LWE h⁻¹.

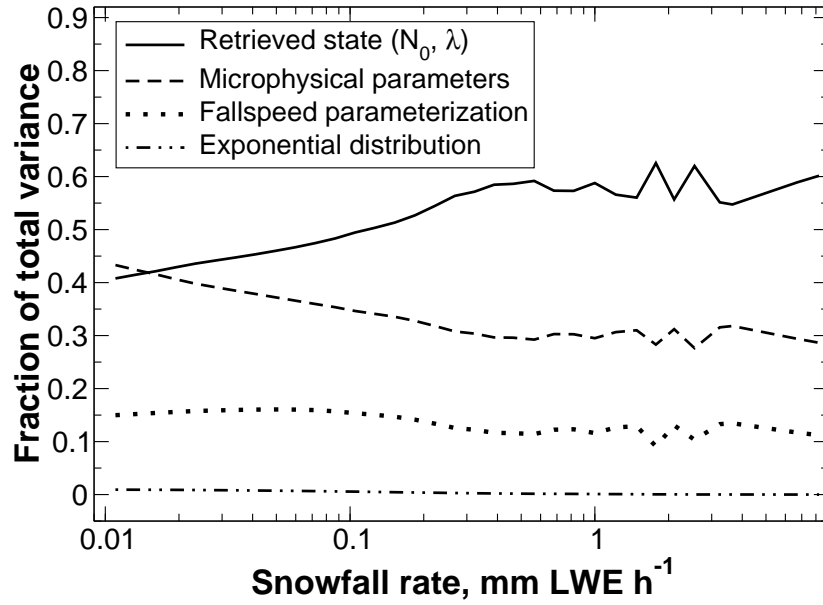


Figure 8.9: Contributions to total variance in snowfall rate from distinct sources.

Above 1 mm LWE h⁻¹, the means and standard deviations become quite variable due to the small number of samples in each bin.

In Figure 8.11, fractional uncertainties are shown by source as a function of snowfall rate. These fractional uncertainties were calculated simply as the square root of the individual variance (state, microphysical parameters, fallspeed parameterization, or exponential distribution) divided by the total variance. Note that since the total uncertainty is calculated as the square root of the sum of the variances, this sort of decomposition of the uncertainty sources is not mathematically accurate, but does allow the trends in each source to be shown as a function of snowfall rate. For snowfall rates below about 0.08 mm LWE h⁻¹, uncertainties due to all four sources increase with decreasing snowfall rate. Above 0.08 mm LWE h⁻¹, the uncertainties due to the retrieved state increase with increasing snowfall rate, while the other terms stay approximately constant or decrease. Thus the increase in fractional uncertainties above 0.08 mm LWE h⁻¹ shown in Figure 8.10 is caused by increases in the uncertainties attributable to the retrieved state.

The calculation of the snowfall rate uncertainties contributed by the retrieved state is given in matrix form, applicable to a profile of retrieval results, by (7.39). For a single radar

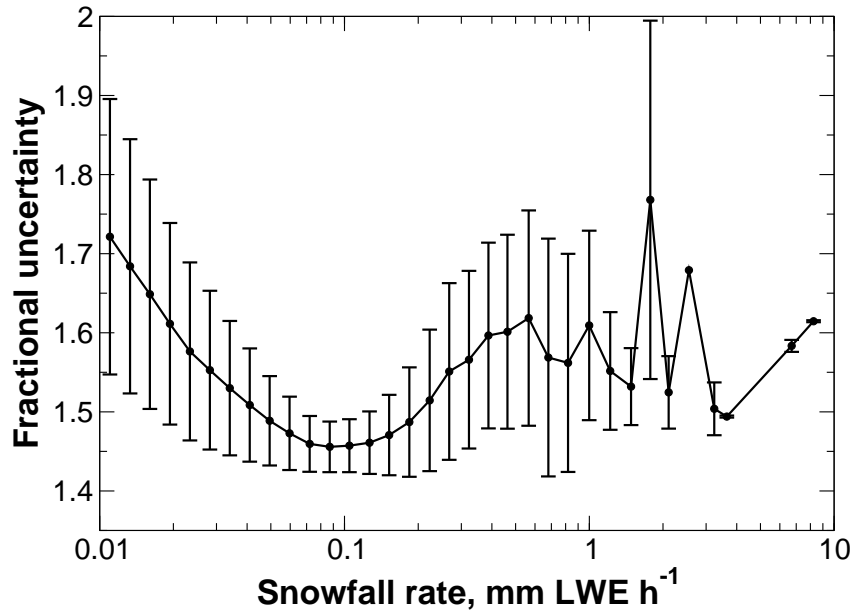


Figure 8.10: Fractional uncertainties in snowfall rate for CloudSat granule 3916. The central line shows mean fractional uncertainties and the error bars show +/- 1 standard deviation.

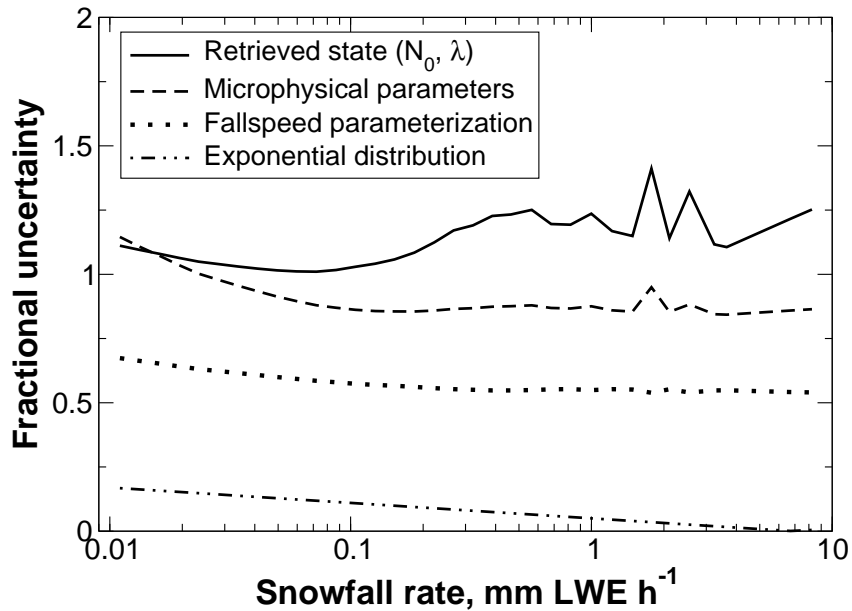


Figure 8.11: Fractional uncertainties in snowfall rate for CloudSat granule 3916, separated by source. Note that the sum of fractional uncertainties from all sources in this plot is larger than the total fractional uncertainty in Figure 8.10 because the total uncertainty is calculated as the square root of the summed variances.

bin, the calculation can be written as

$$\begin{aligned}
 s^2(P) &= \underbrace{\left(\frac{\partial P}{\partial \log(N_0)}\right)^2 s^2(\log(N_0))}_{Term\ A} \\
 &= + \underbrace{\left(\frac{\partial P}{\partial \log(\lambda)}\right)^2 s^2(\log(\lambda))}_{Term\ B} \\
 &\quad + \underbrace{2\frac{\partial P}{\partial \log(N_0)}\frac{\partial P}{\partial \log(\lambda)}s(\log(N_0), \log(\lambda))}_{Term\ C}.
 \end{aligned} \tag{8.2}$$

Terms A and B are positive, but term C is negative because the covariance is positive and the partial derivatives differ in sign. The magnitude of term C is slightly smaller than the sum of terms A and B. The value of $s^2(P)$ is then the result of the sum of terms A and B being largely offset by term C, as shown by Figure 8.12. The increase in $s^2(P)$ with increasing snowfall rate is not attributable to a single dominant source in (8.2), as all three terms increase in magnitude with increasing snowfall rate. Table 8.2 shows typical values for the elements of (8.2) for snowfall rates between 0.1 and 1.0 mm LWE h^{-1} . The variance of $\log(N_0)$ is a factor of 10 larger than that of $\log(\lambda)$, suggesting that improvements to the uncertainties in retrieved values of $\log(N_0)$ could be a means to reduce the uncertainties in snowfall rate; however, the derivative term associated with $\log(N_0)$ is about a factor of 10 smaller than that for $\log(\lambda)$. As a result, a fractional improvement to the variance of $\log(N_0)$ will have a similar impact on snowfall rate uncertainties as the same fractional improvement in the variance of $\log(\lambda)$.

8.2.2 Reflectivity-snowfall rate relations

The relationship between reflectivity and snowfall rate is often described using so-called Ze-S relations, typically using the general form

$$Ze = aS^b \tag{8.3}$$

where S is snowfall rate. Note that in earlier notation, P was used to represent snowfall rate to distinguish it from covariance matrices \mathbf{S} , but “Ze-S” will be used in this discussion.

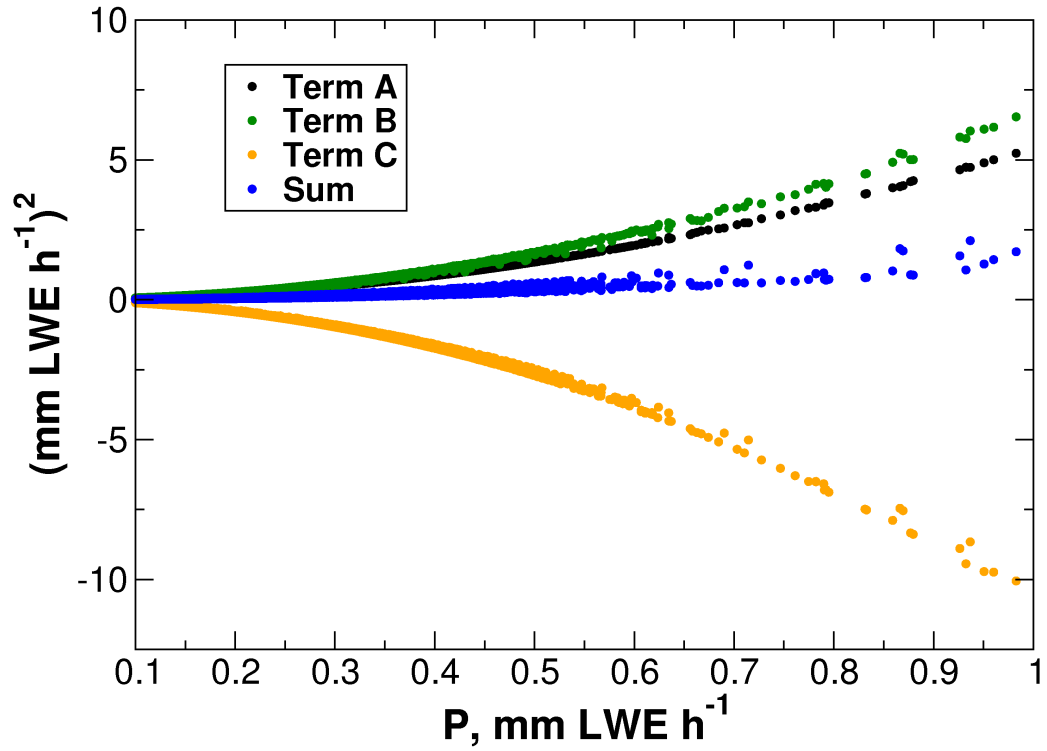


Figure 8.12: Terms A, B, and C from (8.2) versus snowfall rate. The range of snowfall rates coincides with the range in Figure 8.11 for which snowfall rate uncertainties attributable to the uncertainties in the retrieved state are increasing with snowfall rate.

Table 8.2: Typical values for the elements of (8.2). The values are averages over snowfall rates between 0.1 and 1.0 mm LWE h⁻¹.

Element	Average
$\left(\frac{\partial P}{\partial \log(N_0)}\right)^2$	0.30
$\left(\frac{\partial P}{\partial \log(\lambda)}\right)^2$	3.45
$\frac{\partial P}{\partial \log(N_0)} \frac{\partial P}{\partial \log(\lambda)}$	-1.02
$s^2(\log(N_0))$	0.94
$s^2(\log(\lambda))$	0.094
$s(\log(N_0), \log(\lambda))$	0.27

Such relations encapsulate assumptions about particle masses, fallspeeds, size distributions, and frequency-dependent radar backscattering properties. At 94 GHz, where scattering by precipitation-sized particles is non-Rayleigh, assumptions about particle shape are also incorporated via the backscattering properties. Given these assumptions, snowfall rate and reflectivity may be calculated via (3.11) and, if attenuation is neglected, (6.10).

The relation between reflectivity and snowfall rate may also be extracted from the snowfall retrieval results. Because the retrieval incorporates scene-dependent estimates of the a priori state, forward model uncertainties, and attenuation in a probabilistic framework, the resulting Ze-S relation is not linear in log-space; rather, a distribution of reflectivities and expected values of snowfall rate is produced, with each snowfall rate having an associated variance that describes a normally distributed PDF.

The distribution of the retrieved snowfall rates and observed reflectivities for granule 3916 is shown as a 2D frequency distribution in Figure 8.13. The histogram itself, in grayscale, shows the distribution of expected values of snowfall rates, calculated using the expected values of $\log(\lambda)$ and $\log(N_0)$ from the retrieval results. To account for differences in the frequency of occurrence of different reflectivity values, a CFAD-like treatment (Yuter and Houze, 1995) was used. The samples were subset into 1-dBZe bins and the snowfall rates in each subset were histogrammed using bins evenly spaced in the log of the snowfall rate. For each subset, the bin counts were normalized by the bin widths and by the total number of points in the subset.

The variance of the snowfall rate estimated from the retrieval results is typically substantial, and causes the posterior distribution of snowfall rates to be much broader than the distribution of expected values shown in Figure 8.13. The width of this posterior distribution of snowfall rates was estimated by using Monte Carlo sampling to construct a synthetic distribution. For each retrieved snowfall rate and its variance, a sample of 500 snowfall rates was drawn from the corresponding normal distribution. These samples were accumulated along with the corresponding observed reflectivities. This synthetic distribution was subset into 1-dBZe bins, then the mean and standard deviation of snowfall rate was calculated for each subset. In Figure 8.13, the means are shown with the heavy black line while the upper bounds based on +1 standard deviation are shown by the thin black line. Note that since

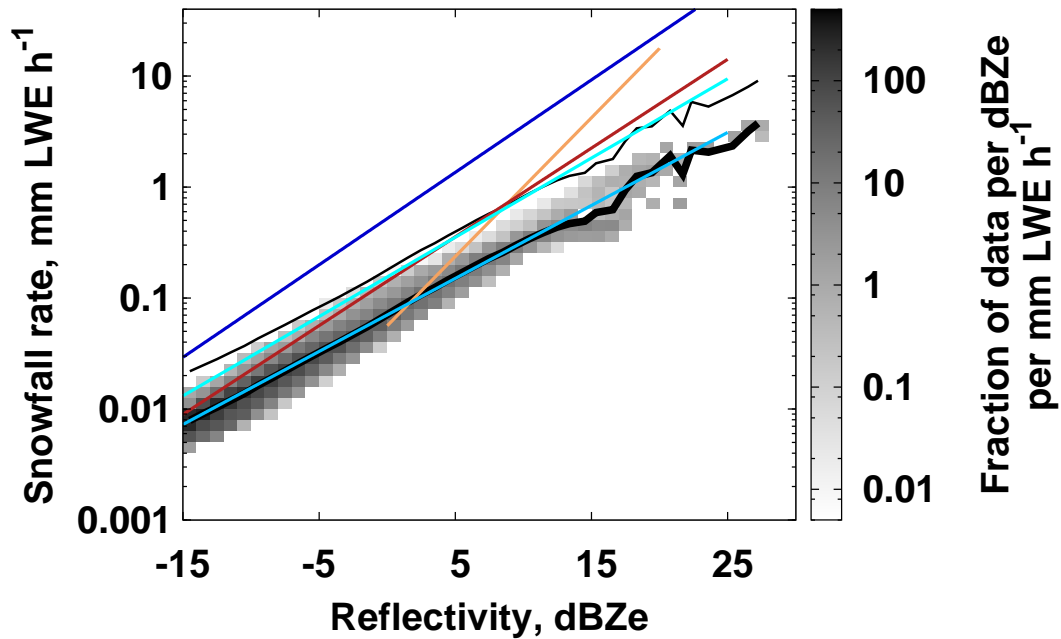


Figure 8.13: Frequency histogram of observed reflectivities and retrieved snowfall rates from CloudSat granule 3916 in grayscale. The black lines show the mean (heavy) and mean plus one standard deviation (thin) of snowfall rate for each reflectivity bin. The remaining lines are Ze-S relations from other studies: red: Liu (2008a); orange: Matrosov (2007); cyan, medium blue, and dark blue: Kulie and Bennartz (2009), models LR3, HA, and SS, respectively.

the standard deviations are larger than the rates themselves, the lower bounds cannot be represented on the logarithmic scale used for snowfall rate.

As 94 GHz radars have not traditionally been used for precipitation research, only a few studies (e.g., Matrosov, 2007; Liu, 2008a; Kulie and Bennartz, 2009) have developed applicable Ze-S relations. Representative relations from these studies are shown in Figure 8.13. Differences among the relations are likely attributable mainly to differences in scattering property models and size distribution assumptions, although differences in fallspeeds will have some affect. Given these differences, the resemblance of the Ze-S relation from CloudSat to that of the Kulie and Bennartz HA relation is striking. More significantly, these results illustrate that although the CloudSat snowfall retrieval nominally relates snowfall to reflectivity in a way similar to these other relations, it allows for a more complex relation than a simple power law.

8.2.3 Results from CARE

The weather for the 22 January 2007 snowfall event was characterized by an extensive, deep, snow-producing system that was over CARE at the time of the 07:30 UTC descending overpass. The system was associated with a low pressure center that was moving from northeastern Indiana into northwestern Ohio during the time of the overpass. A weak low level trough extended from the low pressure center eastward over Lake Erie and into central New York. The system produced light to moderate snowfall over the region north of the trough, covering much of Michigan, southern Ontario and western New York with snow. Observers on the ground at CARE indicated moderate to heavy snowfall occurred between about 03:00 and 08:30 UTC, consisting predominantly of stellar crystals and aggregates early in the event. The DFIR at CARE showed an accumulation of 2.6 mm liquid water equivalent for the 24 hours prior to 13:00 UTC on 22 January, and snowfall rates from the FD12P peaked around 1.5 mm LWE h⁻¹(Figure 8.14). The National Research Council Canada's Convair-580 research aircraft operated near CARE prior to the overpass, performing a spiral descent followed by straight flight legs at several altitudes, then flew along the CloudSat ground track during the overpass. Figure 8.15 shows the profiles of CloudSat reflectivity from the segment of the overpass near CARE. As noted above, CARE is located approximately 24 km west of this segment.

Figure 8.16 shows the snowfall rates and retrieved size distribution parameters for the scene in Figure 8.15. Peak snowfall rates are near 0.35 mm LWE h⁻¹, located in two distinct cells that spatially correspond with peak reflectivities. Values for λ generally increase toward the surface. This pattern is consistent with the temperature-based a priori constraint, but is also clearly influenced by the variations in reflectivity. For example, between 43° and 43.5° latitude, values for $\log(\lambda)$ near the top of the precipitation at 2.5 km AGL are similar to values near 4.5 km between 44° and 44.5°, even though the temperatures at these altitudes are quite different. In contrast, values for $\log(N_0)$ show predominantly vertical variation with weaker horizontal structure. These behaviors are consistent with the information content analysis for the ACR retrieval results, which showed that the retrieved values of

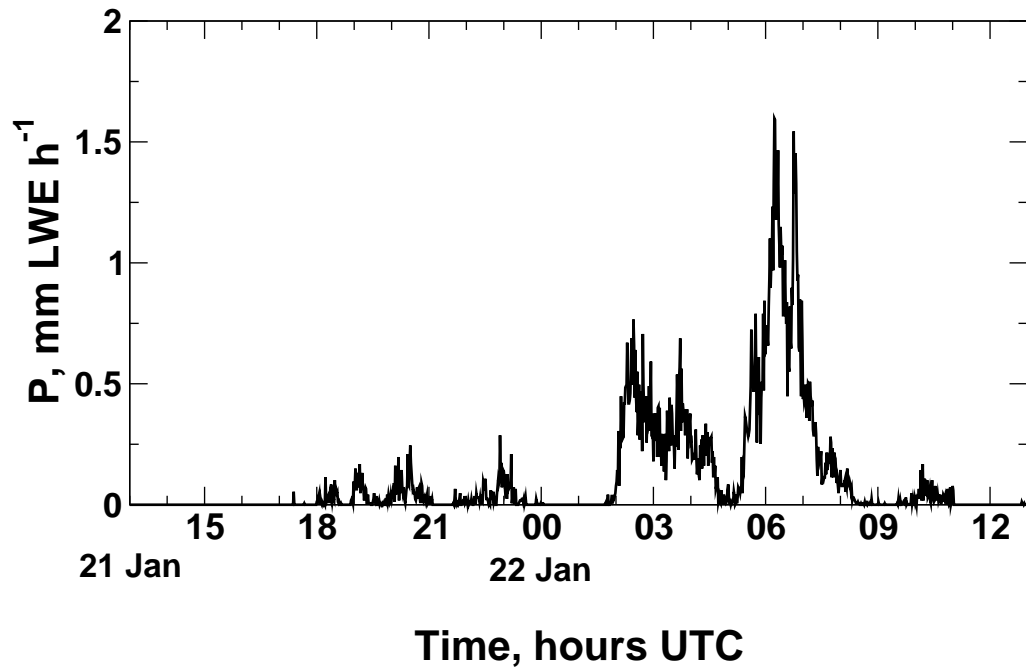


Figure 8.14: Snowfall rates from the FD12P for the 22 January 2007 snowfall event at CARE. The time scale runs from 1300 UTC on 21 January to 1300 UTC on 22 January, the time period over which the daily accumulation is reported. The FD12P rates have been scaled to match the DFIR accumulation.

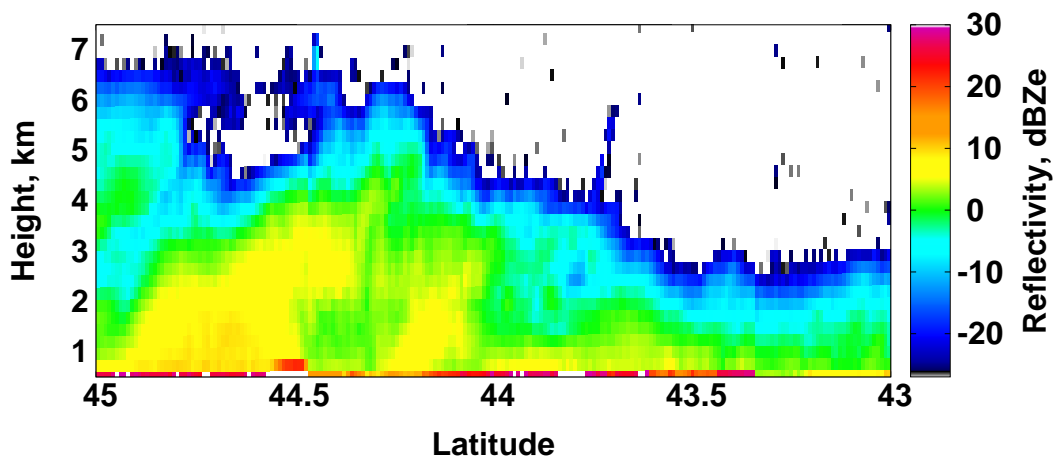


Figure 8.15: CloudSat CPR reflectivities for the 22 January 2007 07:30 UTC pass near CARE. The latitude of CARE is 44.2°.

$\log(\lambda)$ were determined in large part by the reflectivity observations, while retrieved values of $\log(N_0)$ were determined mainly by the a priori state.

Observations of instantaneous precipitation rates or short-term (e.g., hourly) accumulations near the CloudSat ground track are lacking. The nearest instantaneous precipitation rates, shown in Figure 8.14, were at CARE, located approximately 24 km west of the ground-track. Figure 8.17 shows the estimated snowfall rates at the surface and the uncertainties obtained from the CloudSat retrieval. The peak rates from CloudSat are about 0.35 mm LWE h^{-1} , considerably smaller than the peak rates observed at CARE (1.5 mm LWE h^{-1}). At the time of the CloudSat overpass at 07:30 UTC, snowfall at CARE was weakening and had decreased to about 0.2 mm LWE h^{-1} . The low snowfall rates from CloudSat may represent a region of weaker precipitation, but more complete observations would be required to confirm this.

Environment Canada does operate a number of synoptic and climate observing stations in the vicinity of CARE and the CloudSat groundtrack, however. These synoptic and climatic observations of snowfall are typically reported as accumulations over 6-hour or 24-hour intervals. Comparisons of these accumulations for a single snowfall event against accumulations estimated from CloudSat-retrieved instantaneous snowfall rates are likely of limited quantitative value, but can give a qualitative indication of retrieval performance. Accumulation observations from these stations, lying within a $\pm 1^\circ$ latitude and longitude box centered on CloudSat's groundtrack at CARE's latitude of 44.2° , were obtained from the Environment Canada National Climate Data and Information Archive (http://climate.weatheroffice.gc.ca/climateData/canada_e.html, data provided by Peter Rodriguez). The available observations were limited to 24-hour accumulations. The locations of the CloudSat groundtrack, CARE and the stations are shown in Figure 8.18.

For CARE, 24-hour accumulation measurements are made nominally at 08:00 local time, or 13:00 UTC when standard time is in effect, and this is thought to be true for climate stations in the vicinity of CARE (Peter Rodriguez, 22 May 2008, personal communication). CloudSat accumulations and uncertainties were synthesized by taking the instantaneous retrieved snowfall rates and uncertainties from the groundtrack segment shown in Figure 8.18, then multiplying them by an estimated duration of precipitation in the 24 hours

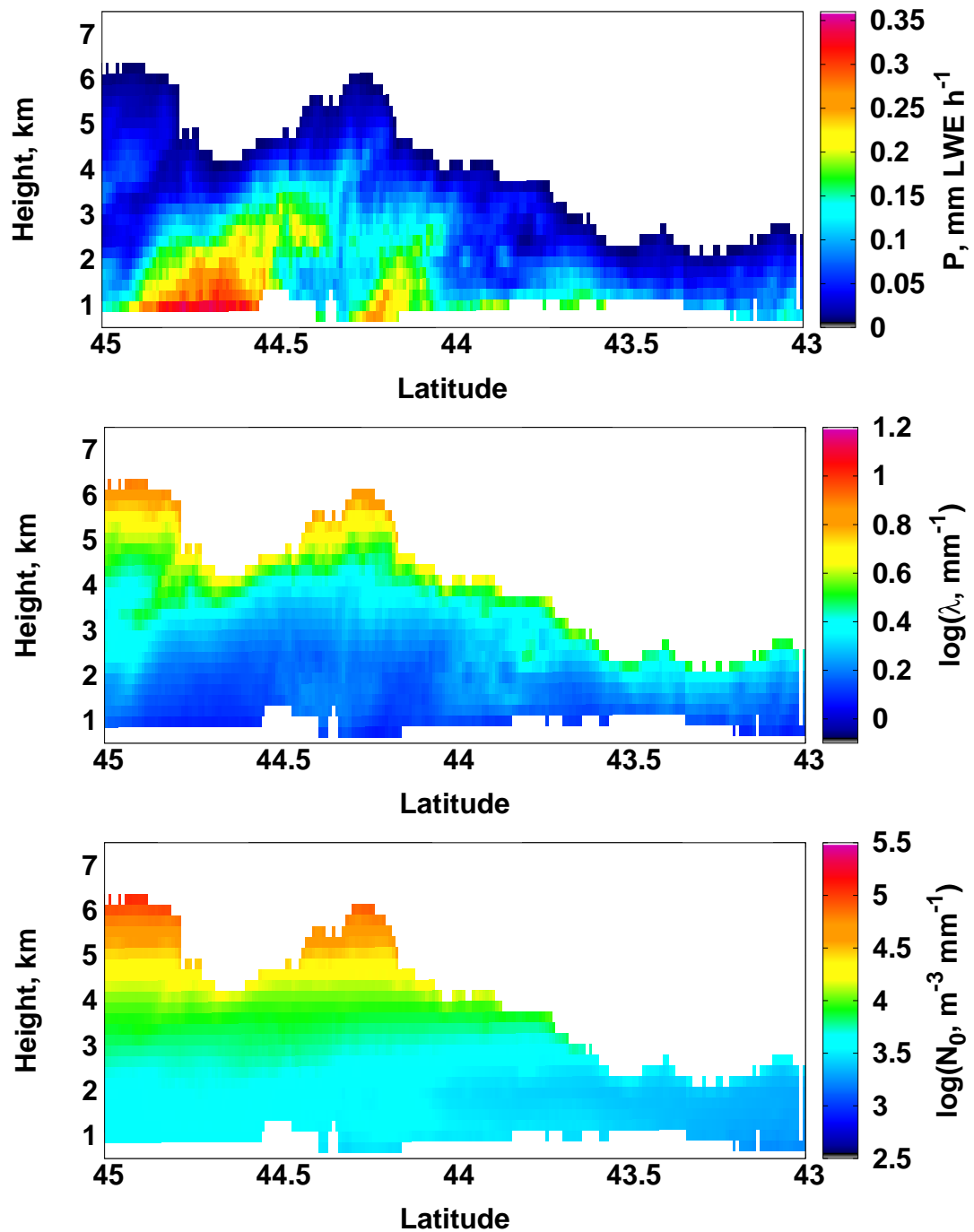


Figure 8.16: Retrieval results for the 22 January 2007 07:30 UTC CloudSat overpass near CARE.

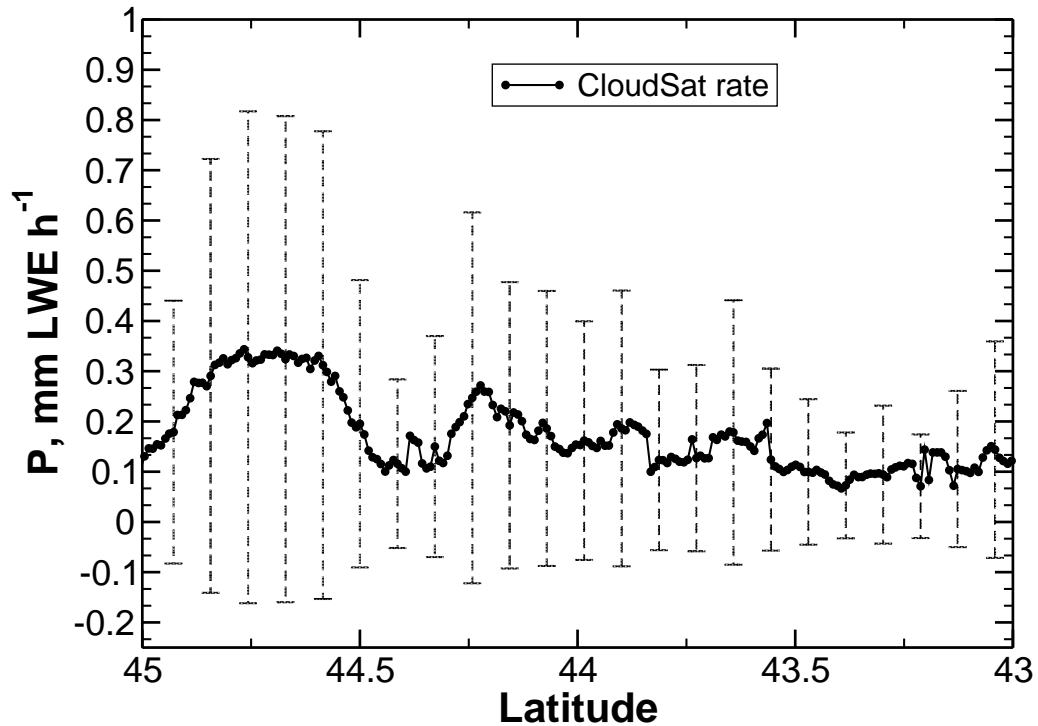


Figure 8.17: Snowfall rates at the surface and uncertainties from CloudSat for the 07:30 UTC overpass on 22 Jan 2007.

prior to 13:00 UTC. This duration of precipitation at CARE, estimated by examining the FD12P precipitation rate time series (Figure 8.14), was 12.4 hours. Four stations reported accumulations substantially higher than the CloudSat accumulations, while four reported no accumulations (Figure 8.19). Of the four with no accumulations, three reported missing values for total rain and total snow but reported zero for total precipitation, while the fourth (at 44.20°N, 78.93°W) reported zero for all three values. Other reported accumulations are in fair agreement with the CloudSat accumulations. Averaged over the entire latitude range, the CloudSat accumulation is 1.52 mm LWE. The average of the observed accumulations including the zero values is 1.26 mm LWE, while with the zero values excluded it is 1.45 mm LWE.

The Convair-580 did not perform a spiral through the storm at the CloudSat ground track during the overpass, but did perform a spiral near CARE between 06:00 and 06:24 UTC. The aircraft was instrumented with a Nevzorov hot-wire probe (Korolev et al., 1998) and a Counterflow Virtual Impactor (CVI) (Twohy et al., 1997) for measuring total water content, in addition to the 2D-C and 2D-P probes. Figure 8.20 compares size distribution

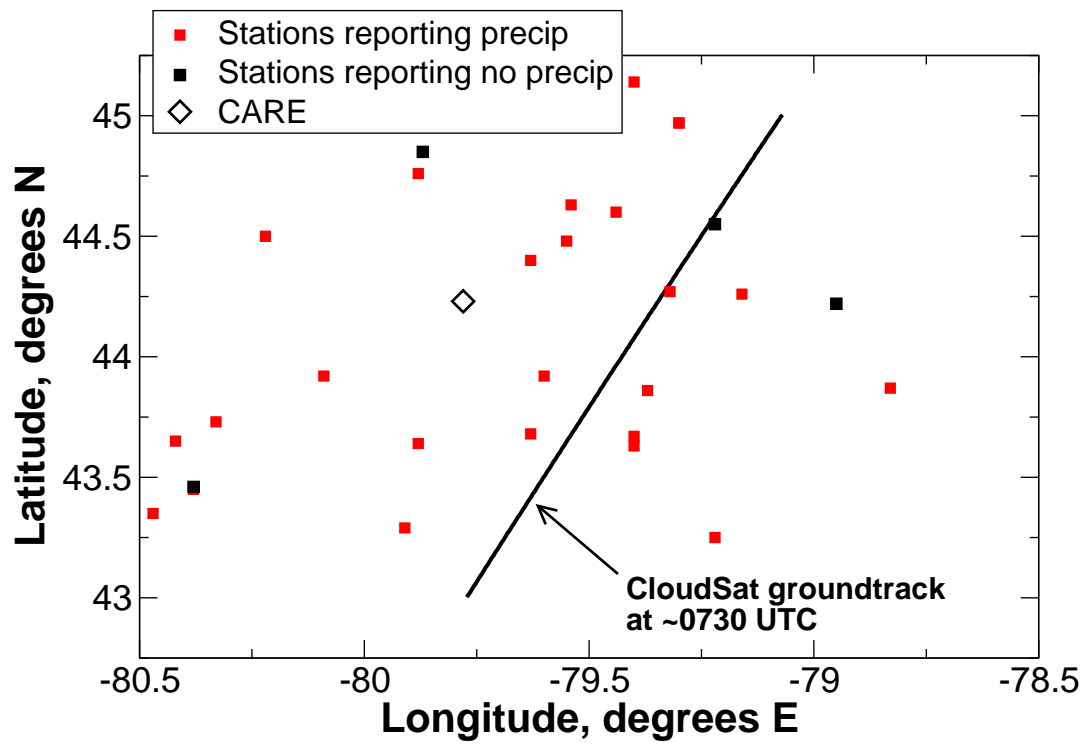


Figure 8.18: Locations of the groundtrack for the 22 January 2007 07:30 UTC CloudSat overpass near CARE and stations reporting 24-hour snowfall accumulations. Stations reporting non-zero accumulations are shown in red, while stations reporting zero accumulations are shown in black.

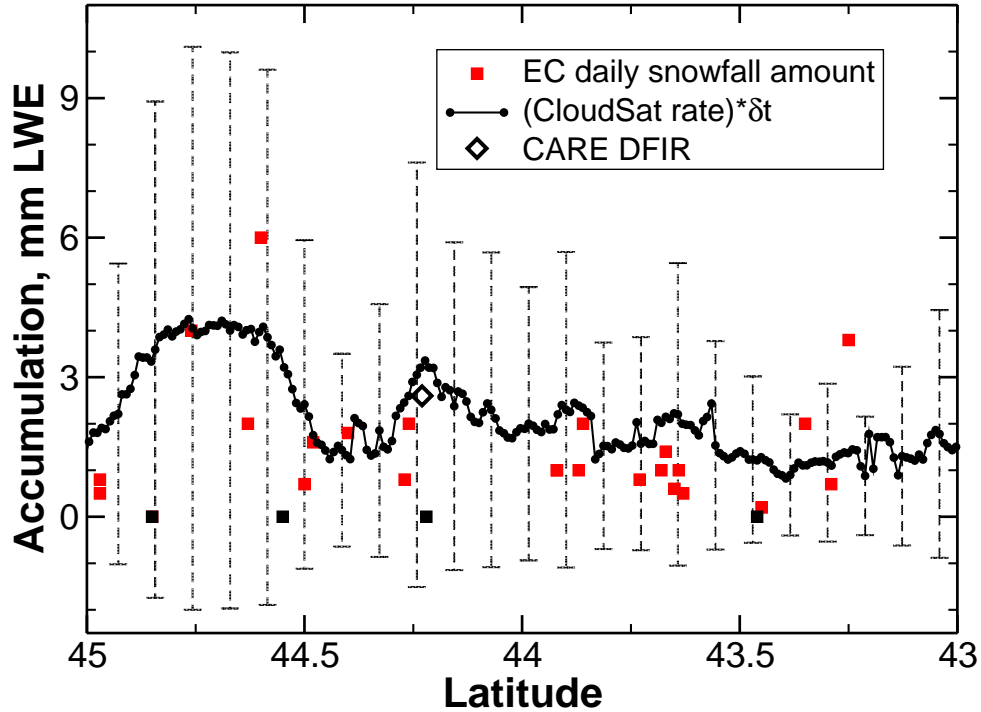


Figure 8.19: Observed snow accumulations compared against accumulations synthesized from snowfall rates retrieved from CloudSat. Black squares indicate observed accumulations that were reported as zero.

parameters obtained from the retrieval and from aircraft observations. The aircraft observations are from the entire duration of the 22 January flight. Retrieved values and their uncertainties were binned into 0.5 km height increments and averaged. For the aircraft, the parameters fitted to the 2D-C and 2D-P observations were similarly binned, then means and standard deviations were computed. The agreement between the retrieved and observed profiles for $\log(\lambda)$ are quite good. For $\log(N_0)$, the uncertainties in the retrieved values are substantially larger than the observed standard deviations, and there is a tendency for the retrieval to underestimate $\log(N_0)$ up to about 5 km.

Figure 8.21 shows ice water contents computed using the retrieved size distribution parameters with the masses from the retrieval particle model. Total water contents observed by the Nevzorov probe and CVI during the spiral descent near CARE are shown for comparison. The cloud was glaciated, with temperatures ranging from 236 K to 262 K during the spiral. The Nevzorov liquid water content measurements were not recorded during this flight, but the CLEX-10 operations log indicates very little supercooled liquid water was

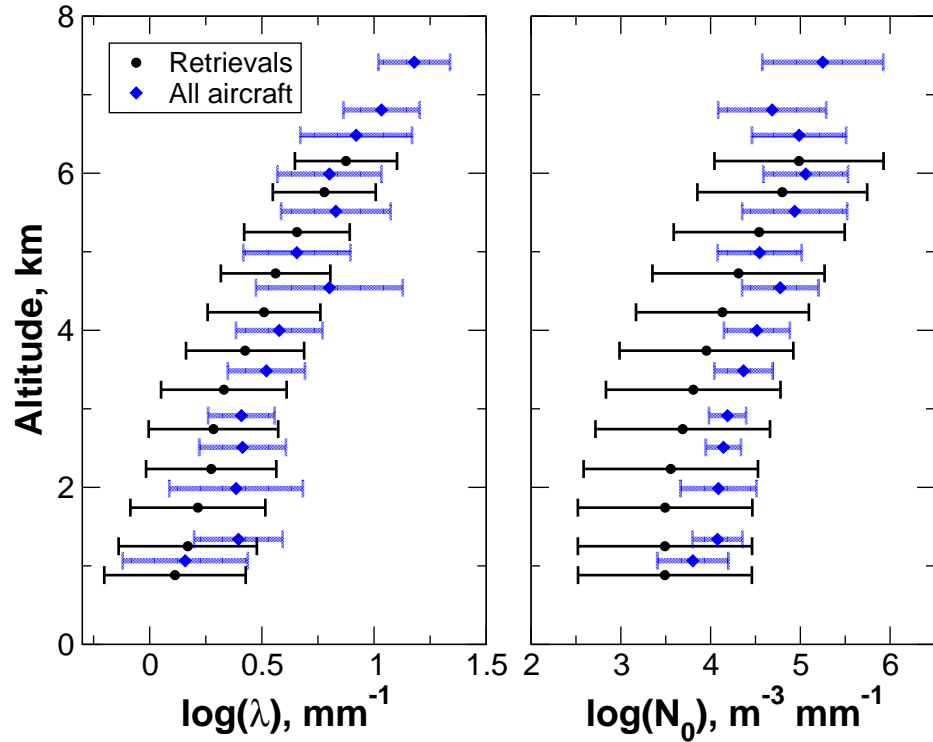


Figure 8.20: Vertical profiles of retrieved and observed size distribution parameters for the 22 January 2007 snowfall event. Black points and error bars indicate vertically binned and averaged values for the retrieved parameters and their uncertainties, obtained from the CloudSat retrieval results for the 07:30 UTC overpass near CARE. Blue points and error bars indicate the means and standard deviations of vertically binned parameters fitted to the aircraft 2D-C and 2D-P observations from the Convair-580 spiral near CARE between 06:00 and 06:24 UTC. Bins were 0.5 km in height.

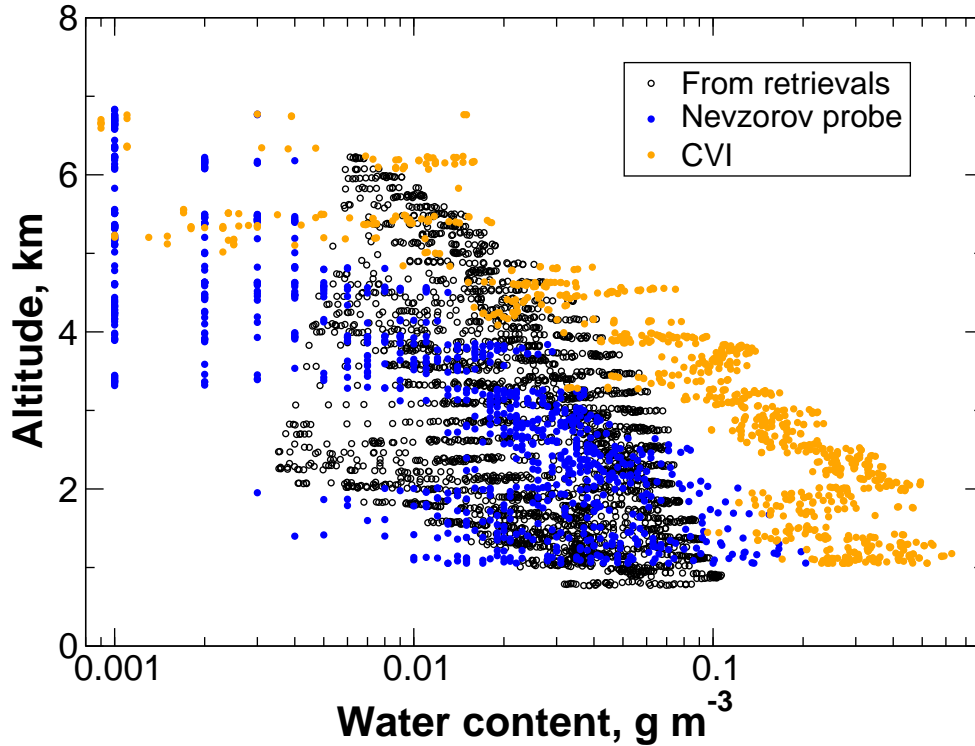


Figure 8.21: Comparison of observed and retrieved water contents from the 22 January 2007 snow event. Observed values were obtained during an aircraft spiral descent near CARE approximately an hour prior to the CloudSat overpass. Nevzorov and CVI measurements are total water content, while the retrieval values are ice water content.

present (CIRA, 2009), presumably based on King probe observations. The retrieved values are in general agreement with those from the Nevzorov at altitudes below 3 km. For higher altitudes, the retrieved values are larger than those from the Nevzorov but similar to those from the CVI. Using observations from the entire C3VP experiment, Korolev et al. (2008) found that when large particles were present, ice water contents measured by the CVI could be a factor of 1.5 to 2 larger than those measured by the Nevzorov, but that the Nevzorov agreed well with ice water contents calculated from 2D probe observations. They concluded that additional studies are required to resolve the discrepancies.

Chapter 9

Discussion and conclusions

A means has been developed for quantifying snowfall that will help to fill in the understanding of the hydrologic cycle, particularly in higher latitudes where snowfall is a significant component of the cycle and where measurements are lacking. This means leverages the observations of radar backscattering profiles available from a satellite-based cloud radar, the CloudSat Cloud Profiling Radar, or CPR. The radar is nadir-looking only, but the orbital configuration is such that the satellite observes latitudes from near 82°N to 82°S , providing a unique view of the structure of clouds and precipitation in remote regions of the Earth. Although designed as a cloud radar, scattering by precipitation-sized particles including snow is significant at the 94 GHz frequency of the radar.

Just as importantly, this research has aimed to assess the strengths and limitations of these observations when used to estimate snowfall. One critical component of this assessment is an appropriate characterization of the errors in the estimated snowfall rates. A second critical component is an evaluation of so-called information content metrics, quantities which illustrate how the reflectivity observations influence the retrieved state, the estimated snowfall rates and the associated uncertainties. Although a number of studies have developed relationships between 94 GHz reflectivity and snowfall rate, this work provides a more complete accounting of the sources of uncertainty and the propagation of these sources into the snowfall rate. This more complete accounting provides for a robust evaluation of the information content metrics. The limitations revealed by these information content metrics can provide guidance about the configuration of future observing systems.

9.1 Overview of the method

The fundamental obstacle addressed in this work is the non-uniqueness of the relationship between radar reflectivity and the microphysical properties of snow particles within a radar range bin. Radar reflectivity alone cannot completely constrain even a simplistic representation of snow particle properties (mass, area and number concentration as functions of particle size) needed to determine snowfall rate. A solution is to incorporate suitable a priori information via Bayesian techniques. This approach was used here, implemented using optimal estimation. Optimal estimation provides the mechanisms not only for incorporating a priori information, but also for propagating measurement, model and a priori uncertainties into the retrieved quantities and for extracting information content metrics. Although limited generally to purely Gaussian representations of probability density functions, it provides a tractable means to initially address these issues.

Prior information about snow microphysical properties is essential to the snowfall retrieval. This information, which describes the expected values and uncertainties in the microphysical properties in the scene observed by the radar, has by necessity often been given cursory treatment in the development of radar-based snowfall retrievals. Early in the work, it was realized that the available a priori information on these properties was insufficient for use in the optimal estimation snowfall retrieval algorithm. While estimates of the best-fit parameters of mass- and area-dimension relations for various habits were available in the literature, there was no reasonable way to construct the required probability density functions for these parameters. In many cases, estimates of both mass and area parameters were not available from the same sample of particles. Thus there was little guarantee of consistency between the mass and area representations.

To address this issue, a bootstrap approach was used. A retrieval was developed which could estimate the probability density functions for these microphysical properties using multisensor observations of snowfall. The results from application of this retrieval to a set of field experiment data then formed the prior microphysical information needed by the snowfall retrieval.

Consequently, the work progressed in two parts. First, the optimal estimation retrieval algorithm was constructed for estimating the probability density functions of the significant microphysical parameters for snow. The algorithm was designed around the observations available from a highly instrumented ground site used for a snowfall field validation campaign. This algorithm was conditioned using an a priori estimate of these properties that was drawn from an extensive set of ground-based measurements of snow properties. Uncertainties for the observations and the associated forward models were characterized. The algorithm was applied to observations from four events, including snow from both synoptic front and lake-effect processes. The resulting PDFs from individual retrievals were then pooled using a Monte Carlo technique to give a single representative PDF for the microphysical properties.

Second, the optimal estimation method was applied to the problem of retrievals from CloudSat CPR observations. The state to be retrieved was defined as vertical profiles of the parameters of exponential size distributions. The expected values from the PDFs of microphysical properties from the first part were used to design particle models with physically consistent mass, area, fallspeed and radar scattering properties. The discrete dipole approximation was applied to a range of particle shapes. This approach allowed forward model uncertainties due to shape to be evaluated, and comparisons against observed reflectivities provided guidance for the selection of a representative shape. Sensitivities of scattering properties to the microphysical parameters were also calculated. These sensitivities allowed the uncertainties in microphysical properties to be propagated into the uncertainties in the retrieved state, and thence into the calculated snowfall rates. A priori estimates of the PDFs of the state variables, the exponential distribution parameters, were derived from aircraft and surface observations from the field validation campaign, but were shown to be consistent with aircraft and surface observations from other field experiments. The resulting retrieval was applied to 94 GHz radar observations from the ground validation site, and also to an orbit of CloudSat observations.

9.2 Principal results

9.2.1 The snow microphysics retrieval

The snow microphysics retrieval of the first part represents a novel approach to integrating independent observations of Rayleigh-regime radar reflectivity, snowfall rate, particle fall-speeds and size distributions to extract snow microphysical properties. Traditional processes for determining these properties can be onerous (e.g., measuring diameters of melted drops to determine the mass of individual particles) or make less complete use of the observations to look at restricted aspects of the microphysical properties (e.g., 2DVD disdrometer estimates of snow particle volume combined with precipitation accumulation to estimate snow particle bulk density). The snow microphysics retrieval produces estimates of size-dependent particle mass and area that give a consistent representation of Rayleigh scattering properties, fallspeeds and snowfall rate for a population of particles. Additionally, these estimates are constructed as PDFs. These PDFs provide information about the variability and uncertainties of these properties, and so have use as inputs to Bayesian retrieval methods.

The results of the retrieval’s application to the C3VP observations showed nontrivial correlations between $\ln(\alpha)$ and $\ln(\gamma)$, between β and σ , and between $\ln(\alpha)$ and σ . These correlations, likely the result of the dependence of fallspeed on $\frac{\alpha}{\gamma}$ and $\beta - \sigma$, are new results which were not apparent in the a priori estimates of these parameters because of the limitations of previous analyses. These correlations form off-diagonal elements in the covariance matrix describing the multidimensional PDF for these parameters, and potentially have significant effects on Bayesian retrievals which incorporate these PDFs.

The retrieval was tasked with determining five pieces of information ($\ln(\alpha)$, β , $\ln(\gamma)$, σ , and ϕ) from five observations (Ze , P , V_0 , ΔV_1 , and ΔV_2). The information content metrics from synthetic tests showed that, given the a priori information, only about two independent and significant pieces of information were provided by the measurements. The measurements contributed principally to the determination of $\ln(\alpha)$, with less significant contributions to the determination of β and $\ln(\gamma)$. Relatively little information was provided for σ and ϕ . Nevertheless, the inclusion of ϕ was found to be essential for correct performance of the retrieval. The Shannon Information Content, H , for these synthetic tests was near

3, indicating that approximately 8 distinct states can be resolved within the state space defined by the a priori.

These information content metrics were used to characterize the benefits that might be achieved by improvements to various aspects of the observations and the retrieval. In particular, the impacts of reduced uncertainties for a number of the inputs to the retrieval were evaluated. The significant uncertainties were due to ground clutter in the VertiX radar profiles, which necessitated the use of reflectivities well above the ground; to the lack of replicate observations of snowfall rate; to the small sample volumes of the SVI; and to uncertainties in the fallspeed forward model. The simulated uncertainty reductions were achieved by assuming that radar reflectivity could be measured adjacent to the other observations; that four replicate snowfall rate measurements were available; that the SVI sample volume was doubled; and that the fallspeed forward model uncertainties were reduced to 10%. While modest improvements to H , the Shannon Information Content, and to d_s , the degrees of freedom for signal, were obtained from the first three improvements, the most significant improvements were achieved when the fallspeed forward model uncertainties were reduced. The overall improvements were an increase from 3.07 to 4.80 for H and an increase from 1.83 to 2.32 for d_s .

9.2.2 The CloudSat snowfall retrieval

The combined information about particle mass and area obtained from the snow microphysics retrieval was exploited in an innovative way for the development of particle scattering models. The discrete dipole approximation model for each particle was constructed using solid-ice dipoles; the placement and number of those dipoles was configured to match not only the mass, but also the horizontally projected area for that particle, ensuring the particle had proper fallspeed characteristics and eliminating the need for approximate treatments of the dipole dielectric properties. Mass and horizontally-projected area, however, were found insufficient to constrain scattering properties to match observed 94 GHz reflectivities; proper vertical aspect ratio was also necessary. Simulated reflectivities calculated using various particle models and observed SVI size distributions were compared against observed reflectivities from the ACR. These particle models used the same mass-dimension

and area-dimension relations but different shapes. Biases computed from these comparisons showed the best agreement between the simulated and observed reflectivities was provided by the B8pr-30 shape, an 8-arm branched spatial shape with a vertical aspect ratio of 0.5. This shape was selected for use in the CloudSat retrieval.

A simple evaluation was performed in which the CloudSat retrieval was applied to ACR observation from C3VP. The retrieved snowfall rates generally agreed with observed rates. Uncertainties in the retrieved rates were typically 100% - 200% and these bounds encompassed most of the observed rates from the FD12P. Uncertainties in the microphysical properties were the dominant contribution to uncertainties in the forward modeled reflectivity, especially for higher reflectivities associated with heavier snow rates. Two anomalies were identified and, in one case, associated with snowfall with microphysical properties that were inconsistent with the assumptions of the retrieval. Of the total accumulation measured during the ACR observations, the retrieval captured 87% with the anomalies removed, 73% with the anomalies included.

Information content metrics showed that, given the a priori information about the size distribution parameters, $\log(N_0)$ was only weakly constrained by the observations. $\log(\lambda)$ was moderately constrained for broad distributions and more strongly constrained for narrower distributions. An unusual, negative value for the \mathbf{A} diagonal element associated with $\log(N_0)$ was shown to be due to the strong positive covariance between $\log(\lambda)$ and $\log(N_0)$ in the a priori. The vertical variations of N_0 and λ within a snow-containing column construct a picture of the microphysical processes occurring in the column. With this retrieval, part of that picture is revealed through λ . The remainder of the picture, however, relies heavily on a priori assumptions describing the temperature dependence of $\log(N_0)$ and the covariance between $\log(N_0)$ and $\log(\lambda)$. The need is clear for additional measurements which would more strongly constrain $\log(N_0)$.

From the application of the retrieval to an orbit of CloudSat data, PDFs of snowfall rate were obtained as a function of reflectivity and cast as a Ze-S relation. The Ze-S relation allows concise comparisons between the results of different studies, but is a limited representation of the true nature of the results of a snowfall retrieval scheme. The expected values from the CloudSat relation bore similarity to a number of recently published Ze-

S relations for 94 GHz radar observations. Most significantly, however, the comparison illustrated the ability of the CloudSat retrieval to explicitly quantify the uncertainties for the retrieved snowfall rates. Truly useful comparisons of such relations can be made when the associated uncertainties are understood.

9.3 Prospects for future work

While insights regarding snowfall at higher latitudes and remote regions will be valuable, higher value will be provided if questions can be answered about the nature of the micro-physical processes producing that snowfall. Given the demonstrated sensitivity of polar climates in general circulation models to greenhouse-gas-induced perturbations, ensuring the adequacy of the parameterizations used by these models seems essential. The zeroth-order question is whether snowfall is reproduced correctly in such models. A first-order, and much richer, question is to ask whether a particular parameterization which might be adequately reproducing observed snowfall is doing so for the right reasons. Answers to such questions will benefit from the results of work like this, especially if the influence of the a priori assumptions on the retrieved state can be reduced.

A fundamental need, then, is to enhance the measurement-based information the retrieval can provide about N_0 , and about λ when distributions are broad. The likely path to meet this need is to incorporate additional observations into the retrieval. Dual-wavelength radar observations have been used to estimate the characteristic particle size, another measure of the distribution width. High frequency microwave brightness temperatures have been shown to be sensitive to ice water path in clouds containing precipitation-sized ice particles. Using the foundation established by the radar-only CloudSat retrieval, additional observations can be introduced and information content metrics evaluated. Toward this end, the DDA models used in this work were constructed to allow calculations of scattering properties for frequencies up to 183 GHz. Calculations for several common radar frequencies (C, Ku and Ka) have been completed and will be extended to include appropriate passive microwave observing frequencies.

A principal concern with the present work is the representativeness of the particle models used in the CloudSat retrieval. These models were derived primarily from surface observations from a single field experiment. While the retrieved microphysical properties used to develop the particle models are not inconsistent with observations from other sources, a number of steps may be taken to improve confidence in these models. An obvious first step is to apply the microphysics retrieval to observations from other field experiments. An initial candidate is the Light Precipitation Validation Experiment (LPVEx), a campaign held in southern Finland September - December 2010. This experiment will provide a rich set of observations of snow using instrumentation similar to C3VP but in a maritime-influenced environment quite different from that of C3VP.

As a second step, aircraft-based radar and in-situ observations can provide several of the quantities needed for the microphysics retrieval, such as Rayleigh-regime radar reflectivity and particle size distributions. Although other observations are lacking (precipitation rate and fallspeeds), the aircraft platform adds observations such as water content and direct measurements of the horizontally-projected areas of particles via images from 2D probes. The optimal estimation framework used for the microphysics retrieval is readily adaptable to these other observations. These sorts of analyses applied to observations from aircraft spirals could provide potentially useful information about the vertical variations and correlations of microphysical properties, and could help reduce forward model uncertainties caused by uncertainties in microphysical properties. Analyses of observations from several aircraft-based field experiments have been initiated.

Finally, the limited testing of the retrieval presented in this work clearly does not demonstrate its validity at global scales. The narrow field-of-view sampling of the nadir-viewing radar and the often high spatial variability of precipitation act to limit the significance of comparisons of retrieved and observed snowfall at small space and time scales. Two avenues suggest themselves for further testing of the retrieval. First, basin- or regional-scale comparisons between CloudSat-derived and observed seasonal accumulations may be useful. These comparisons could be made using locations that have been heavily instrumented for hydrometeorology purposes (e.g., the National Oceanic and Atmospheric Administration's Hydrometeorology Testbed HMT-West effort in the American River Basin of California

and Nevada). With appropriate compensation for CloudSat's sampling of such a region, meaningful comparisons might be developed. Second, synthetic testing could be pursued. Simulations of snowfall events using high-resolution (e.g., cloud-resolving) models could function as synthetic testbeds to which the retrieval could be applied. Although not reported in this work, such a simulation has been completed for a C3VP snow event using Colorado State University's Regional Atmospheric Modeling System (RAMS), and will be used in this manner. LPVEx will provide additional opportunities for such simulations and tests.

Bibliography

- Abraham, F. F., 1970: Functional dependence of drag coefficient of a sphere on Reynolds number. *Phys. Fluids*, **13**, 2194-2195.
- Alexander, M. A., R. Tomas, C. Deser, and D. M. Lawrence, 2010: The atmospheric response to projected terrestrial snow changes in the late twenty-first century. *J. Clim.*, **23**, 6430-6437, doi:10.1175/2010JCLI3899.1.
- Atlas, D., M. Kerker, and W. Hitschfeld, 1953: Scattering and attenuation by non-spherical atmospheric particles. *J. Atmos. Terr. Phys.*, **3**, 108-119.
- Auer, A. H., Jr., and D. L. Veal., 1970: The dimensions of ice crystals in natural clouds. *J. Atmos. Sci.*, **27**, 919-926.
- Austin, R. T., T. S. L'Ecuyer, and C. Seaman, 2007: C3VP ACR operator's log. Unpublished manuscript, in possession of the author.
- Barnett, T. P., L. Dümenil, U. Schlese, E. Roeckner, and M. Latif, 1989: The effect of Eurasian snow cover on regional and global climate variations. *J. Atmos. Sci.*, **46**, 661-685.
- Barnett, T. P., J. C. Adam, and D. P. Lettenmaier, 2005: Potential impacts of a warming climate on water availability in snow-dominated regions. *Nature*, **438**, 303-309, doi:10.1038/nature04141.
- Barthazy, E., S. Goke, R. Schefold, and D. Hogg, 2004: An optical array instrument for shape and fall velocity measurements of hydrometeors. *J. Atmos. Oceanic Technol.*, **21**, 1400-1416.

- Battan, L. J., 1973: *Radar observation of the atmosphere*, TechBooks, Herson, VA, 324 pp.
- Boggs, P. T., R. H. Byrd, J. E. Rogers, and R. B. Schnabel, 1992: User's reference guide for ODRPACK version 2.01 software for weighted orthogonal distance regression. U. S. Department of Commerce, National Institute of Standards and Technology, Applied and Computational Mathematics Division, Gaithersburg, MD. NISTIR 92-4834. 99 pp.
- Bohm, H. P., 1989: A general equation for the terminal fall speed of solid hydrometeors. *J. Atmos. Sci.*, **46**, 2419-2427.
- Bohren, C. F., and S. B. Singham, 1991: Backscattering by nonspherical particles: A review of methods and suggested new approaches. *J. Geophys. Res.*, **96**, 5269-5277.
- Bouniol, D., A. Protat, A. Plana-Fattori, M. Giraud, J.-P. Vinson, and N. Grand, 2008: Comparison of airborne and spaceborne 95-GHz radar reflectivities and evaluation of multiple scattering effects in spaceborne measurements. *J. Atmos. Ocean. Tech.*, **25**, 1983-1995, doi:10.1175/2008JTECHA1011.1.
- Braham, R. R., Jr., 1990: Snow particle spectra in lake effect snows. *J. Appl. Meteorol.*, **29**, 200-207.
- Brandes, E. A., K. Ikeda, G. Zhang, M. Schoenhuber, and R. M. Rasmussen, 2007: A statistical and physical description of hydrometeor distributions in Colorado snowstorms using a video disdrometer. *J. Appl. Meteorol. Clim.*, **46**, 634-650, doi:10.1175/JAM2489.1.
- Brandes, E. A., K. Ikeda, and G. Thompson, 2008: Aggregate terminal velocity/temperature relations. *J. Appl. Meteorol. Clim.*, **47**, 2729-2736, doi:10.1175/2008JAMC1869.1.
- Brown, P. R. A. and P. N. Francis, 1995: Improved measurements of the ice water content in cirrus using a total-water probe. *J. Atmos. Oceanic Tech.*, **12**, 410-414.
- Cooperative Institute for Research in the Atmosphere, cited 2009: CLEX-10 daily operations page [Available online at http://www.cira.colostate.edu/cira//GeoSci/CLEX/clex_main/clex10/clex10.html].

- Clark, M. P., M. C. Serreze, and R. G. Barry, 1996: Characteristics of Arctic Ocean climate based on COADS data, 1980-1993. *Geophys. Res. Lett.*, **23**, 1953-1956.
- Cohen, J., and D. Rind, 1991: The effect of snow cover on the climate. *J. Clim.*, **4**, 689-706.
- Connor, B. J., H. Boesch, G. Toon, B. Sen, C. Miller, and D. Crisp, 2008: Orbiting carbon observatory: Inverse method and prospective error analysis. *J. Geophys. Res.*, **113**, D05305, doi:10.1029/2006JD008336.
- Davis, C. I., 1974: The ice nucleating characteristics of various AgI aerosols. Ph. D. dissertation, University of Wyoming, Department of Mechanical Engineering, 267 pp.
- Dennis, J. E., and R. B. Schnabel, 1983: *Numerical methods for unconstrained optimization and nonlinear equations*. Prentice-Hall, Englewood Cliffs, N. J., 378 pp.
- Doviak, R. J., and D. S. Zrnić, 1993: *Doppler radar and weather observations*. Academic Press, San Diego, 562 pp.
- Draine, B. T., 1988: The discrete-dipole approximation and its application to interstellar graphite grains. *Astrophys. J.*, **333**, 848-872.
- Draine, B. T., and P. J. Flatau, 1994: Discrete-dipole approximation for scattering calculations. *J. Opt. Soc. Am. A*, **11**, 1491-1499.
- Draine, B. T., and P. J. Flatau, 2010: User guide to the discrete dipole approximation code DDSCAT 7.1. [Available online at <http://arXiv.org/abs/1002.1505v1>].
- Eyre, J. R., G. A. Kelly, A. P. McNally, E. Anderson, and A. Persson, 1993: Assimilation of TOVS radiance information through one-dimensional variational analysis. *Q. J. Roy. Meteor. Soc.*, **119**, 1427-1463.
- Fabry, F. and I. Zawadzki, 1995: Long-term radar observations of the melting layer of precipitation and their interpretation. *J. Atmos. Sci.*, **52**, 838-851.
- Feldman, R. M., and C. Valdez-Flores, 2010: *Applied probability and stochastic processes*, 2nd ed. Springer-Verlag, Berlin Heidelberg, 397 pp., doi:10.1007/978-3-642-05158-5.

- Field, P. R., R. J. Hogan, P. R. A. Brown, A. J. Illingworth, T. W. Choullarton, and R. J. Cotton, 2005: Parameterization of ice-particle size distributions for mid-latitude stratiform cloud. *Q. J. Roy. Meteor. Soc.*, **131**, 1997-2017.
- Field, P. R., A. J. Heymsfield, and A. Bansemmer, 2006: Shattering and particle interarrival times measured by optical array probes in ice clouds. *J. Atmos. Ocean. Tech.*, **23**, 1357-1371.
- Gertzman, H. S., and D. Atlas, 1977: Sampling errors in the measurement of rain and hail parameters. *J. Geophys. Res.*, **82**, 4955-4966.
- Goodison, B. E., P. Y. T. Louie, and D. Yang, 1998: WMO solid precipitation measurement intercomparison: Final report. World Meteorological Organization Instruments and Observing Methods Report No. 67, WMO/TD - No. 872. 88 pp. plus 212 pp. Annexes.
- Gordon, G. L., and J. D. Marwitz, 1984: An airborne comparison of three PMS probes. *J. Atmos. Ocean. Tech.*, **1**, 22-27.
- Gordon, G. L., and J. D. Marwitz, 1986: Hydrometeor evolution in rainbands over the California valley. *J. Atmos. Sci.*, **43**, 1087-1100.
- Gosset, M., and H. Sauvageot, 1992: A dual-wavelength radar method for ice-water characterization in mixed-phase clouds. *J. Atmos. Ocean. Tech.*, **9**, 538-547.
- Greco, M., and W. S. Olson, 2008: Precipitating snow retrievals from combined airborne cloud radar and millimeter-wave radiometer observations. *J. Appl. Meteorol. Clim.*, **47**, 1634-1650, doi:10.1175/2007JAMC1728.1.
- Hanesch, M., 1999: Fall velocity and shape of snowflakes. Ph. D. dissertation, Swiss Federal Institute of Technology, 117 pp.
- Haynes, J. M., T. S. L'Ecuyer, G. L. Stephens, S. D. Miller, C. Mitrescu, N. B. Wood, and S. Tanelli, 2009: Rainfall retrieval over the ocean with spaceborne W-band radar. *J. Geophys. Res.*, **114**, D00A22, doi:10.1029/2008JD009973.

- Herzogh, P. H., and P. V. Hobbs, 1985: Size spectra of ice particles in frontal clouds: correlations between spectrum shape and cloud conditions. *Q. J. Roy. Meteor. Soc.*, **111**, 463-477.
- Heymsfield, A. J., 1972: Ice crystal terminal velocities. *J. Atmos. Sci.*, **29**, 1348-1357.
- Heymsfield, A. J., and R. G. Knollenberg, 1972: Properties of cirrus generating cells. *J. Atmos. Sci.*, **29**, 1358-1366.
- Heymsfield, A. J., and M. Kajikawa, 1987: An improved approach to calculating terminal velocities of plate-like crystals and graupel. *J. Atmos. Sci.*, **44**, 1088-1099.
- Heymsfield, A. J. and L. M. Miloshevich, 2003: Parameterizations for the cross-sectional area and extinction of cirrus and stratiform ice cloud particles. *J. Atmos. Sci.*, **60**, 936-956.
- Heymsfield, A. J. and C. D. Westbrook, 2010: Advancements in the estimation of ice particle fall speeds using laboratory and field measurements. *J. Atmos. Sci.*, **67**, 2469-2482, doi:10.1175/2010JAS3379.1.
- Heymsfield, A. J., S. Lewis, A. Bansemer, J. Iaquinta, L. M., Milshevich, M. Kajikawa, C. Twohy, and M. R. Poellet, 2002: A general approach for deriving the properties of cirrus and stratiform ice cloud particles. *J. Atmos. Sci.*, **59**, 3-29.
- Heymsfield, A. J., P. Field, and A. Bansemer, 2008: Exponential size distribution for snow. *J. Atmos. Sci.*, **65**, 4017- 4031, doi:10.1175/2008JAS2583.1.
- Heymsfield, A. J., C. Schmitt, and A. Bansemer, 2010: Improved representation of ice particle masses based on observations in natural clouds. *J. Atmos. Sci.*, **67**, 3303-3318, doi:10.1175/2010JAS3507.1.
- Hobbs, P. V., S. Chang, and J. D. Locatelli, 1974: The dimension and aggregation of ice crystals in natural clouds. *J. Geophys. Res.*, **79**, 2199-2206.

- Hogan, R. J., P. R. Field, A. J. Illingworth, R. J. Cotton, and T. W. Choullarton, 2002: Properties of embedded convection in warm-frontal mixed-phase cloud from aircraft and polarimetric radar. *Q. J. Roy. Meteor. Soc.*, **128**, 451-476.
- Hogan, R. J., P. N. Francis, H. Flentje, A. J. Illingworth, M. Quante, and J. Pelon, 2003: Characteristics of mixed-phase clouds. I: Lidar, radar and aircraft observations from CLARE'98. *Q. J. Roy. Meteor. Soc.*, **129**, 2089-2116.
- Houze, R. A., Jr., P. V. Hobbs, P. H. Herzegh, and D. B. Parsons, 1979: Size distributions of precipitation particles in frontal clouds. *J. Atmos. Sci.*, **36**, 156-162.
- Huang, G.-J., V. N. Bringi, R. Cifelli, D. Hudak, and W. A. Petersen, 2010: A methodology to derive radar reflectivity-liquid equivalent snow rate relations using C-band radar and a 2D video disdrometer. *J. Atmos. Ocean. Tech.*, **27**, 637-651.
- Hudak, D., H. Barker, P. Rodriguez, and D. Donovan, 2006a: The Canadian CloudSat validation project. *Proc. Fourth European Conf. on Radar in Hydrology and Meteorology*, Barcelona, Spain, 609-612. [Available online at <http://www.erad2006.org/>].
- Hudak, D., P. Rodriguez, G. Lee, A. Ryzhkov, F. Fabry, and N. Donaldson, 2006b: Winter precipitation studies with a dual polarized C-band radar. *Proc. Fourth European Conf. on Radar in Hydrology and Meteorology*, Barcelona, Spain, 9-12. [Available online at <http://www.erad2006.org/>].
- Jiusto, J. E., and H. K. Weickmann, 1973: Types of snowfall. *B. Am. Meteorol. Soc.*, **54**, 1148-1162.
- Johnson, N. L., S. Kotz, and N. Balakrishnan, 1994: *Continuous univariate distributions*, Vol. 1, 2nd ed. John Wiley & Sons, Inc., New York. 756 pp.
- Jones, E., T. Oliphant, P. Peterson, and co-authors, 2001: SciPy: Open Source Scientific Tools for Python. Accessed 24 Sep 2010. [Available online at <http://www.scipy.org/>].
- Joss, J. and A. Waldvogel, 1969: Raindrop size distribution and sampling size errors. *J. Atmos. Sci.*, **26**, 566-569.

- Kajikawa, M., 1972: Measurement of falling velocity of individual snow crystals. *J. Meteorol. Soc. Jpn.*, **50**, 577-584.
- Kajikawa, M., 1975: Measurements of falling velocity of individual graupel particles. *J. Meteorol. Soc. Jpn.*, **53**, 476-481.
- Kajikawa, M., 1976: Observation of falling motion of columnar snow crystals. *J. Meteorol. Soc. Jpn.*, **54**, 276-283.
- Kajikawa, M., 1982: Observation of the falling motion of early snow flakes, Part I: Relationship between the free-fall pattern and the number and shape of component snow crystals. *J. Meteorol. Soc. Jpn.*, **60**, 797-803.
- Kajikawa, M., 1989: Observations of the falling motion of early snowflakes, Part II: On the variation of falling velocity. *J. Meteorol. Soc. Jpn.*, **67**, 731-738.
- Kim, M.-J., 2004: A physical model to estimate snowfall over land using microwave measurements. Ph. D. dissertation, University of Washington, Department of Atmospheric Science, 152 pp.
- Korolev, A. and G. Isaac, 2003: Roundness and aspect ratio of particles in ice clouds. *J. Atmos. Sci.*, **60**, 1795-1808.
- Korolev, A. V., J. W. Strapp, G. A. Isaac, and A. N. Nevzorov, 1998: The Nevzorov airborne hot-wire LWC-TWC probe: Principle of operation and performance characteristics. *J. Atmos. Ocean. Tech.*, **15**, 1495-1510.
- Korolev, A. V., J. W. Strapp, G. A. Isaac, and E. Emery, 2008: Improved airborne hot-wire measurements of ice water content in clouds. *Extended Abstracts, 15th Conference on Clouds and Precipitation*, Cancun, Mexico, International Commission on Clouds and Precipitation, CD-ROM, P13.4.
- Kruger, A. and W. F. Krajewski, 2002: Two-dimensional video disdrometer: a description. *J. Atmos. Ocean. Tech.*, **19**, 602-617.

- Kulie, M. S., and R. Bennartz, 2009: Utilizing spaceborne radars to retrieve dry snowfall. *J. Appl. Meteorol. Clim.*, **48**, 2564-2580, doi:10.1175/2009JAMC2193.1.
- L'Ecuyer, T. S., P. Gabriel, K. Leesman, S. J. Cooper and G. L. Stephens, 2006: Objective assessment of the information content of visible and infrared radiance measurements for cloud microphysical property retrievals over the global oceans. Part I: Liquid clouds. *J. Appl. Meteorol. Clim.*, **45**, 20-41.
- Liu, G., 2008a: Deriving snow cloud characteristics from CloudSat observations. *J. Geophys. Res.*, **113**, D00A09, doi:10.1029/2007JD009766.
- Liu, G., 2008b: A database of microwave single-scattering properties for nonspherical ice particles. *B. Am. Meteorol. Soc.*, **89**, 1563-1570.
- Liu, C.-L., and A. J. Illingworth, 1997: Error analysis of backscatter from discrete dipole approximations for different ice particle shapes. *Atmos. Res.*, **44**, 231-241.
- Lo, K. Kenneth, and R. E. Passarelli, Jr., 1982: The growth of snow in winter storms: An airborne observational study. *J. Atmos. Sci.*, **39**, 697-706.
- Lobl, E. S., K. Aonashi, B. Griffith, C. Kummerow, G. Liu, M. Murakami, and T. Wilheit, 2007: Wakasa Bay, an AMSR precipitation validation campaign. *B. Am. Meteorol. Soc.*, **88**, 551-558.
- Locatelli, J. D. and P. V. Hobbs, 1974: Fall speeds and masses of solid precipitation particles. *J. Geophys. Res.*, **79**, 2185-2197.
- Löffler-Mang, M., and J. Joss, 2000: An optical disdrometer for measuring size and velocity of hydrometeors. *J. Atmos. Ocean. Tech.*, **17**, 130-139.
- Mace, G., 2007: Level 2 GEOPROF product process description and interface control document. Algorithm version 5.3. [Available online at http://cloudsat.cira.colostate.edu/ICD/2B-GEOPROF/2B-GEOPROF_PDICD_5.3.doc]
- Magono, C., and T. Nakamura, 1965: Aerodynamic studies of falling snowflakes. *J. Meteorol. Soc. Jpn.*, **43**, 139-147.

- Magono, C., and C. W. Lee, 1996: Meteorological classification of natural snow crystals. *J. Fac. Sci., Hokkaido Univ., Ser. 2*, **7**, 321-335.
- Marks, C. J. and C. D. Rodgers, 1993: A retrieval method for atmospheric composition from limb emission measurements. *J. Geophys. Res.*, **98**, 14939-14953.
- Marshall, J. S., 1953: Precipitation trajectories and patterns, *J. Meteorol.*, **10**, 25-29.
- Matrosov, S. Y., 1998: A dual-wavelength radar method to measure snowfall rate. *J. Appl. Meteorol.*, **37**, 1510-1521.
- Matrosov, S. Y., 2007: Modeling backscatter properties of snowfall at millimeter wavelengths. *J. Atmos. Sci.*, **64**, 1727-1736, doi:10.1175/JAS3904.1.
- Matrosov, S. Y., and A. Battaglia, 2009: Influence of multiple scattering on CloudSat measurements in snow: A model study. *Geophys. Res. Lett.*, **36**, L12806, doi:10.1029/2009GL038704.
- Matrosov, S. Y., A. J. Heymsfield, and Z. Wang, 2005a: Dual-frequency radar ratio of nonspherical atmospheric hydrometeors. *Geophys. Res. Lett.*, **32**, L13816, doi:10.1029/2005GL023210.
- Matrosov, S. Y., R. F. Reinking, and I. V. Djalalova, 2005b: Inferring fall attitudes of pristine dendritic crystals from polarimetric radar data. *J. Atmos. Sci.*, **62**, 241-250.
- Matrosov, S. Y., K. A. Clark, and D. E. Kingsmill, 2007: A polarimetric radar approach to identify rain, melting-layer, and snow regions for applying corrections to vertical profiles of reflectivity. *J. Appl. Meteorol. Clim.*, **46**, 154-166.
- Matrosov, S. Y., C. Campbell, D. Kingsmill, and E. Sukovich, 2009: Assessing snowfall rates from X-band radar reflectivity measurements. *J. Atmos. Ocean. Tech.*, **26**, 2324-2339, doi:10.1175/2009JTECHA1238.1.
- Mitchell, D. L., 1996: Use of mass- and area-dimensional power laws for determining precipitation particle terminal velocities, *J. Atmos. Sci.*, **53**, 1710-1723.

- Mitchell, D. L., and A. J. Heymsfield, 2005: Refinements in the treatment of ice particle terminal velocities, highlighting aggregates. *J. Atmos. Sci.*, **62**, 1637-1644.
- Mitchell, D. L., R. Zhang, and R. L. Pitter, 1990: Mass-dimension relationships for ice particles and the influence of riming on snowfall rates. *J. Appl. Meteorol.*, **29**, 153-163.
- Mitchell, D. L., A. Macke, and Y. Liu, 1996: Modeling cirrus clouds. Part II: Treatment of radiative properties. *J. Atmos. Sci.*, **53**, 2967-2988.
- Morrison, H., and J. O. Pinto, 2006: Intercomparison of bulk cloud microphysics schemes in mesoscale simulations of springtime Arctic mixed-phase stratiform clouds. *Mon. Weather Rev.*, **134**, 1880-1900.
- Muramoto, K., K. Matsuura, and T. Shiina, 1995: Measuring the density of snow particles and snowfall rate. *Electron. Comm. Jpn.*, **3**, 78, 71-79.
- Nakaya, U. and T. Tuneo, 1934: Physical investigations on snow. Part I, snow crystals observed in 1933 at Sapporo and some relations with meteorological conditions. *J. Fac. Sci., Hokkaido Univ., Ser. 2*, **1**, 149-162.
- Nakaya, U. and T. Terada, Jr., 1935: Simultaneous observations of the mass, falling velocity and form of individual snow crystals. *J. Fac. Sci., Hokkaido Univ., Ser. 2*, **1**, 191-200.
- Newman, A. J., P. A. Kucera, and L. F. Bliven, 2009: Presenting the snowflake video imager (SVI). *J. Atmos. Ocean. Tech.*, **26**, 167-179.
- Noh, Y.-J., G. Liu, E.-K. Seo, J. R. Wang, and K. Aonashi, 2006: Development of a snowfall retrieval algorithm at high microwave frequencies. *J. Geophys. Res.*, **111**, D22216, doi:10.1029/2005JD006826.
- Okamoto, H., 2002: Information content of the 95-GHz cloud radar signals: Theoretical assessment of effects of nonsphericity and error evaluation of the discrete dipole approximation. *J. Geophys. Res.*, **107**, doi:10.1029/2001JD001386.

- Okamoto, H., A. Macke, M. Quante, and E. Raschke, 1995: Modeling of backscattering by non-spherical ice particles for the interpretation of cloud radar signals at 94 GHz. An error analysis. *Contrib. Atmos. Phys.*, **68**, 319-344.
- Ono, A., 1969: The shape and riming properties of ice crystals in natural clouds. *J. Atmos. Sci.*, **26**, 138-147.
- Passarelli, R. E., Jr., 1978: Theoretical and observational study of snow-size spectra and snowflake aggregation efficiencies. *J. Atmos. Sci.*, **35**, 882-889.
- Peterson, B. J., J. McClelland, R. Curry, R. M. Holmes, J. E. Walsh, and K. Aagaard, 2006: Trajectory shifts in the Arctic and subarctic freshwater cycle. *Science*, **313**, doi:10.1126/science.1122593.
- Petty, G. W., and W. Huang, 2010: Microwave backscatter and extinction by soft ice spheres and complex snow aggregates. *J. Atmos. Sci.*, **67**, 769-787, doi:10.1175/2009JAS3146.1.
- Potter, B. E., 1991: Improvements to a commonly used cloud microphysical bulk parameterization. *J. Appl. Meteorol.*, **30**, 1040-1042.
- Rodgers, C., 1976: Retrieval of atmospheric temperature and composition from remote measurements of thermal radiation, *Rev. Geophys. Space Phys.*, **14**, 609-624.
- Rodgers, C., 2000: *Inverse methods for atmospheric sounding*, World Scientific Publishing, Singapore. 240 pp.
- Rogers, D. C., 1973: The aggregation of natural ice crystals. M. S. thesis, University of Wyoming, 91 pp.
- Ryan, B. F., 1996: On the global variation of precipitating layer clouds. *B. Am. Meteorol. Soc.*, **77**, 54-70.
- Sadowy, G. A., 1999: A 95 GHz airborne cloud radar: Statistics of cloud reflectivity and analysis of beam-filling errors for a proposed spaceborne cloud radar. Ph. D. dissertation, University of Massachusetts Amherst, 79 pp. [Available from UMI, 300 N. Zeeb Rd., Ann Arbor, MI 48103., UMI number 9932344].

- Schneider, T. L., and G. L. Stephens, 1995: Theoretical aspects of modeling backscattering by cirrus ice particles at millimeter wavelengths. *J. Atmos. Sci.*, **52**, 4367-4385.
- Schönhuber, M., G. Lammer, and W. L. Randeu, 2007: One decade of imaging precipitation measurement by 2D-video-distrometer. *Adv. Geosci.*, **10**, 85-90.
- Sekelsky, S. M., L. Li, G. A. Sadowy, S. L. Durden, S. J. Dinardo, F. K. Li, A. C. Huffman III, G. L. Stephens, H. W. Rosenberger, D. M. Babb, and T. P. Ackerman, 1999: Radar calibration validation for the SGP CART Summer 1998 DC-8 cloud radar experiment. *Proc. Ninth ARM Science Team Meeting*, San Antonio, TX, U. S. Department of Energy, 1-5.
- Sekhon, R. S., and R. C. Srivastava, 1970: Snow size spectra and radar reflectivity. *J. Atmos. Sci.*, **27**, 299-307.
- Sellers, W. D., 1969: A global climatic model based on the energy balance of the Earth-atmosphere system. *J. Appl. Meteorol.*, **8**, 392-400.
- Sheppard, B. E., 1990: Measurement of raindrop size distributions using a small Doppler radar. *J. Atmos. Ocean. Tech.*, **7**, 255-268.
- Sheppard, B. E. and P. I. Joe, 2008: Performance of the precipitation occurrence sensor system as a precipitation gauge. *J. Atmos. Ocean. Tech.*, **25**, 196-212.
- Skofronick-Jackson, G. M., M.-J. Kim, J. A. Weinman, and D.-E. Chang, 2004: A physical model to determine snowfall over land by microwave radiometry. *IEEE T. Geosci. Remote*, **42**, 1047-1058.
- Smith, P. L., 1986: On the sensitivity of weather radars. *J. Atmos. Ocean. Tech.*, **3**, 704-713.
- Stephens, G. L., and N. B. Wood, 2007: Properties of tropical convection observed by millimeter-wave radar systems. *Mon. Weather Rev.*, **135**, 821-842, doi:10.1175/MWR3321.1.

- Stephens, G. L., and coauthors, 2002: The CloudSat mission and the A-train: A new dimension of space-based observations of clouds and precipitation. *B. Am. Meteorol. Soc.*, **83**, 1771-1790.
- Stephens, G. L., and coauthors, 2008: CloudSat mission: Performance and early science after the first year of operation. *J. Geophys. Res.*, **113**, D00A18, doi:10.1029/2008JD009982.
- Sutherland, W., 1893: The viscosity of gases and molecular force. *Philos. Mag., Series 5*, **36**, 507-531.
- Tanelli, S., S. L. Durden, E. Im, K. S. Pak, D. G. Reinke, P. Partain, J. M. Haynes, and R. T. Marchand, 2008: CloudSat's cloud profiling radar after two years in orbit: Performance, calibration and processing. *IEEE T. Geosci. Remote*, **46**, 3560-3573.
- Tang, C., and K. Aydin, 1995: Scattering from ice crystals at 95 and 220 GHz millimeter wave frequencies. *IEEE T. Geosci. Remote*, **33**, 93-99.
- Taylor, J. R., 1997: *An introduction to error analysis*, University Science Books, Sausalito, CA. 327 pp.
- Thurai, M. and V. N. Bringi, 2005: Drop axis ratios from a 2D video disdrometer. *J. Atmos. Sci.*, **22**, 966-978.
- Thurai, M., D. Hudak, and V. N. Bringi, 2008: On the possible use of copolar correlation coefficient for improving the drop size distribution estimates at C band. *J. Atmos. Ocean. Tech.*, **25**, 1873-1880, doi:10.1175/2008JTECHA1077.1
- Twohy, C. H., A. J. Schanot, and W. A. Cooper, 1997: Measurement of condensed water content in liquid and ice clouds using an airborne counterflow virtual impactor. *J. Atmos. Ocean Tech.*, **14**, 197-202.
- Uijlenhoet, R., J. M. Porrá, D. S. Torres, and J.-D. Creutin, 2006: Analytical solutions to sampling effects in drop size distribution measurements during stationary rainfall: Estimation of bulk rainfall variables. *J. Hydrol.*, **328**, 65-82.

- Vaisala Oyj, 2002: Weather sensor FD12P user's guide M210296en-A, Vaisala Oyj, Helsinki, 154 pp.
- van de Hulst, H. C., 1981: *Light scattering by small particles*. Dover Publications, New York. 470 pp.
- Vavrus, S., 2007: The role of terrestrial snow cover in the climate system. *Clim. Dyn.*, **29**, 73-88, doi:10.1007/s00382-007-0226-0.
- Warren, S. G., 1984: Optical constants of ice from the ultraviolet to the microwave. *Appl. Optics*, **23**, 1206-1225.
- Warren, S. G. and R. E. Brandt, 2008: Optical constants of ice from the ultraviolet to the microwave: A revised compilation. *J. Geophys. Res.*, **113**, D14220, doi:10.1029/2007JD009744.
- Winker, D. M., W. H. Hunt, and M. J. McGill, 2007: Initial performance assessment of CALIOP. *Geophys. Res. Lett.*, **34**, L19803, doi:10.1029/2007GL030135.
- Woods, C. P., M. T. Stoelinga, and J. D. Locatelli, 2008: Size spectra of snow particles measured in wintertime precipitation in the Pacific Northwest. *J. Atmos. Sci.*, **65**, 189-205, doi:10.1175/2007JAS2243.1.
- Yuter, S. E., and R. A. Houze, Jr., 1995: Three-dimensional kinematic and microphysical evolution of Florida cumulonimbus. Part II: Frequency distributions of vertical velocity, reflectivity, and differential reflectivity. *Mon. Weather Rev.*, **123**, 1941-1963.
- Zawadzki, I., F. Fabry, and W. Szyrmer, 2001: Observations of supercooled water and secondary ice generation by a vertically pointing X-band Doppler radar. *Atmos. Res.*, **59-60**, 343-359.
- Zikmunda, J., and G. Vali, 1972: Fall patterns and fall velocities of rimed ice crystals. *J. Atmos. Sci.*, **29**, 1334-1347.
- Zikmunda, J., and G. Vali, 1977: Corrigendum. *J. Atmos. Sci.*, **34**, 1675.

Appendix A

Disdrometer dimensional errors

To evaluate the magnitudes of these differences, a series of simulations were done using idealized snow particles modeled as scalene ellipsoids. The ellipsoids were defined using three distinct dimensions: a long dimension “ a ” lying nominally in the horizontal plane along the x axis, a short dimension “ b ” also lying nominally in the horizontal plane normal to “ a ” and along the y axis, and a short vertical dimension “ c ” normal to the horizontal plane and lying along the z axis. The true maximum dimension of the particle is $2a$. Particle orientation was varied by applying uniformly distributed rotations about the z axis and canting at two distinct angles about the x and y axes. The canting angles were distributed over the range of $\pm 21^\circ$ and weighted per a normal distribution with a standard deviation of 9° based on the estimates of Matrosov et al. (2005b) for pristine particles.

Various measures of particle dimension consistent with the disdrometer observations were estimated from the simulations, averaged over all orientations and compared with the true maximum dimension for a range of particle aspect ratios defined by b/a and c/a . Table A.1 summarizes these measures. The value of a was fixed at 0.5, giving a true maximum dimension of 1.0, while $0.05 \leq b \leq a$ and $0.05 \leq c \leq b$. These ranges produced particles that varied from column-like to plate-like to spherical. Values for ϕ , the ratio of the observed to the true maximum dimension, ranged from 0.3 to 1.0 (Figure 3.1). The measure based on area ($D_{SVI,ec}$) is sensitive to both the vertical aspect ratio c/a and the horizontal aspect ratio b/a , while those based on maximum width or feret diameter are minimally sensitive to the vertical aspect ratio. Of the latter, the measure based on feret diameter shows somewhat

Table A.1: Definitions of particle dimensions measured by SVI and 2DVD disdrometers.

Dimension	Description
$D_{SVI,ec}$	Diameter of a circle with area equal to that observed by the SVI
$D_{SVI,w}$	Distance between horizontal extrema of the SVI particle image
$D_{SVI,f}$	Distance between the two furthest removed points on the SVI particle image (feret diameter)
$D_{2DVD,w}$	Maximum of the horizontal extrema obtained from the two oblique 2DVD particle images

less sensitivity to the horizontal aspect ratio than do those based on width. Calculations using canting angles with a standard deviation of 18° showed similar results. The variation in ϕ is due mainly to the variation in particle shape, rather than canting angle, provided canting angles are not extreme.

How significant are the errors introduced by treating a disdrometer observation of D as the maximum dimension? An exponential size distribution based on the true maximum dimension D_M is

$$N(D_M) = N_{0,M} \exp(-\lambda_M D_M). \quad (\text{A.1})$$

Transforming this distribution to use D_{obs} as the independent variable gives

$$N(D_{obs}) = N(D_M) \frac{\partial D_M}{\partial D_{obs}} = \frac{N_{0,M}}{\phi} \exp\left(-\frac{\lambda_M}{\phi} D_{obs}\right). \quad (\text{A.2})$$

where it has been assumed that ϕ is constant over the entire distribution. The transformation from D_M to D_{obs} results in a distribution with steeper slope and larger intercept. Although the zeroth moments are the same for both distributions, higher order moments are different and quantities such as reflectivity which depend on higher order moments will be affected. Reflectivities can be calculated for both cases, one in which the disdrometer truly observes D_M and a second in which D_{obs} is erroneously taken to be D_M . Applying the mass power law (3.23) with the distribution (A.2) and calculating reflectivity per (3.16)

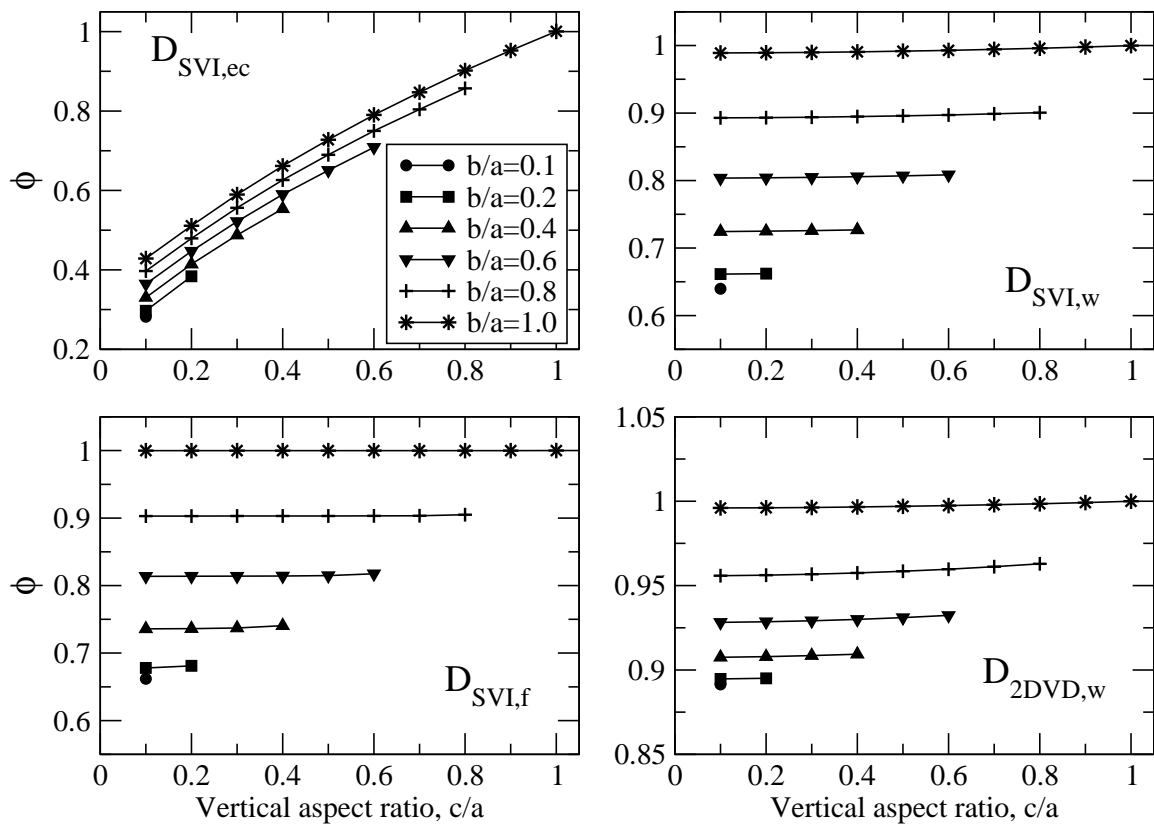


Figure A.1: Figure 3.1, reproduced here for convenience. Values of ϕ , the ratio of D observed by SVI and 2DVD disdrometers to true maximum dimension D_M .

gives

$$Z_{e,obs} = \frac{36\alpha^2}{\pi^2 \rho_{ice}^2} \frac{\|K_i\|^2}{\|K_w\|^2} \frac{N_{0,M}}{\phi} \frac{\Gamma(2\beta + 1)}{(\lambda_M/\phi)^{2\beta+1}}, \quad (\text{A.3})$$

while that for distribution (A.1) is

$$Z_{e,M} = \frac{36\alpha^2}{\pi^2 \rho_{ice}^2} \frac{\|K_i\|^2}{\|K_w\|^2} N_{0,M} \frac{\Gamma(2\beta + 1)}{\lambda_M^{2\beta+1}}, \quad (\text{A.4})$$

where Γ is the gamma function. The ratio of the reflectivities is

$$\frac{Z_{e,obs}}{Z_{e,M}} = \frac{N_{0,M}/\phi}{N_{0,M}} \frac{\lambda_M^{2\beta+1}}{(\lambda_M/\phi)^{2\beta+1}} = \phi^{2\beta}. \quad (\text{A.5})$$

Taking a typical horizontal aspect ratio of 0.6 (Korolev and Isaac, 2003) gives $\phi \approx 0.82$ for $D_{obs} = D_{SVI,f}$. A common estimate for b is 1.9 (Brown and Francis, 1995), resulting in a reflectivity ratio of 0.47. Thus Z_e modeled using $N(D_{obs})$ will be underestimated by 3.2 dBZ. In order for a modeled value of $Z_{e,obs}$ to match an observed Z_e , the coefficient α would have to be overestimated by almost 50%. The cap on particle mass exacerbates this effect. A secondary but significant effect of this overestimate of particle mass is that particle areas would also have to be overestimated in order to match observed fallspeeds. Because of the cap placed on particle areas, the fallspeed forward model might be unable to match observed fallspeeds, causing the retrieval to either fail to converge or to produce large χ^2 values.

Appendix B

A priori data sets

The a priori mass-dimension relations used in this work include results from Zikmunda and Vali (1972), Locatelli and Hobbs (1974), and Mitchell et al. (1990), as well as relations from Mitchell (1996) which do not duplicate results from the earlier studies. Values of α and β for these studies are tabulated in Table B.1. Additionally, new power laws were derived from the Kajikawa observations introduced in Section 3.4. The methods used to develop these new power laws and the resulting parameter values are described in section B.1 below.

Similarly, a priori area-dimension relations used in this work include results from Heymsfield (1972), Mitchell (1996), and Heymsfield and Miloshevich (2003), except that the results in Heymsfield and Miloshevich (2003) given for observations by M. Kajikawa are omitted in favor of the results shown in Section B.1 below. Values for γ and σ from these studies are tabulated in Table B.3 below, and those derived from the Kajikawa observations are described in section B.1 below.

B.1 Analysis of Kajikawa observations

Kajikawa (1972, 1975, 1982) made observations of snow particles representing a wide range of habits over a number of winter seasons. The observations included measurements of fallspeeds, photomicrographs of individual particles, and measurements of melted drop diameters from which particle masses could be assessed. Heymsfield and Kajikawa (1987) utilized Kajikawa's observations of the planar crystals and graupel to develop mass-dimension

Table B.1: A priori estimates of α and β for various habits. P(a) is “Assemblages of planar polycrystals in cirrus clouds”. Suffixes on the habit codes indicate densely rimed (R), rimed (r), fragments (f) and aggregated (a). In some cases, habit codes are approximate based on textual descriptions in the referenced sources. The values for bullet rosettes (C2a) from M96 are for 5-arm rosettes. M96: Mitchell (1996); LH74: Locatelli and Hobbs (1974); Mea90: Mitchell et al. (1990); ZV72: Zikmunda and Vali (1972).

Habit	α	β	Dmin	Dmax	Source
	(cgs)		μm	μm	
P1a	0.00739	2.45	15	100	M96
P1a	0.00739	2.45	100	3000	M96
N1e	0.1677	2.91	30	100	M96
N1e	0.00166	1.91	100	300	M96
N1e	0.000907	1.74	300	–	M96
R1b	0.00145	1.8	200	2400	M96
P1b	0.00614	2.42	10	40	M96
P1b	0.00142	2.02	40	2000	M96
P1c	0.00583	2.42	10	100	M96
P1c	0.000516	1.80	100	1000	M96
P1d	0.00583	2.42	10	90	M96
P1d	0.000270	1.67	90	1500	M96
C2a	0.00308	2.26	200	1000	M96
P(a)	0.00739	2.45	20	450	M96
R4b	0.042	3.0	500	2000	LH74
R4b	0.0492	2.8	500	3000	LH74
R4b	0.0702	2.7	500	1000	LH74
R4c	0.0291	2.6	800	3000	LH74
R4a	0.0350	2.9	800	3200	LH74
R3b	0.00743	2.1	500	2200	LH74
R3a	0.00527	2.4	800	2800	LH74
R1b	0.00658	2.3	800	2000	LH74
R2b	0.00299	2.3	1800	4000	LH74

Table B.2: Continuation of Table B.1.

Habit	α	β	Dmin	Dmax	Source
	(cgs)		μm	μm	
P7b(R)	0.00491	2.1	800	2800	LH74
P7b(a)	0.00183	1.4	2000	10000	LH74
P7b(Ra)	0.00294	1.9	2000	12000	LH74
S3(a)	0.00294	1.9	1000	3000	LH74
S1(a)	0.00100	1.4	500	4000	LH74
N1a	0.000309	1.8	600	2700	Mea90
R1a	0.000755	2.1	500	2800	Mea90
N1e	0.000757	1.8	200	1500	Mea90
R1b	0.001451	1.8	200	2400	Mea90
N2c	0.00107	1.8	200	2600	Mea90
N2c(r)	0.00199	1.9	300	4900	Mea90
C1e	0.0255	2.6	200	600	Mea90
P1a	0.00885	2.5	200	1000	Mea90
P7a	0.00239	2.1	200	3000	Mea90
S1	0.00419	2.3	300	2500	Mea90
R3b	0.0108	2.2	200	2800	Mea90
R3b(f)	0.00135	1.7	300	1900	Mea90
S1(a)	0.00333	2.2	600	4100	Mea90
S3	0.00277	2.1	800	4500	Mea90
P7a(a)	0.000414	1.8	800	7700	Mea90
R3b(fa)	0.0034	2.0	500	4800	Mea90
R4b	0.079	2.53	750	2300	ZV72
R4c	0.035	2.15	600	1900	ZV72

Table B.3: A priori estimates of γ and σ for various habits. P(a) is “Assemblages of planar polycrystals in cirrus clouds” for M96 and “Aggregate planar crystals” for HM03. The values for bullet rosettes (C2a) from M96 are for 5-arm rosettes, and the C2a values from HM03 are based on samples consisting predominantly of 5-arm rosettes. Suffixes on the habit codes indicate densely rimed (R), rimed (r), fragments (f) and aggregated (a). In some cases, habit codes are approximate based on textual descriptions in the referenced sources. M96: Mitchell (1996); H72: Heymsfield (1972); HM03: Heymsfield and Miloshevich (2003).

Habit	γ	σ	Dmin	Dmax	Source
	(cgs)		μm	μm	
P1d	0.109	1.52	240	–	H72
P1c	0.178	1.62	300	–	H72
P1e	0.178	1.62	300	–	H72
P2g	0.122	1.37	700	–	H72
P1a	0.25	1.85	15	100	M96
P1a	0.65	2.00	100	3000	M96
N1e	0.684	2.00	30	100	M96
N1e	0.0696	1.50	100	300	M96
N1e	0.0512	1.414	300	–	M96
R1b	0.0512	1.414	200	2400	M96
P1b	0.24	1.85	10	40	M96
P1b	0.55	1.97	40	2000	M96
P1c	0.24	1.85	10	100	M96
P1c	0.21	1.76	100	1000	M96
P1d	0.24	1.85	10	90	M96
P1d	0.11	1.63	90	1500	M96
R2b	0.21	1.76	1800	4000	M96
S1	0.2285	1.88	300	2500	M96
C2a	0.0869	1.57	200	1000	M96
S1(a)	0.2285	1.88	600	4100	M96
S3(a)	0.2285	1.88	800	4500	M96
P(a)	0.2285	1.88	20	450	M96
R4b	0.50	2.0	500	3000	M96
C2a	0.0982	1.649	100	1000	HM03
C2a(a)	0.1272	1.68	200	1500	HM03
C2a(a)	0.1461	1.753	100	1400	HM03
C2a	0.1076	1.554	380	1610	HM03
N1e	0.0479	1.589	90	470	HM03
S1	0.254	1.834	130	1140	HM03
S1	0.1178	1.591	380	1680	HM03
S1(a)	0.245	1.859	510	2100	HM03
P1a,P1b	0.384	1.864	130	970	HM03
P1c,P1e	0.0558	1.426	270	980	HM03
P1c,P1e	0.192	2.00	1110	3770	HM03
P(a)	0.204	1.623	1740	4760	HM03

power laws for these habits. Recently, Heymsfield and Westbrook (2010) applied digital image edge detection techniques to Kajikawa’s particle images to obtain improved estimates of dimensions and areas, using the resulting data in conjunction with the fallspeed observations to evaluate and improve particle fallspeed models. The data are nearly unique, representing some of the few observations for which simultaneous evaluations of particle habit, dimension, mass, and area can be made.

As part of this work, these reanalyzed data were used to develop new mass-dimension and area-dimension power laws which were then incorporated into the a priori constraints for the snow microphysics retrieval. In all, fits were performed for 24 distinct single-particle habits (437 particles); 8 varieties of early aggregates (185 particles), consisting of 2-6 crystals of similar habit; and 5 types consisting of rosettes or of assemblages containing side planes (79 particles). The reanalyzed single-particle data consist primarily of planar particles. Properties of some of these single particles, observed at the surface at Hokkaido University’s Mount Teine Observatory (1024 m MSL) at temperatures of -7°C , were previously described by Kajikawa (1972). The early aggregates were also observed at Mount Tiene Observatory (Kajikawa, 1982). The rosettes and assemblages were collected at the surface at Akita University’s Mount Hachimantai Observatory (1200 m MSL) at temperatures of -9° to -11°C (Heymsfield et al., 2002).

Particles were first grouped by habit, then fits were performed using a Python-based implementation of ODRPACK (Boggs et al., 1992; Jones et al., 2001) configured for orthogonal distance regression. Uncertainties in mass, area and dimension were not provided with the data and were estimated. Measurement uncertainties for particle dimension are likely dependent on magnification and contrast in the original photomicrographs, as well as the resolution at which the images are digitized. Visual examination of typical photomicrographs (e.g., Figures 2 and 3 from Kajikawa (1972), and Figure 2 from Mitchell et al. (1990)) suggests that uncertainties in D on the order of 0.025 to 0.05 mm would be reasonable, although this estimate is undoubtedly influenced by the resolution at which the photomicrographs were reproduced for publication. Other factors influence the dimensional uncertainty. After settling onto the collection surface, particles could be oriented such that the true D_M would not be evident in the image. Portions of particles may collapse or de-

form after they are collected. Limited depth of field may cause portions of spatial particles and aggregates to be out of focus when photographed, causing those portions to be ignored during edge detection. See for example Figure 4 of Heymsfield et al. (2002). Estimating the magnitudes of the uncertainties for these additional factors is difficult without additional data. Lacking this data, it was assumed that each photomicrograph adequately represent the dimensions of the particle, that edge detection identifies the complete outline of the particle, and that D_M is determined with an uncertainty of 0.05 mm.

The techniques commonly used to determine particle mass in these observations were to measure the diameter of liquid droplets resulting when the snow particles were melted on a substrate of silicone oil or on a substrate of white Vaseline. The former technique results in nearly spherical liquid droplets and was used for the single particle observations as described by Kajikawa (1972), while the latter technique produces nearly hemispherical droplets and was used for the early aggregate observations (Kajikawa, 1982). For the spherical droplets, the measured diameter associated with an observed mass m is given by

$$D_{sphere} = \left(\frac{6m}{\pi\rho_{liq}} \right)^{1/3} \quad (\text{B.1})$$

where ρ_{liq} is the density of liquid water. Assuming this diameter is measured to the same uncertainty 0.05 mm as is D_M and ignoring any additional errors due to nonsphericity or breakup of a particle into multiple drops, an estimate of the error δ_m in mass is given by

$$\delta_m = \rho_{liq} \frac{\pi}{6} \left[(D_{sphere} + 0.005)^3 - D_{sphere}^3 \right] \quad (\text{B.2})$$

where D_{sphere} is in cm. The above expressions were used to evaluate errors for the pristine particles, and similar expressions developed for hemispherical droplets were applied for the early aggregates, rosettes and assemblages.

Uncertainties for area were estimated using the standard deviations of samples of particles with identical habit and approximately equal dimension. For each habit, particles were binned by dimension using bins of width 0.05 mm. Twenty three bins contained three or more particle, and standard deviations were computed for each of these bins. The standard

deviations varied approximately linearly with the measured areas (Figure B.1). Uncertainties for area were modeled as 12% of the measured area, with minimum uncertainties set at 0.0001 cm² based on the lower limits of the results in Figure B.1.

Table B.4 gives mass-dimension fit results for the pristine habits, while Table B.5 contains results for the early aggregates, rosettes, and assemblages. The habit codes follow the scheme of Magono and Lee (1996), and the early aggregates are indicated by the suffix “(a)” added to the habit code. Estimated uncertainties for α and β are shown in parentheses following the fitted values. Also shown is the covariance between α and β , and the normalized χ^2 value for each fit. A normalized χ^2 value near 1.0 suggests a good fit. Tables B.6 and B.7 give area-dimension fit results in the same format. Poor fits, as evidenced by large uncertainties or unphysical values for the fitted parameters, generally occur when the range of particle sizes for a particular sample is small (e.g., the C1h, P4b, P1b(a), C2b and CP2a habits).

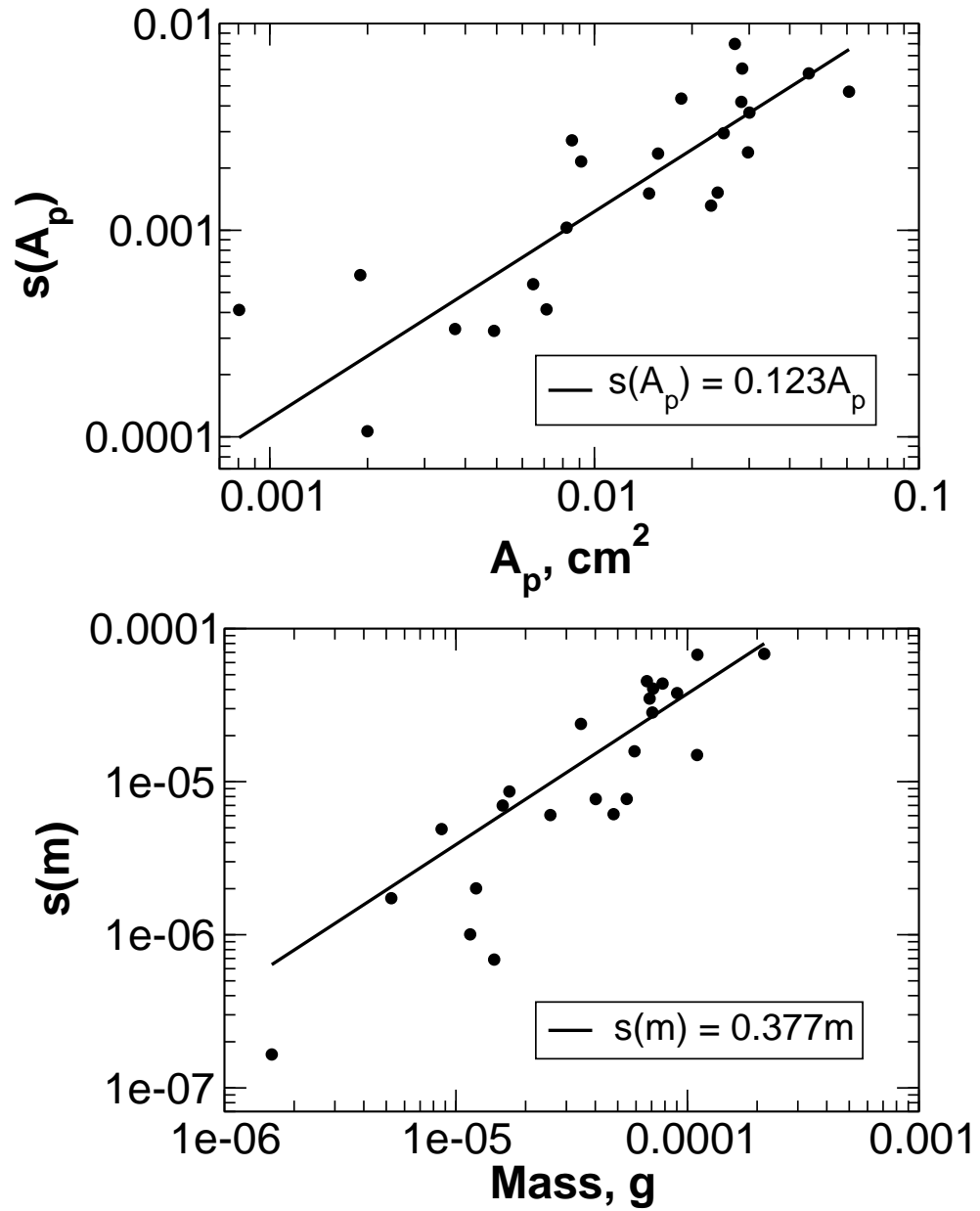


Figure B.1: Standard deviations of area (upper panel) and mass (lower panel) for samples from the reanalysis of Kajikawa's snow particles.

Table B.4: Mass fit results for Kajikawa pristine particles.

Habit	N	Dmin	Dmax	α	β	Covariance	Normed
		μm	μm	(cgs)			chi-sq
P1a	32	25	149	0.00364 (0.00375)	2.47 (0.46)	0.00171	1.45
C1h	8	30	54	0.00451 (0.00253)	2.13 (1.74)	0.0439	0.161
P1b	19	39	162	0.00297 (0.00352)	2.53 (0.55)	0.00193	0.269
P2e	18	47	211	0.00190 (0.00164)	2.42 (0.48)	7.76e-04	0.450
P2f	5	83	234	0.00253 (0.00278)	2.37 (0.63)	0.00173	0.0363
P2g	10	70	280	0.0106 (0.0110)	3.50 (0.71)	0.00774	0.368
R1c	6	75	270	0.00107 (7.85e-04)	1.75 (0.39)	3.02e-04	1.60
R2a	16	70	220	4.05e-04 (2.32e-04)	1.01 (0.31)	7.12e-05	2.94
P6c	17	155	488	3.40e-04 (1.57e-04)	1.60 (0.39)	6.06e-05	0.809
P6d	26	197	650	5.95e-04 (1.22e-04)	2.18 (0.21)	2.44e-05	0.704
P1c	35	50	276	0.00129 (6.10e-04)	2.30 (0.25)	1.48e-04	0.313
P1d	23	39	237	3.78e-04 (4.08e-04)	2.18 (0.56)	2.23e-04	0.163
P1e	56	57	533	5.13e-04 (1.01e-04)	2.20 (0.16)	1.50e-05	0.234
P1f	4	81	433	6.48e-04 (5.60e-04)	2.60 (0.77)	4.11e-04	0.193
P2a	11	72	298	0.00156 (0.00141)	2.46 (0.61)	8.46e-04	1.16
P2b	6	98	442	5.16e-04 (2.56e-04)	1.69 (0.35)	8.61e-05	0.149
P2c	30	132	562	5.18e-04 (1.41e-04)	1.98 (0.23)	3.14e-05	1.76
P4b	3	155	190	0.0279 (0.117)	3.86 (3.21)	0.376	0.105
R1d	48	71	525	3.85e-04 (6.20e-05)	1.48 (0.13)	7.48e-06	2.73
R2b	30	110	474	0.00111 (2.18e-04)	1.79 (0.16)	3.30e-05	5.81
P7a	3	124	320	0.00150 (0.00143)	2.41 (0.68)	9.42e-04	0.344
P7b	8	116	332	7.91e-04 (7.19e-04)	2.28 (0.66)	4.69e-04	0.696
R2c	11	302	620	3.59e-04 (1.28e-04)	1.03 (0.39)	4.82e-05	1.01
R3b	5	196	364	2.46e-04 (2.08e-04)	0.73 (0.66)	1.36e-04	1.93

Table B.5: Mass fit results for Kajikawa early aggregates, rosettes and other assemblages.

Habit	N	Dmin	Dmax	α	β	Covariance	Normed
		μm	μm	(cgs)			chi-sq
P1e(a)	52	190	790	3.32e-04 (3.52e-05)	1.84 (0.120)	3.94e-06	4.06
P1c(a)	4	190	400	3.87e-04 (2.66e-04)	1.95 (0.567)	1.46e-04	9.40
P2e(a)	16	165	530	4.32e-04 (1.15e-04)	1.81 (0.233)	2.57e-05	3.00
P2a(a)	69	180	770	4.64e-04 (3.92e-05)	1.81 (0.091)	3.36e-06	5.44
P1b(a)	4	155	235	0.0155 (0.0217)	3.49 (0.839)	0.0181	0.473
R1c(a)	3	115	370	8.65e-05 (5.27e-05)	0.482 (0.386)	1.95e-05	0.174
P6d(a)	11	255	660	3.59e-04 (5.99e-05)	1.74 (0.200)	1.08e-05	5.55
R1d(a)	23	220	630	3.48e-04 (6.23e-05)	1.52 (0.182)	1.08e-05	2.85
C2b	5	40	60	9.82e-05 (8.81e-08)	-2.20 (3.01)	2.65e-07	0.248
S3	15	55	145	3.95e-04 (3.74e-04)	1.47 (0.407)	1.51e-04	0.596
S2	15	65	180	9.53e-04 (9.80e-04)	1.88 (0.468)	4.57e-04	0.383
CP2a	5	75	120	0.0329 (0.107)	3.29 (1.42)	0.151	0.383
C2a	32	40	185	0.00218 (0.00110)	2.03 (0.218)	2.37e-04	0.596

Table B.6: Area fit results for Kajikawa pristine particles.

Habit	N	Dmin	Dmax	γ	σ	Covariance	Normed
		μm	μm	(cgs)			chi-sq
P1a	32	25	149	0.525 (0.116)	1.96 (0.09)	0.0109	1.41
C1h	8	30	54	1.28 (2.21)	2.18 (0.55)	1.21	0.136
P1b	19	39	162	0.429 (0.105)	1.91 (0.11)	0.0112	0.788
P2e	18	47	211	0.414 (0.087)	2.02 (0.11)	0.00943	1.77
P2f	5	83	234	0.291 (0.100)	1.78 (0.18)	0.0178	0.605
P2g	10	70	280	0.596 (0.145)	2.24 (0.15)	0.0211	1.17
R1c	6	75	270	0.186 (0.048)	1.51 (0.13)	0.00607	1.25
R2a	16	70	220	0.286 (0.070)	1.72 (0.13)	0.00906	2.80
P6c	17	155	488	0.268 (0.038)	1.81 (0.11)	0.00410	1.38
P6d	26	197	650	0.370 (0.035)	2.08 (0.09)	0.00301	0.846
P1c	35	50	276	0.295 (0.038)	1.88 (0.06)	0.00236	1.48
P1d	23	39	237	0.172 (0.031)	1.78 (0.09)	0.00259	0.790
P1e	56	57	533	0.291 (0.016)	1.94 (0.04)	5.67e-04	1.33
P1f	4	81	433	0.220 (0.042)	1.78 (0.12)	0.00472	0.271
P2a	11	72	298	0.231 (0.045)	1.71 (0.12)	0.00532	1.17
P2b	6	98	442	0.186 (0.040)	1.62 (0.13)	0.00526	1.64
P2c	30	132	562	0.212 (0.024)	1.62 (0.09)	0.00200	1.47
P4b	3	155	190	0.883 (1.517)	2.54 (0.97)	1.47	0.0618
R1d	48	71	525	0.335 (0.023)	1.89 (0.05)	0.00108	1.59
R2b	30	110	474	0.352 (0.035)	1.91 (0.07)	0.00243	1.47
P7a	3	124	320	0.349 (0.117)	2.02 (0.21)	0.0239	0.304
P7b	8	116	332	0.595 (0.156)	2.45 (0.18)	0.0274	1.14
R2c	11	302	620	0.406 (0.079)	2.10 (0.21)	0.0159	3.26
R3b	5	196	364	0.318 (0.112)	1.91 (0.27)	0.0297	2.94

Table B.7: Area fit results for Kajikawa early aggregates, rosettes and other assemblages.

Habit	N	Dmin	Dmax	γ	σ	Covariance	Normed
		μm	μm	(cgs)			chi-sq
P1e(a)	52	190	790	0.156 (0.009)	1.74 (0.06)	4.69e-04	3.69
P1c(a)	4	190	400	0.148 (0.043)	1.50 (0.22)	0.00919	1.71
P2e(a)	16	165	530	0.154 (0.022)	1.72 (0.11)	0.00233	5.89
P2a(a)	69	180	770	0.201 (0.010)	1.76 (0.05)	4.51e-04	2.86
P1b(a)	4	155	235	0.568 (0.388)	2.22 (0.39)	0.152	0.497
R1c(a)	3	115	370	0.090 (0.022)	1.17 (0.15)	0.00304	1.96
P6d(a)	11	255	660	0.246 (0.026)	2.08 (0.11)	0.00281	1.36
R1d(a)	23	220	630	0.164 (0.017)	1.65 (0.10)	0.00156	2.31
C2b	5	40	60	–	–	–	–
S3	15	55	145	0.254 (0.095)	2.05 (0.16)	0.0151	3.40
S2	15	65	180	0.134 (0.045)	1.65 (0.15)	0.00665	0.650
CP2a	5	75	120	0.266 (0.312)	2.01 (0.51)	0.158	0.758
C2a	32	40	185	0.408 (0.091)	2.17 (0.09)	0.00838	3.43